PSI-1457/1530/
TR-2208

Infrasonic Frequency Sensor System for Preventing Third Party Damage to Gas Lines

Final Report for the period 8 November 2004 – 31 March 2007

Contract: Agreement 12/02/02 Phase 2B

Marten F. Byl, Gary R. Galica, Surjeet K. Paintal, William B.G. Agassounon, and B. David Green

Prepared for:

Northeast Gas Association
1515 Broadway, 43rd Floor
New York, NY 10036-5701

2 April 2007

Physical Sciences Inc.
20 New England Business Center
Andover, MA 01810

The technical data contained herein was prepared at private expense and shall not be released without the appropriate protections; i.e., Non-disclosure Agreements and Notices

This document contains proprietary information of Physical Sciences Inc. and is to be used only for the purpose for which it has been supplied. This document shall not be duplicated nor disclosed in whole or in part without prior written permission from a duly authorized representative of Physical Sciences Inc. The data subject to this restriction are contained in the sheets marked Confidential Proprietary Information within the document.

Acknowledgement of Support and Disclaimer

This material is based upon work supported by the Department of Transportation and the Northeast Gas Association under Contract Number DTRS56-04-T-0007. Any opinions, findings and conclusions or recommendations expressed in this material are those of the author(s) and do not necessarily reflect the views of DoT and NGA.

TABLE OF CONTENTS

Section Page

1. Introduction 1
   1.1 Sensor Development 3
   1.2 Algorithm Development 4
   1.3 Field Testing 4
2. EP-1 Sensor Development 5
   2.1 Optimizing Sensor Response 5
   2.2 Mechanical design 6
   2.3 PIGPEN EP-1 Sensor Development 8
   2.4 EP-1 Algorithm Development 12
   2.5 Fabrication of Six PIGPEN EP-1 Sensors and Data Acquisition System 16
   2.6 Test and Calibration of EP-1 Sensors 17
3. Field Test Preparations 23
   3.1 Field Test Sites 23
   3.2 EP-1 Data Acquisition System 24
   3.3 Field Checkout – Somerset, MA 27
4. Johnson City Field Test 31
   4.1 Signatures 37
   4.2 EP-1 Sensitivity and Range 48
   4.3 Signature Variability of Similar Equipment 49
   4.4 Signature Variation with Time 50
   4.5 Triangulation 51
   4.6 Algorithm Testing 57
   4.7 Optimization of Algorithm 60
5. Post Johnson City Field Test Improvements/Analysis 60
   5.1 Develop Alternative Data Acquisition System 60
   5.2 Site Characterization Data 62
   5.3 Triangulation Data 67
   5.4 Interaction with Geophysical Consultant 68

6. EP-2 Design 69
6.1 EP-1 Data Review and EP-2 Design Review 71
6.2 EP-2 Field Checkout and Field Test 71
6.3 Network Interface Specifications.....75
6.4 Additional Field Testing Requirement.....76
7. Planned PIGPEN Testing in Complex Soil Conditions (Kansas Field Test).....78
7.1 Introduction.....78
7.2 Field test Plan Overview.....78
7.3 Test Site 80
7.4 Test Equipment 81
7.5 Test Configurations.....81
7.6 Schedule.....84
7.7 Analysis of Kansas Field Testing 85
7.8 Geophysical Modeling Effort 137
7.9 Summary.....139
Appendix A 141
Appendix B 153
Appendix C 157

LIST OF FIGURES

Figure		Page
1.	Detailed drawing of inertial mass and restraint system.	7
2.	Overall assembly drawing.	7
3.	Mechanical configuration of EP-1.	9
4.	Expected noise from the EP-1 sensor compared to the Phase 1 electronics.	11
5.	Frequency response of the EP-1 amplifier compared to the Phase 1 amplifier.	11
6:	(a) PIGPEN signal generated by a backhoe digging intermittently over a 1-minute time period, (b) Preliminary threat detection result.	13
7:	(a) Power spectral density of signal generated using a jackhammer (b) Power spectral density of signal generated using a backhoe	13
8	(a) Filter bank architecture for spectral analysis (b) Example of frequency responses of ideal filters.	14
9:	(a) Signature of signal generated using a jackhammer (b) Signature of signal generated using a backhoe.	14
10.	Probability of detection and false alarm using preliminary robust identification algorithm.	16
11.	EP-1 sensor head exterior.	16
12.	EP-1 sensor head interior.	17
13.	EP-1 and wireless data acquisition system.	17
14.	Natural frequency sweep of EP-1. There is a strong resonance at 1100 Hz, that is close to the predicted natural frequency of 1200 Hz. There is also a weaker resonance near 400 Hz.	18
15.	Response of EP-1 during excitation at 80-120 Hz. The weak resonance at 375 Hz is 45-50 dB less weaker than the excitation signature.	19
16.	There is no visible amplification when the sensor is excited near the 375 Hz resonance.	20
17.	Signal and Power Spectral Density from PIGPEN EP-1 during 0.1 G 10 Hz excitation.	21
18:	Candidate test site, Rehobeth MA.	24
19.	Radiotronix short-haul transceiver.	25
20.	Block diagram of EP-1 and wireless data acquisition system.	25
21.	Data illustrating buffering time lag and data drop-outs.	26

22. Aerial view of Somerset site showing location relative to a nearby river and highway.. 27

23. Sensor geometry at Somerset site. 28

24. Background time series (top) and spectral (bottom) data from the 19 Apr 05 field test in Somerset, MA. 29

25. Backhoe time series (top) and spectral (bottom) data from the 19 Apr 05 field test in Somerset, MA. 30

26 Signatures of a backhoe previously acquired during an Aug03 field test as part of the NGA Phase 2A program..... 31

27. Johnson City Field Test layout. 32

28. Trackhoe (right) and backhoe (left). 34

29. Jackhammer attachment to Trackhoe..... 34

30. Tamper. 35

31. EP-1 unit in the ground before backfilling. The TX unit remains above ground. 35

32. Noise measured at the Johnson City site compared to the EP-1 noise model and the measured Phase 1 system noise. 37

33. Data acquired during tamper operation: red = sensor1, blue = sensor2, green = sensor3. The top curve shows the time series data. The bottom curve shows the power spectral density. 39

34. Sensor 3 data during tamper operation (25.5 m range)..... 39

35. Sensor 1 data during tamper operation (80 m range)..... 40

36. Sensor 2 data during tamper operation (175 m range)..... 40

37. Data acquired during trackhoe digging operation: red = sensor1, blue = sensor2, black = sensor4. 41

38. Sensor 2 (175 m) data collected during trackhoe digging. 41

39. Data acquired during trackhoe idling: red = sensor1, blue = sensor2, black = sensor4. The spikes in the time series data represent data drop-outs in the wireless communication system. 42

40. Sensor 4 (80 m) data collected during trackhoe idling. 42

41. Data acquired during wheeled backhoe digging: red = sensor1, blue = sensor2, green = sensor3, black = sensor4..... 43

42. Sensor 2 (175 m) data collected during backhoe digging..... 43

43. Data collected during jackhammer operation: red = sensor1, blue = sensor2, green = sensor3..... 44

44. Sensor 2 (175 m) data collected during jackhammer operation. 44
45. Sensor 1 (70 m) data collected during jackhammer operation. 45
46. Sensor 3 (25.5 m) data collected during jackhammer operation. 45
47. Data collected while backhoe is driving back and forth. 46
48. Sensor 2 data collected while backhoe is driving back and forth. 46
49. Sensor 3 data collected while backhoe is driving back and forth. 47
50. Data collected while the trackhoe bucket hits the ground. 47
51. Data collected while a passenger vehicle idles roughly 30 m from sensor 4. 48
52. Trackhoe (top) and backhoe (bottom) signatures acquired with sensor 2. 49
53. Backhoe signatures acquired at different times with sensor 2. The bottom trace was acquired at 08:30:51and the top trace at 11:25:07. 50
54. Data of hammer strokes acquired with sensors collocated. 51
55. Expanded scale of Figure 38 showing time lags around t = 3 sec. 52
56. Expanded scale of Figure 38 showing time lags around t = 8 sec. 52
57. Cross-correlation between two simple waveforms. 54
58. Cross-correlation of sensors 2 and 3 from hammer stroke data. The blue curve is the raw correlation function. The red curve is the running average. 55
59. Time series data acquired while trackhoe is hitting the ground with its shovel. 56
60. Cross-correlation of sensors 2 and 3 for data between t=6 sec and t=8 sec. 56
61. Result of processing 18 backhoe files (4 sensors) through the preliminary threat identification algorithm. No attempt was made to optimize the algorithm before the test. 58
62. Result of processing 8 cement mixer files through the preliminary threat identification algorithm. No attempt was made to optimize the algorithm before the test. 58
63. Result of processing 38 jackhammer files through the preliminary threat identification algorithm. No attempt was made to optimize the algorithm before the test. 59
64. Result of processing 54 tamper files through the preliminary threat identification algorithm. No attempt was made to optimize the algorithm before the test. 59
65. Build-2 algorithm result for backhoe (left) and jackhammer (right) identification. 60
66. Wireless data acquisition system used at the Johnson City test. 61

67. The wireless acquisition system introduced non-reproducible times lags between the four sensor data streams. 61

68. Analog DAQ system that will ensure relative synchronization of the four sensor data streams. 62

69. The measurement configuration for the site characterization. 63

70. Unfiltered data from site characterization measurements. 64

71. 200 Hz high-pass filtered data from site characterization. 65

72. Overlay of unfiltered and 200 Hz high-pass filtered data. 66

73. Aerial view of Andover field test site. 67

74. EP-1 sensor head integrated with the DSP board to create EP-2. 69

75. Time series data (top) and intermediate algorithm outputs (bottom). The bottom trace shows an overlay of the Build-2 MATLAB algorithm and the Build-2 DSP algorithm. The agreement is excellent. 70

76. Spectra acquired and calculated by the DSP during excitation with three known frequencies. 71

77. PIGPEN EP-1 sensor head and EP-2 prototype processor. 72

78. EP-2 test; 50 yards; no threat. 73

79. EP-2 test; 50 yards; jackhammer on. 73

80. EP-2 test; 50 yards; jackhammer on. 74

81. EP02 test; 200 yards; no threat. 74

82. EP-2 test; 200 yards; jackhammer on. 75

83. EP-2 test; 200 yards; jackhammer on. 75

84. Surface waves refract at interfaces of differing soil types leading to erroneous calculation of source location. 77

85. Schematic configuration of the proposed complex soil condition field test. 79

86. Topographic map of the site. 80

87. Aerial photograph of the site. 80

88. Configuration 1: 3 sensor T formation in both soil types. 82

89. Configuration 1: Three sensor T formation (blue stars) and impact locations (red circles) 82

90. Rough sensor locations for long and short field tests. 83

91. Error Field for a 100 x 100 m Diamond for a uniform soil speed of 1600 ft/s with a zero mean 0.002 s Gaussian Time Error. 83

92. Sensor (Blue Stars) and Impact Locations (A-C). 84

93. Aerial photograph of the site and sensor configurations 1A and 1B. The "A" region comprises sandy loam. The "B" region comprises shale/limestone. 86

94. Sensor and threat positions for Configurations 1A and 1B. 87

95. Aerial photograph of the test site overlaid with the sensor and threat positions for configurations 2 and 3. 87

96. Elevation contours of the site. 88

97. Photograph of the Kansas site looking south. The field is in the foreground. The shale/limestone ridge is in the background. 88

98. The downhole gun close-up. 89

99. Downhole gun in operation. 89

100. Case 580 Super L backhoe. 89

101. Average Signal to Noise ratio vs Threat Position in sandy loam. (Solid black line indicates the minimum SNR required for analysis). 91

102. Average Signal to Noise ratio vs Threat Distance in sandy loam. 92

103. Average Time Difference of Arrival between Sensors 1 and 2, and Sensors 1 and 3 versus path length difference. 93

104. Time difference of arrival between sensors 2 and 3 versus threat location. 94

105. Time difference of arrival between sensors 1 and 2, and sensors 1 and 3 versus threat location. 95

106. Down-hole gun signature in sandy loam. 96

107. Down-hole gun power spectral density signature in sandy loam. (A – Raw data, B- Filtered Data) 96

108. Average signal to noise ratio versus threat position for configuration 1B (TShale). 98

109. Average signal to noise ratio versus distance for configuration 1B (TShale). 99

110. Average time difference of arrival for sensors 1 and 2, and sensors 1 and 3 versus path length difference. Time difference determined from cross-correlation. 100

111. Time difference of arrival between sensors 1 and 2, and sensors 1 and 3 versus threat location. 100

112. Time difference of arrival between sensors 2 and 3 for threat positions 1 through 6 in shale. 101

113. Time signature for a rifle shot at threat position T1 in the shale (Sensor 4 not active). 102

114. Power spectral density plot for a rifle shot at threat position T1 in the shale (time series shown in Figure 20). 102

115. Spectrograph for a rifle shot at threat position T1 in the shale (time series shown in Figure 113). 103

116. Low pass filtered cross-correlation output for a shot at threat location T1 in the shale. 104

117. Average time difference of arrival for sensors 1 and 2, and sensors 1 and 3 versus distance. Time difference determined from wave front arrival. 105

118. Average time difference of arrival for sensors 1 and 2, and sensors 1 and 3 versus distance. Time difference determined from wave front arrival. 106

119. Average time difference of arrival for sensors 2 and 3 versus distance. Time difference determined from wave front arrival. 107

120. Time signature for a rifle shot at threat position T2 in the shale (Sensor 4 not active). 107

121. Power spectral density plot for a rifle shot at threat position T2 in the shale (time series shown in Figure 27). 108

122. Low pass filtered cross-correlation output for a shot at threat location T1 in the shale. 108

123. Spectrograph for a rifle shot at threat position T2 in the shale (time series shown in Figure 27). 109

124. Signal to noise ratio vs distance along the BE threat line. 112

125. Signal to noise ratio for sensors 1 and 2 versus distance along BE threat line. 112

126. Signal to noise ratio for sensors 3 and 4 versus distance along the BE threat line. 113

127. Signal to noise ratio vs distance along the C threat line. 114

128. Signal to noise ratio for sensors 1 and 2 versus distance along C threat line. 115

129. Signal to noise ratio for sensors 3 and 4 versus distance along the C threat line. 115

130. Signal to noise ratio vs distance along the BW threat line. 117

131. Signal to noise ratio for sensors 1 and 2 versus distance along BW threat line. 117

132. Signal to noise ratio for sensors 3 and 4 versus distance along the BW threat line. 118

133. Signal to noise ratio vs distance along the AE threat line. 119

134. Signal to noise ratio for sensors 1 and 2 versus distance along AE threat line. 120

135. Signal to noise ratio for sensors 3 and 4 versus distance along the AE threat line. 120

136. Signal to noise ratio vs distance along the BE threat line. 121

137. Signal to noise ratio for sensors 1 and 2 versus distance along BE threat line. 122

138. Signal to noise ratio for sensors 3 and 4 versus distance along the BE threat line. 122

139. Signal to noise ratio vs distance along the C threat line. 123

140. Signal to noise ratio for sensors 1 and 2 versus distance along C threat line. 123

141. Signal to noise ratio for sensors 3 and 4 versus distance along the C threat line. 124

142. Average time difference of arrival for sensors 1 and 2 versus distance C threat line. Time difference determined from both wave front arrival and cross correlation. 125

143. Signal to noise ratio vs distance along the BW threat line. 126

144. Signal to noise ratio for sensors 1 and 2 versus distance along BW threat line. 127

145. Signal to noise ratio for sensors 3 and 4 versus distance along the BW threat line. 127

146. Average time difference of arrival for sensors 1 and 2 versus distance BW threat line. Time difference determined from both wave front arrival and cross correlation. 128

147. Signal to noise ratio vs distance along the AW threat line. 129

148. Signal to noise ratio for sensors 1 and 2 versus distance along AW threat line. 130

149. Average time difference of arrival for sensors 1 and 2 versus distance AW threat line. Time difference determined from both wave front arrival and cross correlation. 130

150. Power spectral density for the backhoe during bucket impact (Location AE180). 132

151. Power spectral density for the backhoe idling (Location BW120). 132

152. Backhoe signal to noise ratio versus distance. 59(A) Impact versus Backhoe Idle. 59(B) Impact versus quite background (no equipment). 59(C) Backhoe idle versus quite background. 133

153. Backhoe signal to noise ratio versus distance. 60(A) Impact versus Backhoe Idle. 60(B) Impact versus quiet background (no equipment). 60(C) Backhoe idle versus quiet background. 134

154. Spectrogram of the Backhoe impacts. 135

155. Spectrogram of the backhoe idling. 135

156. Time signature of the backhoe impacts at BE180. 137

157. Geophysical modeling results for the Andover field site (Simulated results left, measured fieldtest data right). 139

LIST OF TABLES

Table		Page
1.	Comparison Matrix for Sensor Selection	5
2.	Sensitivity and Noise for Several Sensor Configurations	10
3.	Predicted and Measured Responses of EP-1 (relative to the bare sensor)	21
4.	Summary of EP-1 Absolute Response	21
5.	Results of Restraining Pin Characterization	22
6.	Sensor Response as a Function of Tilt Angle	23
7.	Summary of Sensor and Threat Positions.	33
8.	Summary of Equipment at Johnson City Field Test	33
9.	Summary of Data Collected and Configuration During Johnson City Field Test	36
10.	Summary of Example Signatures Included in the Report	38
11.	Tamper Fundamental Frequency Signal Intensity as a Function of Range and Extrapolated Effective Range	48
12.	Summary of Time Lags Between Sensors from t = 3 sec and t = 8 sec of Figure 53	53
13.	Comparison of Cross-Correlation Results Using Raw Correlation Function and Smoothed Correlation Function with the Best Eyeball Determination of the Time Lags	55
14.	Data Sets Used to Test Preliminary Algorithms	57
15.	Summary of Triangulation Measurement Results	68
16.	Test Plan Summary	85
17.	Cross-Correlation output for TLoam	97
18.	Cross-Correlation and Manual Time Difference of Arrival Values for Configuration 1B	110
19.	Cross-Correlation and Manual Time Difference of Arrival for Longfield BE Threat Line	113
20.	Cross-Correlation and Manual Time of Arrival for Longfield C Threat Line	116
21.	Cross-Correlation and Manual Time of Arrival for Longfield BW Threat Line	118
22.	Cross-Correlation and Manual Time of Arrival for Shortfield C Threat Line	125
23.	Cross-Correlation and Manual Time of Arrival for Shortfield BW Threat Line	128
24.	Cross-Correlation and Manual Time of Arrival for Shortfield AW Threat Line	131
25.	Preliminary Cross-Correlation Backhoe BW Threat Line	136
26.	Preliminary Cross-Correlation Backhoe BE Threat Line	136

ABSTRACT

This report details the Phase 2B program to develop and demonstrate the performance of the PIGEN infrasonic sensors in detecting real world threats with performance adequate to warrant its commercial application to third party damage avoidance. In this stage of the program we improved the sensor head performance, improved the electronics, improved the algorithms and detection approach. We demonstrated system performance in two separate field tests.

1. Introduction

In the initial stages of the program PSI optimized the sensor response, the analog amplifier design to improve noise performance, and developed threat identification algorithms all in preparation for the demonstration field test. The expected noise of the EP-1 system is at least 10 dB less than the Phase 1 electronics noise. This translates into extended detection range. Our goal for typical threat sources is 500 – 1000 meters with a SNR of 6 or 16 dB.

After completing the PIGPEN EP-1 sensor design, we fabricated six PIGPEN EP-1 sensors and the data acquisition system. We then tested and calibrated the EP-1 sensors on the bench. Analysis of the calibration data indicated that design goals had been achieved. This system has wireless communication between the individual sensors.

The main conclusions we draw from our initial testing and analyses include:

- EP-1 met all of its design criteria
- EP-1 natural frequency is 1100 Hz (goal >1000 Hz)
- EP-1 responsivity is 12 dB greater that the Phase 1 sensor (goal 10 dB increase)
- EP-1 noise is 15-25 dB lower than Phase 1 sensor (goal 10 dB decrease)
- EP-1 response is not affected by non-level mounting up to 30 deg (PDR action item)

We then prepared the system for field checkouts near PSI's facility and in Johnson City, New York. The purpose of the checkouts was to verify system performance and validate algorithm performance. We were able to further optimize the threat algorithm using data from these tests. We also further characterized the test site measurements to support consultant activities to develop concepts to compensate for complex geological conditions. At the Andover location we were able to make the first measurements of triangulation performance.

We acquired three days of field data with four EP-1 units at a site near PSI (Somerset, MA) and at a NGA site (Johnson City, NY). The sensors performed well.

We measured the signatures of all the equipment available during the Johnson City Test with high SNR at ranges up to 175 m. The signatures are similar to previously acquired data but have significantly higher SNR. From the Johnson City data, we extrapolated the maximum range for the sensor to be 1750 m with SNR=16 dB under quiet conditions.

During the Johnson City test, we acquired data from two types of excavators at multiple times over the two day test. The variability in these data will enable us to ensure that the algorithms are robust.

Upon detailed analysis of the data, we determined that the relative timing of the four EP-1 data streams was corrupted by the data acquisition system. As a result, the site characterization data from Johnson City is of limited use. The triangulation data can be used; however, we cannot determine absolute range. We demonstrated 3.5 m (11 ft) triangulation accuracy at a nominal range of 150 m (490ft), thus satisfying the design goal

We demonstrated the ability to process the data to autonomously determine a range using a cross-correlation technique. Because the data acquisition system corrupted the timing of the data streams, we were unable to determine absolute range.

The algorithm correctly identifies jackhammer and backhoe signatures from several pieces of equipment. The Build-2 algorithm was fully implemented and tested on the EP-2 hardware.

This analysis and discussions with our development partners guided the design of the EP-2 system, culminating in a design review. EP-2 was fabricated and tested in the laboratory testing. We also fabricated a second data acquisition system as an alternative to the wireless data acquisition system used in the Johnson City field test. At Johnson City we chose wireless communication to enable acquisition at long distances between sensors and to acquire data from all sensors simultaneously and synchronously. However, the wireless system introduced non-reproducible artifacts in the data that made it impossible to perform triangulation analysis.

PSI provided requirements to NYSEARCH for communication and other interface to NYSEARCH's real time sensing system called GasNet. We discussed plans for extending the work for numerical modeling and field tests in complex soil conditions to address valid concerns about location accuracy raised by the independent consultant (Prof. Don Steeples). recommendation regarding location accuracy. PSI participated in discussions with NYSEARCH regarding PIGPEN specifications and triangulation accuracy requirements. We undertook this program with a goal of repeatedly achieving 10 foot location accuracy in all soil conditions.

After a several month hiatus, we were pleased to perform a second field test at a site in Kansas which was identified by Prof. Steeples. The site had a sharp boundary discontinuity between loam vs shale. As part of this program we prepared and undertook a full week of testing at the site, with the support and guidance of Mr. Janega of NYSEARCH and Prof. Steeples (Kansas Univ.). We completed the entire test matrix obtaining over 500 acoustic events in multiple sensor configurations. We were able to verify real time (via computer display) that the PIGPEN sensors detected over 99% of these events. PSI conducted an extensive analysis of the large data set collected during the November field test near Lawrence, Kansas. This analysis has resulted in the following conclusions:

1. PIGPEN can detect the 30-06 down-hole rifle to a range of 400 ft in sand/loam.
2. PIGPEN can detect the 30-06 down-hole rifle to a range of 200 ft in limestone/shale.
3. Threat signatures are degraded 20-30 dB (depending on initial signal strength) as they transition from limestone to sand. We were able to observe attenuated threat signatures across this discontinuity in both directions.
4. In the best case, PIGPEN can localize threats repeatable to ±7 ft in sand (pg. 13)
5. In the best case, PIGPEN can localize threats repeatable ±9.6 ft in slate (pg. 22).
6. Worst cases exhibited much (10x) poorer performance.
7. We were able to observe the unique signature and repeated strikes from a Backhoe across the discontinuity at all sensors.

Due to the signal degradation across the soil discontinuity, PSI has not been able to establish the positional accuracy across the soil transition for the down-hole rifle acoustic source. In addition, positional accuracy may be degraded by steep slopes within soil types. Further algorithm development in conjunction with on-site calibration will be required to correct for non-uniform soil conditions.

Geophysical modeling of the Andover, MA test site have been completed.

In parallel with the analysis, PSI assembled and bench tested the components for an advanced prototype (AP) sensor network.

1.1 Sensor Development

1.1.1 Optimizing Sensor Response

- We used our validated sensor model to optimize the sensor performance and system noise characteristics.
- We compared the responsivity and noise performance of sensor with differing areas and thicknesses, layering and as consequence capacitance.
- The goal increase in sensitivity of 10 dB over our previous version sensor was achieved.
- The goal decrease in noise of 10-20 dB over our previous amplifier design was achieved.

1.1.2 Mechanical Design

- During the EP-1 we evaluated the shortcomings of the previous PIGPEN sensor design. We also considered the environment and handling circumstances the final instrument will need to survive in order to be successful.
- Because sensor orientation is critical to proper functioning, we designed the chassis to ensure the correct orientation naturally during installation.
- We made improvements in the design to minimize 60 Hz EMC noise transmitted both electrically and magnetically.
- We took significant steps toward making the sensor significantly more rugged, by constraining the inertial mass to eliminate shear and compressive forces that could damage the sensor.

1.1.3 PIGPEN EP-1 Sensor Design

PSI completed the design of the 1st PIGPEN Experimental Prototype (EP-1), including the mechanical design, front-end electronics design, and the preliminary algorithm. We presented the results of that design to the NYSEARCH committee at Design Review-1, held on 16 February 2005 in Saratoga Springs, NY. The design review information is found in PSI document VG05-031, “Infrasonic-Frequency Seismic Sensor System for Preventing Third Party Damage to Gas Lines”.

1.1.4. Fabrication of six PIGPEN EP-1 sensors and data acquisition system

Based on the approved design, PSI fabricated six EP-1 sensors. Those sensors included the sensor, weatherproof mechanical housing, and front-end electronics. We fabricated a data acquisition system that included wireless communication to enable data acquisition in the field at long ranges.

We also fabricated a wireless data acquisition system to transmit data simultaneously from each sensor to the control computer. During previous field tests, it was difficult to synchronize the data acquisition from multiple sensors because of the large distances between sensors. We chose the wireless communication to enable acquisition at long distances between sensors and to acquire data from all sensors simultaneously and synchronously.

1.1.5. Test and Calibration of EP-1 sensors

Though bench testing and calibration, we validated the EP-1 design. The EP-1 sensor met the design goals of increased sensitivity and reduced noise. The front-end electronics also met the desired frequency bandwidth requirements. The resonance frequency was out-of-band as designed. We conducted calibration testing at Sypris Test and Measurement in Burlington, MA. The facility achieved excitations of 3 Hz and 1/10 G. At Sypris, we measured the sensor response and identified the natural resonances of the EP-1.

1.2 Algorithm Development

During this EP phase, we refined our preliminary algorithms, and tailored them for the future on-board digital signal processor. We exercised them against our database of threat signatures collected during previous field tests. We concentrated on refining the threat detection and threat identification algorithms. The threat detection algorithm uses the time domain signal and follows two steps. First the signal is rectified because only its amplitude carries the necessary information (i.e., its sign does not matter). Secondly, the algorithm takes into account how long the amplitude of the rectified signal has remained high. Tests against our field-test database have shown promising results. We performed trade-offs to refine the methodology for the threat identification algorithm. We compared the performance using a full spectral technique (FFT and PSD calculations) to a filter bank technique applied in the time domain. We evaluated it against jackhammer and backhoe signatures.

We developed the circuit concept/architecture for the preamplifier based upon data acquired in previous program phases.

1.3 Field Testing

We identified local sites near PSI in Massachusetts suitable for preliminary field measurements. We prepared a draft test plan and the data acquisition system to support those field tests.

As part of the system checkout, we conducted three half-day field exercises at a location near PSI. At these field exercises, we acquired data using a sledgehammer as the source. We also conducted a full-day field checkout with a private contractor at a building site in the Boston area. At this field checkout, we acquired data of two types of excavators. These field exercises and checkouts were in preparation for the field test hosted by the Northeast Gas Association in Johnson City NY. That test was conducted on 25-27 April 2005.

We fabricated six PIGPEN EP-1 sensor units to participate in these tests. The EP-1 testing comprised three segments: 1) calibration and characterization at a vibration test facility, 2) field checkout at a site near PSI and, 3) field testing in Johnson City, NY in cooperation with the Northeast Gas Association (NGA).

2. EP-1 Sensor Development

2.1 Optimizing sensor response

We investigated methods for enhancing the performance of the sensor using our validated sensor model. The tradeoffs include sensor area and thickness (which dictate the response) and sensor capacitance (which dictates amplifier characteristics, frequency response and noise).

The predicted capacitance is important for designed an appropriate amplifier which is appropriately impendence matched to the sensor. One methodology for increasing the sensor performance (higher response and lowering noise floor) requires the use of multiply layers of PVDF connected in series. Table 1 compares the response of a single 28 micron layer, single 52 micron layer and that of a 2 52 micron layers connected in series. In prior work, a 52-micron thick single layer of PVDF was used in the sensor design.

Table 1. Comparison Matrix for Sensor Selection

response	thick	area	mass	losstan	rs	xc	njoh	ncurrent	cap	freq	njoh
dB re V/G	m	m^2	kg		ohms	ohms	V/Hz^0.5	A/Hz^0.5	F	Hz	dBreV 1 Hz
28 micron single layer											
-23.19	2.80E-05	6.10E-04	0.454	0.02	1.27E+07	6.35E+08	4.53E-07	7.13E-16	**2.51E-09**	0.10	-126.9
-23.19	2.80E-05	6.10E-04	0.454	0.015	9.53E+05	6.35E+07	1.24E-07	1.95E-15	**2.51E-09**	1.00	-138.1
-23.19	2.80E-05	6.10E-04	0.454	0.01	6.35E+04	6.35E+06	3.20E-08	5.04E-15	**2.51E-09**	10.00	-149.9
-23.19	2.80E-05	6.10E-04	0.454	0.005	3.18E+03	6.35E+05	7.16E-09	1.13E-14	**2.51E-09**	100.00	-162.9
-23.19	2.80E-05	6.10E-04	0.454	0.005	3.18E+02	6.35E+04	2.26E-09	3.56E-14	**2.51E-09**	1000.00	-172.9
52 micron single layer											
-17.82	5.20E-05	6.10E-04	0.454	0.02	2.36E+07	1.18E+09	6.17E-07	5.23E-16	**1.35E-09**	0.10	-124.2
-17.81	5.20E-05	6.10E-04	0.454	0.015	1.77E+06	1.18E+08	1.69E-07	1.43E-15	**1.35E-09**	1.00	-135.4
-17.81	5.20E-05	6.10E-04	0.454	0.01	1.18E+05	1.18E+07	4.36E-08	3.70E-15	**1.35E-09**	10.00	-147.2
-17.81	5.20E-05	6.10E-04	0.454	0.005	5.90E+03	1.18E+06	9.75E-09	8.27E-15	**1.35E-09**	100.00	-160.2
-17.81	5.20E-05	6.10E-04	0.454	0.005	5.90E+02	1.18E+05	3.08E-09	2.61E-14	**1.35E-09**	1000.00	-170.2
2 52 micron layers in parallel											
-11.80	1.04E-04	6.10E-04	0.454	0.02	2.36E+07	1.18E+09	6.17E-07	5.23E-16	**1.35E-09**	0.10	-124.2
-11.79	1.04E-04	6.10E-04	0.454	0.015	1.77E+06	1.18E+08	1.69E-07	1.43E-15	**1.35E-09**	1.00	-135.4
-11.79	1.04E-04	6.10E-04	0.454	0.01	1.18E+05	1.18E+07	4.36E-08	3.70E-15	**1.35E-09**	10.00	-147.2
-11.79	1.04E-04	6.10E-04	0.454	0.005	5.90E+03	1.18E+06	9.75E-09	8.27E-15	**1.35E-09**	100.00	-160.2
-11.79	1.04E-04	6.10E-04	0.454	0.005	5.90E+02	1.18E+05	3.08E-09	2.61E-14	**1.35E-09**	1000.00	-170.2

PSI Proprietary Information

For the EP-1 sensor we proposed to use 2 layers in series which will provide a higher response. For example, for a sensor composed of 2 layers of 52 micron PVDF connected in series, the predicted response is -11.8 dBreV/G. This is at least 10 dB reV/G higher than the response predicted for a single layer of 28 micron thick PVDF and 6 dBreV/G higher than the response predicted for a single layer of 52 micron thick PVDF while maintaining a comparable noise floor.

2.2 Mechanical Design

In designing the next generation of the pigpen instrument, we evaluated the Phase 1 design short-comings. We also considered the environment and handling circumstances the final instrument will need to survive in order to be successful.

2.2.1 Sensor Orientation

Sensor orientation is critical to proper functioning. To assure that the instrument in installed in the ground in the correct orientation, we have designed the box that encourages the correct orientation naturally. By having the output cable exit from the top center, the instrument will naturally be installed with this cable pointed up. This also limits the side loading on the cable by dirt and gravel as the instrument is buried. The cable will be strain relieved, so that it can withstand the inevitable, although discouraged, case of being lowered into the ground by the cord.

2.2.2 EMC Shielding

The phase one sensor proved to be susceptible to 60 Hz noise from AC power. In order to minimize this disturbance, we have located the sensor pre-amplifier as close to the sensor as possible. Minimizing the cable length between the sensor and the preamp with reduce its effectiveness as an antenna to pick up radiated magnetic EMI from overhead lines and nearby buildings. In addition, the cabling will be constructed to further reduce this susceptibility by twisting the wires.

2.2.3 Ruggedness

Mechanically the sensor is most susceptible to side loading during handling, such a being dropped or banged. The sensor is bonded to the enclosure and to the mass. This adhesive selection is critical in that it needs to provide enough strength to hold the components during a shear load, but not damped out the vibrations we are trying to measure. For the EP-1 design, we have added a central pin with precision bearing that minimizes the side loading on the adhesive and the sensor, but still allows minimally restricted vertical motion. The shear strength of the sensor was compared to the reduced load induced by the restricted motion. This load is well under the shear strength of the sensor.

The single degree of freedom sensor mass is restrained from motion in undesired directions by a pin and low friction bearing. The pin in the bearing allows vertical motion with minimal loss due to friction. The pin prevents lateral motion which could shear the adhesive and/or sensor. The pin also incorporates an anti-rotation device to eliminate the possibility of the sensor or adhesive failing in torsion. See Figure 1.

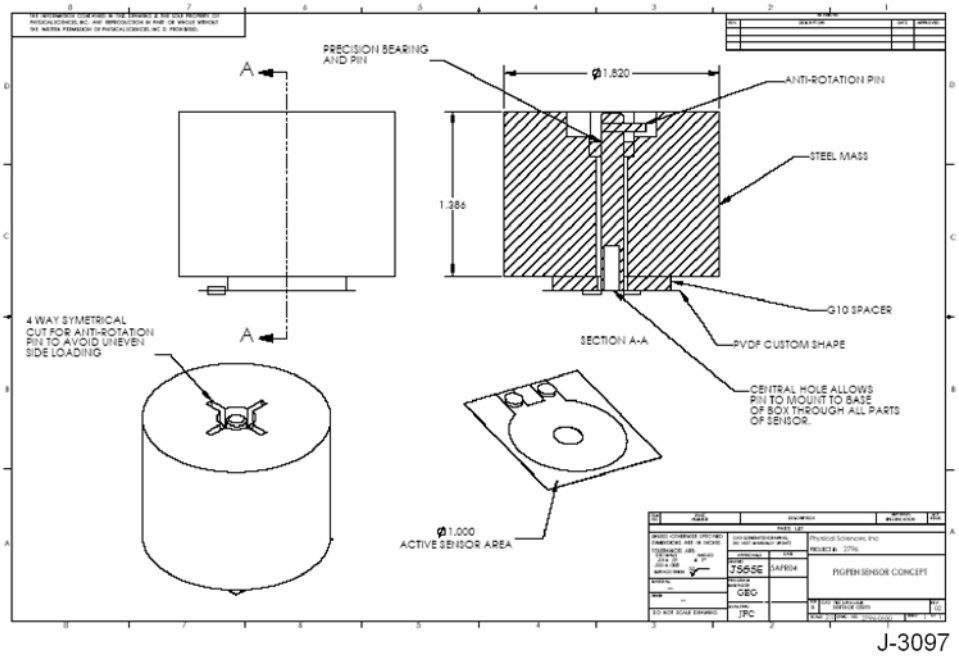

Figure 1. Detailed drawing of inertial mass and restraint system.

The only motion not prevented by the pin/bearing design is vertical motion if the sensor is turned upside down. This motion is only possible during handling. To prevent this motion that can damage the sensor, a latch has been added that must be released before deploying the device. The latch is a simple quarter turn mechanism that while activated engages a pawl that provides downward force to the top of the mass. The latch's slotted actuator clearly shows the position of the latch. The latch can be reengaged of necessary. See Figure 2.

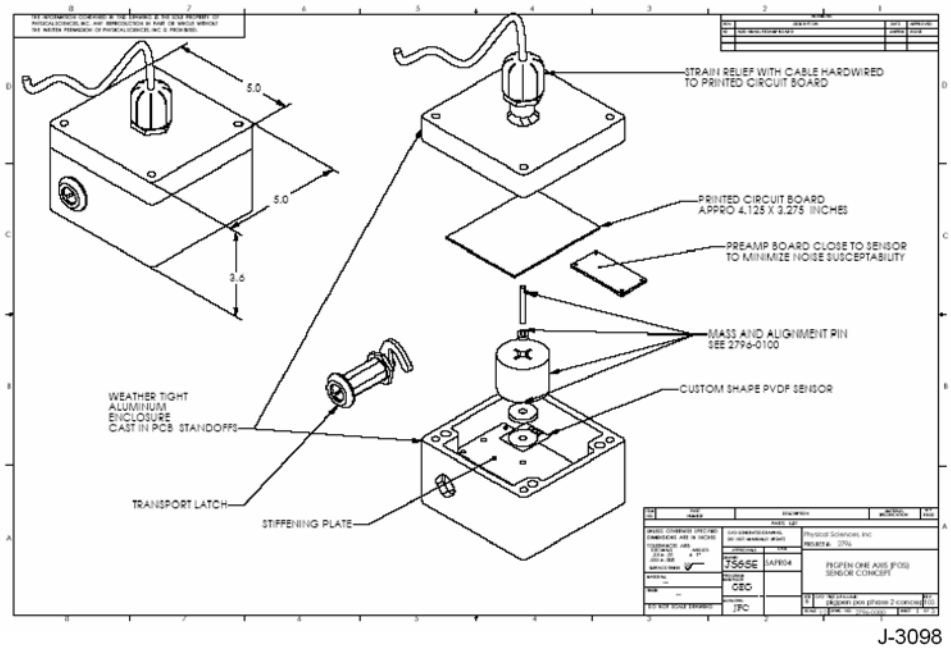

Figure 2. Overall assembly drawing.

PSI Proprietary Information

First the design of the custom shape of the PVDF sensor needed to be finalized with the sensor manufacturer. A concept to mount the sensor directly to the pre-amplifier circuit board to minimize electrical noise pick up was developed. These two items are the most critical to the functionality of the sensor. The pinned mass design was also finalized to minimize the off-axis motion at a minimum of fabrication cost. An off-the-shelf bearing and pin pair was used. The bearing is positioned in the opposite side of the mass to the sensor to minimize the moment arm of any motion. This also allows for a very shallow bearing hole, which minimizes machining costs. Another goal of the design is to minimize fasteners, which will keep assembly costs down for production volumes. The balance of the detail design involved working out the assembly sequence to make sure all the part would go together keeping in mind the adhesive steps. The goal of this phase of the mechanical design is to create as close to the final configuration as possible. The mechanical response of the sensor could affect the sensor output, so our goal was to create a design that will work for production there are no adverse results during the field test.

A model analysis was preformed to determine the natural frequency of the system. The goal was to put the sensors natural frequency outside of the measurement range. This analysis determined that the sensor mounting plate needed to be thicker and stiffer, as well as needing additional support in this area. These features were incorporated into the design. The final predicted natural frequency is over 1100 Hz.

The final design is shown in 2796-0000 rev 05.PDF. The major features are:

- IP66 enclosure
- Transportation latch to prevent sensor de-lamination during handling
- Direct sensor to pre-amp board connection
- Pinned mass to prevent side motion
- DSP board (developed in next phase) to be located away from sensitive pre-amp
- Offset cable out of top to maximize space for DSP

The DSP board design in scheduled for the next phase of the program. A very preliminary area study show the space allowed is marginal. The goal will be to minimize the board space, there for minimizing the instrument size. In case the DSP board does not fit, a design was completed that puts the entire sensor in the next largest enclosure of the same type.

Measurements were taken to determine the effect the pin has on the sensor output. These tests showed that there is no significant negative impact. All the parts were purchased and fabricated for several sensors for the field testing and demonstration.

2.3 PIGPEN EP-1 Sensor Development

PSI completed the design of the 1st PIGPEN Experimental Prototype (EP-1), including the mechanical design, front-end electronics design, and the preliminary algorithm. We presented the results of that design to the NYSEARCH committee at Design Review-1, held on 16 February 2005 in Saratoga Springs, NY. The design review information is found in PSI document VG05-031, ”Infrasonic-Frequency Seismic Sensor System for Preventing Third Party Damage to Gas Lines”. (Appendix 1)

PSI designed the EP-1 PIGPEN sensor with the intention that once validated, it will closely resemble the final PIGPEN deployed module. By making careful design choices during the EP development, we can avoid redesigning the sensor and electronics at each later development stage.

2.3.1 Mechanical Design

Figure 3 shows an overview of the mechanical design. The overall objective in the mechanical design was to develop a mechanical system for EP-1 as close to final configurations as possible. The overriding design considerations were that the sensor/preamplifier integration is critical to system performance and that ruggedization and environmental compatibility are important to final system.

We incorporated several design features to achieve our overall design goals:

- Box, latch, and strain relief sealed to IP66 or better
- Protection against the inlet of dust and water from a hose down condition
- Box size 5 x 5 x 3.6 inches
- Box is an off-the-shelf cast aluminum
- Cast in supports for the stiffening plate and the DSP board
- Reduced the number of parts and assembly time for production quantities
- First natural frequency of assembly < 1000 Hz
- Box and strain relief provide EMI shielding

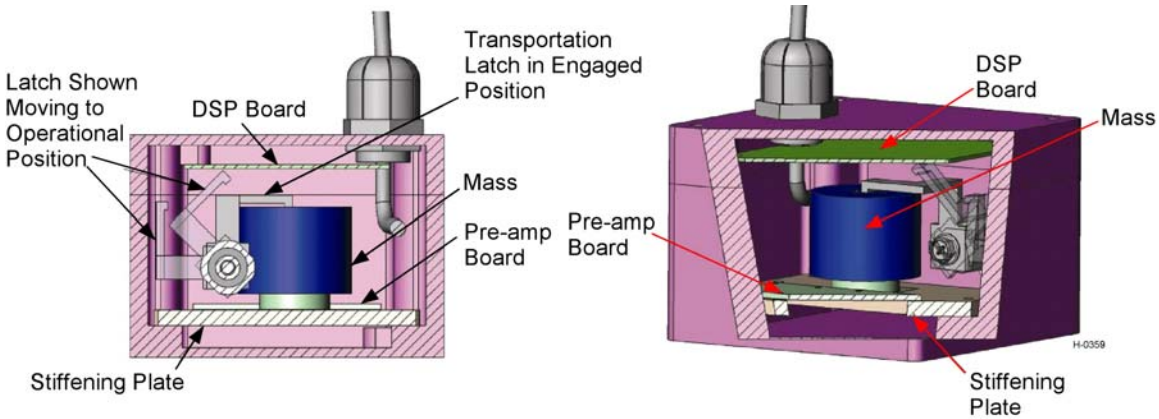

Figure 3. Mechanical configuration of EP-1.

2.3.2 Sensor and Electronics

Our goal for EP-1 performance was to increase the sensitivity by 10 dB and to decrease the electronics noise by 10 db, thereby achieving an improvement in performance of 20 db (in quiet conditions).

Table 2 shows a performance summary for several sensor configurations. The 28 micron single layer and 52 micron single layer sensors were used in earlier programs. The configuration chosen for EP-1 is the 2-layer 52 micron sensor in a "donut" configuration. **The response is more than 10 dB greater than previous sensors with comparable noise.**

Table 2. Sensitivity and Noise for Several Sensor Configurations

response	area	mass	njoh	ncurrent	cap	freq	njoh
dB re V/G	m^2	kg	V/Hz^0.5	A/Hz^0.5	F	Hz	dBreV 1 Hz
28 micron single layer 0.64" x 2.86" in strip							
-28.93	1.18E-03	0.454	3.25E-07	9.92E-16	**4.85E-09**	0.1	-129.8
-28.93	1.18E-03	0.454	8.91E-08	2.72E-15	**4.85E-09**	1.0	-141.0
-28.93	1.18E-03	0.454	2.30E-08	7.01E-15	**4.85E-09**	10.0	-152.8
-28.93	1.18E-03	0.454	5.14E-09	1.57E-14	**4.85E-09**	100.0	-165.8
-28.93	1.18E-03	0.454	1.63E-09	4.96E-14	**4.85E-09**	1000.0	-175.8
52 micron single layer 0.64" x 2.86" in strip							
-23.56	1.18E-03	0.454	4.43E-07	7.28E-16	**2.61E-09**	0.1	-127.1
-23.56	1.18E-03	0.454	1.21E-07	1.99E-15	**2.61E-09**	1.0	-138.3
-23.56	1.18E-03	0.454	3.13E-08	5.15E-15	**2.61E-09**	10.0	-150.1
-23.56	1.18E-03	0.454	7.01E-09	1.15E-14	**2.61E-09**	100.0	-163.1
-23.56	1.18E-03	0.454	2.22E-09	3.64E-14	**2.61E-09**	1000.0	-173.1
2 52 micron layers in parallel donut design							
-11.80	6.10E-04	0.454	6.17E-07	5.23E-16	**1.35E-09**	0.1	-124.2
-11.79	6.10E-04	0.454	1.69E-07	1.43E-15	**1.35E-09**	1.0	-135.4
-11.79	6.10E-04	0.454	4.36E-08	3.70E-15	**1.35E-09**	10.0	-147.2
-11.79	6.10E-04	0.454	9.75E-09	8.27E-15	**1.35E-09**	100.0	-160.2
-11.79	6.10E-04	0.454	3.08E-09	2.61E-14	**1.35E-09**	1000.0	-170.2

Figure 4 shows the calculated noise performance of the EP-1 sensor and electronics. Figure 4 shows noise from several sources including the sensor itself, the preamplifier voltage noise and preamplifier current noise. The noise of the Phase 1 system electronics is shown for reference. **The expected noise of the EP-1 system is at least 10 dB less than the Phase 1 electronics noise**.

Figure 5 shows the frequency response of the EP-1 electronics design calculated using SPICE. The frequency response of the Phase 1 electronics is shown for comparison. The EP-1 amplifier design will achieve the desired 0.1 to 500 Hz response bandwidth.

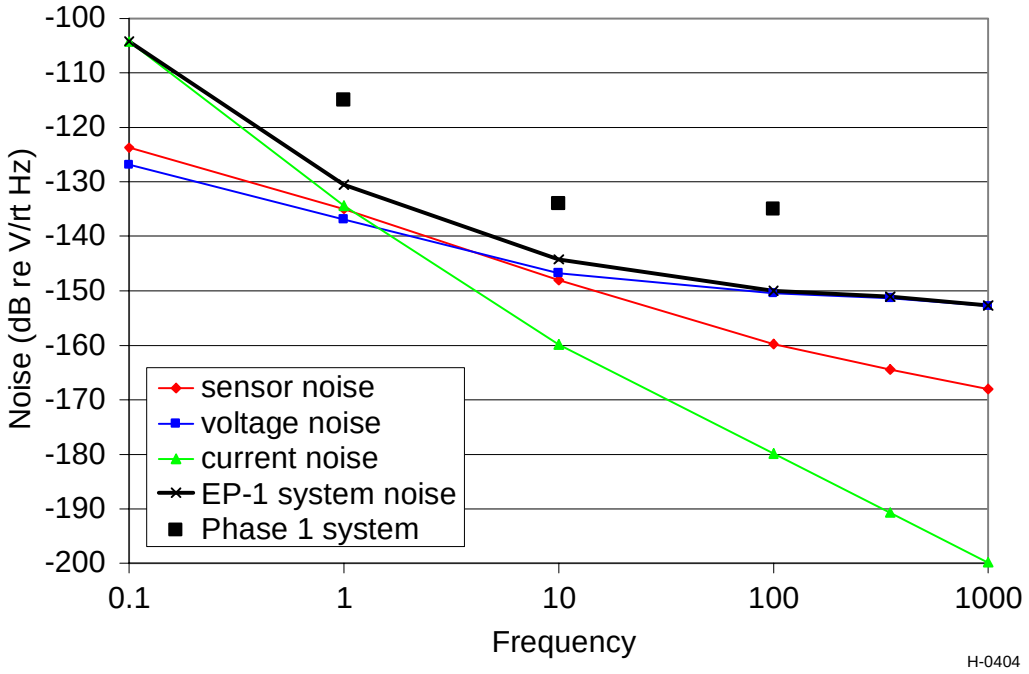

Figure 4. Expected noise from the EP-1 sensor compared to the Phase 1 electronics.

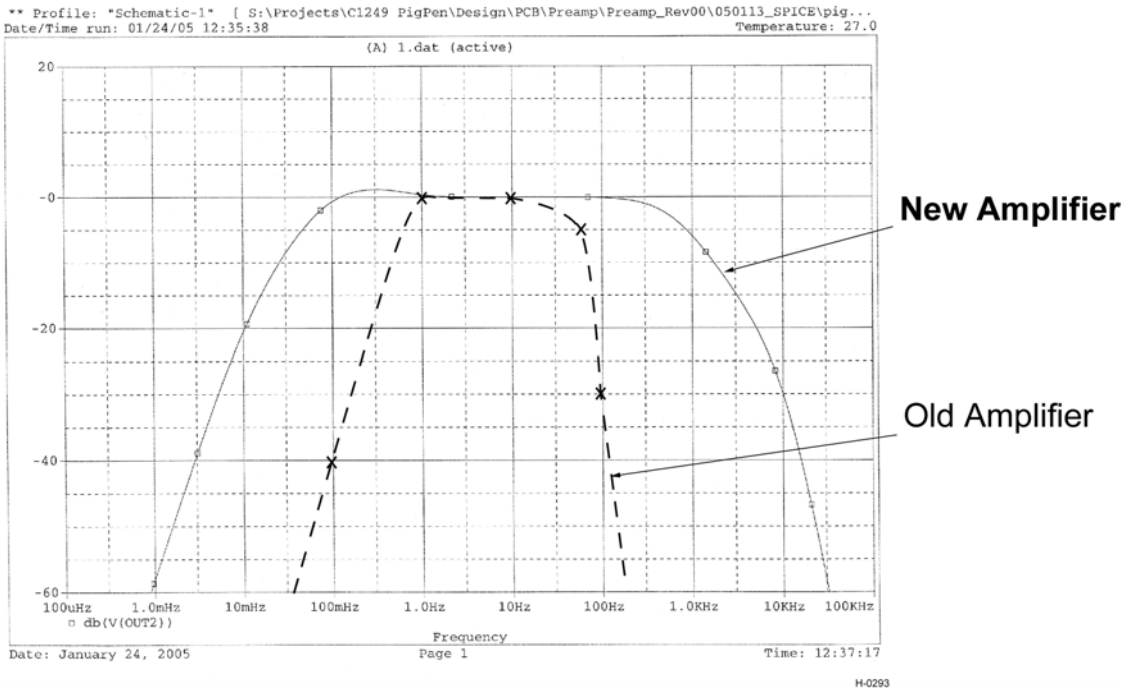

Figure 5. Frequency response of the EP-1 amplifier compared to the Phase 1 amplifier.

2.4 EP-1 Algorithm Development

During the previous phases of the program, PSI developed basic algorithms for threat detection, threat identification and triangulation. During this EP phase, we are refining those algorithms, and tailoring them for the future on-board digital signal processor. We are exercising them against our database of threat signatures collected during previous field tests.

2.4.1 Threat Detection

The method -- The current threat detection algorithm uses the time domain signal and follows the following two steps.

1. ***The signal is rectified because only its amplitude carries the necessary information (i.e., its sign does not matter).*** Figure 6 shows the signal generated by a backhoe digging intermittently over period of 1-minute. In this figure, it is clear that for detecting the occurrence of a threat, the sign of the signal does not matter. The time periods when the backhoe was effectively digging can easily be seen to be characterized by strong signal amplitude (e.g., absolute value above 0.10) located around 7 seconds, 25 seconds, and 40 seconds from the start.

2. ***The algorithm takes into account how long the amplitude of the rectified signal has remained high.*** This consideration is necessary because noise (e.g., caused by the electronic circuit, the sensor-computer interface, etc.) may also generate signals (i.e., spikes) of large amplitudes.

Preliminary results -- In the current implementation of the algorithm, we rectify the sinusoidal signal, use a sliding time window of fixed size (e.g., 6 seconds) and count the how long the amplitude of the rectified signal has remained above a certain threshold value (e.g., 0.08 V) in the time window. Then, when the number of values above the threshold within the window is at least equal to a certain fraction of the size of the time window (e.g., 42%) the algorithm concludes that a threat was a present in the time window.

The preliminary results of the software implementation are presented by the ON/OFF, red curve in Figure 6b. When the red curve is ON it indicates the presence of a threat and when it is OFF it indicates the absence of threat. ***Figure 6b shows that the current threat detection algorithm identifies portions of the recorded signal as threat-portion and others portions as non-threat portions depending on both the strength of the signal and the duration of the perturbation***. We will test and refine the current algorithm and determine the influence of the various thresholds, the width of sliding time window, and also incorporate a power-saving (i.e., sleeping) mode.

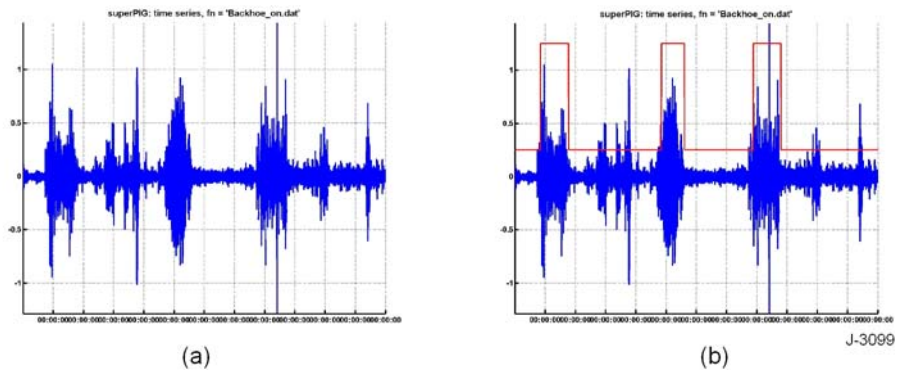

Figure 6: (a) PIGPEN signal generated by a backhoe digging intermittently over a 1-minute time period, (b) Preliminary threat detection result.

2.4.2 Threat Identification Algorithm

Method -- We cast the threat identification problem in a more general automatic identification framework and propose, therefore, the following step in identifying threat type.

1- ***Define threat classes***: In this step we attempt to find sets of parameters that uniquely identify each threat type (e.g., Jackhammer, Backhoe, etc.), and we define this set as the signature of a distinct class.

Figures 7a and 7b represent the power spectral densities of signals generated by a jackhammer and a backhoe, respectively. From these figures, it clearly appears that various threat types may be identified by their respective spectral responses. However, using the full spectral response of the signal as its signature may prove computationally inefficient and memory-wise intensive. Therefore, we propose to use spectral analysis by filtering the signal using a filter bank to calculate the (average) spectra of the signal in distinct frequency bands. Then we use the set of average spectra as the low dimensional, compact signature of each signal. Figure 8 represents the proposed structure for the spectral analysis of the PIGPEN signal.

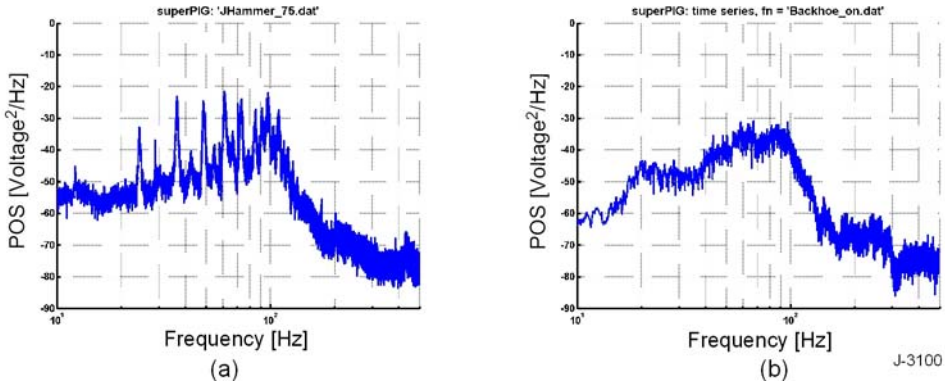

Figure 7: (a) Power spectral density of signal generated using a jackhammer (b) Power spectral density of signal generated using a backhoe

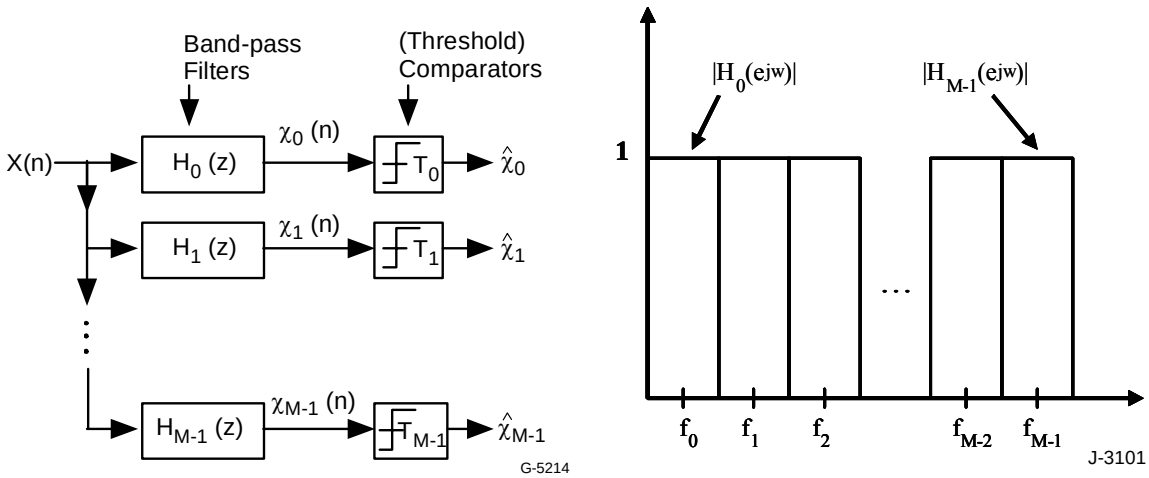

Figure 8 (a) Filter bank architecture for spectral analysis (b) Example of frequency responses of ideal filters.

2. ***Create look-up table/database of classes consisting of the above signatures***. In the final design this database will be stored in the onboard memory of the embedded PIGPEN sensor.

3. ***Define comparison metric*** (e.g., Euclidian distance, combined metric) such that as the sensor records data, it will compute the signature of the recorded signal and compare it to those in the onboard look-up table and decide upon the class/type of the threat present in the signal.

Preliminary results – For the results presented below, we used a uniform filter bank of 100 filters dividing the spectrum into frequency bands of 5 Hz of width. Figures 9a and 9b present the signatures of the signals of Figures 7a and 7b, respectively. We can notice that the signature curves correctly follow the shape of the power spectral density curves, and thus effectively represent the original signal in a compact form in a much lower dimension (actually the dimension is equal to number of filters used) than the PSD. Figures 9a and 9b show that the proposed method effectively captures the minima and maxima present in the PSD of the signal.

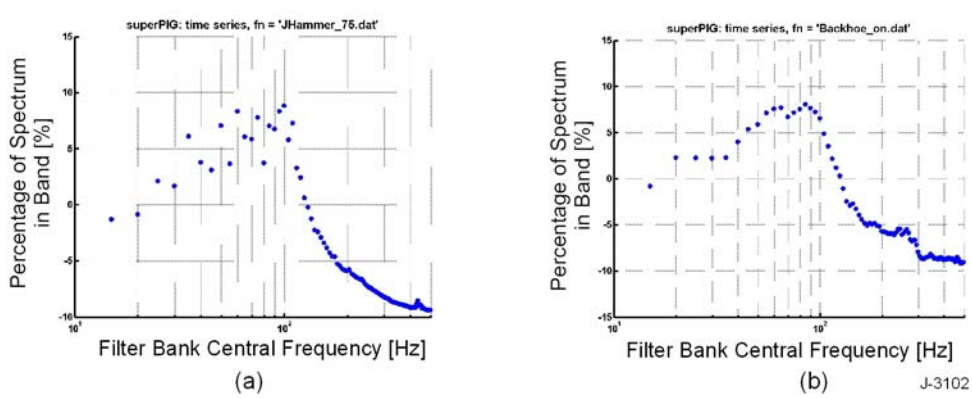

Figure 9: (a) Signature of signal generated using a jackhammer (b) Signature of signal generated using a backhoe.

Thus far, we have noticed that the peaks (maxima) present in various jackhammer generated signals are very similar, thus offering a pattern that will enable to uniquely identify all jackhammer generated signals. Similarly, we have noticed that most backhoe generated signal have minima and maxima located roughly in similar frequency bands of their spectra, and thus will soon be able to define a distinct class for all backhoe generated signals. Once the various distinct classes have been created, we will create the database and define the comparison metric necessary for the automatic threat identification.

2.4.3 Algorithm

We have design a preliminary algorithm to discriminate between different types of excavating equipment. We have developed the algorithm in MATLAB but also implemented it in the C programming language for incorporation in to the digital signal processor.

In a typical, automatic classification method development first one defines different classes. For example, one finds signatures that uniquely identify each known threat class/type (e.g., Jackhammer, Backhoe, etc.). For computational efficiency, signature must be represented in compact form. Next one creates a look-up table/database of classes consisting of the above signatures.. Finally one defines a comparison metric.

We have chosen to implement a Filter Bank Approach. This approach results in a significant reduction in dimensionality. The filter bank enables shorter run time and development/implementation of more complex algorithms. This approach also results in a controllable spectral analysis frequency bands. Along with improved computational efficiency. Memory requirements are reduced, and computational speed is improved.

As an example we have processed a file of 80 sec of data (80,000 samples) with a 1000-filter spectral analyzer, on 2.8 GHz P4 computer. In MATLAB, this case requires 3.1 seconds to run. In "C", this case requires 1.2 seconds to run. If we extrapolate these run times to a processor comparable to the eventual PIGPEN DSP (300 MHz), the run time becomes ~11.2 second, thereby meeting the requirement to process data in real time (with ample margin).

We are relying on spectral identification; however, we also realize that the details of the spectral signatures will likely change from manufacturer to manufacturer. That is a Kubota backhoe and a Caterpillar backhoe will have similar general spectral features but the detailed frequencies may be different. AS such we have developed an algorithm that is robust to changes in fundamental frequency

Figure 10 shows the results of processing several data sets through the preliminary robust identification algorithm. Figure 4-left shows the probability of detection for 42 jackhammer files processed with the jackhammer ID algorithm. Figure 4-right shows the probability of false alarm for 42 jackhammer files through the backhoe ID algorithm. With a suitable selection of algorithm thresholds, we can increase the Pd to nearly 100% and reduce the Pfa to nearly zero – for these test cases.

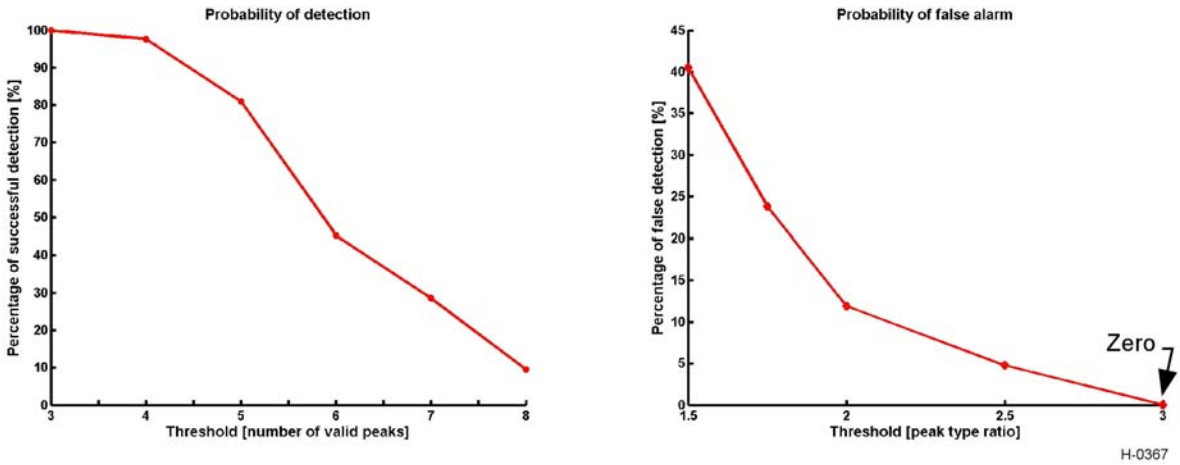

Figure 10. Probability of detection and false alarm using preliminary robust identification algorithm.

2.5 Fabrication of six PIGPEN EP-1 sensors and data acquisition system

Based on the approved design, PSI fabricated six EP-1 sensors. Those sensors included the sensor, weatherproof mechanical housing, and front-end electronics. We fabricated a data acquisition system that included wireless communication to enable data acquisition in the field at long ranges.

Figures 11 through 13 show the fabricated EP-1 hardware. Figure 11 shows the exterior of the EP-1 sensor head. Figure 12 shows the interior of the EP-1 sensor head. Figure 13 shows the EP-1 connected to the wireless data acquisition system.

J-3103

Figure 11. EP-1 sensor head exterior.

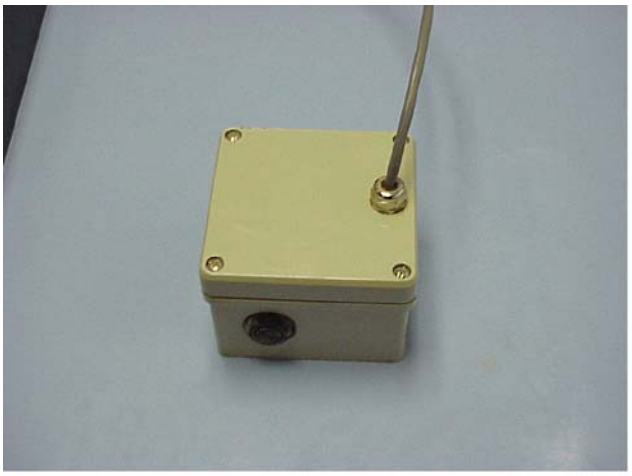

J-3103

Figure 12. EP-1 sensor head interior.

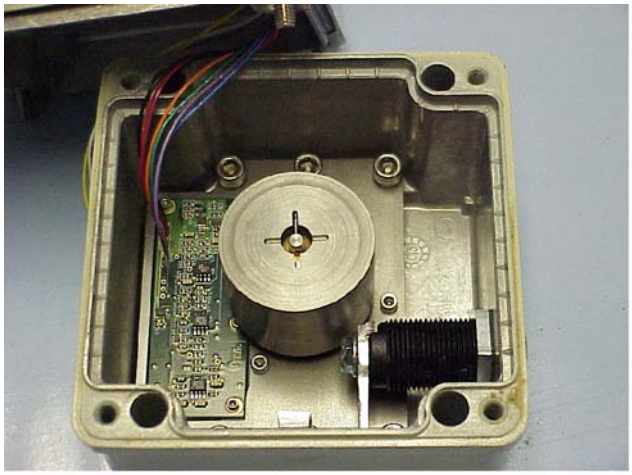

J-3104

Figure 13. EP-1 and wireless data acquisition system.

2.6 Test and Calibration of EP-1 sensors.

PSI prepared test plans that covered the laboratory test, field checkout and field test of the EP-1 system. The field test plan is found in PSI document "Infrasonic-Frequency Seismic Sensor System for Preventing Third Party Damage to Gas Lines, Field Test Plan, Revision B, 7 April 2005".

2.6.1 Bench Test and Instrument Calibration

Though bench testing and calibration, we validated the EP-1 design. The EP-1 sensor met the design goals of increased sensitivity and reduced noise. The front-end electronics also met the desired frequency bandwidth requirements. The resonance frequency was out-of-band as designed.

We conducted calibration testing at Sypris Test and Measurement in Burlington, MA. At Sypris, we measured the EP-1 response, identified the natural resonances of the EP-1, characterized key design features of the sensor head, and characterized the effect of non-level mounting on EP-1 performance.

2.6.2 Natural Frequency measurement

To confirm the instrument natural frequency we performed a slow sine sweep from 5 to 1500 Hz at 0.25 G for approximately 7 minutes. We confirmed the natural frequency to be 1200 Hz (see Figure 14). The predicted value of the natural frequency was 1100 Hz. We also observed a small resonance at 375 Hz that is probably due to a vibration in an internal component (such as the latch). That mode is weak and is not coupled strongly into the sensor. Figure 15 shows the response of the sensor during excitation at 80-120 Hz. The resonance at 375 Hz is present, but 45-50 dB (200-300 x) less than the excitation signature. In addition, when EP-1 is excited at the 375 Hz resonance, there is no apparent amplification in the sensor response (see Figure 16).

EP-1 meets its design criteria of maintaining its resonance above the Nyquist frequency of 500 Hz.

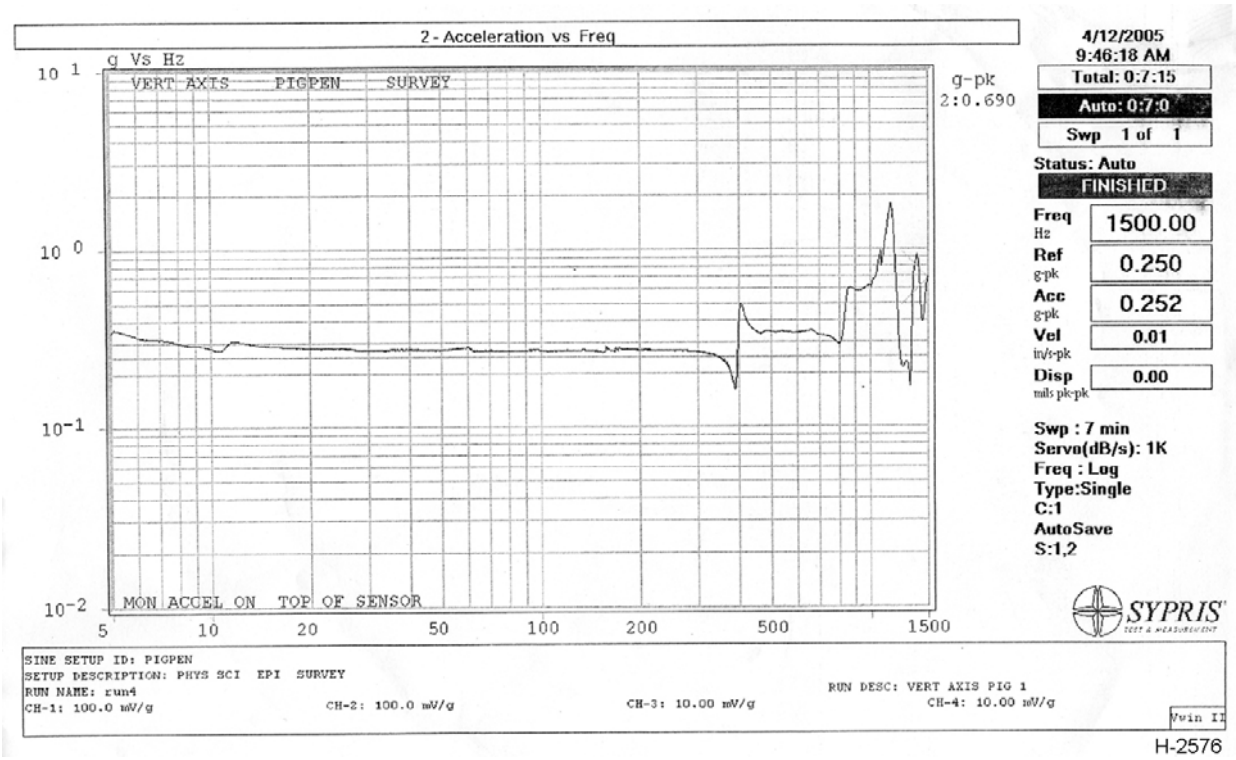

Figure 14. Natural frequency sweep of EP-1. There is a strong resonance at 1100 Hz, that is close to the predicted natural frequency of 1200 Hz. There is also a weaker resonance near 400 Hz.

PSI Proprietary Information

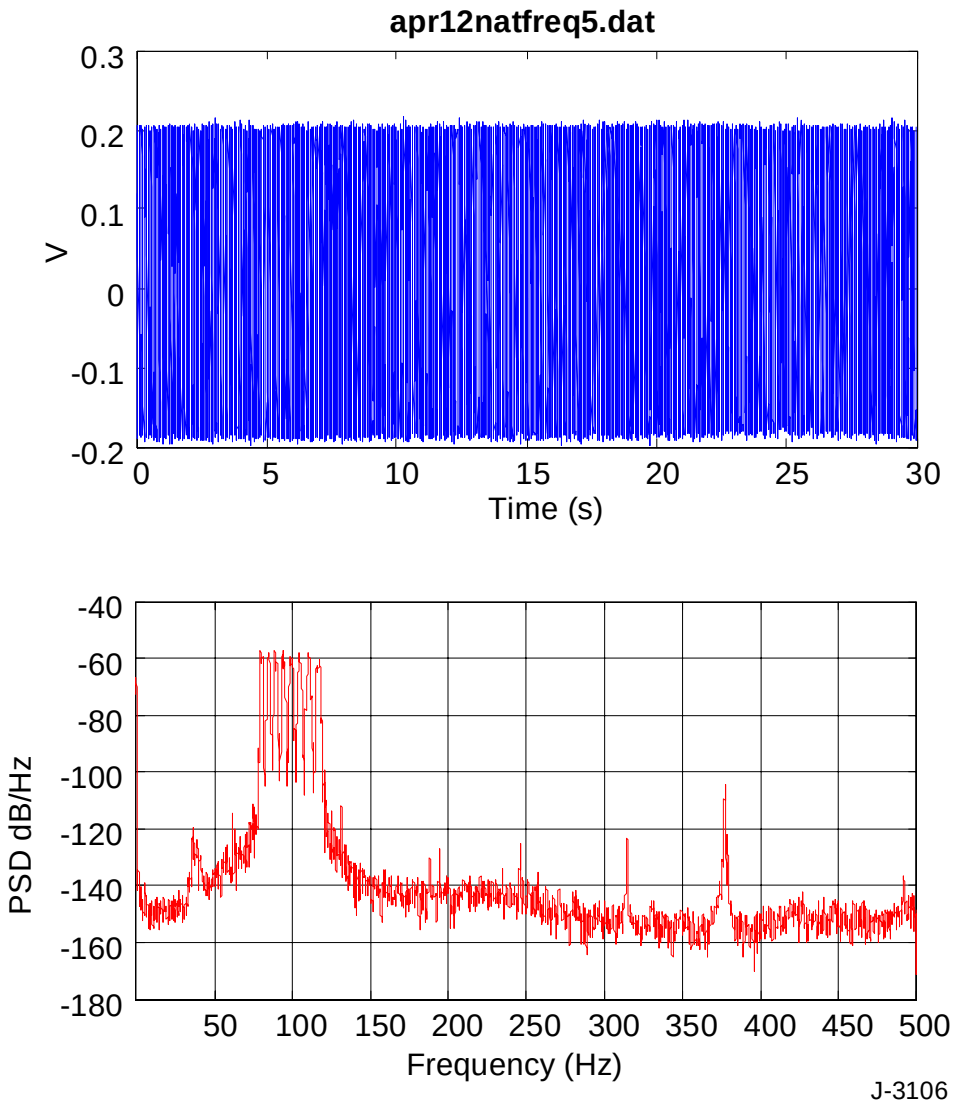

Figure 15. Response of EP-1 during excitation at 80-120 Hz. The weak resonance at 375 Hz is 45-50 dB less weaker than the excitation signature.

PSI Proprietary Information

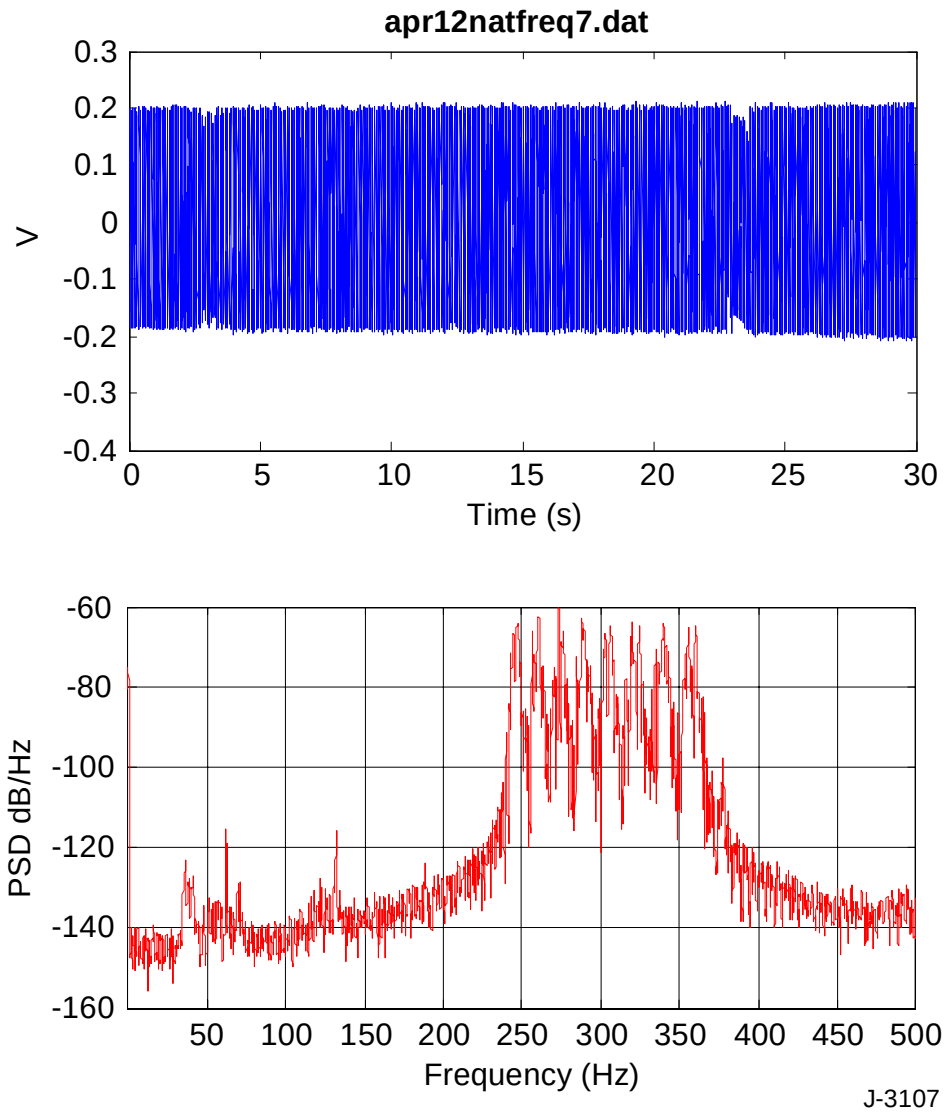

Figure 16. There is no visible amplification when the sensor is excited near the 375 Hz resonance.

2.6.3 Response Calibration

We calibrated the response of the sensor to known acceleration levels (see Figure 17). The measured response for a 0.1 G excitation was -35.6 dB re V^2/Hz (or -12.6 dB re V/G relative to the bare sensor) compared to the predicted value of -34.1 dB re V^2/Hz (or -11.8 dB re V/G).

We calibrated the sensor at 0.1 G and 0.5 G at several frequencies from 3 Hz to 500 Hz. Between 3 Hz and 100 Hz, the sensor response was within 1-2 dB of the predicted response. At high frequency, the sensor response rolls off, as expected. At lower frequency, the sensor response is slightly greater than predicted.

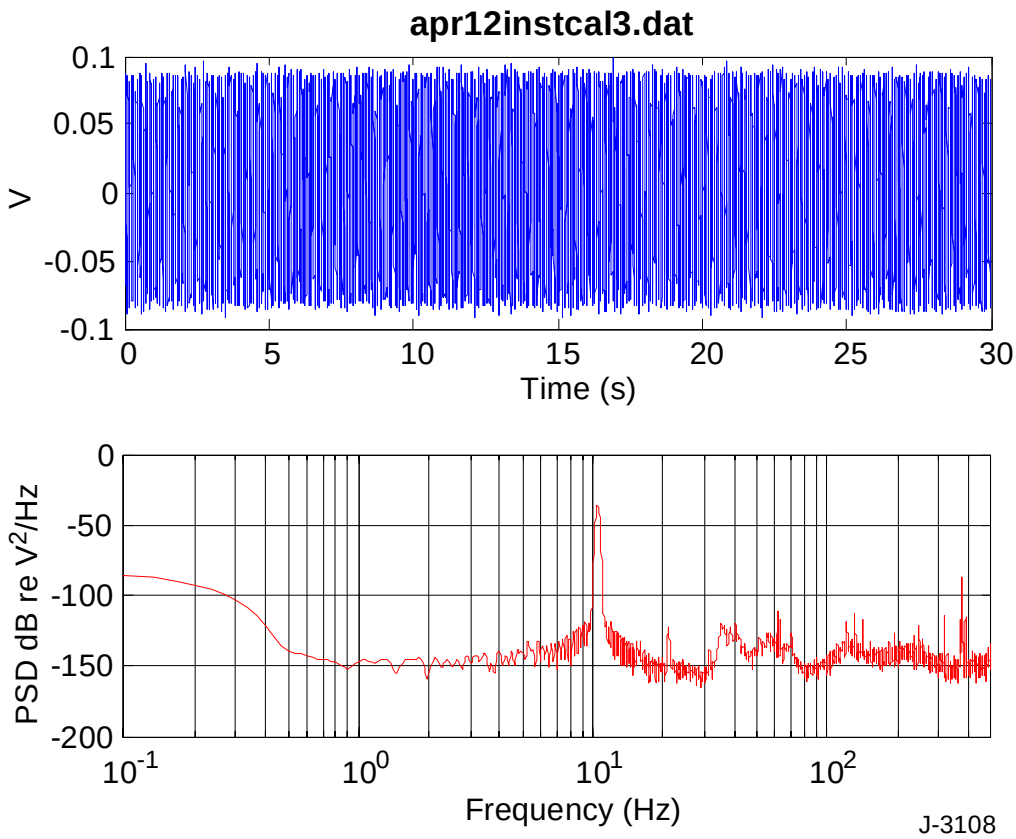

Figure 17. Signal and Power Spectral Density from PIGPEN EP-1 during 0.1 G 10 Hz excitation.

Table 3. Predicted and Measured Responses of EP-1 (relative to the bare sensor)

magnitude	**Predicted response (dB re V^2/Hz)**	**Measured response (dB re V^2/Hz relative to bare sensor)**			
		3 Hz	**10 Hz**	**100 Hz**	**500 Hz**
0.1 G	-33.5	-29.5	-35.6	-36.2	-45.5
0.5 G	-17.6	-16.9	-19.7	-20.4	-24.8

From these calibration data, we calculate the absolute response of EP-1, including the amplifier. Those responses are summarized in Table 4.

Table 4. Summary of EP-1 Absolute Response

Low gain	0.87 V/G	-1 dB re V/G
High gain	110 V/G	41 dB re V/G

The calibrated sensor response is within 1-2 dB of the sensor model predictions. The response of EP-1 is 12 dB (4 x) greater than the Phase 2A sensor.

2.6.4 Restraining Pin Characterization

EP-1 contains a pin that restrains the mass from horizontal motion. The pin causes the sensor to respond preferentially to vertical ground motion. The pin also prevents internal mode mixing within the sensor.

We characterized the effectiveness of the pin by exciting EP-1 vertically and horizontally with and without the pin in place with 0.5 G at 10 Hz. Table 5 summarizes the results of those measurements. By comparing the results of these four tests, we can assess the effectiveness of the pin.

- In tests A & B, we compare the sensor response to vertical excitation with and without the pin. The friction between the pin and the mass only caused a loss of 2 dB in sensitivity.
- In tests B and D, we compare the horizontal and vertical responses of the sensor without the pin. Even without the pin, the horizontal response is 41 dB less than the vertical response. That is, even without the pin, the sensor responds preferentially to vertical excitation.
- In tests C and D, we compared the sensor response to horizontal excitation with and without the pin. With the pin in place, the horizontal response of the sensor is suppressed by 50 dB.

From these tests, we conclude that the pin does not substantially suppress the vertical response of the sensor, and that the sensor will respond preferentially (by 90 dB) to vertical excitation, over horizontal excitation. This purity of response will help ensure that threat signatures are obtained with high fidelity.

Table 5. Results of Restraining Pin Characterization

Test	Excitation	Pin installed	Peak response dB re V^2/Hz
A	Vertical	Yes	-25.7
B	Vertical	No	-23.4
C	Horizontal	Yes	-117
D	Horizontal	No	-64

2.6.5 Tilt Angle Characterization

We measured the response of EP-1 as a function of mounting angle with respect to horizontal. These measurements verify that if EP-1 were buried in the ground and not properly leveled, or moved from level during backfilling, its response would be only minimally affected. We compared the sensor response at 0, 5, 10, and 30 deg tilt with respect to horizontal. We would predict a cosine effect on the response. For example, at 30 deg tilt, the response would be 0.87 of the response achieved with horizontal mounting (or -1.2 dB). Within the error bars of the measurement, this level of degradation is imperceptible. Table 6 summarizes the results of the measurement. **There is no significant effect in the sensor response for tilt angles up to 30 deg.**

Table 6. Sensor Response as a Function of Tilt Angle

Tilt	Peak response (dB re V^2/Hz
0 deg	-25.7
5 deg	-26.1
10 deg	-26.1
30 deg	-25.8

2.7 Noise Measurements

It is difficult to put the sensors in an environment that is sufficiently isolated from vibration that a true low-background noise measurement can be obtained. The Johnson City site offered the best opportunity to obtain backgrounds in a quiet environment. We acquired background data during lunch and during other times of when there was no obvious activity at the site. Figure 5 shows a plot of the noise measured at Johnson City compared o the EP-1 noise mode (presented at PDR) and the measured noise of the Phase-1 sensor and electronics.

The measured noise is considerably better than the noise model at high frequencies. **We have also more than met our objective of reducing the system noise by more than 10 dB below the Phase-1 system noise**. **The increased sensitivity and the reduced noise will improve detection range considerably over the Phase-1 system, in a quiet environment.**

As the frequency decreases, the measured noise is increasing faster than the model would predict. The input parameters for the noise model were extrapolated from 1 Hz data using some simple assumptions. Therefore it is not surprising that the measured noise does not agree with the model perfectly.

3. Field Test Preparations

3.1 Field Test Sites

We identified a potential test site for preliminary testing. The site is located in Rehobeth, MA. A picture of the site is shown below in Figure 18. The site is located in a rural area far from major traffic. It is approximately, 210 yds by 100yds. Sensors will be buried at several locations at the site. Potential locations for the burial of the Pigpen sensors are identified on the figure. Note that the site is composed of several different soil types. The test site is comprised of areas of clay, sand and gravel. We will monitor several different types of construction equipment at this site.

As part of the system checkout, we conducted three half-day field exercises at a location near PSI. At these field exercises, we acquired data using a sledgehammer as the source. We also conducted a full-day field checkout with a private contractor at a building site in the Boston area. At this field checkout, we acquired data of two types of excavators.

Figure 18: Candidate test site, Rehobeth MA.

These field exercises and checkouts were in preparation for the field test hosted by the Northeast Gas Association in Johnson City NY. That test was conducted on 25-27 April 2005.

3.2 EP-1 Data Acquisition System

We intend to use a laptop PC-based data acquisition (DAQ) system to support the laboratory and field testing. We will have digital data transfer from the PIGPEN electronics to the DAQ. For short range testing, we can use hard-wired connections. However, for long range (>100 yd) testing, wires are rather cumbersome. We assembled a short-haul, wireless communication system to support the field testing (see Figure 19)

We first established a wireless connection between 2 evaluation boards containing Wi.232DTS transceiver modules. We established communication between two PCs and their corresponding transceiver modules and successfully transmitted various files from a PC on the 3rd floor to a PC on the 2nd floor on opposite ends of the building.

Figure 20 shows the block diagram of the EP-1 and wireless communication system that was used during all the field testing. EP-1 comprised the sensor head, integrated front-end electronics and environmentally-compatible chassis. The wireless communication system comprised RS-232 transmitter (TX) and receiver (RX) pairs.

Figure 19. Radiotronix short-haul transceiver.

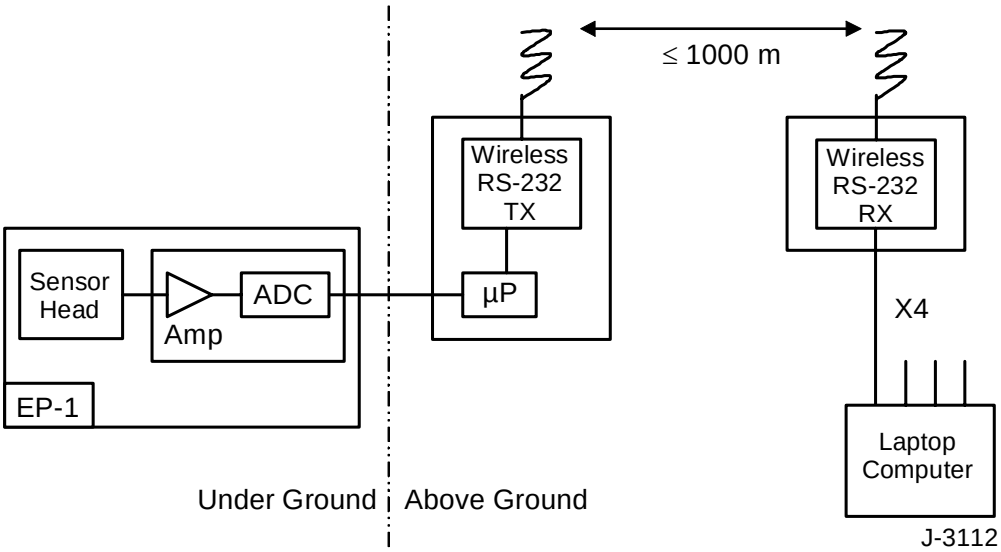

Figure 20. Block diagram of EP-1 and wireless data acquisition system.

The amplifier is a two-stage, charge amplifier that can be remotely switched between low-gain (10 dB) and high-gain (53 dB) amplification. The analog-to-digital converter (ADC) digitizes the amplifier signals at 1 kHz with 16 bit resolution, and transmits the digital data via an SPI interface to the wireless communication unit. By closely integrating the sensor head with the amplifier and ADC, we minimize the effects of internal and external noise sources. Once the signals are converted to digital data, they are relatively immune from noise.

The TX box includes a microprocessor to control the data transmission between the EP-1 electronics and the wireless communication system. We chose wireless communication because of the need to synchronize the data from all four sensors, and because of the long ranges required for testing (up to 1000 m). Wireless communication was the only realistic option that enabled the simultaneous acquisition of data from four remote sensors. The RX units house the wireless receivers and interface to the laptop computer via USB ports (one for each sensor).

While the wireless system was the only logical option for data acquisition, its implementation was not as transparent as we had expected. The wireless system also introduced two unanticipated complicating factors. The first complication arose from the internal buffering that occurs in the USB port communication within the laptop computer. Each USB port has its own internal buffer so that other processing on the computer does not result in lost data. However, the buffering of each USB port is independent and introduces time lags between the four data streams.

The second complicating factor arises from loss of communication on the wireless links. There is no way to determine when communication is momentarily lost. When communication is lost, there is an indeterminate time lag in the data stream from that particular channel. Most of the time, there are only a small number of data drop-outs. However, at other times, the drop-outs occur quite frequently. Because the drop-outs result in an indeterminate time lag in the data stream of a particular sensor, the relative timing of those data is compromised

Figure 21 shows an example of data with the time lags introduced by buffering and data drop outs. In these data, all four sensors are co-located, and are being stimulated with an impulsive source. There is a time lag of several tens of milliseconds between the data streams. The drop-outs appear as spikes in the data stream.

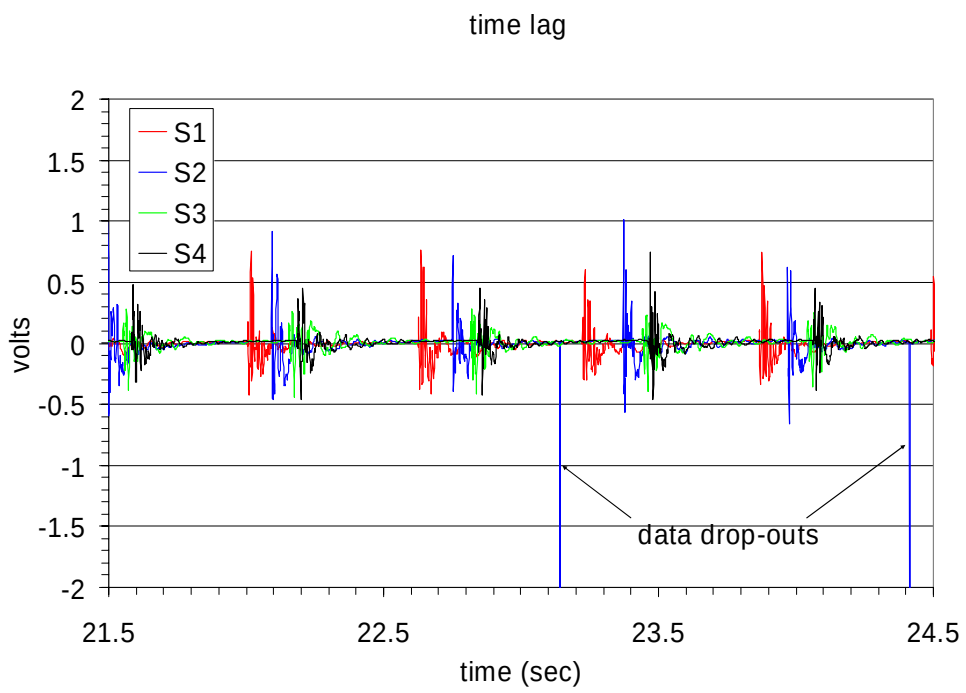

Figure 21. Data illustrating buffering time lag and data drop-outs.

3.3 Field Checkout – Somerset, MA

On 19 Apr 2005, we conducted a field checkout at a construction site in Somerset, MA. The primary objectives of the Field Checkout – Somerset was to prepare for the Johnson City field test, and to acquire data to test the algorithm performance.

Figures 22 and 23 show an aerial view of the site, and the sensor and threat locations. The site was small, and the sensors were placed between 10 yards and 40 yards from the threat location. At the site, there were two backhoes and a portable cement mixer. We acquired approximately 5-½ hours of data primarily of the backhoes digging.

Figures 24 and 25 show signatures of the background and of the backhoe digging from the Somerset site. The backhoe signature shows the same basic characteristics as the backhoe signature acquired during the Aug 03 field test from the NGA-funded Phase 2A program (Figure 26).

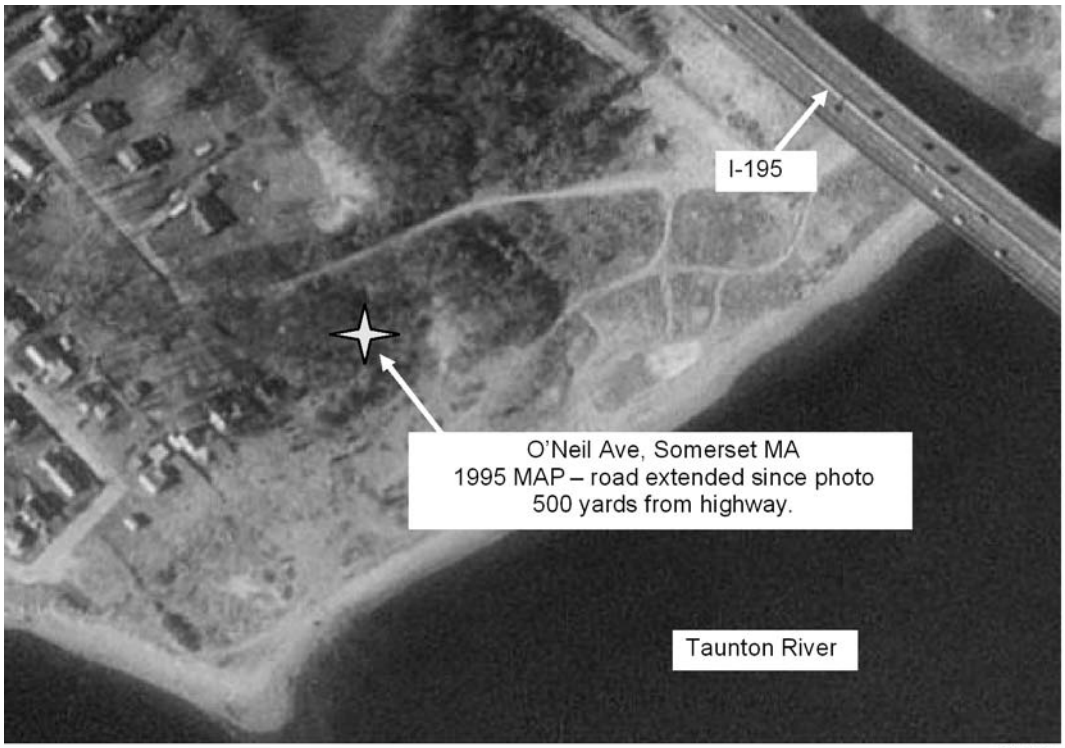

J-3114

Figure 22. Aerial view of Somerset site showing location relative to a nearby river and highway..

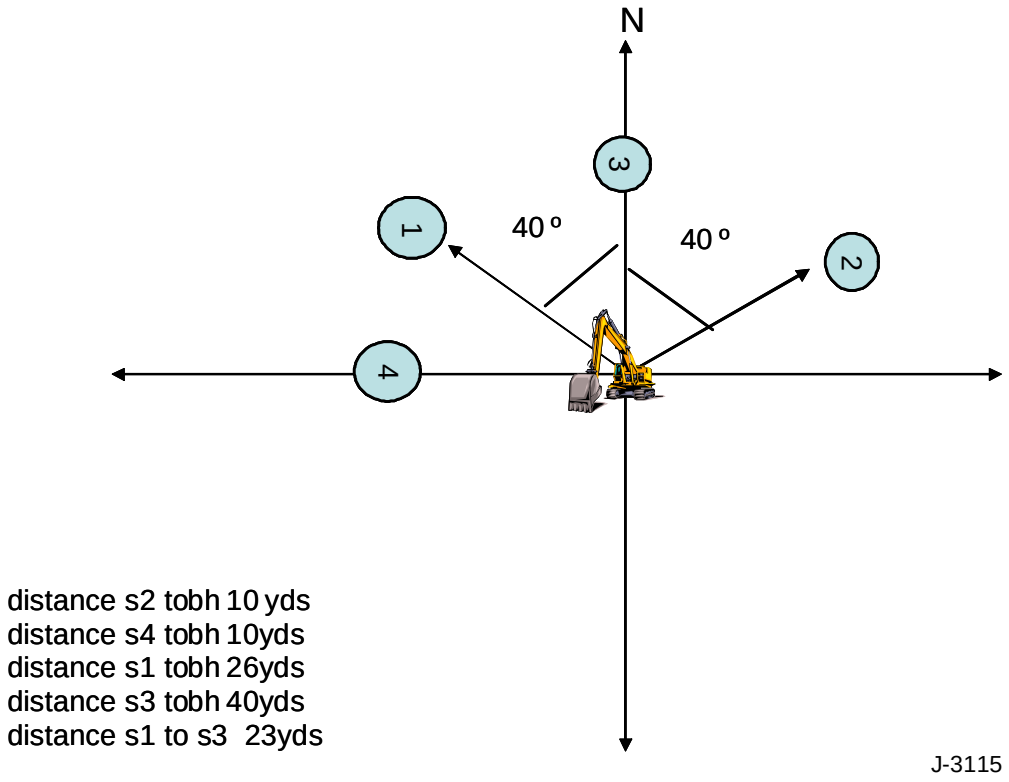

Figure 23. Sensor geometry at Somerset site.

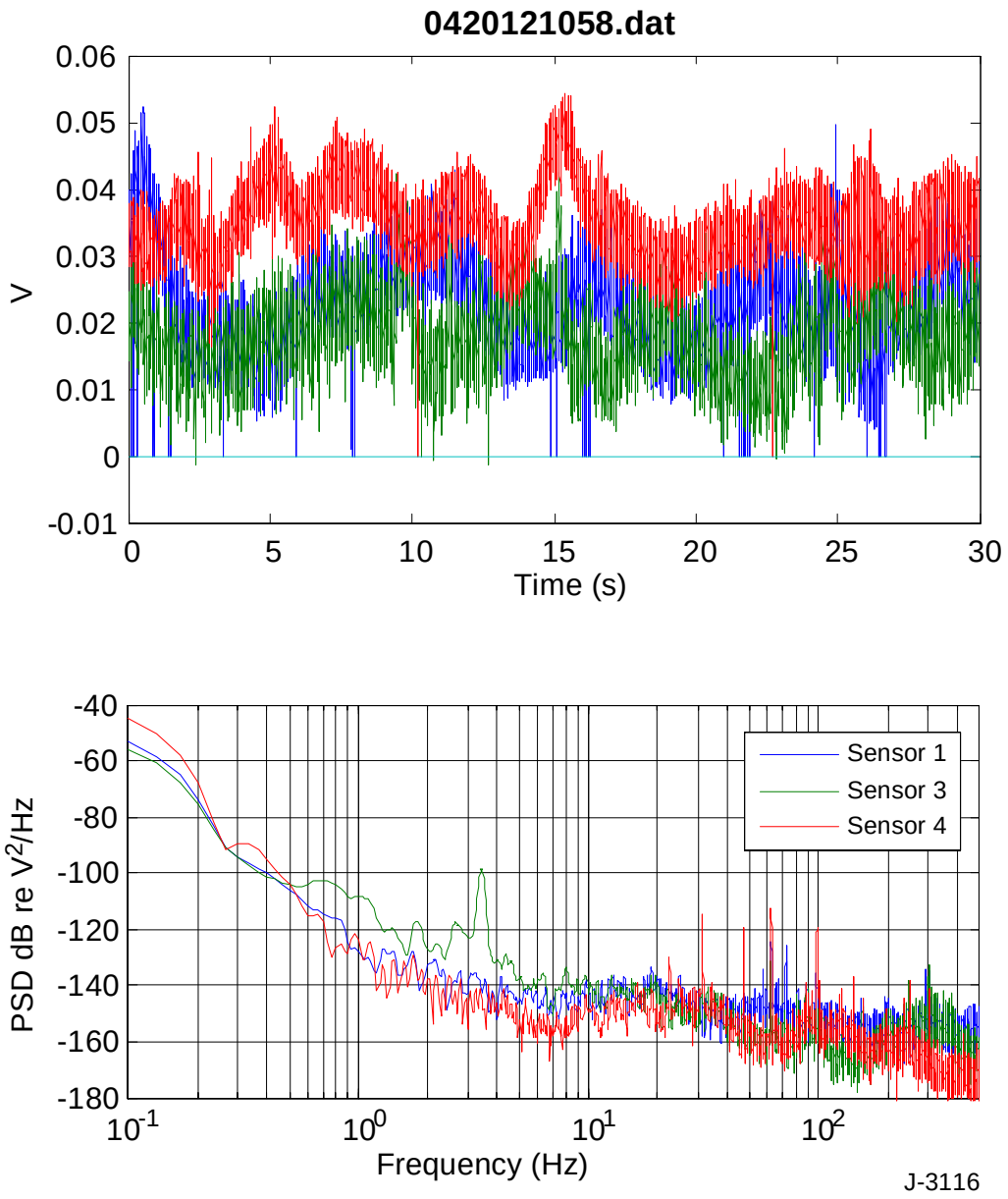

Figure 24. Background time series (top) and spectral (bottom) data from the 19 Apr 05 field test in Somerset, MA.

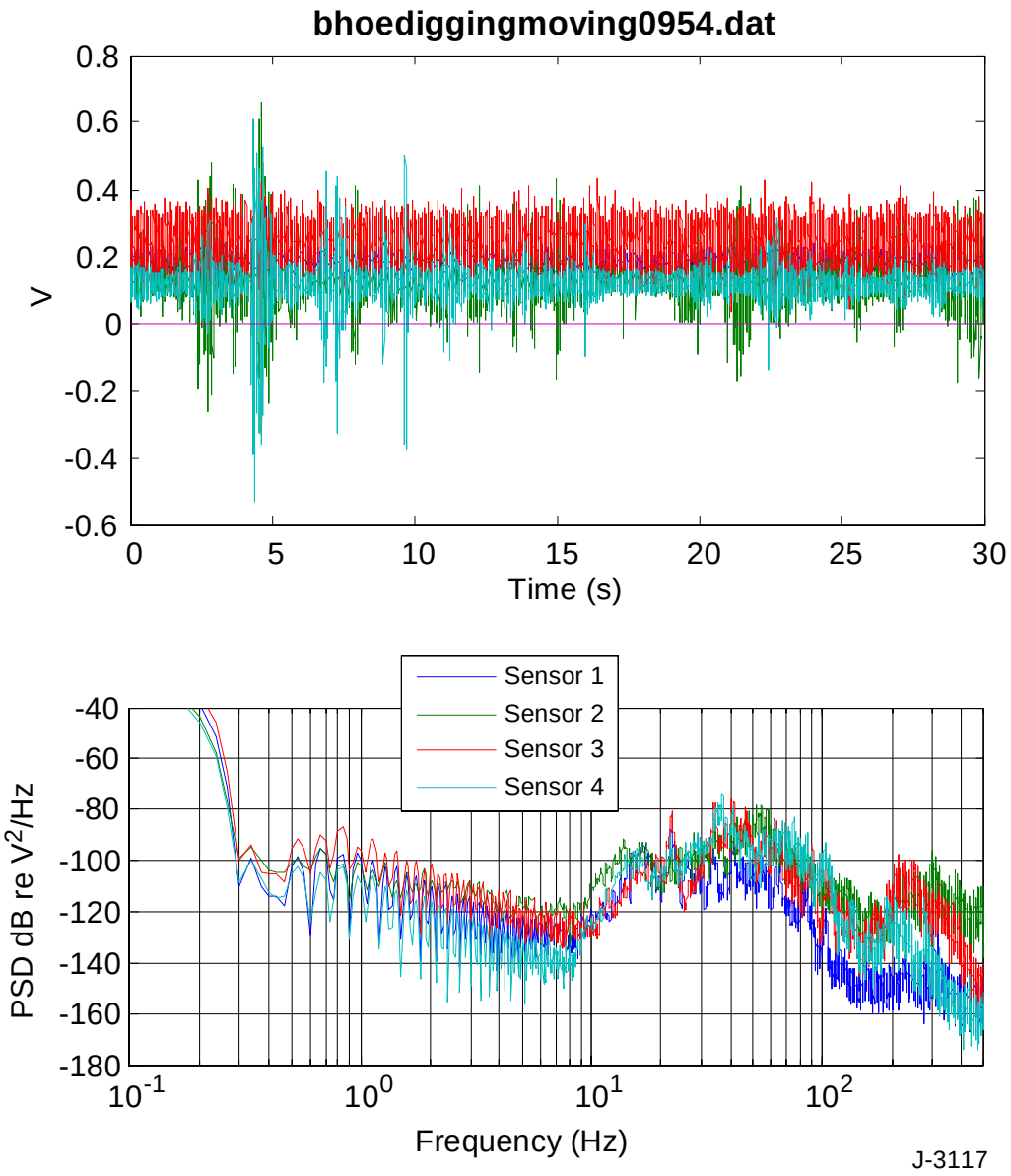

Figure 25. Backhoe time series (top) and spectral (bottom) data from the 19 Apr 05 field test in Somerset, MA.

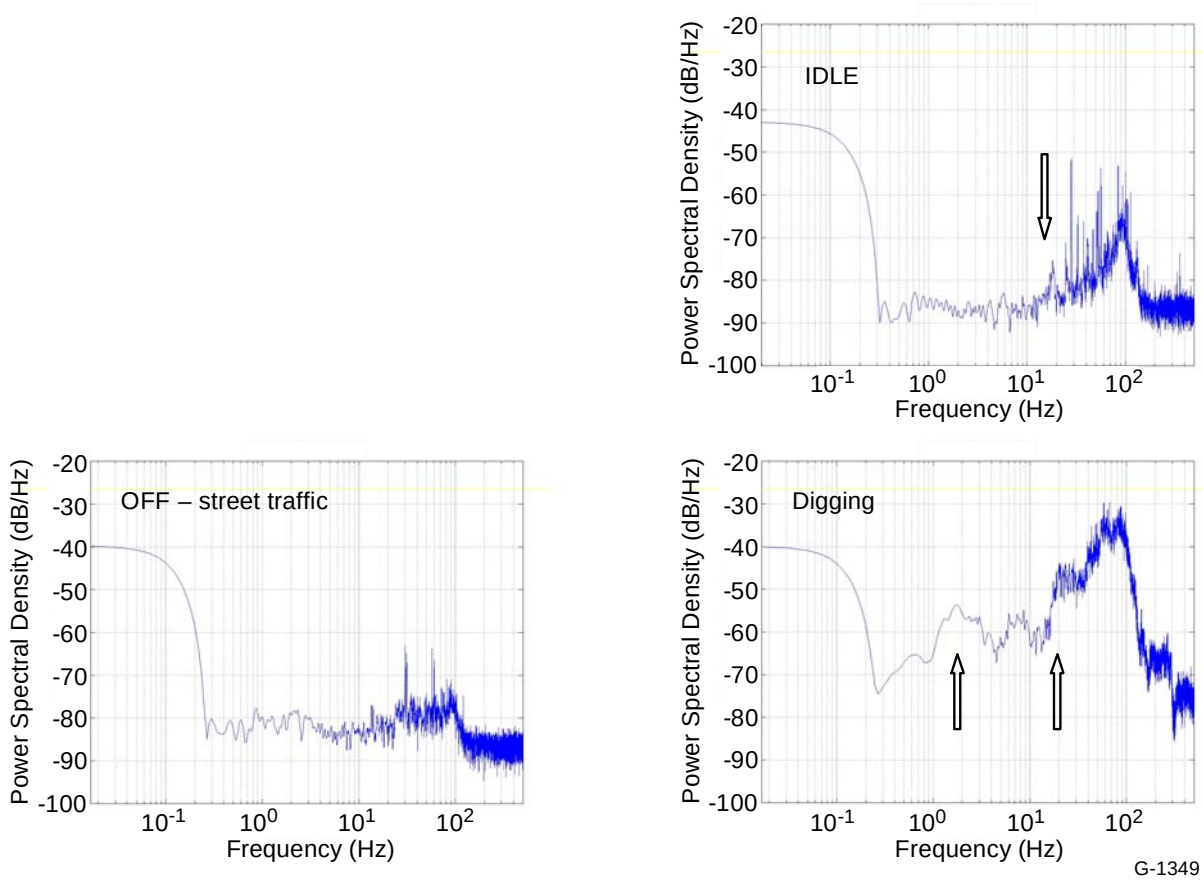

Figure 26 Signatures of a backhoe previously acquired during an Aug03 field test as part of the NGA Phase 2A program.

4. Johnson City Field Test

On 25-26 Apr 05, we conducted a field test of EP-1 in cooperation with the Northeast Gas Association.

Figure 27 shows the site map overlaid with the sensor and threat positions. The sensor and threat positions are summarized in Table 5. The primary methods of determining position were by using a laser rangefinder and sighting magnetic compass. The rangefinder has an uncertainty of +/- 1m; however, since the backhoe moves during excavation, we estimate a range uncertainty of +/- 3 m. The sighting compass has a uncertainty of +/- 2 deg. GPS coordinates were acquired for reference only and have an uncertainty of +/- 7 m along the surface and an unknown, but greater uncertainty in altitude.

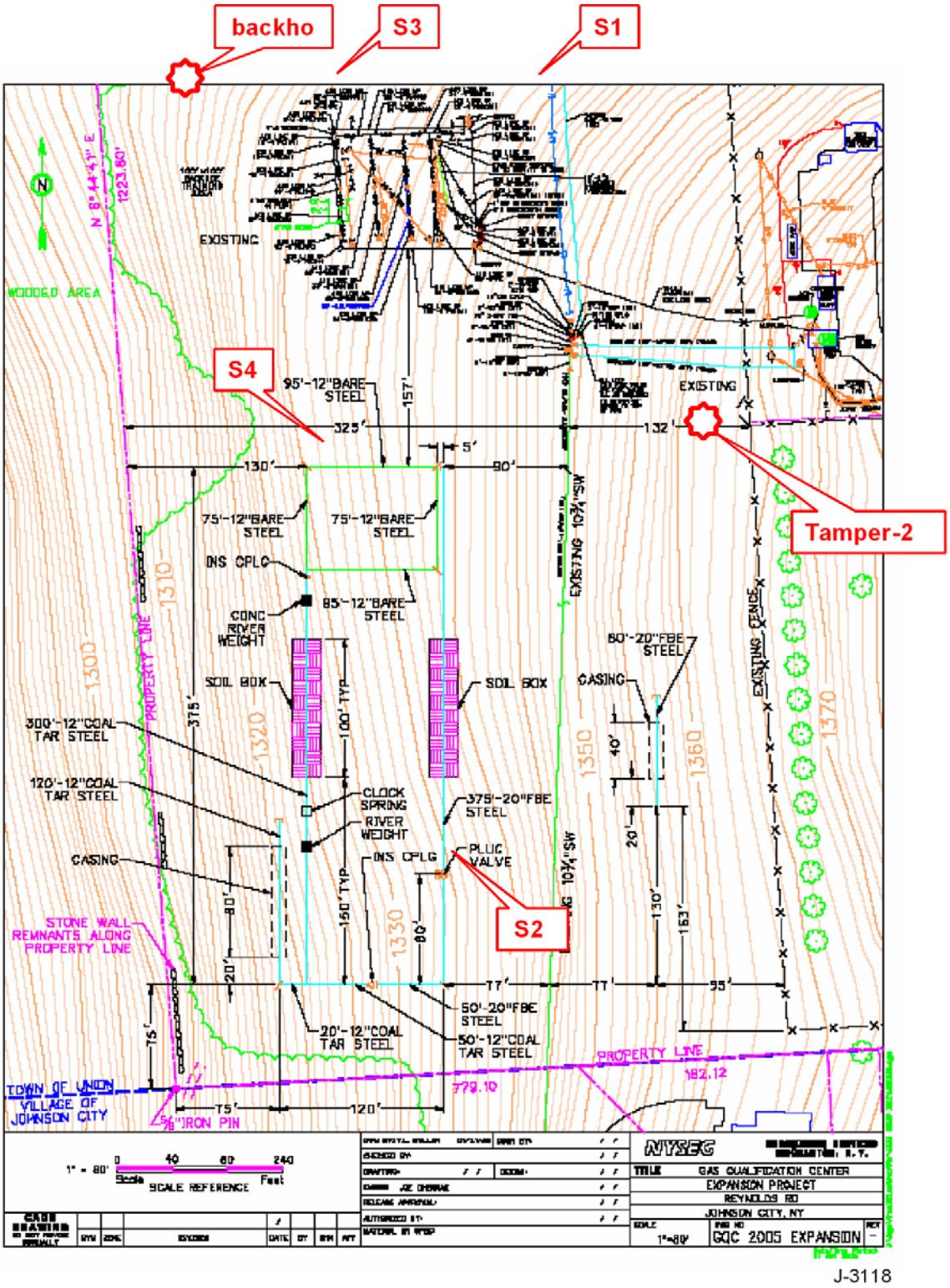

Figure 27. Johnson City Field Test layout.

Table 7. Summary of Sensor and Threat Positions.
Bold text indicates a direct measurement.
Non-bold text indicates a derived measurement.

Location	GPS coordinates (UTM) (+/- 7 m)	Altitude (+/- 7 m)	Range to backhoe (+/- 3 m)	Bearing to backhoe (magnetic) (+/- 2 deg)	Range to Tamper-2 (+/- 3 m)
Backhoe	**18 T 0419769 E 4666463 N**	**402 m**	**0**	**0**	0
Sensor 1	**18 T 0419842 E 4666473 N**	**402 m**	**70 m**	**281 deg**	**87 m**
Sensor 2	**18 T 0419837 E 4666309 N**	**409 m**	**175 m**	**353 deg**	109 m
Sensor 3	**18 T 0419798 E 4666471 N**	**402 m**	**25.5 m**	**281 deg**	**113 m**
Sensor 4	**18 T 0419796 E 4666391 N**	**408 m**	**80 m**	**353 deg**	88 m
Tamper-2	**18 T 0419889 E 4666400 N**	**414 m**	136 m		0

Northeast Gas provided several pieces of equipment, including a large backhoe on tracks (herein called the Trackhoe), a small wheeled backhoe (Backhoe), a tamper, and a jackhammer attachment to the large tracked backhoe (Jackhammer). Table 8 summarizes the equipment. Figures 28 through 30 show the equipment at the site.

Table 8. Summary of Equipment at Johnson City Field Test

Equipment	Manufacturer & Model Number
Backhoe	Caterpillar 10-200 416D
Trackhoe	Caterpillar 225 BLC
Jackhammer	Attachment to Cat 225 BLC
Tamper	Wacker 2_103

J-3119

Figure 28. Trackhoe (right) and backhoe (left).

J-3120

Figure 29. Jackhammer attachment to Trackhoe.

J-3121

Figure 30. Tamper.

The four EP-1 sensors are buried approximately 18 inches below grade. The sensors are leveled using a bubble level, and backfilled by hand. The soil was compressed by hand around the sensor as it was buried (see Figure 32).

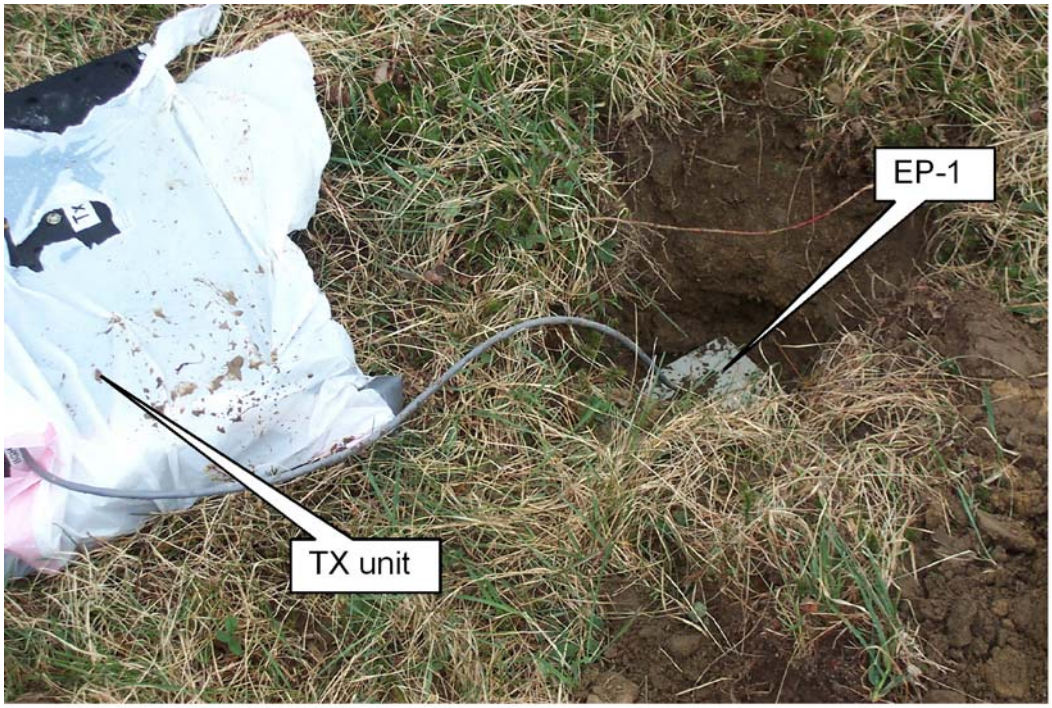

J-3122

Figure 31. EP-1 unit in the ground before backfilling. The TX unit remains above ground.

The nominal data collection period is 30 sec. Most files are named by date and time in the format: MMDDHHMMSS.dat. Some files, are named with a special descriptor. The data acquired and the corresponding activities, or configurations, are summarized in Table 9. Figure 32 shows the noise level achieved for the sensor at the Johnson City test compared to our earlier performance and EP model.

Table 9. Summary of Data Collected and Configuration During Johnson City Field Test

Description	**Date**	**Files**
Site characterization	25 Apr 05	M0 through M10
Trackhoe idling		0425102739 through 0425103830 idle1 through idle 5
Trackhoe bucket hitting the ground		H1 through H32
Trackhoe digging		0425110755 D1 through D99 0425114617 through 0425114657
background		0425125242 through 0425130441
Trackhoe digging		0425134313 through 0425141856
Trackhoe idling		0425142020 through 0425142807
background		0425144837 through 0425142807
Trackhoe moving		0425145700 through 0425152027
Trackhoe digging		0425152830 through 0425154007
Trackhoe off		0425144046 through 0425144239
Trackhoe filling in hole		0425154810 through 0425163819
Background	26 Apr 05	0426081023 through 0426083158
Backhoe digging		0426083305 through 0426083341
Backhoe off and on		0426085501 through 0426070356
Backhoe filling hole		0426090400 through 0426091859
Backhoe driving		0426092723 through 0426093131
Backhoe off		0426094545 through 0426094619
Tamper on		0426094652 through 0426095337 0426095444 through 0426095517
Tamper off		0426095410 0426095551 through 0426103030
Trackhoe idling & moving – attaching jackhammer		0426102324 through 0426111305
Jackhammer on and off		0426111117 through 0426112201
Backhoe digging		0426112317 through 0426112507
Backhoe digging & Trackhoe on		0426112821 through 0426113137
Backhoe digging & jackhammer Mixed activity		0426113642 through 0426114026
Car idling		0426122150 through 0426122615
background		0426123624 through 0426123956
Soil tamper		0426124034 through 0426124439
Airplane flyby with tamper		0426124328 through 0426124404
Tamper on – tampe-2 location		T1 through T11
background		T12
jackhammer		J1 through J41 0426131109

PSI Proprietary Information

Description	Date	Files
tamper		T13 through T59
background		T61 through T62
Backhoe filling in hole		0426134933 Y1 through Y33
Trackhoe driving		Z1 through Z66
Backhoe & trackhoe driving to gate		Z67 through Z81
Hand digging 10 feet from S3 30 feet fro mS3 23 yards from S3		 C1 through C7 C9 through C14 C15 through C19

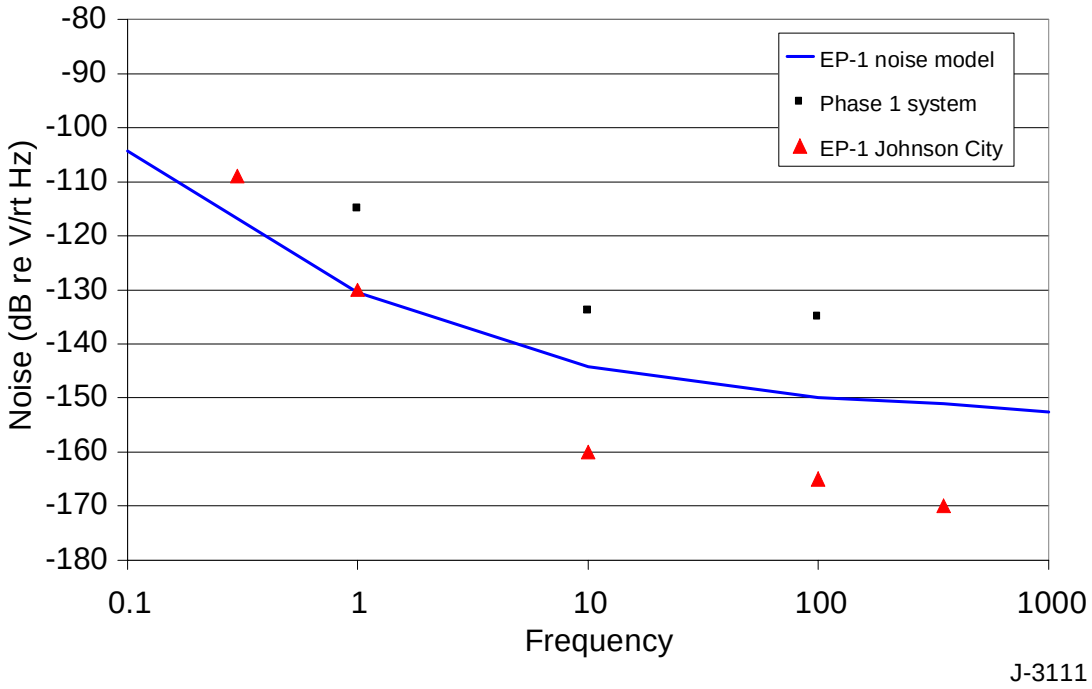

Figure 32. Noise measured at the Johnson City site compared to the EP-1 noise model and the measured Phase 1 system noise.

4.1 Signatures

We detected and measured the unique signatures of all the available equipment during the field test. Overall, the signature data met our expectations and are qualitatively the same as the signatures acquired during earlier field tests. Table 10 summarizes all the example signatures presented in the report.

Table 10. Summary of Example Signatures Included in the Report

Data description	**Figure**
Tamper	Figures 33-36
Trackhoe digging	Figures 37-38
Trackhoe idling	Figures 39-40
Backhoe digging	Figures 41-42
Jackhammer	Figures 43-46
Backhoe driving	Figures 47-49
Trackhoe bucket hitting ground	Figure 50
Passenger vehicle idling	Figure 51

As an example, Figure 33 shows the signature of the tamper. The top curve shows the time series data. The bottom curve shows the power spectral densities (PSDs). The data were acquired with a sampling rate of 1 kHz. Nominal data collection was 30 sec. The data plots are color coded in all the plots: red = sensor1 (70 m range), blue = sensor2 (175 m range), green = sensor3 (25.5 m range), black = sensor4 (80 m range). Sensor 4 was not active during this acquisition. Figures 34 through 36 show the data from the individual sensors.

The signal-to-noise ratio (SNR) at the furthest distances is quite good for all the equipment tested. For the tamper, at 175 m, the fundamental frequency peak intensity is -131 dB. The noise is roughly -167 dB. The SNR is 36 dB, or 63:1.

The trackhoe (Figures 37 and 38) and backhoe (Figures 39 and 40) signatures resemble signatures from older data, and also are qualitatively quite similar. The specific frequencies for the trackhoe and backhoe are different, as expected; however, the broad characteristics that define the “backhoe digging” spectrum for the algorithm are identical.

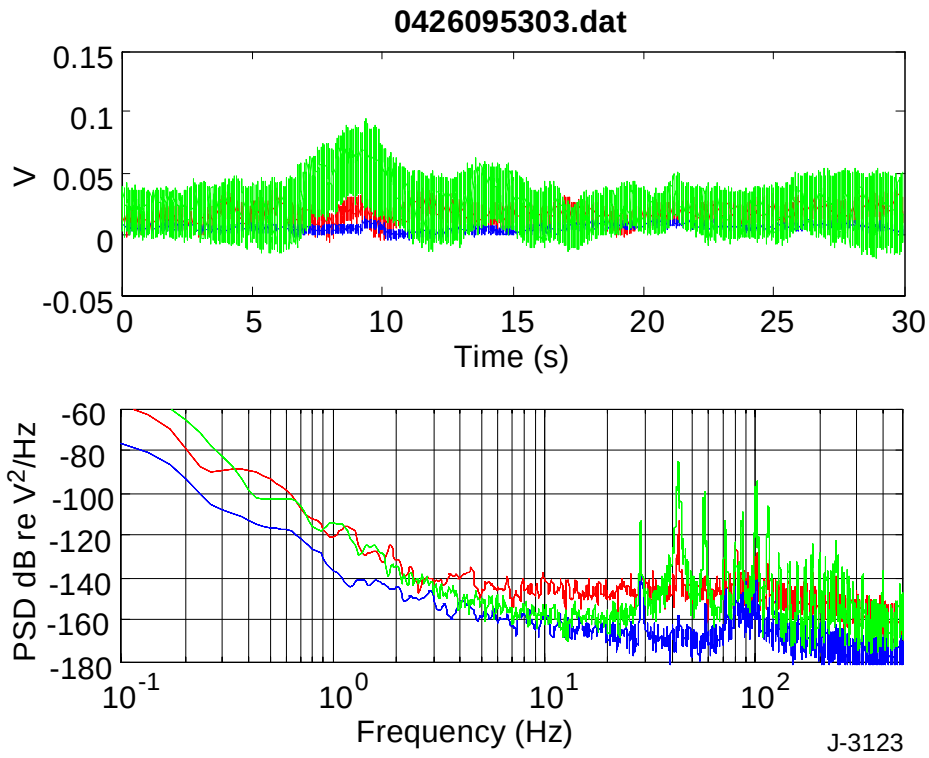

Figure 33. Data acquired during tamper operation: red = sensor1, blue = sensor2, green = sensor3. The top curve shows the time series data. The bottom curve shows the power spectral density.

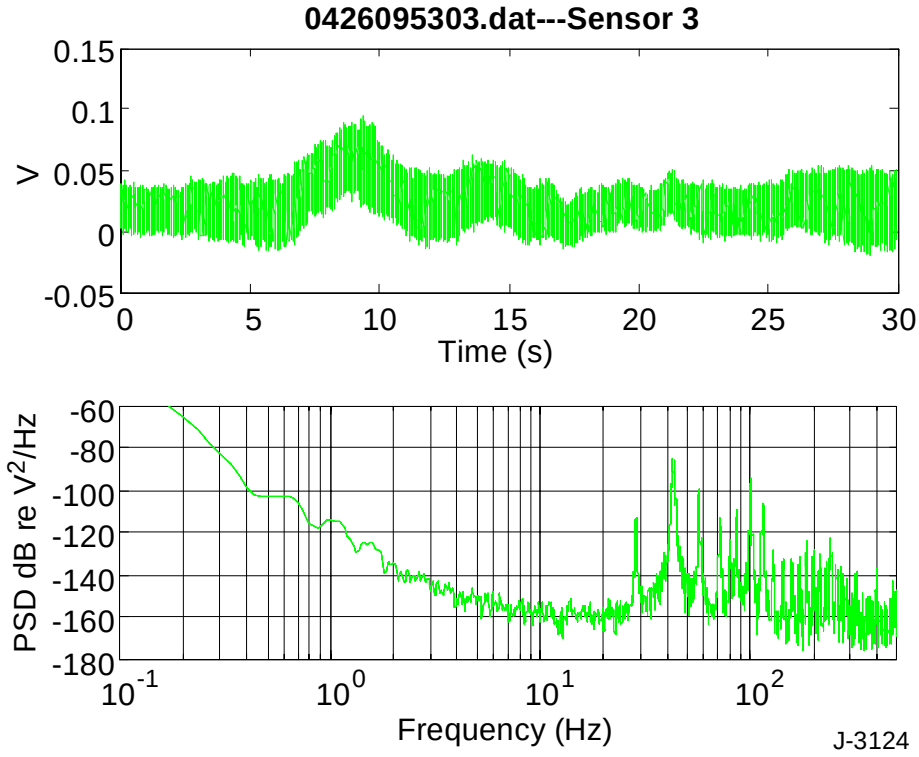

Figure 34. Sensor 3 data during tamper operation (25.5 m range).

PSI Proprietary Information

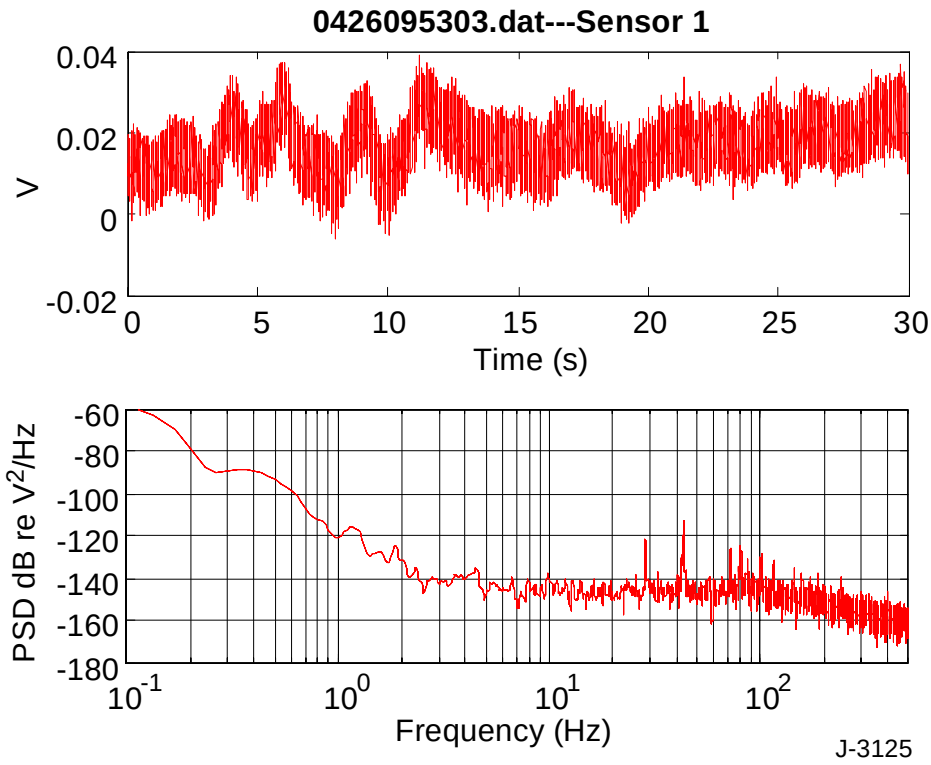

Figure 35. Sensor 1 data during tamper operation (80 m range).

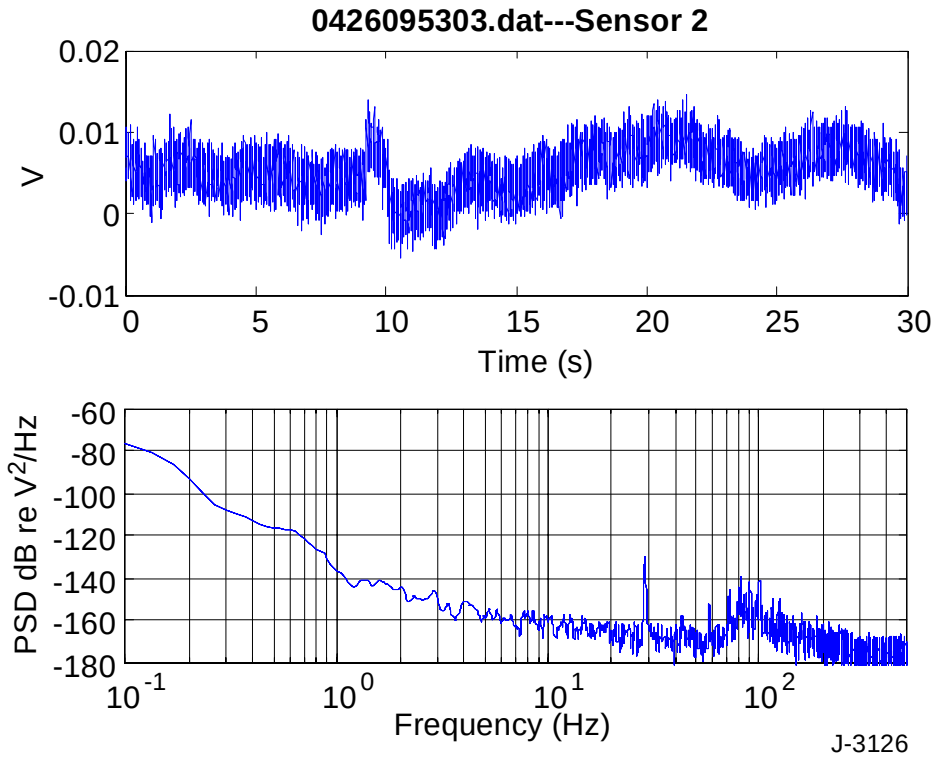

Figure 36. Sensor 2 data during tamper operation (175 m range).

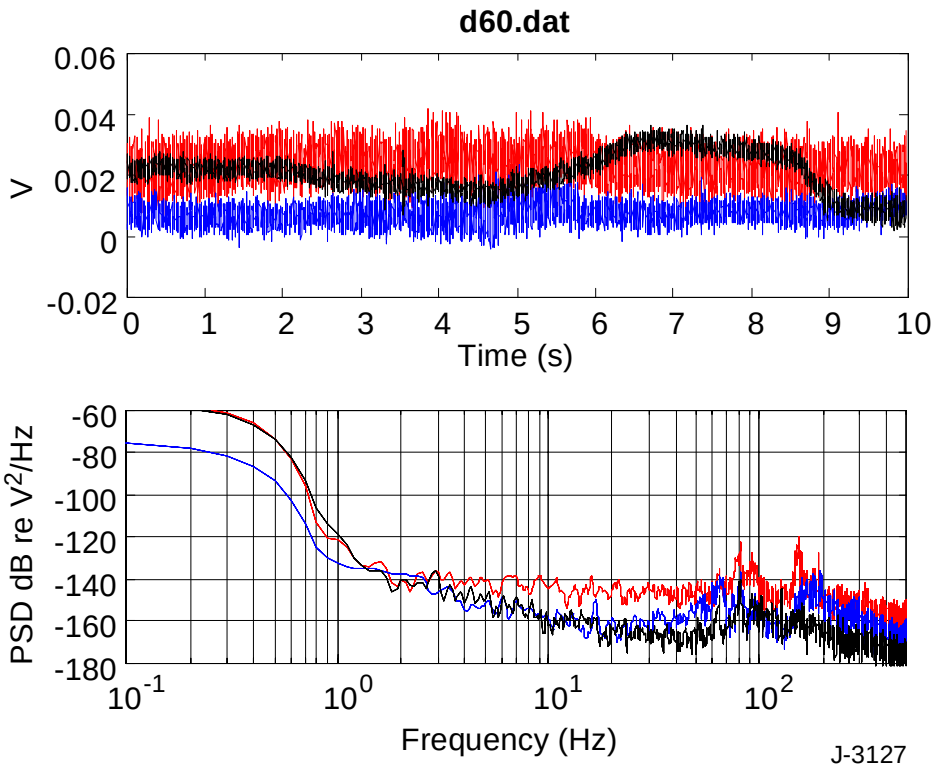

Figure 37. Data acquired during trackhoe digging operation: red = sensor1, blue = sensor2, black = sensor4.

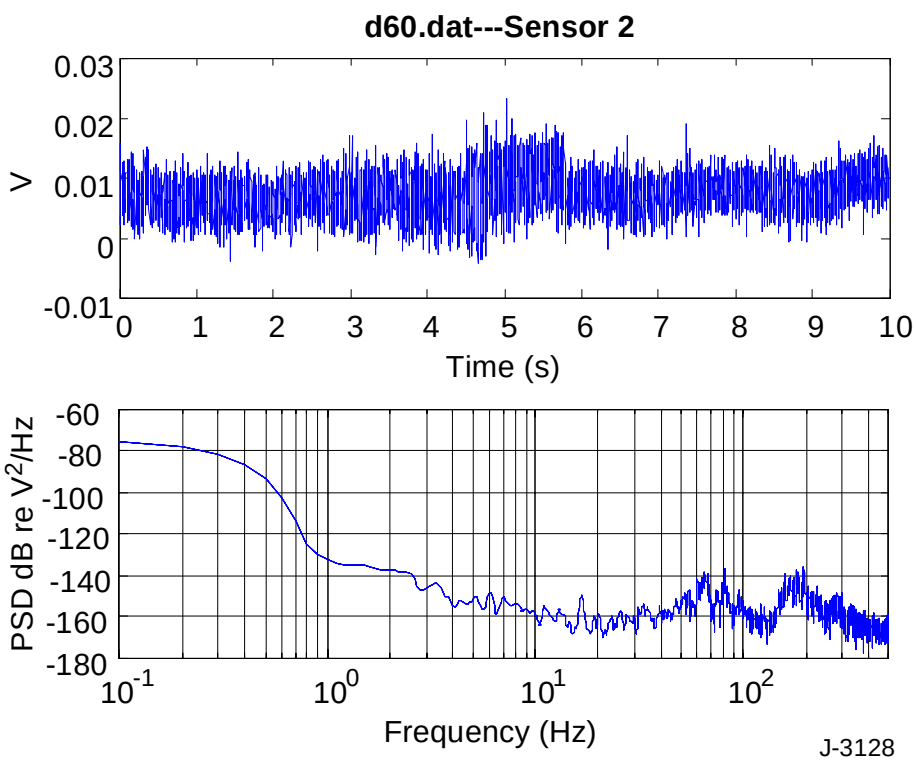

Figure 38. Sensor 2 (175 m) data collected during trackhoe digging.

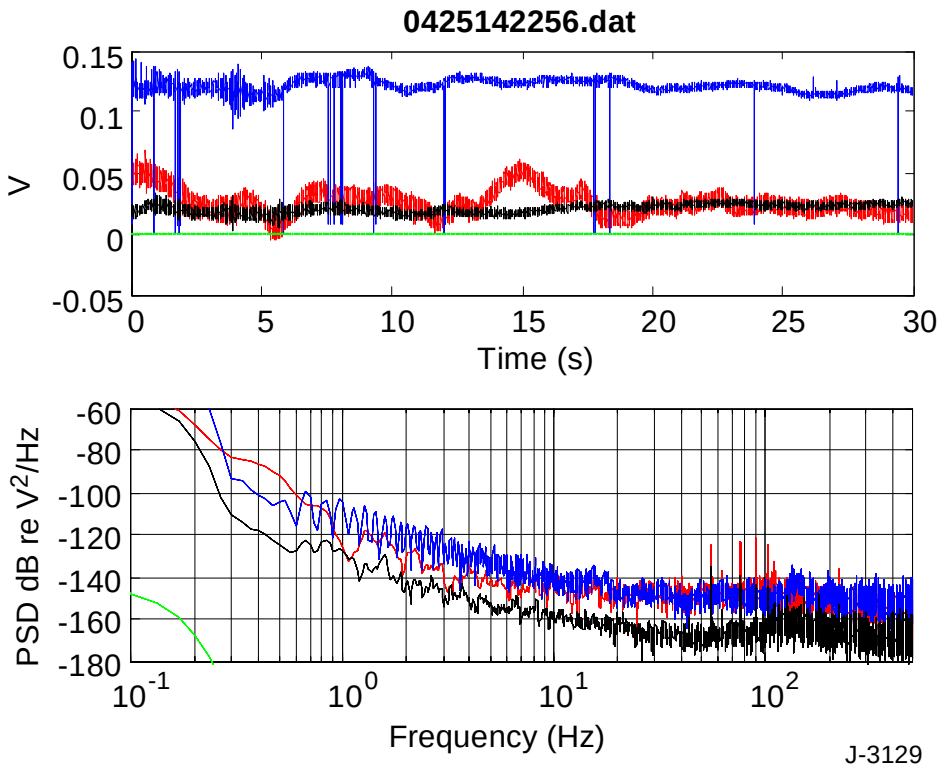

Figure 39. Data acquired during trackhoe idling: red = sensor1, blue = sensor2, black = sensor4. The spikes in the time series data represent data drop-outs in the wireless communication system.

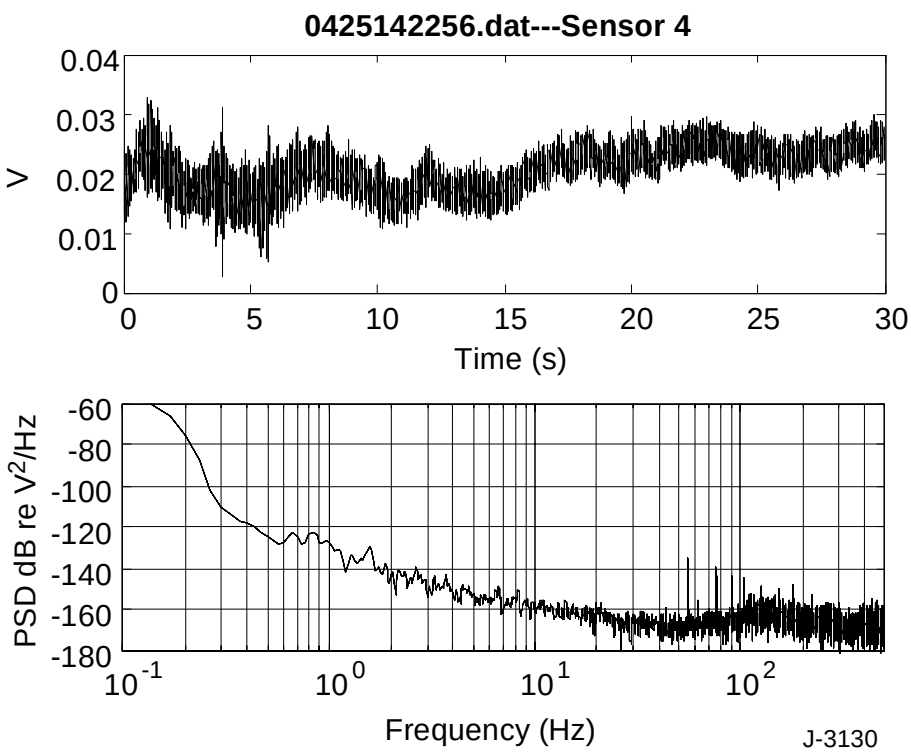

Figure 40. Sensor 4 (80 m) data collected during trackhoe idling.

The jackhammer signatures (Figure 41 through 44) are qualitatively similar to the tamper signature. A more detailed comparison of the signatures will be necessary to devise a differentiating algorithm.

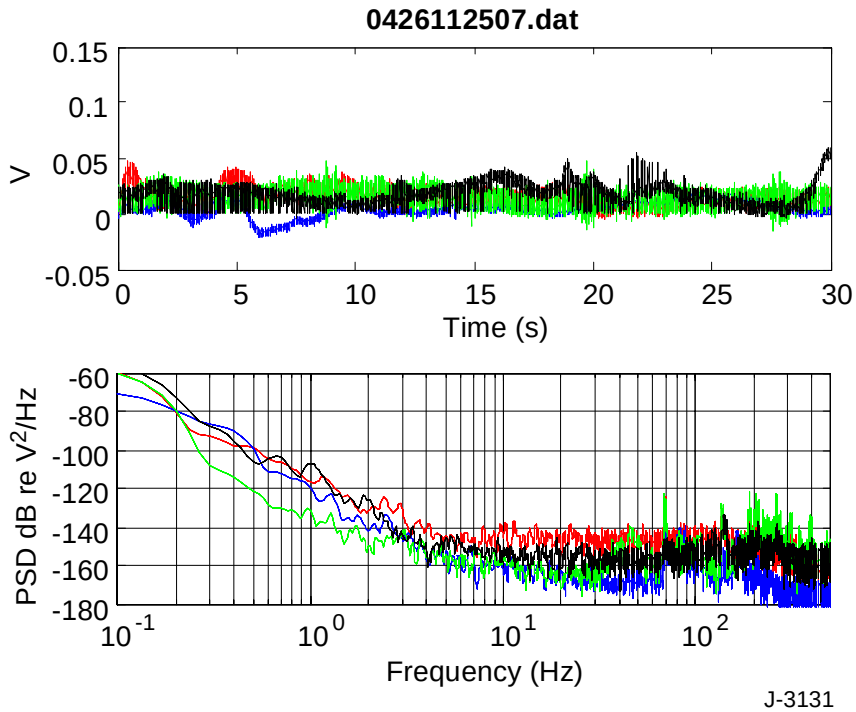

Figure 41. Data acquired during wheeled backhoe digging: red = sensor1, blue = sensor2, green = sensor3, black = sensor4.

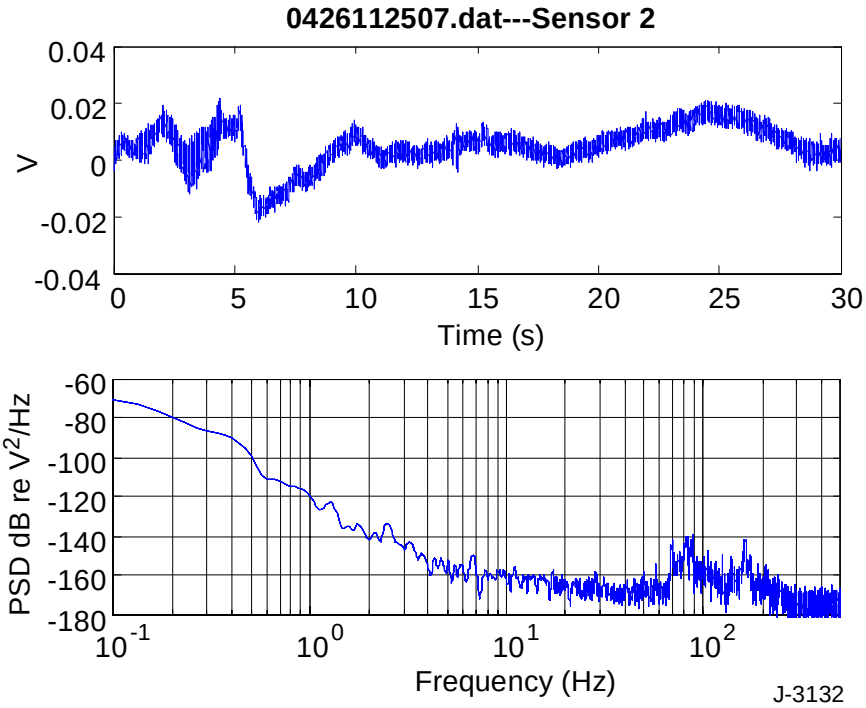

Figure 42. Sensor 2 (175 m) data collected during backhoe digging.

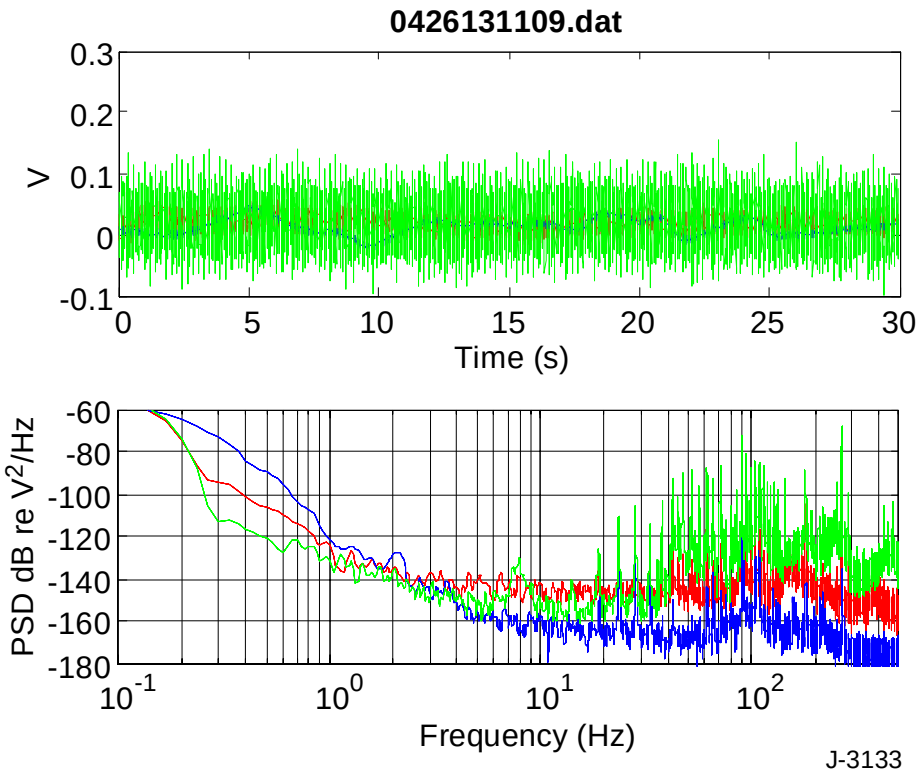

Figure 43. Data collected during jackhammer operation: red = sensor1, blue = sensor2, green = sensor3.

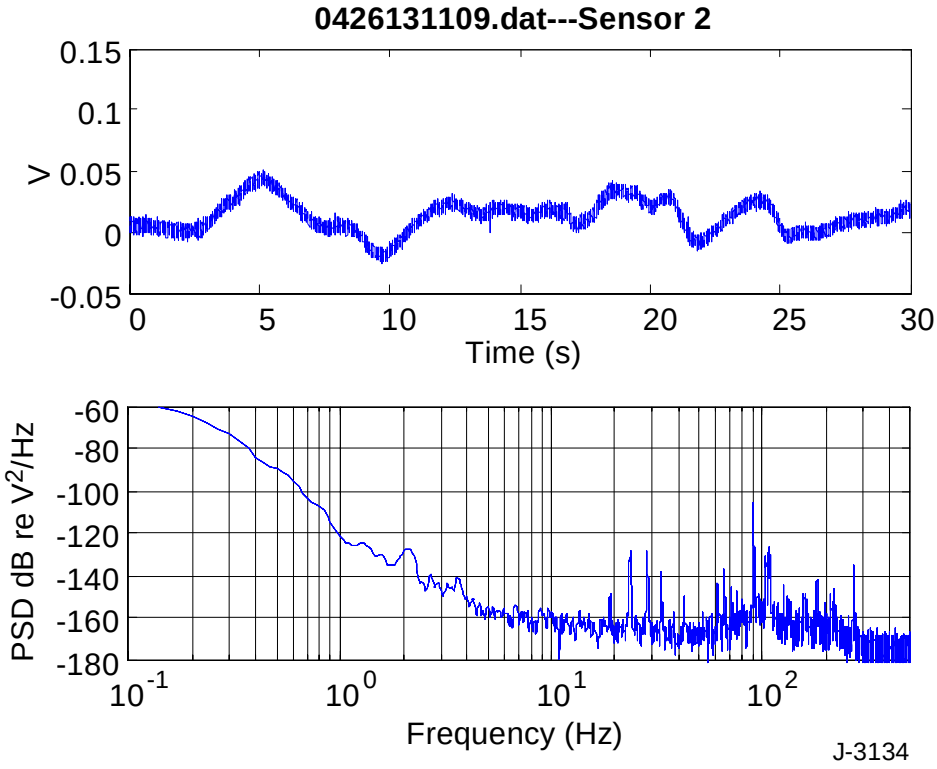

Figure 44. Sensor 2 (175 m) data collected during jackhammer operation.

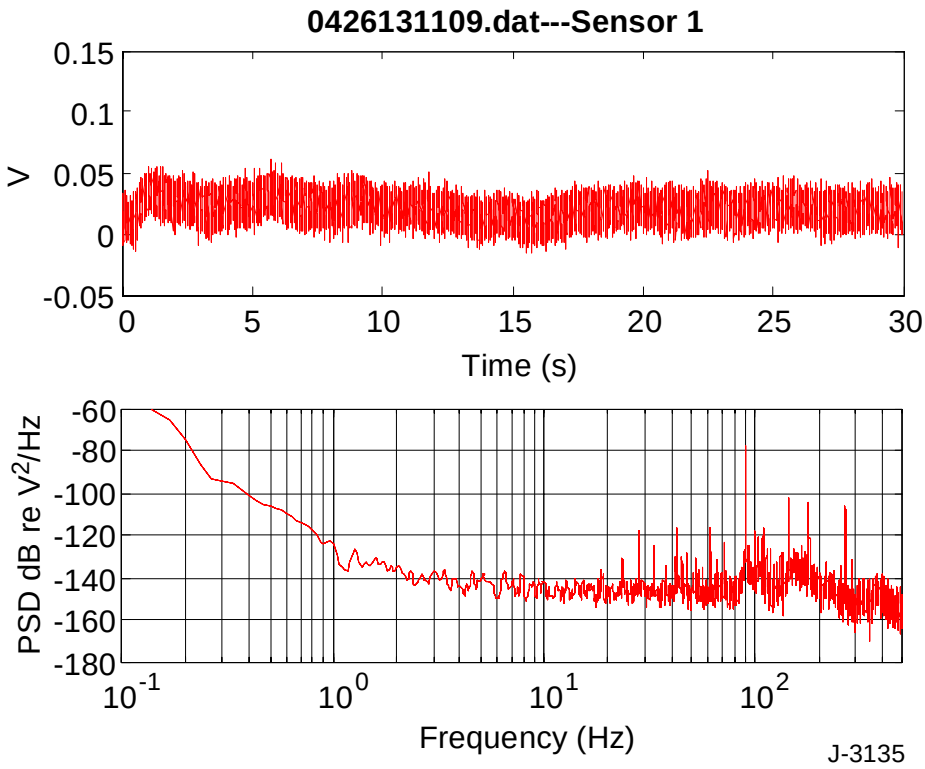

Figure 45. Sensor 1 (70 m) data collected during jackhammer operation.

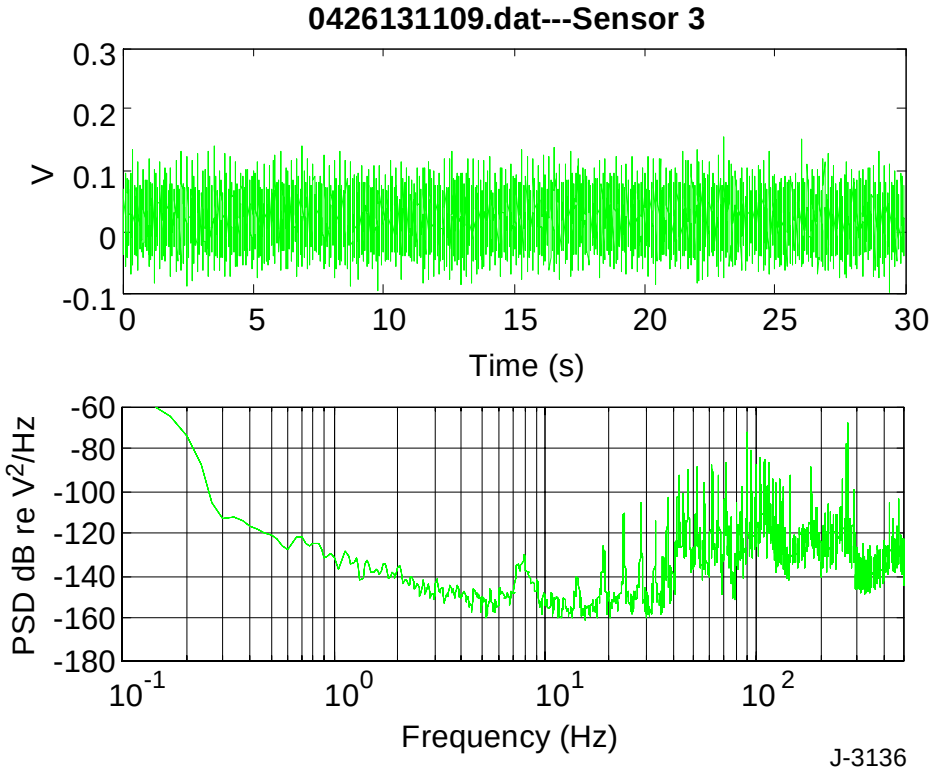

Figure 46. Sensor 3 (25.5 m) data collected during jackhammer operation.

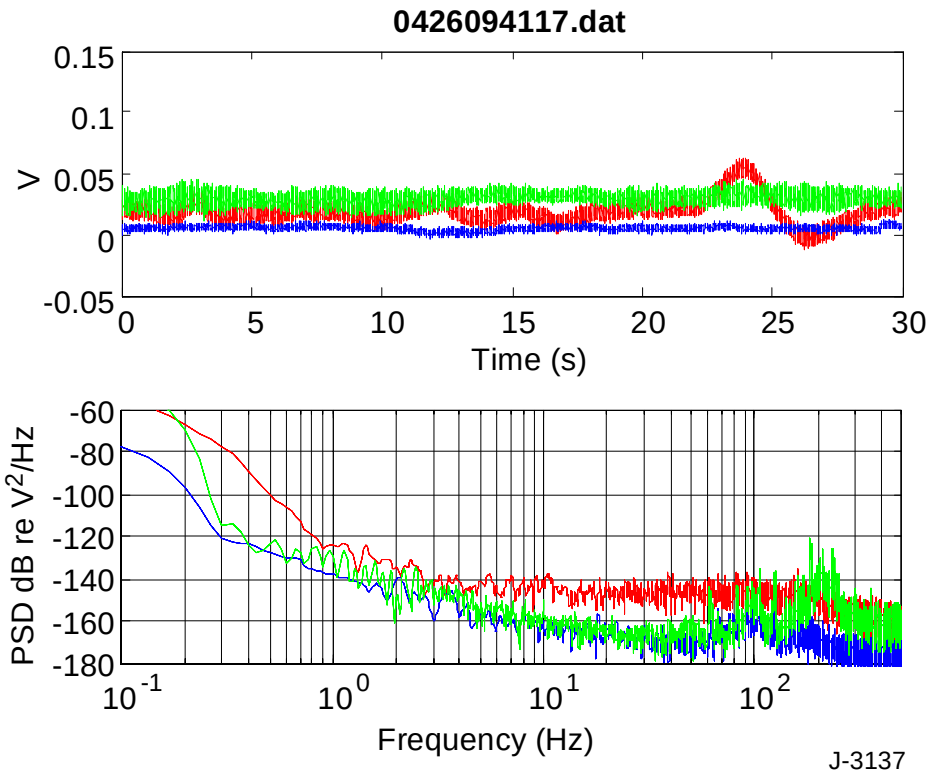

Figure 47. Data collected while backhoe is driving back and forth.

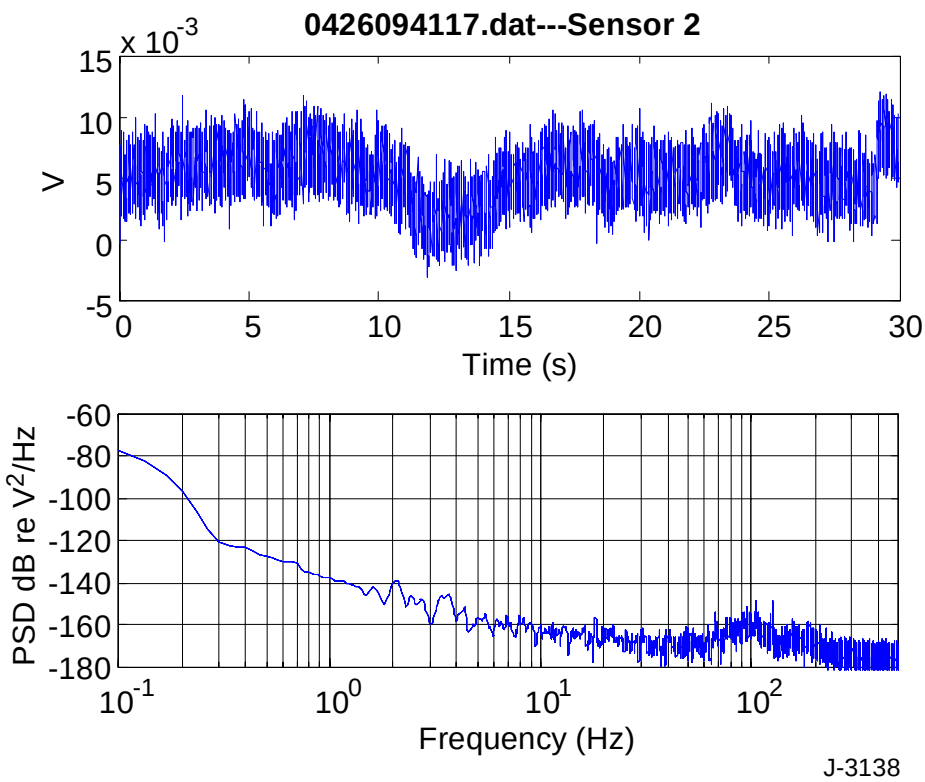

Figure 48. Sensor 2 data collected while backhoe is driving back and forth.

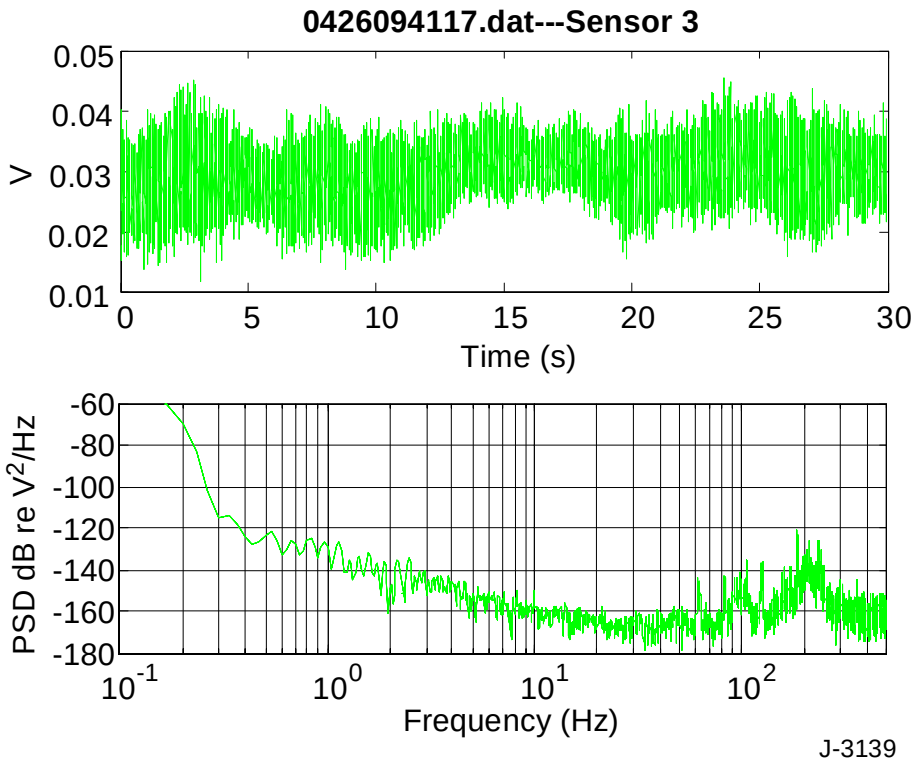

Figure 49. Sensor 3 data collected while backhoe is driving back and forth.

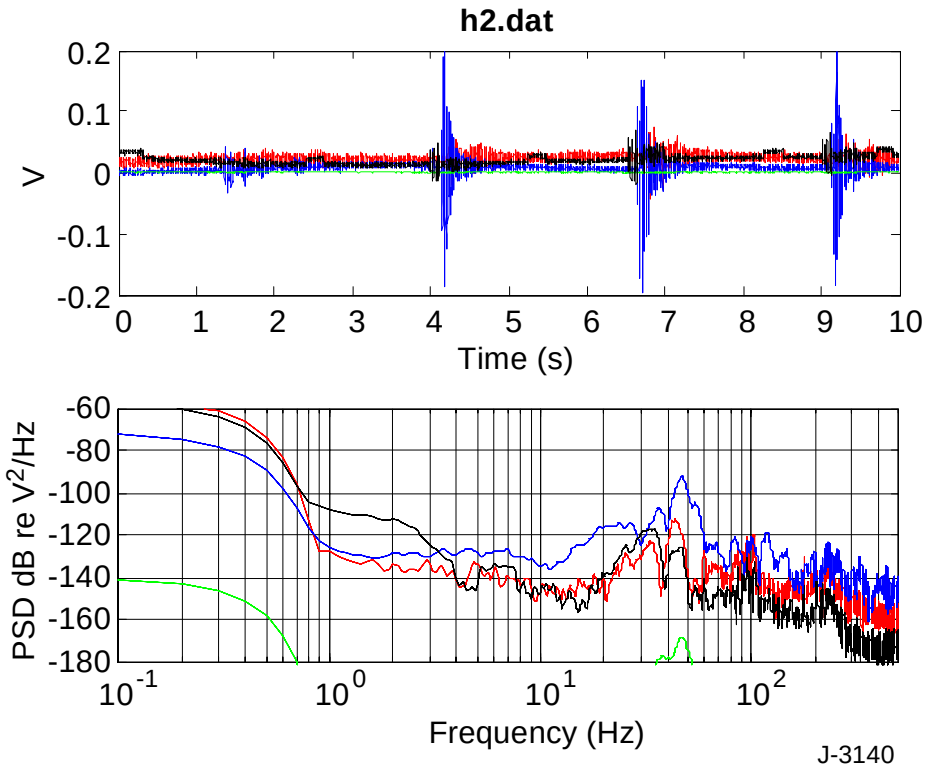

Figure 50. Data collected while the trackhoe bucket hits the ground.

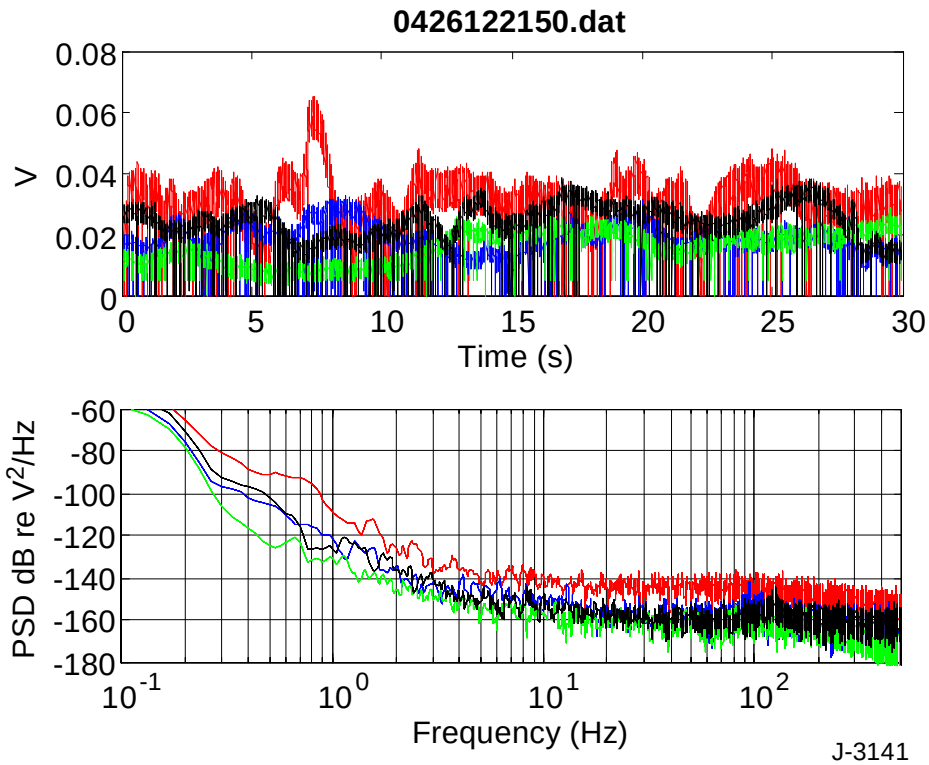

Figure 51. Data collected while a passenger vehicle idles roughly 30 m from sensor 4.

4.2 EP-1 Sensitivity and Range

As described earlier, we succeeded in both increasing the sensor response and decreasing the system noise in EP-1 compared to the previous sensor system. As a result, we expected that the maximum range of the sensor would be increased. Using the Johnson City data, we can estimate the range of the sensor under quiet conditions.

For the tamper, at 175 m, the fundamental frequency peak intensity is -131 dB. The noise is roughly -167 dB. The SNR is 36 dB, or 63:1. If we compare the intensity of the fundamental frequency measured by each sensor, we can estimate the range dependence of the signal intensity. Then we can extrapolate the effective range of EP-1 (see Table 11).

Table 11. Tamper Fundamental Frequency Signal Intensity
as a Function of Range and Extrapolated Effective Range

Sensor	Range	Signal
S3	25.5 m	-113 dB
S1	80 m	-122 dB
S2	175 m	-131 dB
Extrapolated limit	**1750 m**	**-151 dB (SNR=16 dB)**

If we consider all three data points, the signal falls roughly 18 dB for a 17 dB increase in range (or R^{-1}). If we consider only the 2 longer range points, the signal falls slightly more quickly than $R^{-1.3}$at this site. Even for the worst case fall-off of $R^{-1.3}$, the extrapolated effective range is 1750 m (allowing a SNR=6 or 16 dB).

4.3 Signature Variability of Similar Equipment

The Johnson City test provided the first opportunity to measure signatures from different pieces of similar class equipment with a single experimental setup. We acquired data from the trackhoe and the wheeled backhoe. While both pieces of equipment qualify as excavators, they are of vastly different sizes (see Figure 27). Even so, the signatures from these equipment are quite similar (Figure 52).

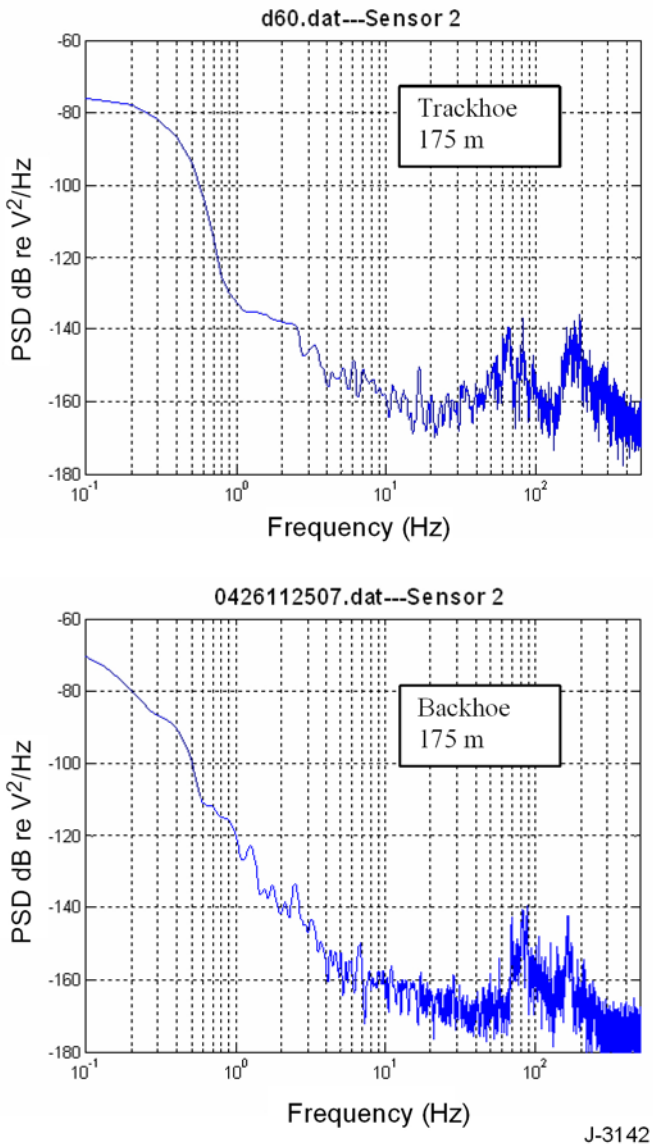

Figure 52. Trackhoe (top) and backhoe (bottom) signatures acquired with sensor 2.

The broad features between 20 and 300 Hz are prevalent. In both cases, there appear to be two broad features. The trackhoe has a somewhat broader and lower frequency spectrum, as compared to the backhoe. This seems intuitive, since the trackhoe is larger and heavier than the backhoe. Both of these signatures satisfy the "backhoe digging" algorithm. We will use these data to refine the algorithms

4.4 Signature Variation with Time

We were also able to acquire signatures of the same equipment at different times. The ideal conditions and the length of time available at the Johnson City site enabled us the investigate reproducibility of the data. On 26 April, the backhoe operated at around 08:30 and then again at 11:30. The signatures from those two times show some variability in the details; however, the overall spectral features remain constant (see Figure 53). We will use these data to refine the algorithms and ensure that the algorithms are robust.

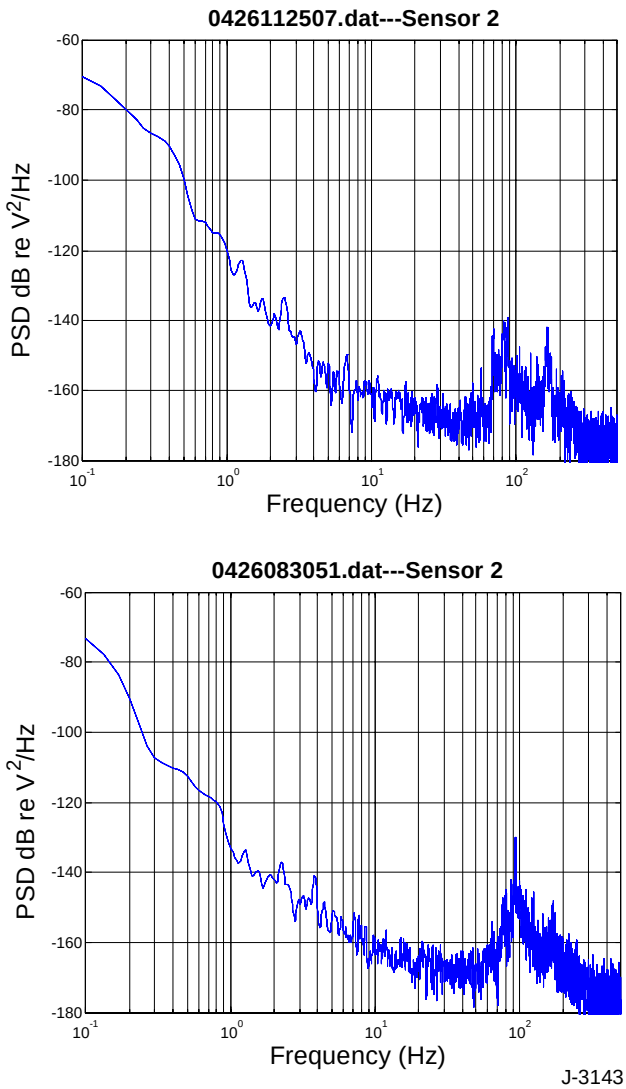

Figure 53. Backhoe signatures acquired at different times with sensor 2. The bottom trace was acquired at 08:30:51and the top trace at 11:25:07.

4.5 Triangulation

At the time of the Johnson City field test, we thought that the time lags in the data caused by the internal USB buffering were consistent, and could be calibrated out of the data. After detailed analysis of the Johnson City data, and some further experimentation, we discovered that those time lags are not consistent from acquisition to acquisition and not even consistent within a given acquisition.

Figure 54 shows an example of data where all four sensors were co-located in the ground, and were excited by remote hammer strokes. In this configuration, we expected that signals in all four sensors to be simultaneous. From Figure 54, it is obvious that the data streams from the four sensors are offset relative to one another. After closer examination, one can see that the time lags between the individual sensors are not even consistent within this single 10 sec period. (see Figures 55 and 56). Table 12 summarizes the time lags between sensors at t = 3 sec and t = 8 sec from this data set. Even in the absence of data drop-outs, there is no consistency in the timing between the data streams. As a result, the site characterization data from EP-1 is of limited use. The triangulation data can be used; however, we cannot determine absolute ranges.

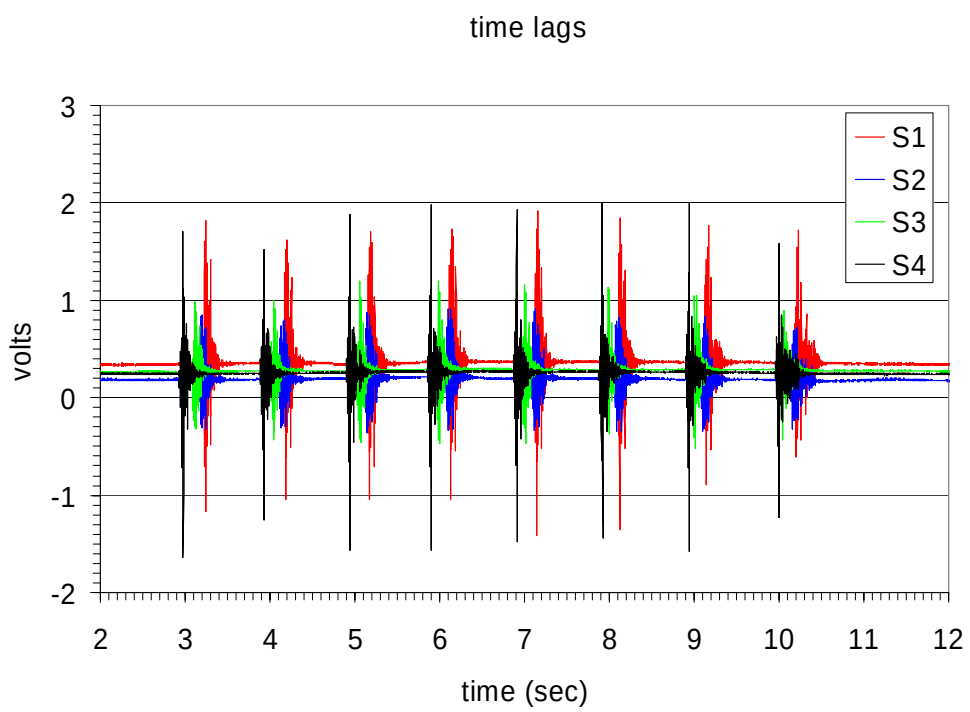

Figure 54. Data of hammer strokes acquired with sensors collocated.

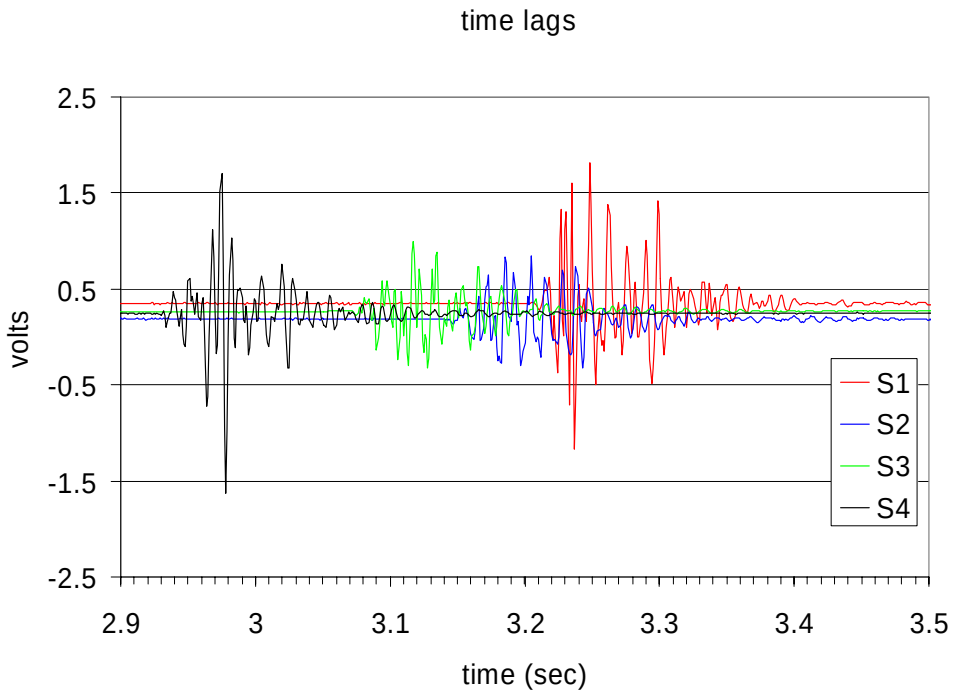

Figure 55. Expanded scale of Figure 38 showing time lags around t = 3 sec.

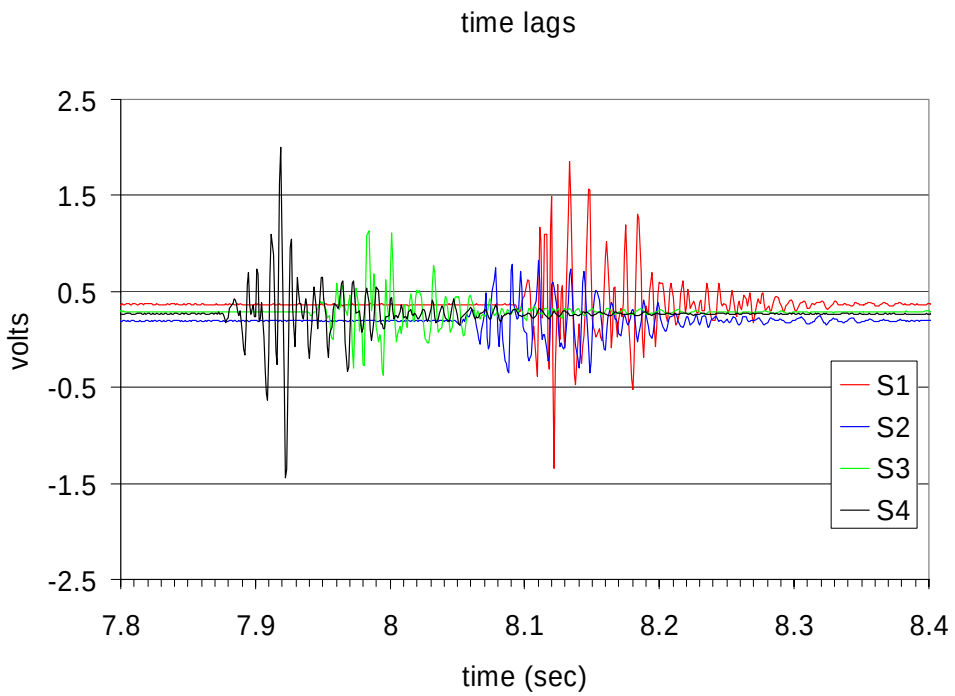

Figure 56. Expanded scale of Figure 38 showing time lags around t = 8 sec.

Table 12. Summary of Time Lags Between Sensors from t = 3 sec and t = 8 sec of Figure 53

Sensor pairs	Time lags (sec)	
	T = 3 sec	T = 8 sec
S4 – S3	0.141	0.071
S4 – S2	0.214	0.179
S4 – S1	0.276	0.216
S3 – S2	0.073	0.108
S3 – S1	0.135	0.145
S2 – S1	0.062	0.037

Although the absolute timing of the data streams is compromised, we can still use the Johnson City data to demonstrate the triangulation technique.

Conceptually, the determination of the time lag between two signals is quite simple. However, creating an algorithm to determine time lags automatically is more complex. When processing complex waveforms, it is not usually as clear exactly how to determine the time lag. For example, the algorithm could determine the time lag using any of the following techniques

- detect the initial rising edges of the waveforms
- detect the peak of the waveforms
- average the times when the waveform transitions above and below a fixed threshold
- determine the best overlap using the entire waveform

Given the complexity of the waveforms, we think that an algorithm that determines the best overlap between waveforms holds the most promise. A simple technique for "aligning" waveforms is the cross-correlation. In the time domain, the cross correlation, xc, is given by

$$xc = \int_{-\infty}^{\infty} f(\tau) \cdot g(t-\tau) d\tau$$

If the two waveforms, f(t) and g(t) are identical, but offset in time, the cross-correlation shows a peak at the corresponding time lag. If f(t) is earlier than g(t), then the cross-correlation shows a positive time lag. If f(t) is later than g(t), the time lag is negative. In practice the cross-correlation is most easily calculated in the frequency domain.

$$xc = FFT^{-1}[F(\omega) \cdot G^{*}(\omega)]$$

where F(ω) is the Fourier transform of f(t) and G*(ω) is the complex conjugate of the Fourier transform of g(t).

Figure 57 shows an example of the cross-correlation between two simple waveforms. The waveforms are separated by 0.1 sec in time and the cross-correlation shows a peak at the corresponding lag time.

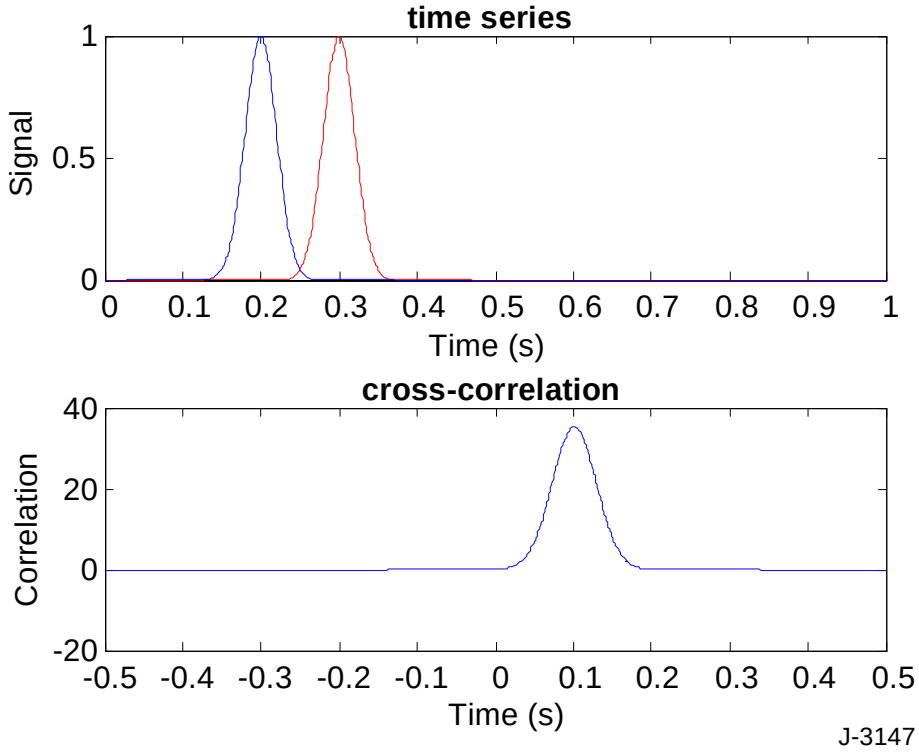

Figure 57. Cross-correlation between two simple waveforms.

We applied the cross-correlation technique to some of the EP-1 data. To demonstrate the technique, we first performed the cross-correlation on the hammer-stroke data of Figures 54 through 56. Figure 58 shows the cross-correlation between sensor 2 and 3 from those data. The blue curve is the absolute value of the cross-correlation. The red curve shows the cross-correlation after smoothing with a running average. Table 13 shows the time lags calculated by the cross-correlation algorithm, both using the raw correlation and the averaged result. The cross-correlation results are compared to the best "eyeball" fit of the time lag.

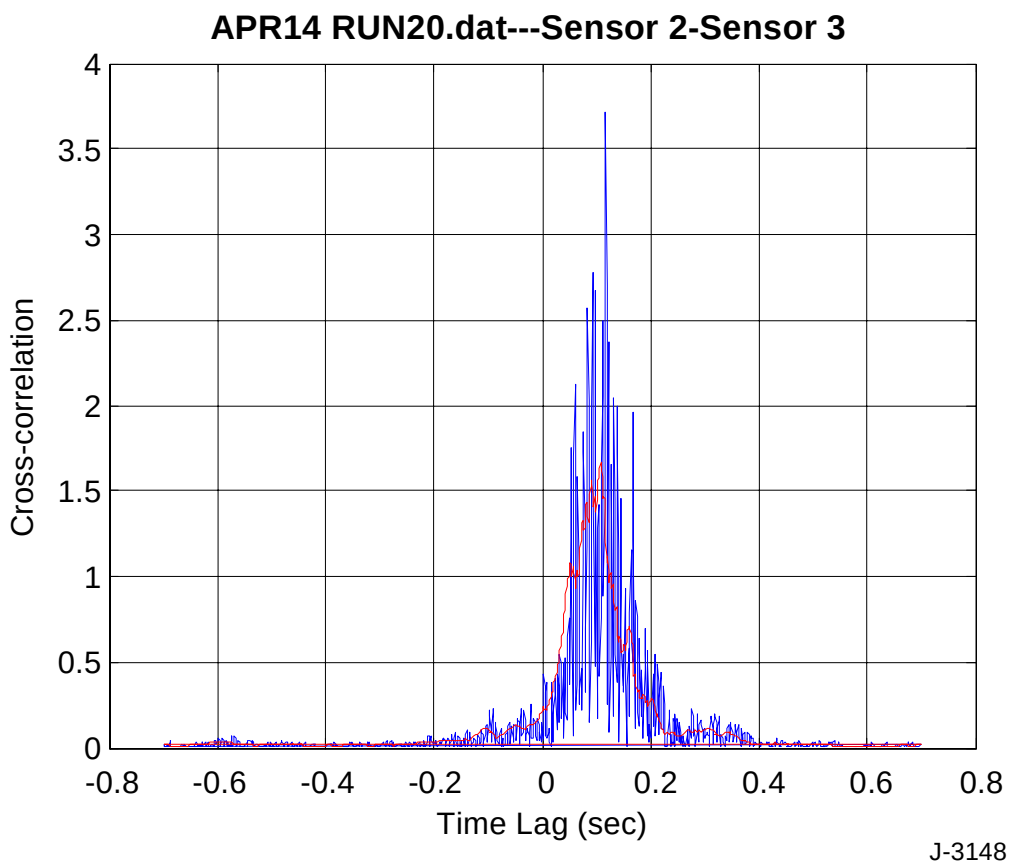

Figure 58. Cross-correlation of sensors 2 and 3 from hammer stroke data. The blue curve is the raw correlation function. The red curve is the running average.

Table 13. Comparison of Cross-Correlation Results Using Raw Correlation Function and Smoothed Correlation Function with the Best Eyeball Determination of the Time Lags

Sensor pairs	Time lags (t = 8 sec data)		
	Raw XC (sec)	**Smoothed XC (sec)**	**Manual determination (sec)**
S4 – S3	0.061	0.069	0.071
S4 – S2	0.168	0.153	0.179
S4 – S1	0.225	0.198	0.216
S3 – S2	0.117	0.108	0.108
S3 – S1	0.139	0.137	0.145
S2 - S1	0.046	0.036	0.037

We also applied the cross-correlation to the Johnson City data. Figure 59 shows data of the trackhoe hitting the ground with its shovel. Sensors 1, 2, and 4 are active during this time. Figure 60 shows the cross-correlation as an example.

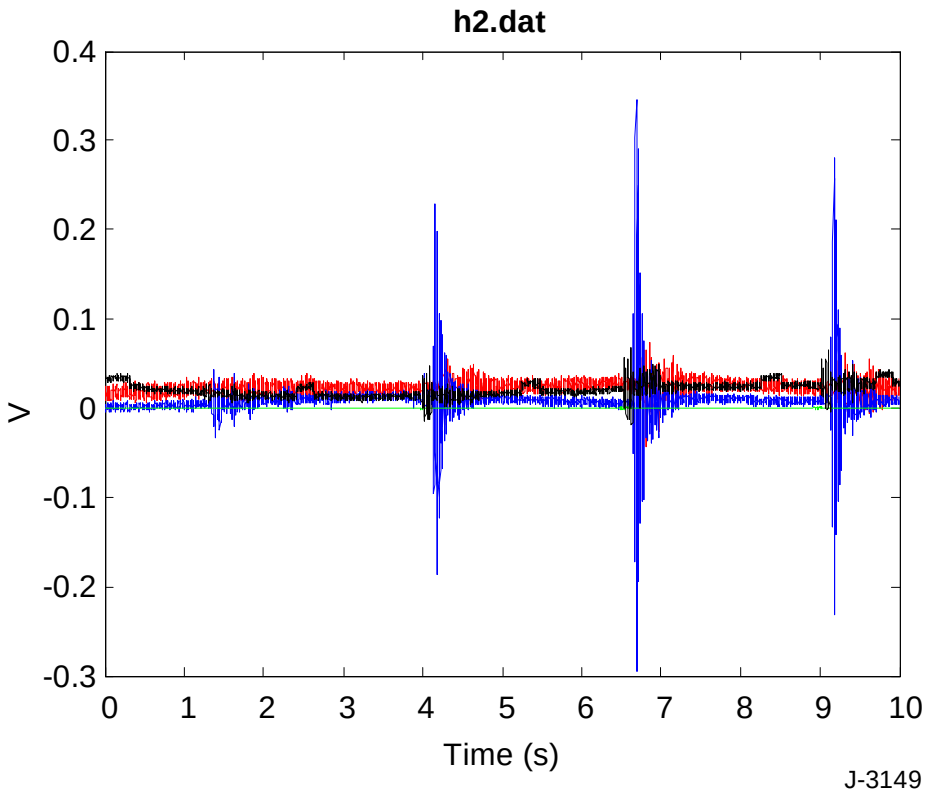

Figure 59. Time series data acquired while trackhoe is hitting the ground with its shovel.

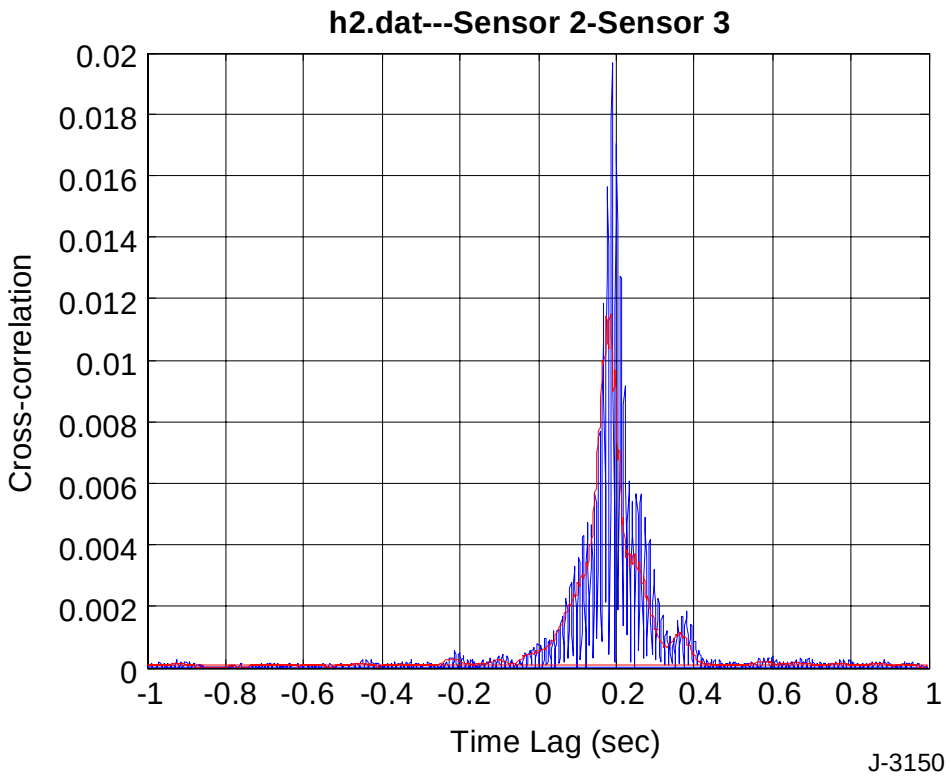

Figure 60. Cross-correlation of sensors 2 and 3 for data between t=6 sec and t=8 sec.

We also applied the cross-correlation to some of the Johnson City data. Figure 59 shows the time series data acquired while the trackhoe was hitting the ground with its shovel. Figure 60 shows the cross-correlation between sensors 2 and 3.

4.6 Algorithm Testing

We used the data from the Somerset Field Checkout and the Johnson City field test to assess the performance of the preliminary algorithms.

The threat identification algorithm was developed using data primarily from the Aug 03 field test. At PDR, we described the algorithm and presented the results of achieved after processing several data sets through the preliminary robust identification algorithm. We shoed that using the Aug 03 data, the algorithm could achieve a probability of detection (Pd) of nearly 100% and a probability of false alarm (Pfa) of nearly zero. We would expect excellent results when the algorithm is tested with the data set originally used to design the algorithm.

The recent EP-1 data provides an excellent database to initially test the preliminary algorithm and then to refine it further. We used four data sets to test the preliminary algorithm. Those data sets are summarized in Table 14. **No attempt was made to use these data to optimize the algorithm before the test. Nor was any attempt made to pre-screen the files for data quality or anomalies. These results are a fair indication of where the algorithm needs to be modified.**

Table 14. Data Sets Used to Test Preliminary Algorithms

Data set	Threat	Number of files
Somerset	Backhoe	17 files
	Cement mixer	8 files
Johnson City	Jackhammer	38 files
	Tamper	54 files

The threat identification algorithm performed quite well on the Somerset backhoe data. Figure 61 shows the results of that test. Before the test, no attempt was made to optimize the algorithm. For S3 and S4, all the files were properly identified as backhoe. For S1 and S2 most of the files were properly identified as backhoe. No files were mis-identified as jackhammer.

Figure 62 shows the results of processing eight cement mixer files through the algorithm. Most of these files were identified as a backhoe. In an operational system, these would represent false positive. Obviously, we must refine the algorithm to make it more robust.

Figures 63 and 64 show the result of processing 38 jackhammer files and 54 tamper files through the preliminary threat identification algorithm. The data from S1 performed reasonably well, given that the tamper signature appears fairly similar to the jackhammer. The data fro mS2 and S3 produced many false positives.

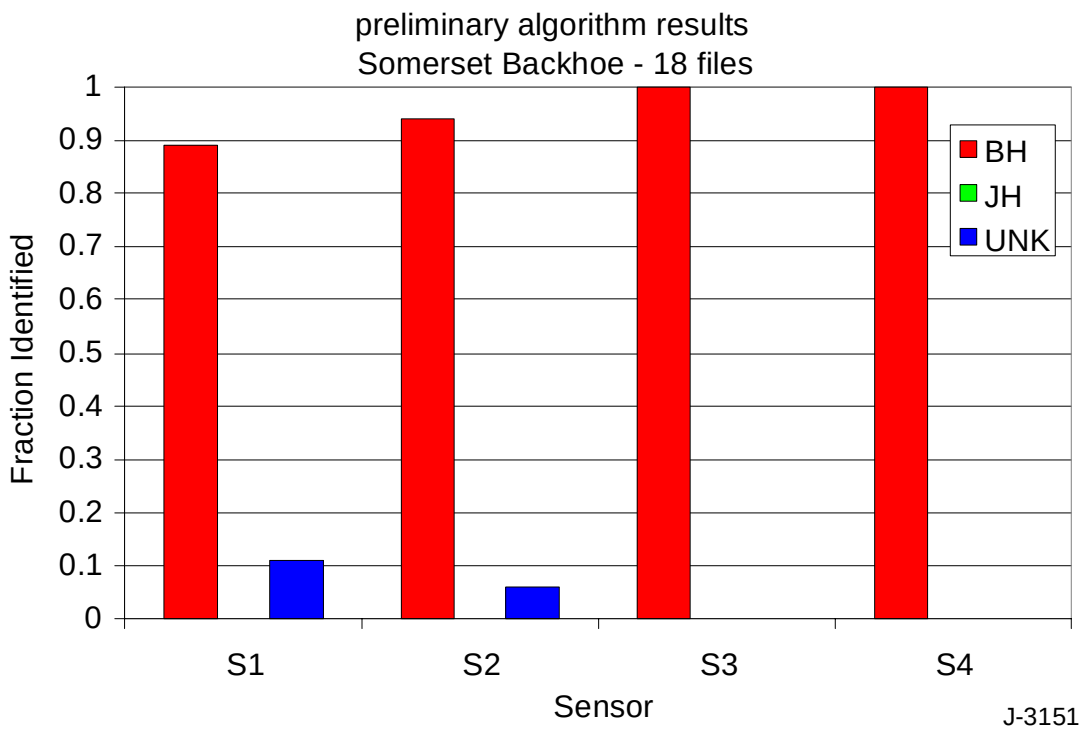

Figure 61. Result of processing 18 backhoe files (4 sensors) through the preliminary threat identification algorithm. No attempt was made to optimize the algorithm before the test.

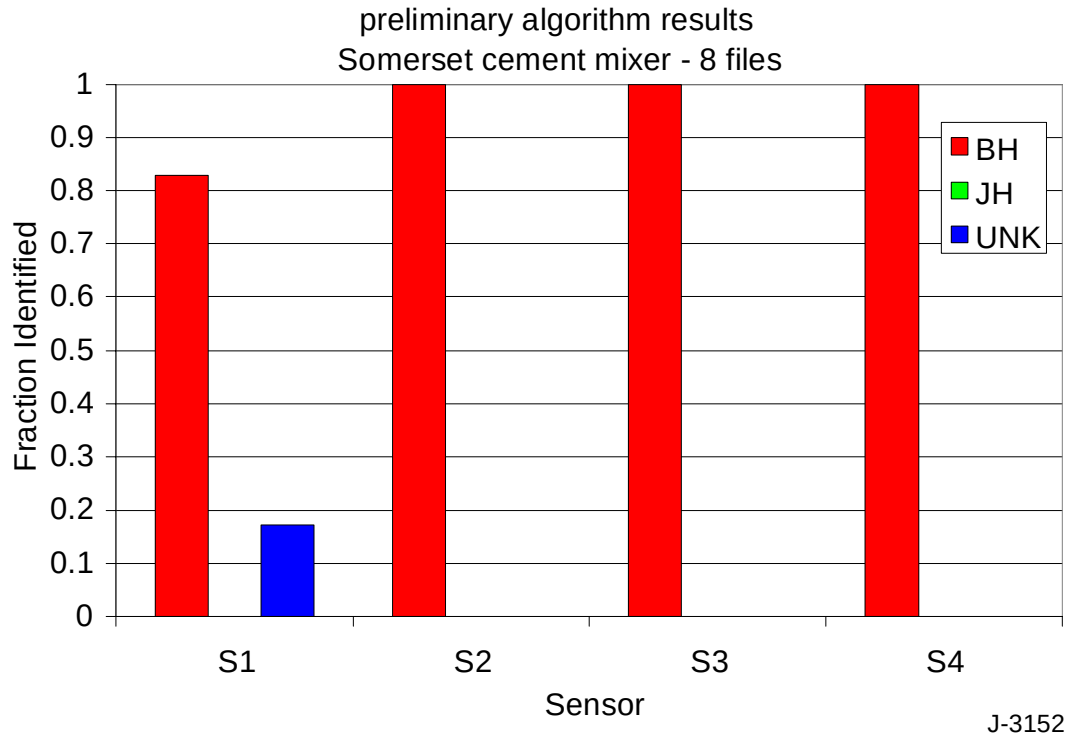

Figure 62. Result of processing 8 cement mixer files through the preliminary threat identification algorithm. No attempt was made to optimize the algorithm before the test.

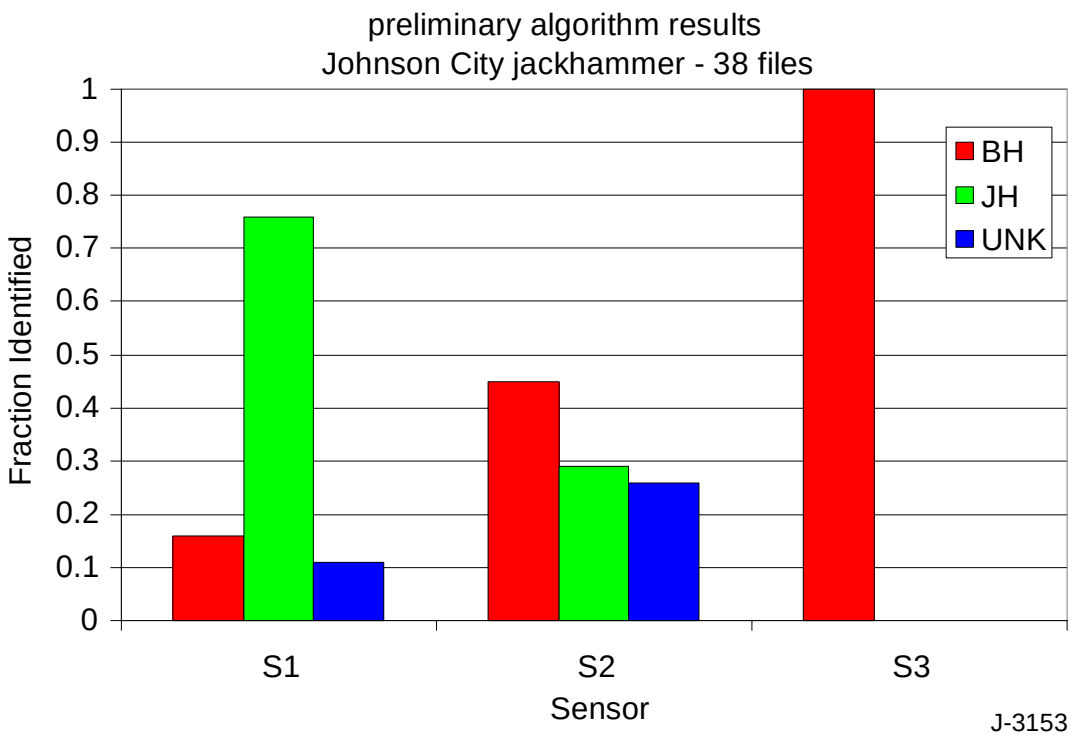

Figure 63. Result of processing 38 jackhammer files through the preliminary threat identification algorithm. No attempt was made to optimize the algorithm before the test.

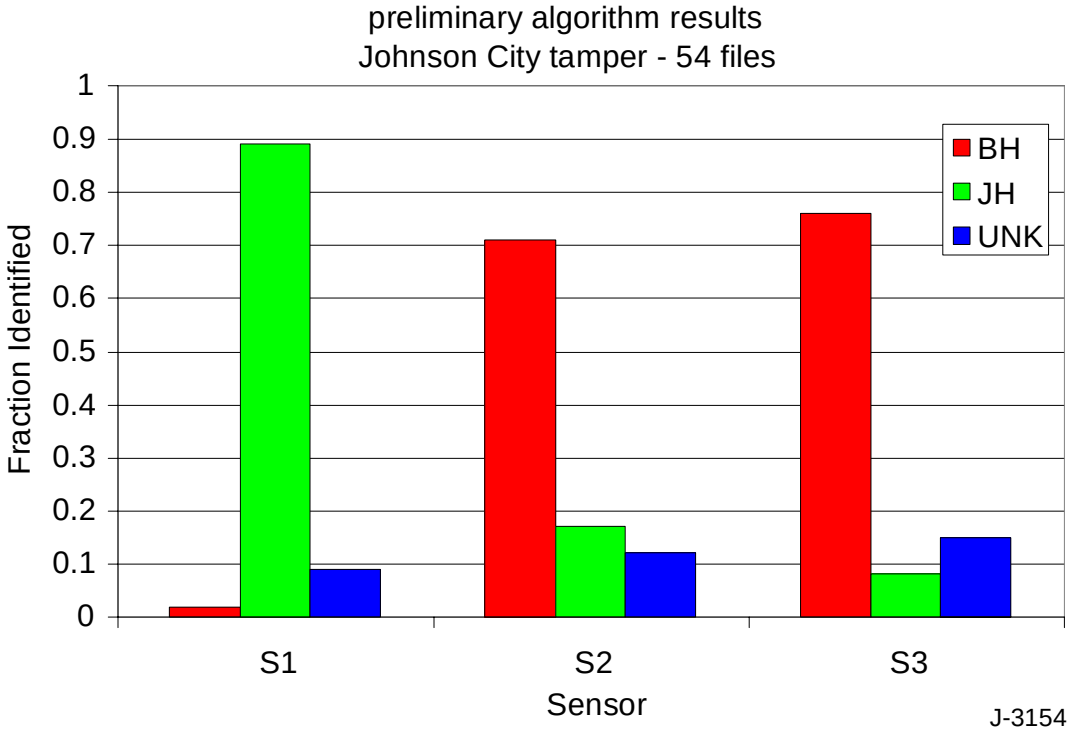

Figure 64. Result of processing 54 tamper files through the preliminary threat identification algorithm. No attempt was made to optimize the algorithm before the test.

These algorithm tests represent the first opportunity to process real EP-1 data with a previously untested algorithm. These results were used to guide algorithm modification and optimization.

4.7 Optimization of Algorithm

PSI developed the Build-1 algorithm using NYSEARCH Phase-1 data as the training set. As described previously, the algorithm uses a filter-bank approach to create a sparse spectrum from the time-series data. The algorithm then compares the spectrum to library spectra.

The Build-1 algorithm provided good results from backhoe identification. The algorithm required optimization to reliably identify jackhammers. After optimization, the Build-2 algorithm provided good identification of both backhoe and jackhammer threats. Figure 65 shows the results of the Build-2 algorithm on 9 minutes of backhoe data and on 20 minutes of jackhammer data. The algorithm correctly identifies the threat nearly all the time on all sensors. By using multiple sensors for the identification, we can improve system performance.

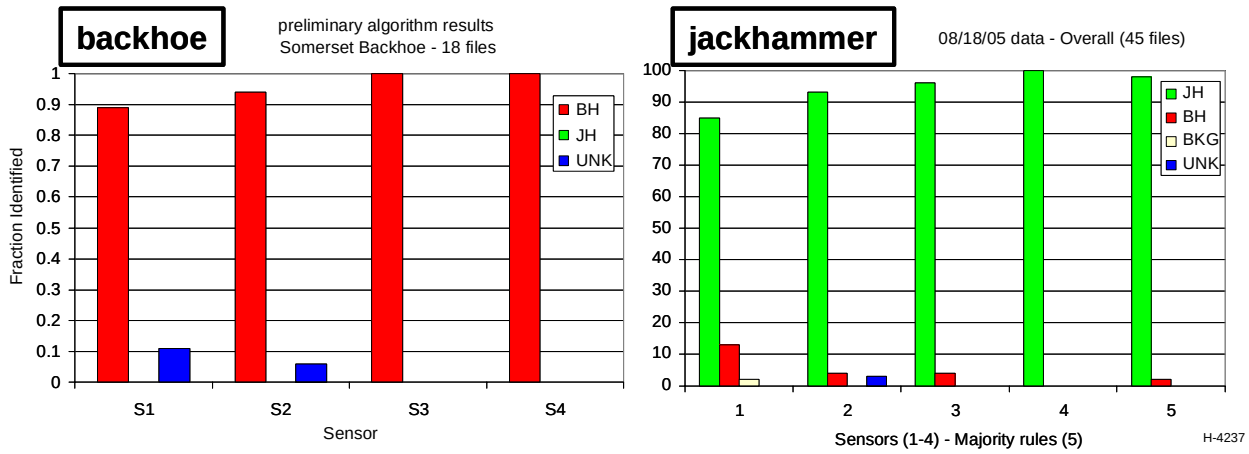

Figure 65. Build-2 algorithm result for backhoe (left) and jackhammer (right) identification.

5. Post Johnson City Field Test Improvements / Analysis

5.1 Develop Alternative Data Acquisition System

At Johnson City, we failed to acquire accurate triangulation data because of the data acquisition system. The relative timing of the data streams from the four sensors was corrected by the data acquisition system (Figure 66). At the Johnson City test, we used wireless serial DAQ system to facilitate acquisition of remote sensor data at long range. The wireless system also enabled the system to transmit digital data, thus minimizing noise interference. However, internal buffering in the computer introduced non-reproducible time lags in the data (Figure 67).

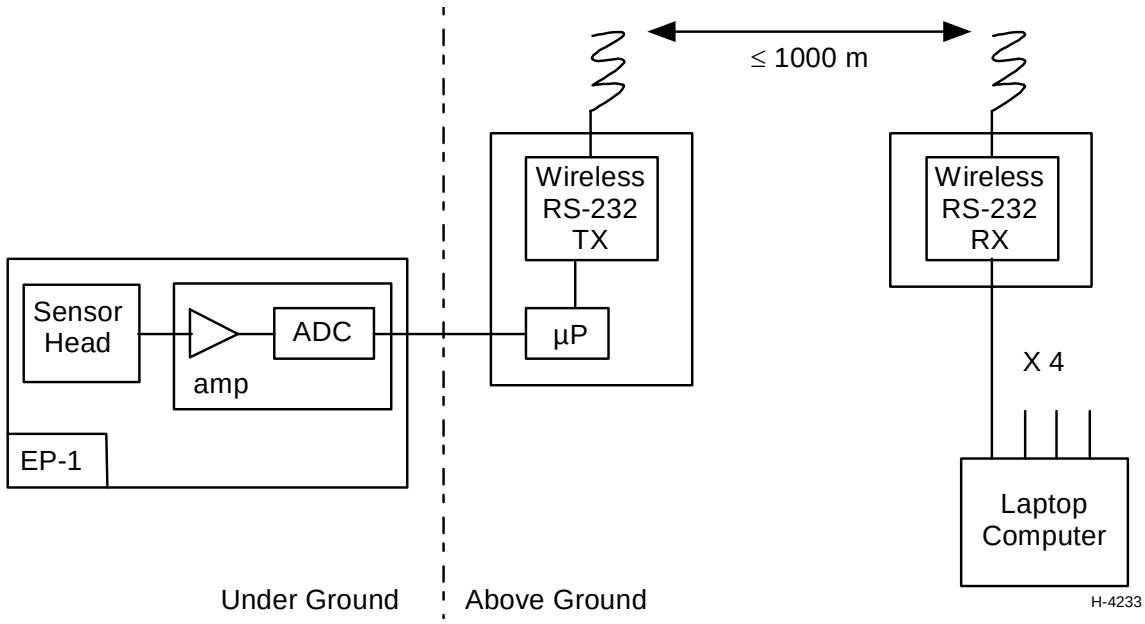

Figure 66. Wireless data acquisition system used at the Johnson City test.

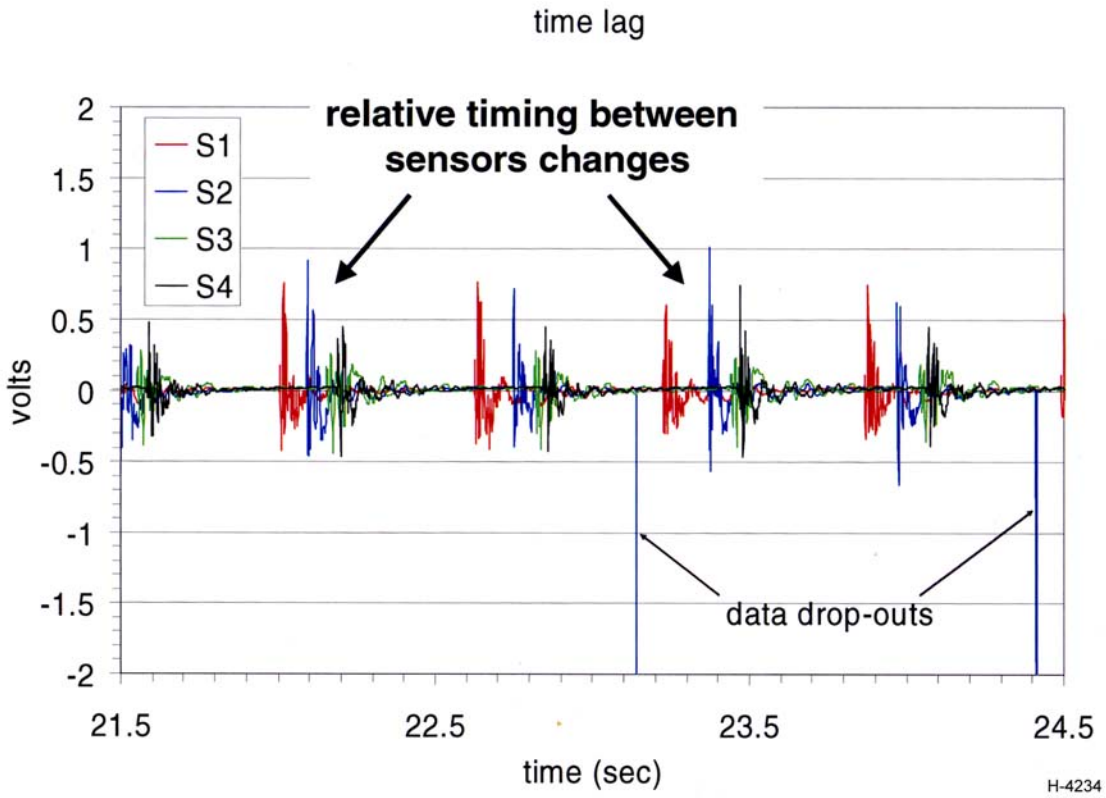

Figure 67. The wireless acquisition system introduced non-reproducible times lags between the four sensor data streams.

In order to acquire reliable triangulation data, the data streams from the four sensors must be precisely synchronized. Under the Phase II SIR program, we implemented a hard-wired analog data acquisition system (see Figure 68). That system demanded differential data transmission as well as use of low capacitance bale. That system has no time lags; however, its range is limited to approximately 250 m due to cable losses.

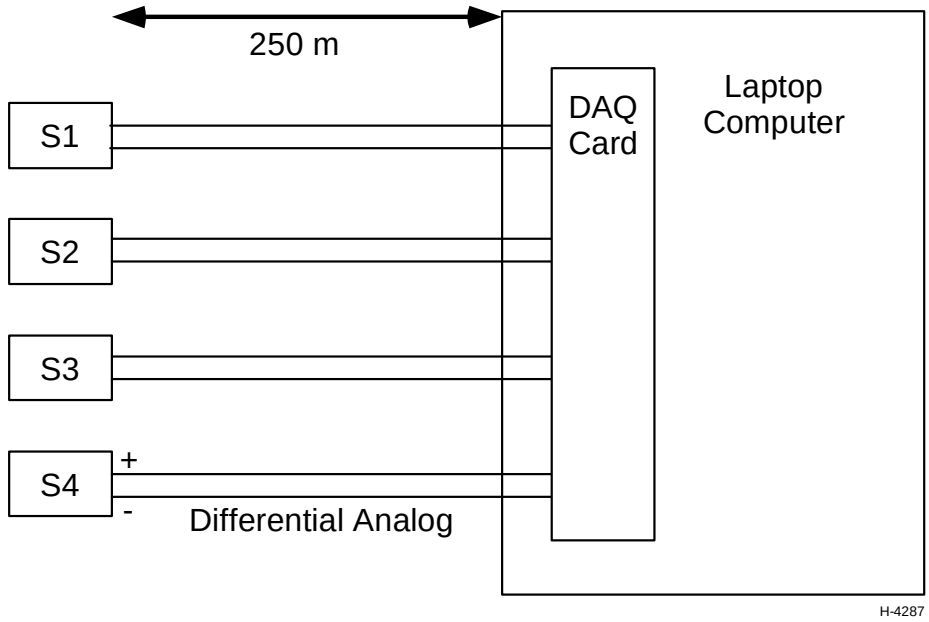

Figure 68. Analog DAQ system that will ensure relative synchronization of the four sensor data streams.

5.2 Site Characterization Data

Using the new data acquisition system, we acquired data to support the consultant activities. We repeated the "site characterization" measurements.

We repeated the site characterization measurements at a location close to PSI. The location is an empty building lot and parking lot approximately 250 x 250 m in size. There are grassy "islands" interspersed throughout the paved parking lot.

We deployed the sensors S2, S3, and S4 on one of these grassy islands. S2, S3, S4 were buried approximately 1.5 feet below grade and spaced 15 feet apart (see Figure 69). S1 was used as the "t=0" sensor and was always placed next to the sledgehammer strike point.

The source was a 16 lb sledgehammer striking a 6 inch diameter 0.5 inch thick steel plate placed on the ground. The distance of the source is measured from S2. The grassy island is 155 feet long. For distances less than 155 feet, the steel plate is placed on the grassy soil. For distances greater than 155 feet, the steel plate is placed on the parking lot macadam.

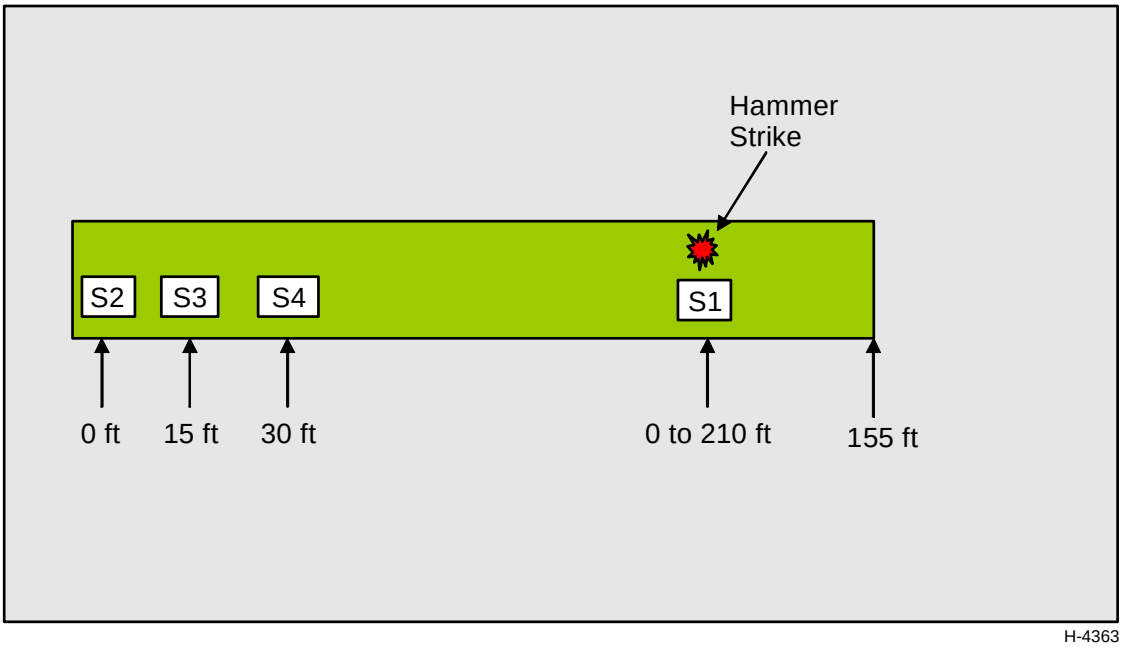

Figure 69. The measurement configuration for the site characterization.

Figures 70 through 72 show examples of the site characterization data provided to the consultant. Figure 70 shows unfiltered data, dominated by the seismic signature. Figure 71 shows data that was high-pass filtered at 200 Hz. These data are dominated by the air-coupled waves. The filters were designed in MATLAB. They are Equiripple filters with F_stop=190 Hz and F_pass of 210 Hz. The rejection is -80 dB. We have compensated for the group delay (of 69 samples) in the plots. Figure 72 shows an overlay of both filtered and unfiltered data.

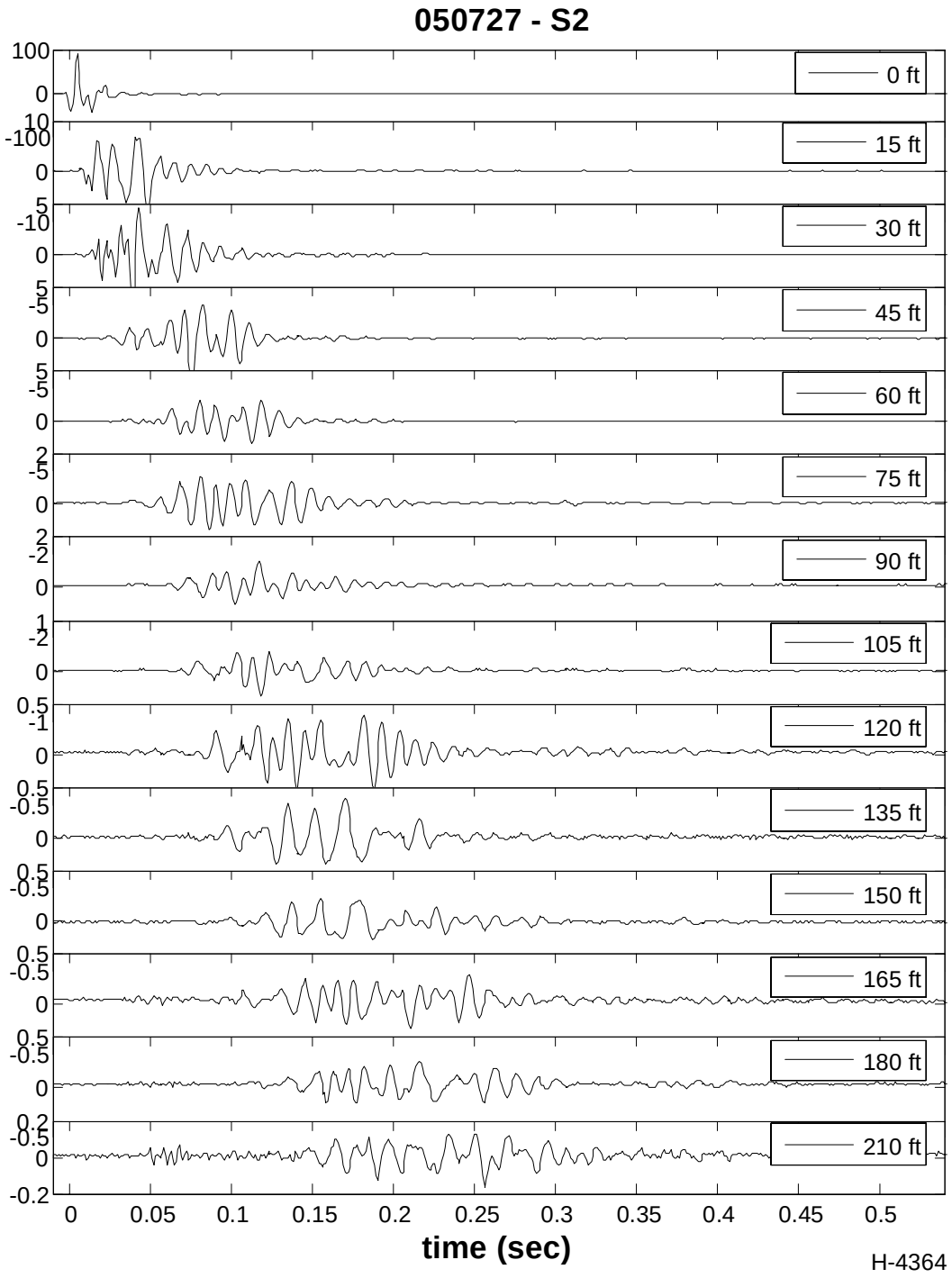

Figure 70. Unfiltered data from site characterization measurements.

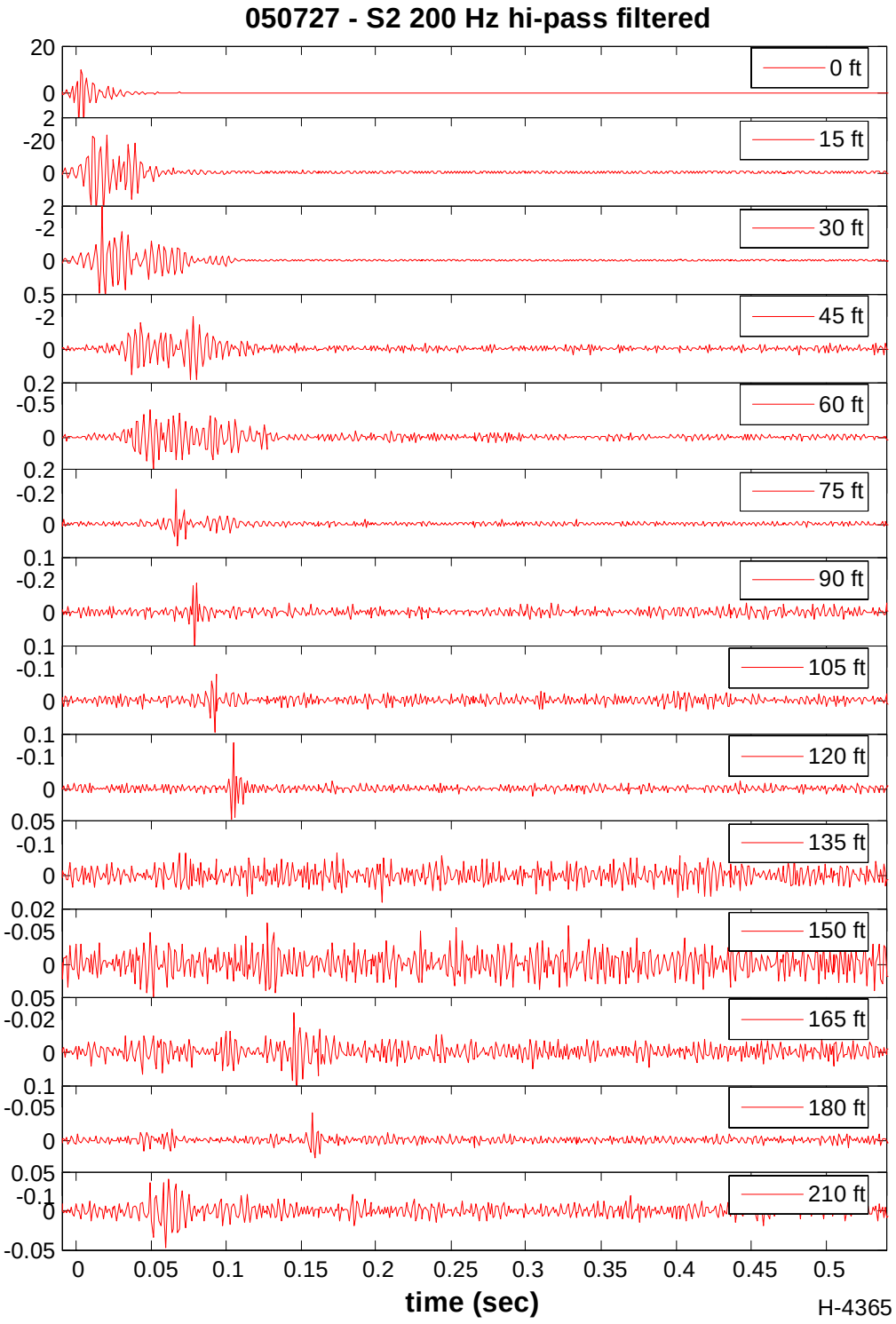

Figure 71. 200 Hz high-pass filtered data from site characterization.

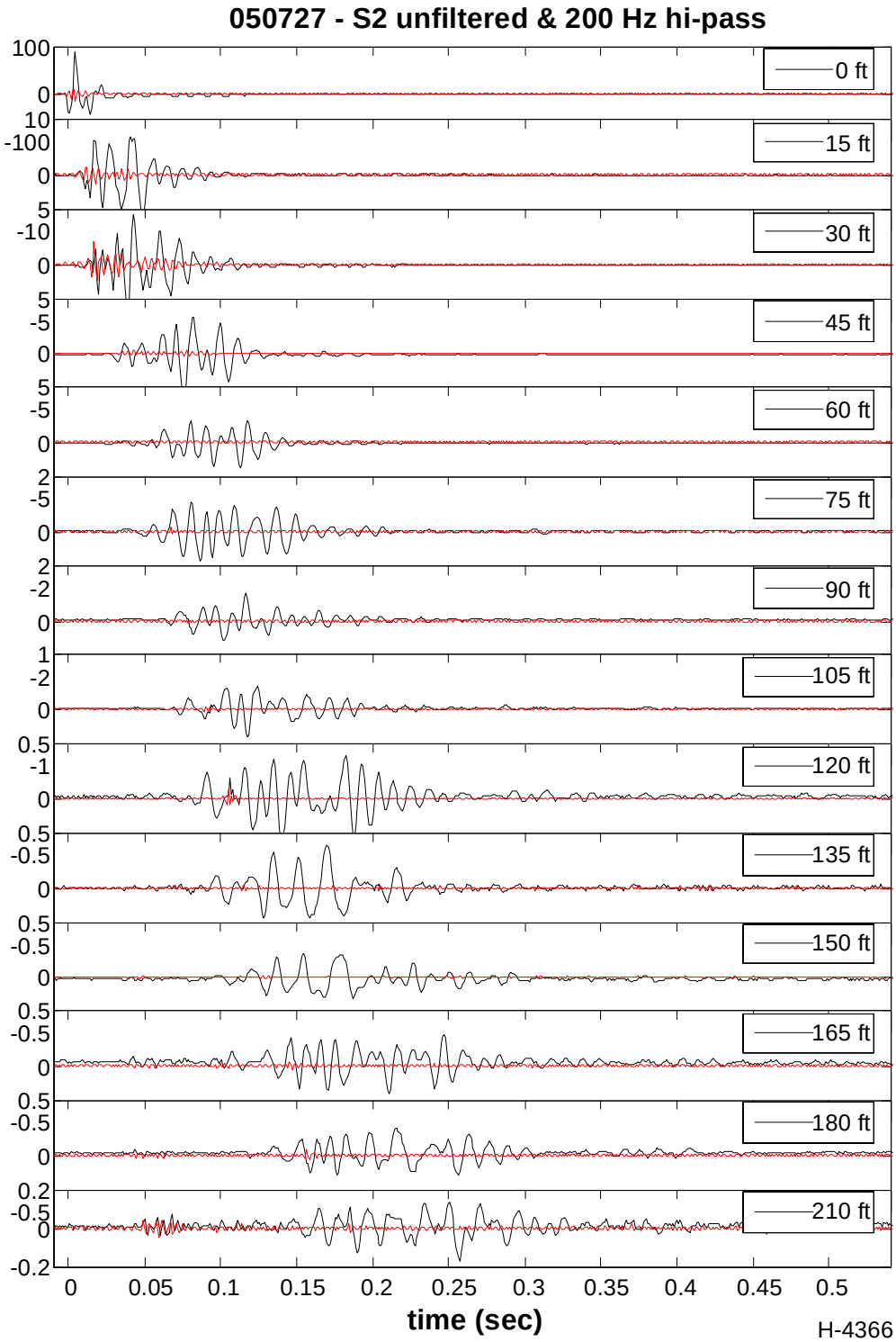

Figure 72. Overlay of unfiltered and 200 Hz high-pass filtered data.

5.3 Triangulation Data

As part of the DOT OPS Phase II SBIR program, we deployed four sensors at a site near PSI's Andover location for long term data acquisition. That site is an empty building lot roughly 250 m x 250 m in size. Figure 73 shows an aerial view of that site. The red stars represent the sensor locations.

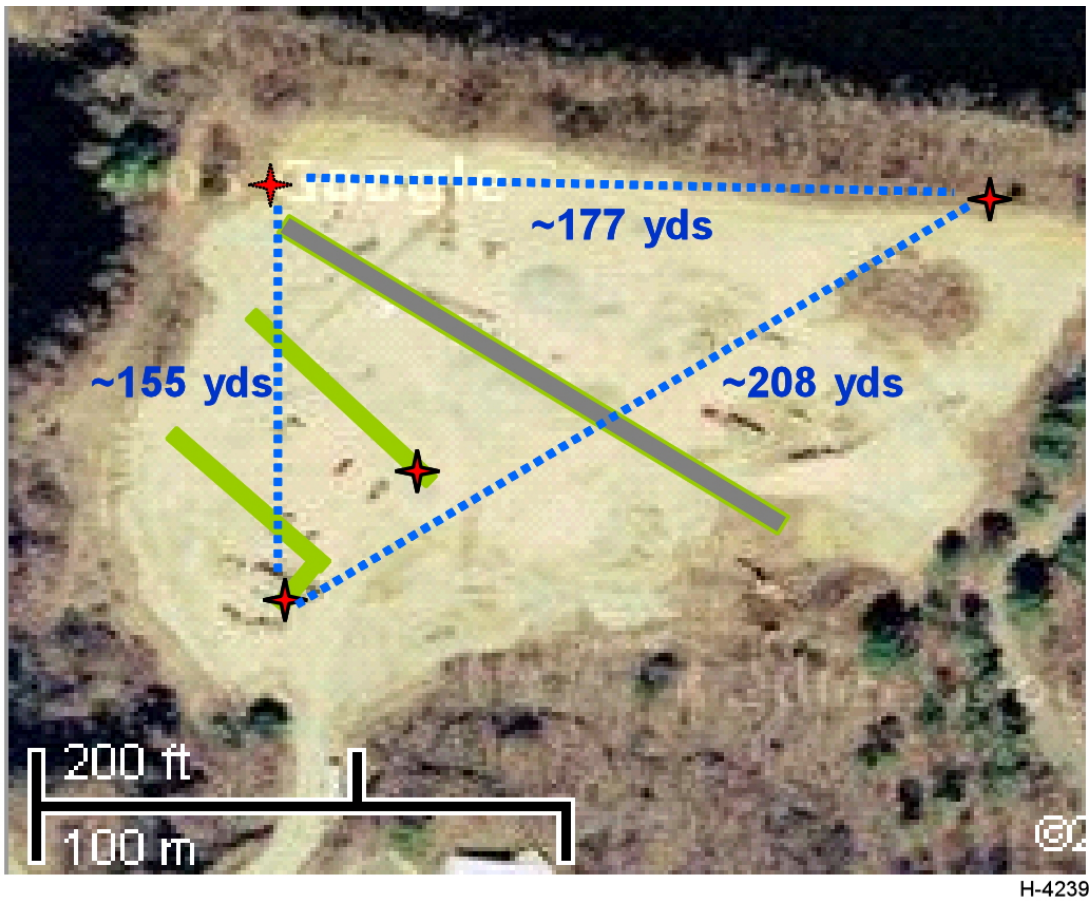

Figure 73. Aerial view of Andover field test site.

As part of the long term data acquisition, we also acquired triangulation data. We used a sledgehammer and a jackhammer as sources at several positions. The sensor and threat positions are surveyed with an accuracy of +/- 1 yard.

For each threat location, we process the time series data from three to four sensors to determine the triangulated position. Table 15 summarizes the results. The triangulated positions are determined with a precision of +/- 1 yd. The accuracy of the triangulated positions is +/- 3.5 yards at a nominal range of 150 yards. The position accuracy varies from 1 – 9 yards. For these tests the accuracy was range independent. The triangulated jackhammer location has same accuracy as sledgehammer location.

Table 15. Summary of Triangulation Measurement Results

	Surveyed (+/- 1 yd)		PIGPEN Measurement	
	X	Y	X	Y
Sledgehammer - U	24.7 yd	23.4 yd	27.8 ± 0.8 yd	25.9 ± 1.1 yd
Sledgehammer - V	65.1 yd	47.9 yd	64.4 ± 1.4 yd	53.5 ± 1.0 yd
Sledgehammer - X	125 yd	-4.5 yd	128 ± 0.6 yd	4.2 ± 1.0 yd
Jackhammer	-22.5 yd	62.4 yd	-18 ± 1.0 yd	64 ± 1.0 yd

The triangulation specification articulated at the beginning of the BAA program was 10 m accuracy at a range of 300 yards. That specification was derived from an angular accuracy; therefore it translates into 3.3 yards at a range of 100 yards (or 33 yards at a range of 1000 yards). **From these data, we conclude that the PIGPEN inherent triangulation accuracy (3.5 yards at 150 yards range) meets the specification**.

5.4 Interaction with Geophysical Consultant

The geophysical consultant has raised several issues regarding triangulation accuracy under complex geological conditions. We acknowledge these issues and have had discussions with NYSEARCH and the consultant regarding techniques for improving accuracy in the field. As such, we suggest the following activities for future programs.

1. Investigate use of the air-couple wave to augment triangulation determinations.
2. Consider the benefit of simple site characterizations during PIGPEN installation to coarsely characterize the velocity fields.
3. Develop a controlled field test specifically to address the question of complex geology on PIGPEN performance.
4. Develop a numerical model to predict system performance, to guide field test planning and to guide system development.

A system model would be beneficial to guide future development. It can be used to identify critical error terms, guide future data acquisition and field tests, optimize sensor grid configuration and CONOPS, and optimize algorithms.

Triangulation uncertainty is a complex, non-linear function of threat position and sensor grid geometry. The error sources can be divided into three elements: 1) Propagation of errors through triangulation algorithm, 2) Error and uncertainty in time lag determination and processing, and 3) Error and uncertainty caused by complex soil conditions. A system model will help to identify and isolate error terms and to exercise mitigation strategies.

Field test data would be used to validate model. The validated model then guides system development. With a model, we can investigate a vast range of soil conditions, configurations, threat scenarios etc. We can optimize data acquisition resulting in cost effective field tests. We can optimize system design, configuration and CONOPs.

6. EP-2 Design

We have completed EP-2 design, fabrication and laboratory testing. EP-2 is based on existing DSP hardware. We are using a slightly modified DSP board that was developed for other applications. The Build-2 algorithm has been implemented and verified in DSP. We are achieving excellent agreement between DSP and MATLAB intermediate results.

DSP hardware integrated with EP-1 sensor head (see Figure 74). The laboratory testing is complete. We will be performing field checkout and field testing in the next quarter.

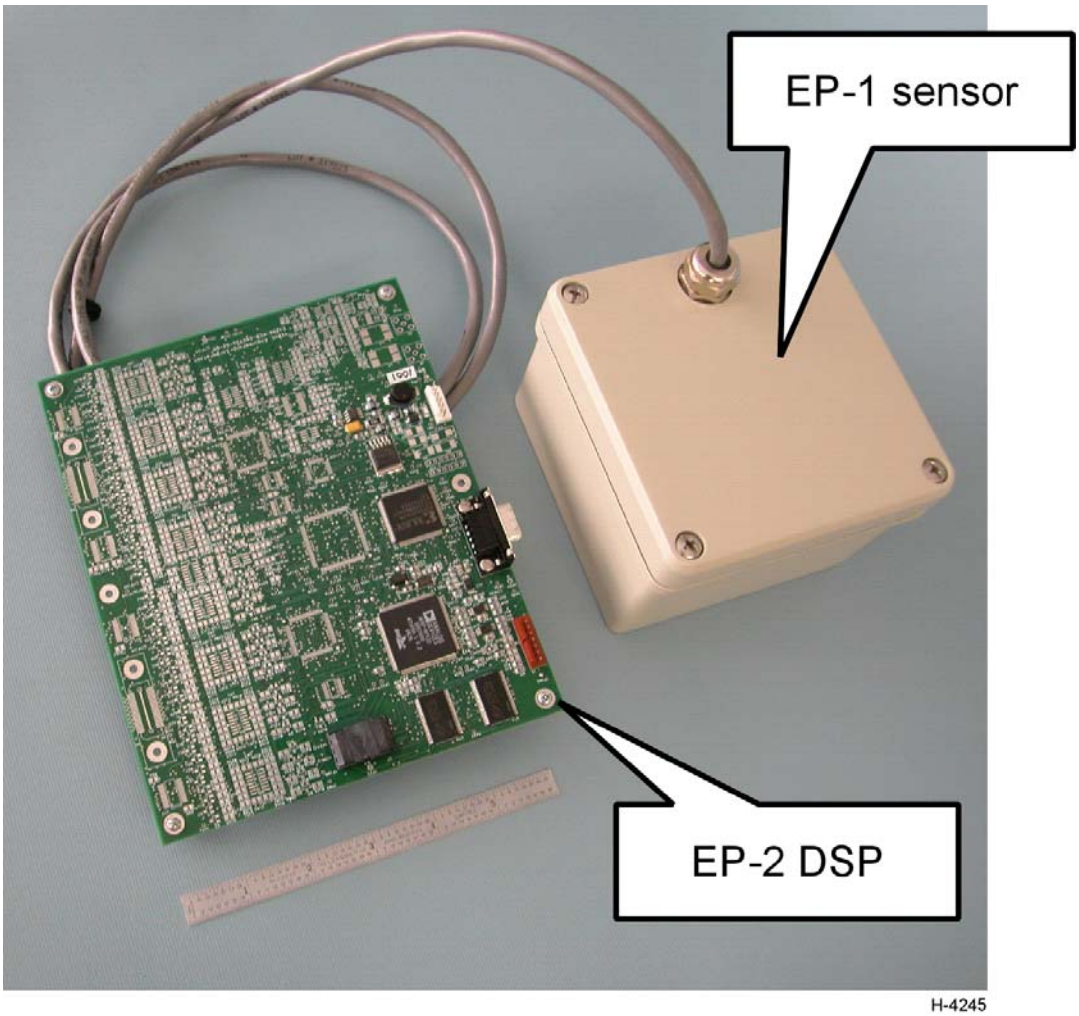

Figure 74. EP-1 sensor head integrated with the DSP board to create EP-2.

The Build-2 algorithm was first developed in Matlab programming environment. We transferred Algorithm to C++ and verified operation using sample input files. We then implemented C++ code onto DSP board and verified operation using sample EP-1 sensor data input files (see Figure 75). The bottom trace shows an overlay of the Build-2 MATLAB algorithm and the Build-2 DSP algorithm. The agreement is excellent. To validate the algorithm, we used 6 Reference Files. The point-by-point error was 1.2%. The overall correlation was 100%.

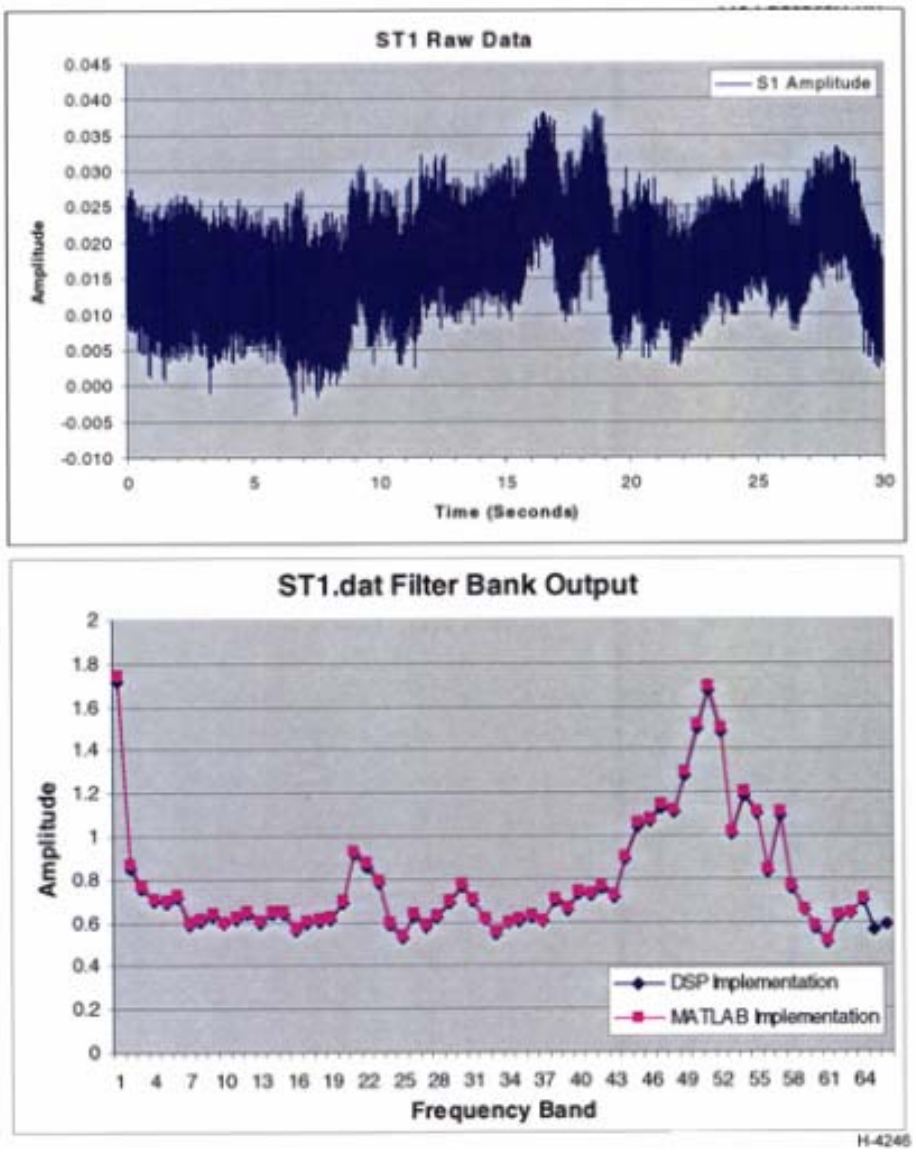

Figure 75. Time series data (top) and intermediate algorithm outputs (bottom). The bottom trace shows an overlay of the Build-2 MATLAB algorithm and the Build-2 DSP algorithm. The agreement is excellent.

We used an audio speaker driven at known frequencies to excite the EP-2 system in the laboratory. The sensor data was read by the DSP and processed. Figure 76 shows the processed spectrum.

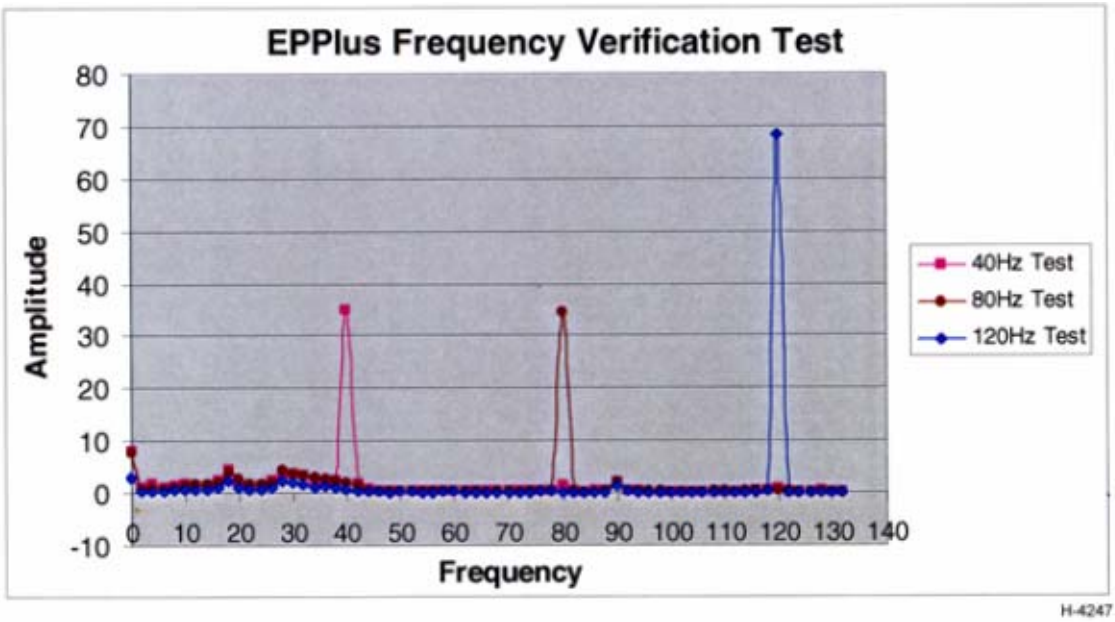

Figure 76. Spectra acquired and calculated by the DSP during excitation with three known frequencies.

6.1 EP-1 Data Review and EP-2 Design Review

PSI met with NYSEARCH members on 21 September. We presented an EP-1 data review and EP-2 design review. Soon after that meeting we provided preliminary interface concepts to NYSEARCH (Section 6.3).

6.2 EP-2 Field Checkout and Field Test

6.2.1 Repaired and redeployed the EP-1 sensor network at the Andover, MA site

One of the EP-1 sensors suffered water infiltration after heavy rains at the test site. While the package is hermetically sealed and weathertight, there is a hermetic feedthrough for the power and signal wires (Figure 77). The wire bundle diameter was at the minimum specified size for the hermetic feedthrough. Upon disassembly and inspection, we found that the feedthrough grommet had been crimped during installation. Water infiltrated along the crimp, found its way to the electronics board and caused a component failure on that board. None of the other PIGPEN sensors suffered from water infiltration.

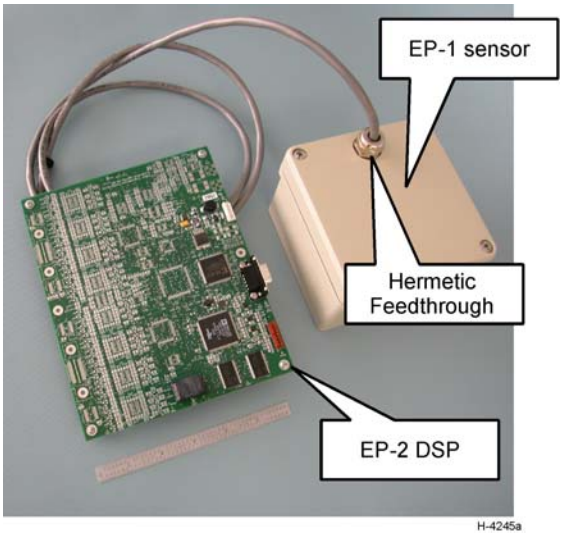

Figure 77. PIGPEN EP-1 sensor head and EP-2 prototype processor.

To eliminate this problem, we increased the size of the wire bundle to be in the middle of the specified size range for the feedthrough. We also conformally coated the electronics boards to prevent shorting in the unlikely event of water infiltration or condensation.

Two of the other sensors suffered damage to their above-ground wire bundles due to unanticipated equipment activity at the site. We repaired and redeployed all the sensors.

Due to the repairs and inclement weather during October, we did not acquire any additional field data.

6.2.2 Refinement of the EP-2 Threat Ddentification Algorithms

To better reject false positives due to backgrounds, we incorporated a user-set threshold into the identification algorithm. That threshold was successful at eliminating false positive detections.

6.2.3 EP-2 Field Test

We conducted fielding testing of EP-2 at a site near PSI on 21 November 2005. NYSEARCH personnel witnessed the testing. We used a jackhammer located at 50 yd, 100 yd and 200 yd. In all cases EP-2 correctly identified the threat. There were no false positive and no misidentifications (see Figures 78 through 83). The field test demonstrates the real-time processing capabilities of the PIGPEN system.

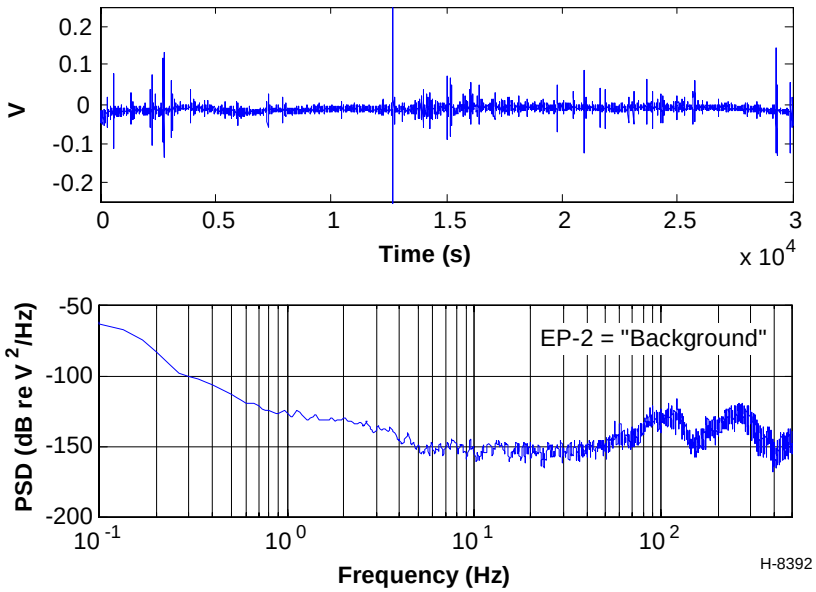

Figure 78. EP-2 test; 50 yards; no threat.

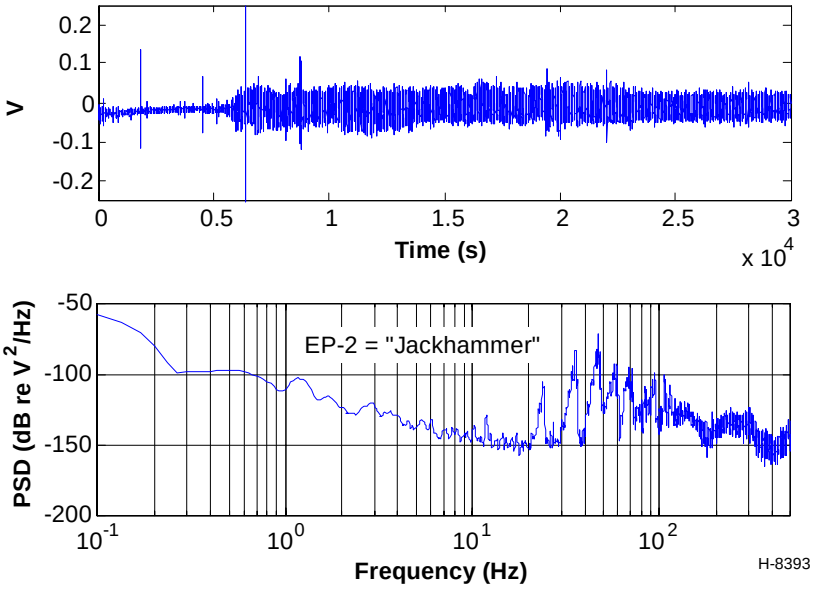

Figure 79. EP-2 test; 50 yards; jackhammer on.

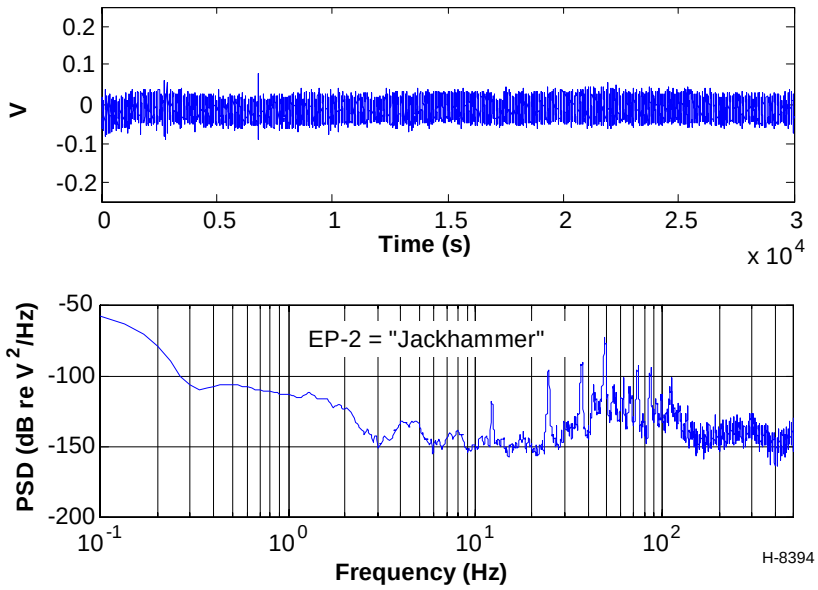

Figure 80. EP-2 test; 50 yards; jackhammer on.

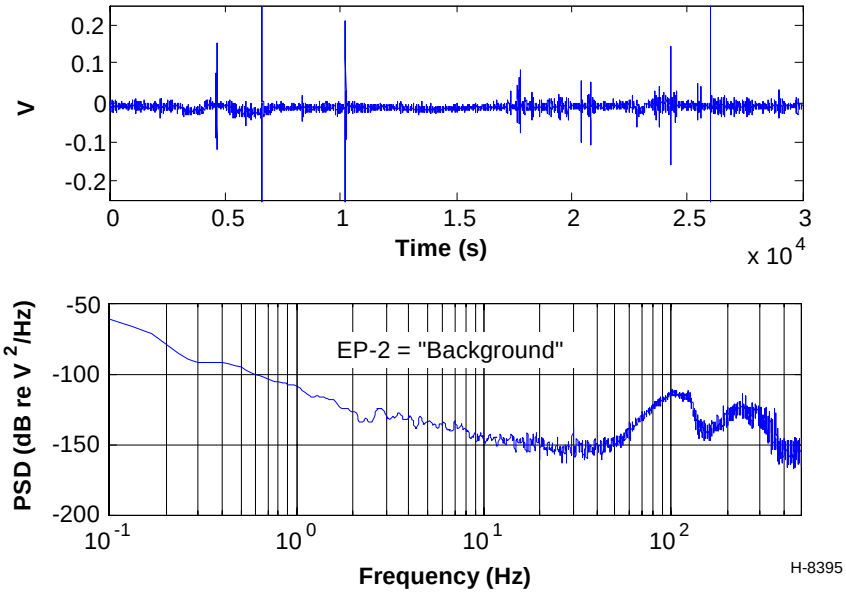

Figure 81. EP02 test; 200 yards; no threat.

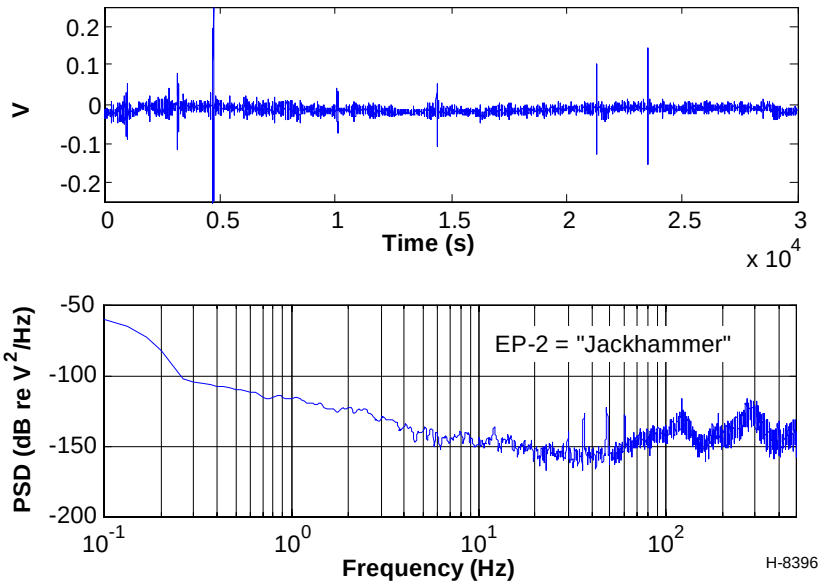

Figure 82. EP-2 test; 200 yards; jackhammer on.

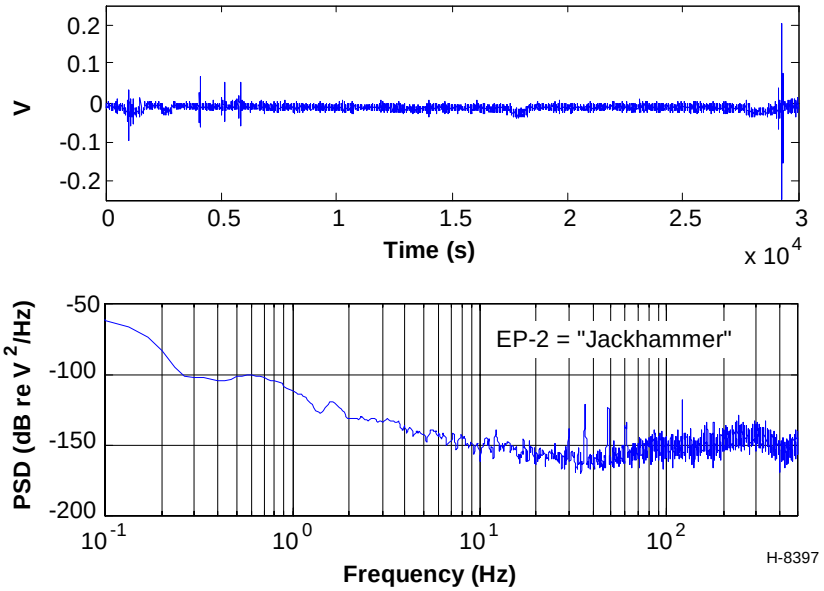

Figure 83. EP-2 test; 200 yards; jackhammer on.

6.3 Network Interface Specifications

In order to assess the ability to integrate the PIGPEN sensors into the GasNet infrastructure, NYSEARCH requested the following information:

- Sensor output protocol. The current configuration on GasNet for the external sensor hookup is RS232 format.

PIGPEN is baselining RS485 as something of an industry standard for SCADA networks. On the PIGPEN side, RS232 is compatible with RS485.

- Power requirements of sensor for different modes of operations in terms of frequency of signal acquisition, alarms strategy, etc.

Quiescent power is 50 mW. Peak power is 1W. If we assume a duty cycle (1%, 10% etc) or fraction of time that the system detects a potential source, then we can create a simple power model.

100% duty cycle:	1W
10% duty cycle:	150 mW
1% duty cycle:	60 mW

- Wiring size and wire jackets. Any limits on what you need to have or can it be what GasNet would like (Teflon jacket or PDC). What is the size of the wires?

Based on current rating and voltage drop considerations 26 ga is probably a reasonable minimum, although we could go smaller. At max power (1 W or roughly 100 mA at 12 V), the voltage drop over 150 ft of cable is 0.6 V.

- Size of electronics to accompany the sensor.

Each 5x5x3.5 inch sensor carries its own electronics. In addition, there is a second processor box for every 16 sensors (also 5x5x3.5 inch).

6.4. Additional Field Testing Requirement

PSI and NYSEARCH discussed plans for extending the work for numerical modeling and field tests in complex soil conditions to address concerns and independent consultant's recommendation regarding location accuracy.

PSI prepared a draft white paper describing the rationale for the additional work as well as the work proposed. The full draft white paper is included as Appendix A.

NYSEARCH's geophysical consultant (Professor Don Steeples of Kansas University) has raised several issues regarding triangulation accuracy under complex geological conditions. We acknowledge these issues and have had discussions with NYSEARCH and the consultant regarding techniques for improving accuracy in the field.

The basic problem is illustrated in Figure 84. Surface waves refract at interfaces of differing soil types leading to erroneous calculation of source location.

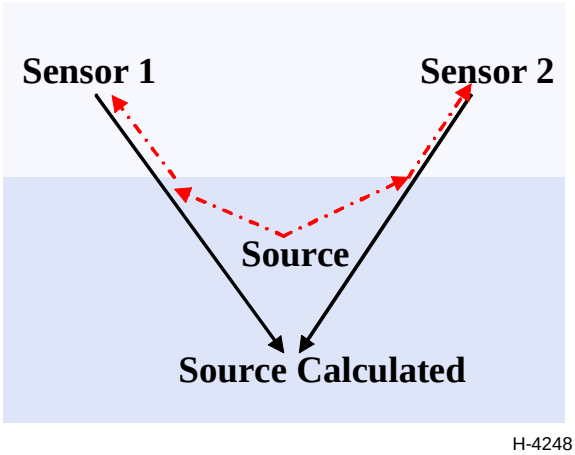

Figure 84. Surface waves refract at interfaces of differing soil types leading to erroneous calculation of source location.

In order assess these effects on PIGPEN performance and to develop means of compensating for these effects, we suggested the following activities for the next stage of the program.

1. Investigate use of the air-coupled wave to augment triangulation determinations.
2. Consider the benefit of simple site characterizations during PIGPEN installation to coarsely characterize the velocity fields.
3. Develop a controlled field test specifically to address the question of complex geology on PIGPEN performance.
4. Develop a numerical model to predict system performance, to guide field test planning and to guide system development.

Under its existing program PSI has already undertaken investigation of air-coupled waves to augment triangulation determination. We are also developing more complex triangulation algorithms that can incorporate site characterization calibrations. We have also already begun modeling of the triangulation accuracy to predict system performance.

We proposed additional activities to address the remaining recommendations made by NYSEARCH's geophysical consultant:

- Incorporate geophysical modeling components into the overall system model to address PIGPEN performance in complex soil conditions
- Conduct additional field testing to address PIGPEN performance in complex soil conditions

These recommendations were accepted and DOT/NYSEARCH added an additional task to perform testing of the PIGPEN sensors in a configuration permitting the effects of complex (different) soils on the sensors to be observed.

7. Planned PIGPEN Testing in Complex Soil Conditions (Kansas Field Test)

7.1 Introduction

With funding from NYSEARCH / NGA and the Department of Transportation's Office of Pipeline Safety, Physical Sciences Inc. has been developing the Proactive Infrasonic Gas Pipeline Evaluation Network (PIGPEN). PIGPEN is a spare network of seismic sensors that protect gas pipeline infrastructure by detecting, identifying, and locating potential third-party threats.

While we have demonstrated threat location with an average accuracy of roughly 3 m at a range of 150 m in uniform soil conditions, NYSEARCH and their independent technical consultant (Dr. Don Steeples) have expressed concern about PIGPEN's ability to triangulate threats in complex soil conditions. In response, PSI proposed to plan and execute a field test designed specifically to characterize PIGPEN's performance under complex soil conditions.

NYSEARCH's geophysical consultant has raised several issues regarding triangulation accuracy under complex geological conditions. We acknowledge these issues and have had discussions with NYSEARCH and the consultant regarding techniques for improving accuracy in the field. The basic problem was illustrated in Figure 84. Surface waves refract at interfaces of differing soil types leading to erroneous calculation of source location

In order to assess these effects on PIGPEN performance and to develop means of compensating for these effects, we proposed additional activities to address the remaining recommendations made by NYSEARCH's geophysical consultant:

- Conduct additional field testing to address PIGPEN performance in complex soil conditions.
- Incorporate geophysical modeling components into the overall system model to address PIGPEN performance in complex soil conditions.

7.2 Field Test Plan Overview

The field test was specifically designed to address the issues of performance in inhomogeneous soils, per the discussions with NYSEARCH and their geological consultant.

Figure 85 shows the schematic field test configuration. We deployed at least 4 EP-1 type PIGPEN sensors over a site that has non-uniform, but well characterized soil conditions. We would deploy threats at multiple locations and measure synchronized time-series data from each sensor. We tested at the maximum range allowed by the available sites. Ranges of 100-500 m are appropriate. Using those data, we will:

- Assess the performance of the existing PIGPEN triangulation algorithm.
- Develop compensation techniques (as discussed previously) to improve triangulation accuracy.
- Validate the error model

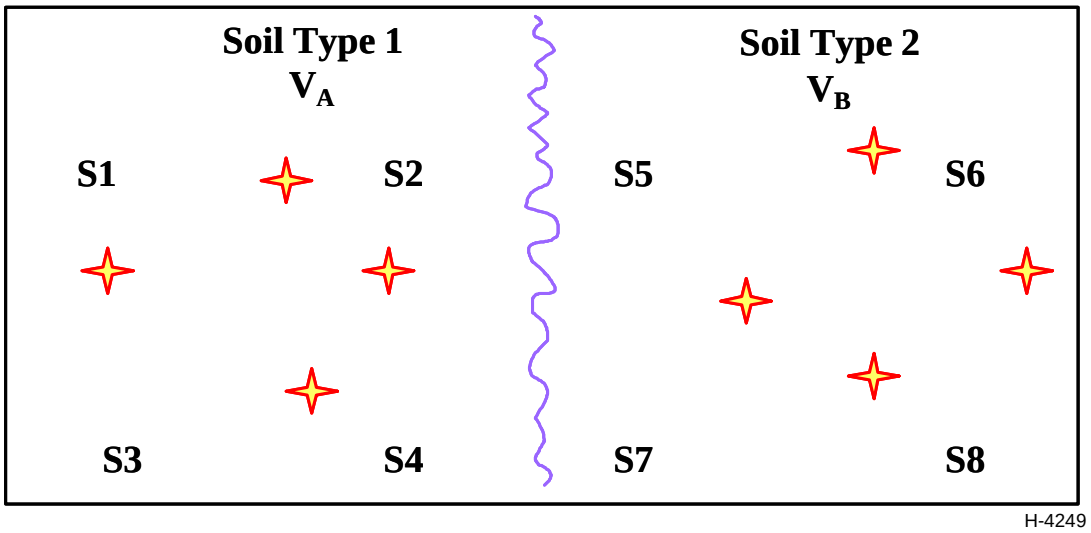

Figure 85. Schematic configuration of the proposed complex soil condition field test.

7.3 Test Site

NYSEARCH's consultant has identified a site that is suitable for the complex soil testing. The site is located near Lawrence, KS at latitude 39 deg 2 min 8 sec North and longitude 95 deg 21 min 59 sec West. Figures 86 and 87 show the topographic map and aerial photographs of the site. The areas labeled A and B are identify different soil types. In addition, there is an elevation change (23% grade) between A and B.

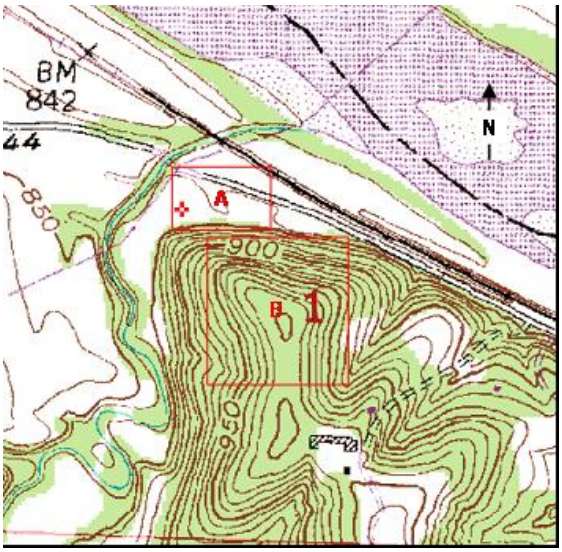

Figure 86. Topographic map of the site.

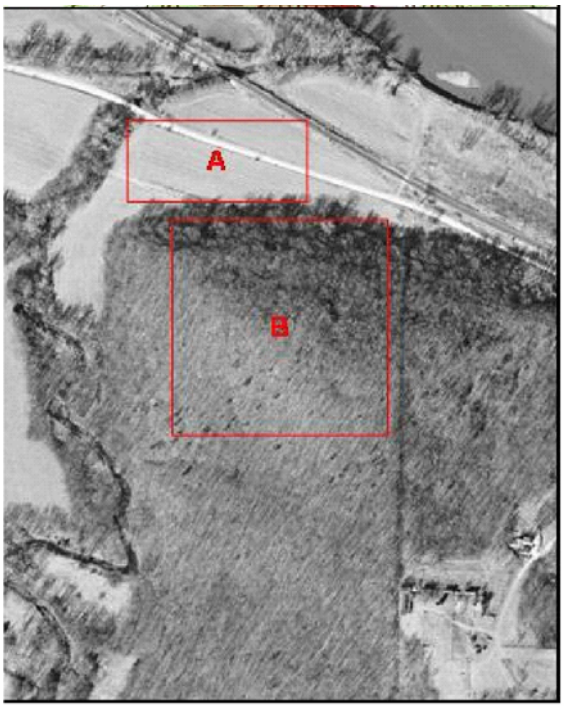

J-3155

Figure 87. Aerial photograph of the site.

The geology on the upland site (Area B) is alternating flat-lying limestones and shales of Pennsylvanian age with average P-wave velocity of about 10,000 feet per second, with Poisson's ratio of about 0.25. The geology on the river valley site (Area A) is about 50 feet of Pleistocene alluvial sands, gravels and clays with an average P-wave velocity of about 1600 feet per second and Poisson's ratio of 0.40 to 0.45. Water table is about 25 feet below ground surface. The seismic velocity in the dry alluvium is about 1000 feet per second. Bedrock at 50 foot depth is flat-lying limestones and shales of Pennsylvanian age.

7.4 Test Equipment

We instrumented the test site using four PIGPEN EP sensors connected to a data acquisition system by cables. We used a combination of single impacts and a tamper as conditions allow. With the current cabling, the sensor separation can be as great at 250 m.

We surveyed the sensor and impact locations on the site using a combination of GPS (+/- 7 m accuracy), tape measures (+/-0.3 m accuracy), and rangefinders (+/- 1 m accuracy).

We will provide a separate analysis computer for data analysis and assessment. The analysis computer will include a post-processor for performing the triangulation algorithm

7.5 Test Configurations

We will instrument the site in three different configurations to accomplish our measurement objectives.

7.5.1 Configuration 1: Individual Area Characterization & Triangulation Performance

In Configuration 1, we will characterize the soil conditions in the two areas as well as determine the triangulation performance within the single soil types (Figure 88). This configuration will show whether inhomogeneity and/or anisotropy are present within the single soil types. It is meant as a preliminary measurement to the complex soil testing (Configurations 2 and 3).

Within each area, a T-formation using 3 sensors will be used. Impacts using the sledgehammer or other impact source will be made every approximately 20 m down the long axis (see Figure 89). Three sets of three strikes will be taken at each location. In this configuration, we expect the time of arrival of the signals at S1 and S2 to be simultaneous. Any time lags observed between S1 and S2 will indicate soil non-uniformities or errors in surveying.

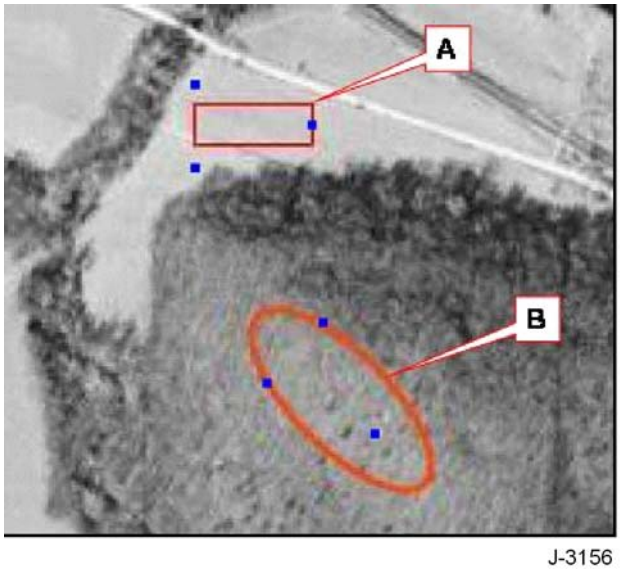

Figure 88. Configuration 1: 3 sensor T formation in both soil types.

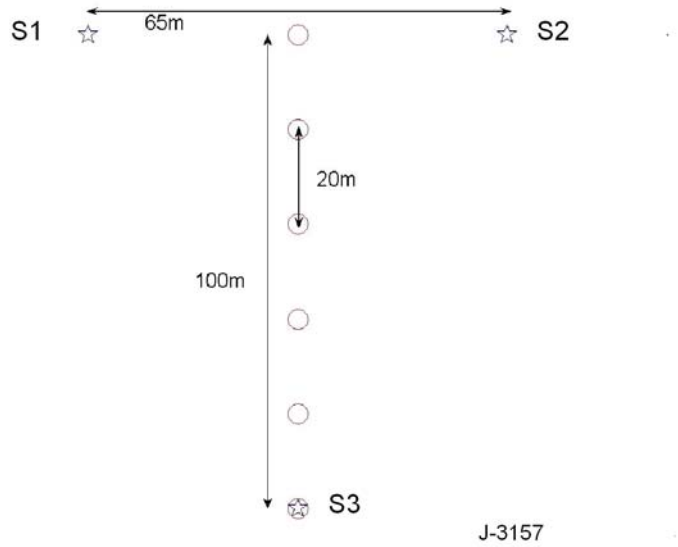

Figure 89. Configuration 1: Three sensor T formation (blue stars) and impact locations (red circles)

7.5.2 Configuration 2: Short Field Complex Soils

A 4 sensor parallelogram deployment with two sensors in each type of soil will be used in the short and long field configurations. (Figure 90) The desired length of one side between sensors is about 100m for the short field configuration. An impact source will be used along with a soil tamper (as conditions allow) for threat sources. Impact locations will include inside as well as outside the sensor parallelogram. Solution error plots were generated for the desired geometry under uniform soil condition assumptions (Figure 91). This uniform soil solution gives a baseline to what solutions might be with a non-uniform soil. Locations where the solution is not strong will be explored, along with other locations outside the diamond formation.

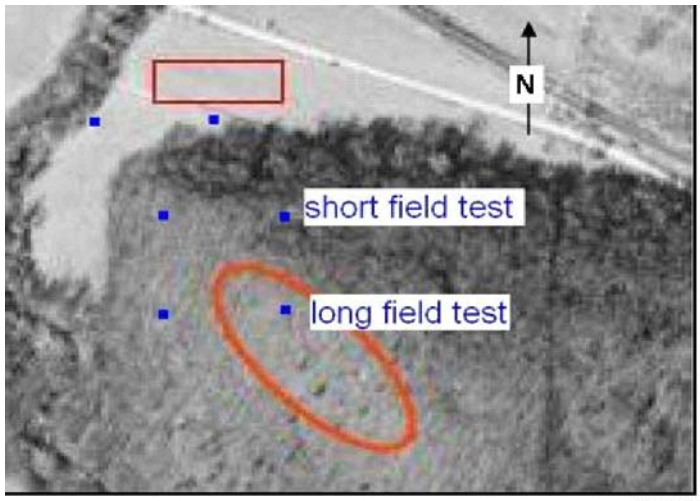

J-3158

Figure 90. Rough sensor locations for long and short field tests.

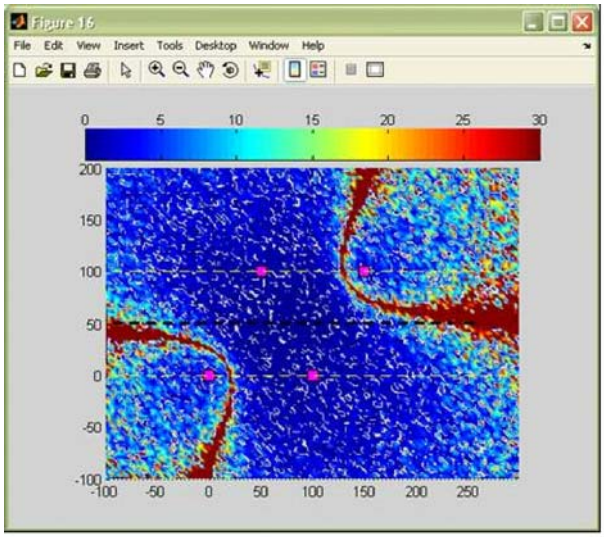

J-3159

Figure 91. Error Field for a 100 x 100 m Diamond for a uniform soil speed of 1600 ft/s with a zero mean 0.002 s Gaussian Time Error.

The source locations are defined in 5 separate north-south running lines (Figure 92). Impact locations B serve both as locations of strong solutions and also allows for a similar T formation as done in the individual soil characterization. Impact locations A are those with weak algorithm solutions outside the parallelogram formation. Impact locations C are within the diamond formation and should have strong algorithm solutions. This will allow for soil characterization for that region of non-uniformity.

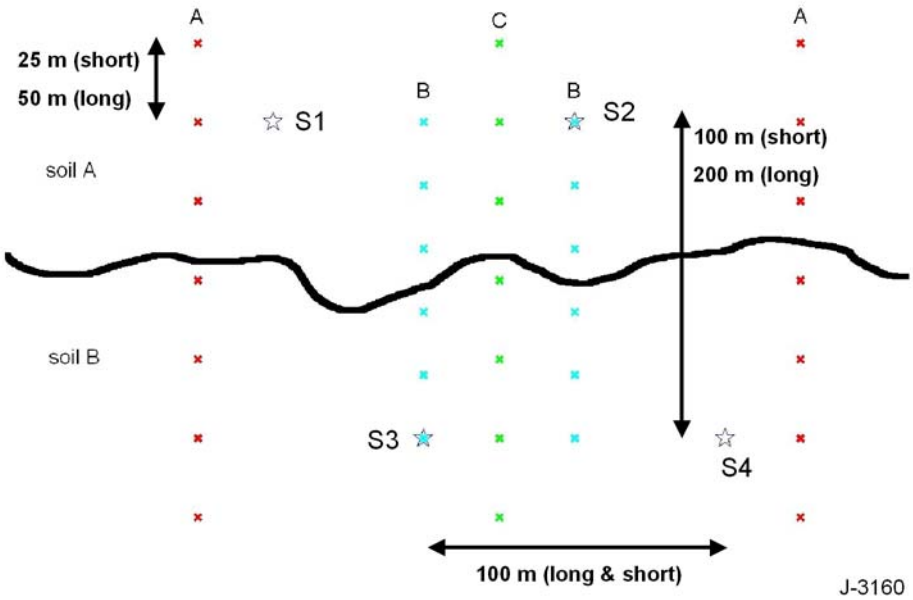

Figure 92. Sensor (Blue Stars) and Impact Locations (A-C).

7.5.3 Configuration 3: Long Field Complex Soils

The long field configuration and test are analogous to the short field except with N-S sensor distances of about 200 to 250 meters. The E-W separation remains at 100 m. An analogous source location pattern with greater spacing than in the short field configuration.

7.6 Schedule

Table 16 summarizes the test schedule.

Table 16. Test Plan Summary

DAY 1	Arrival (PM)
DAY 2	Survey site Survey sensor and threat locations – Config-1 Deploy sensors - Config-1 Sensor and data acquisition system checkout Acquire data Config-1 Assess Config-1 data (PM)
DAY 3	Acquire additional data Config-1 (AM) Survey sensor and threat locations – Config-2 Deploy sensors - Config-2 Acquire data Config-2 Assess Config-2 data (PM)
DAY 4	Acquire additional data Config-2 (AM) Survey sensor and threat locations – Config-3 Deploy sensors - Config-3 Acquire data Config-3 Assess Config-3 data (PM)
DAY 5	Acquire additional data Config-3 (AM) Retrieve Equipment
DAY 6	Extra day

7.7 Analysis of Kansas Field Testing

On 5-11 November 2006, PSI conducted the field test in a soy bean field outside of Lawrence, KS. Sensors were deployed in four configurations and three excitation sources were used:

- Configuration 1A. 3 Sensor T formation in sandy loam, sledgehammer and down-hole-gun
- Configuration 1B: 3 Sensor T formation in shale/limestone, sledgehammer and down-hole-gun
- Configuration 2: 4 sensor Short Field (2 sensors in loam, 2 sensors in rock), down-hole-gun and backhoe
- Configuration 3: 4 Sensor Long Field, shotgun and down-hole-gun

We also acquired serendipitous background data on trains and vehicles.

7.7.1 Test Configuration

Figure 94 shows an aerial view of the site overlaid with the sensor and threat positions for Configurations 1A and 1B. The "A" region comprises sandy loam. The "B" region comprises shale/limestone. The purpose of Configurations 1A and 1B is to determine the acoustic velocity in each soil type and to determine the signal strength versus range in each soil type. Figures 93 and 94 show the sensor and threat positions for Configurations 1A and 1B. Configuration 1A consists of three sensors and eight threat locations. Configuration 1B consists of three sensors and six threat locations. In both configurations, the sixth threat location (T6) is placed 10 feet from sensor 1 to prevent sensor saturation.

Figure 95 shows an aerial photograph overlaid with the sensor and threat positions for Configuration 2 and Configuration 3. In Configurations 2 and 3, the threats were positioned along roughly N-S lines with respect to the sensor positions. Each threat line was labeled with a unique designator. Each threat position was label by the threat line and the distance in feet from the northernmost position along that line: e.g. BE-0, BE-60, BE-120, … , BE-420.

The threat positions were chosen to characterize the triangulation performance both inside and outside of the sensor grid and to allow a comparison of performance with each soil type as well as across a soil boundary. All the positions on the BW line are equidistant from sensors S1 and S2 (nominally zero delay between signal arrival times at S1 and S2). All the positions along the BE line are equidistant from S3 and S4. The C line runs directly through the center of the grid. The AW line is completely outside the sensor grid. The AE line is partially inside and partially outside the sensor grid.

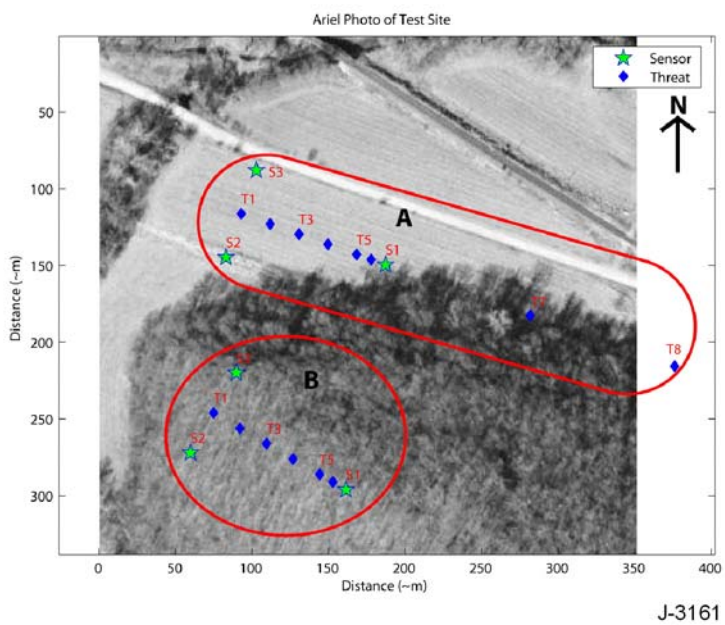

Figure 93. Aerial photograph of the site and sensor configurations 1A and 1B. The "A" region comprises sandy loam. The "B" region comprises shale/limestone.

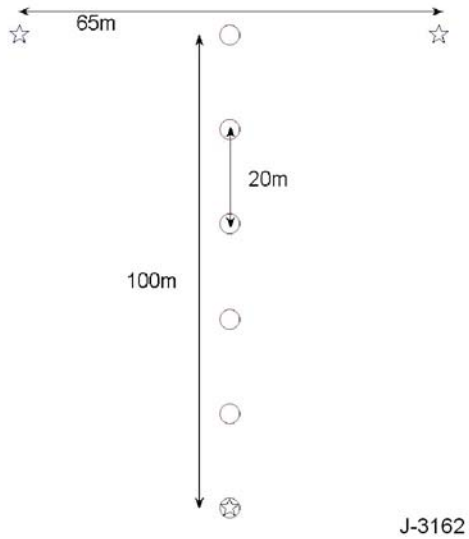

Figure 94. Sensor and threat positions for Configurations 1A and 1B.

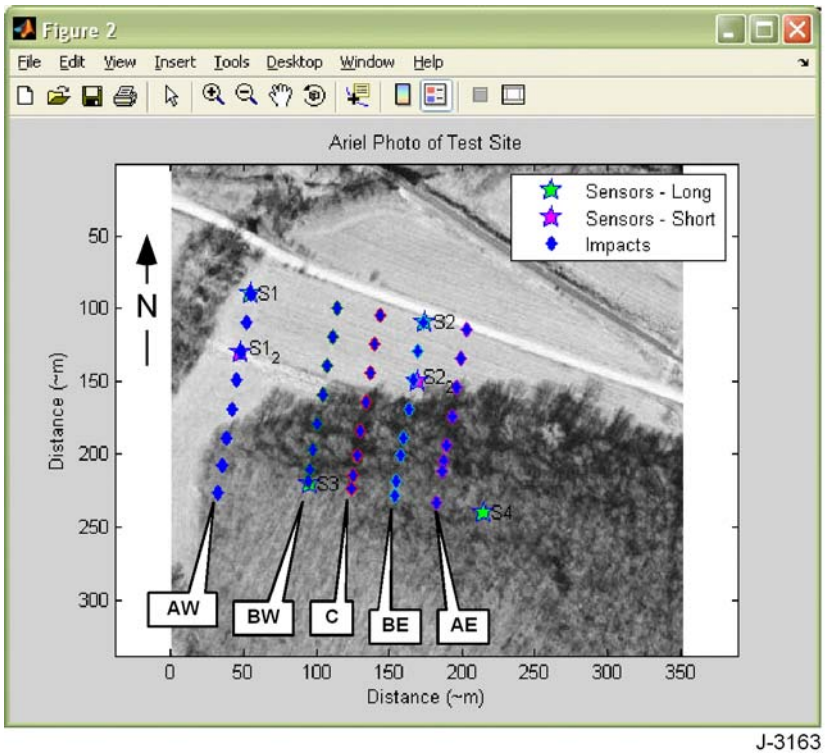

Figure 95.Aerial photograph of the test site overlaid with the sensor and threat positions for configurations 2 and 3.

Figure 96 shows the elevation contour of the site. The shale/limestone ridge rises to about 100 feet above the lower field. The side of the ridge is approximately a 50% grade. Figure 97 shows a photograph of the sight looking south. The lower field is in the foreground and the shale/limestone ridge is in the background.

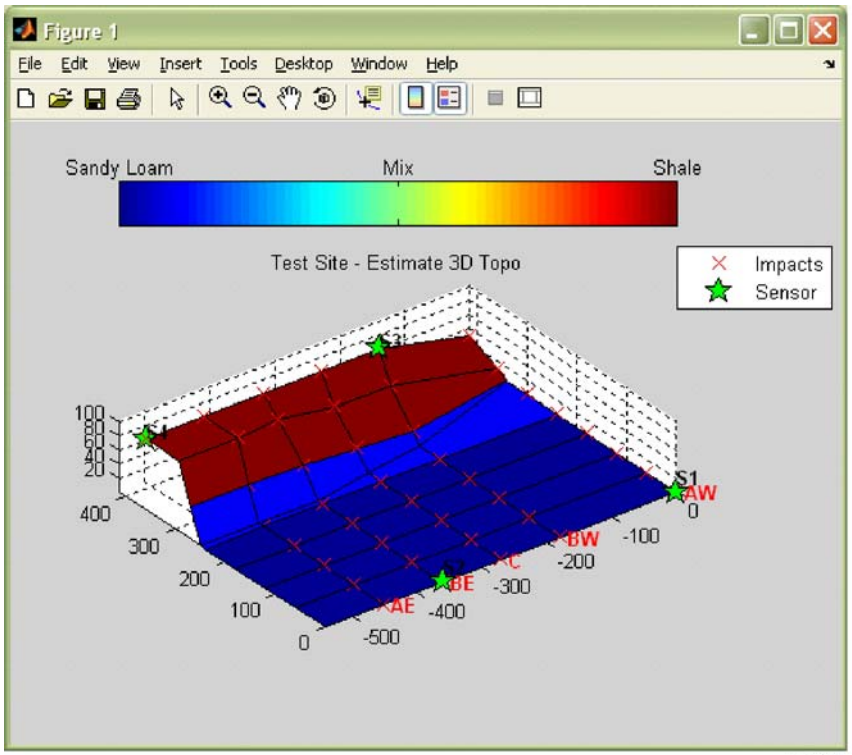

J-3164

Figure 96. Elevation contours of the site.

J-3165

Figure 97. Photograph of the Kansas site looking south. The field is in the foreground. The shale/limestone ridge is in the background.

7.7.2 Sources

We used three primary sources to excite the ground: a sledgehammer and steel plate; a downhole gun (Figure 98). The downhole gun in test operation (Figure 99). The backhoe used in Kansas tests (Figure 100). The downhole gun fires a standard 30-06 rifle cartridge. The 180 grain projectile travels at 2700 feet/sec resulting in an impact energy of 2900 ft lbs. The backhoe was a Case 580 Super L loader weighing roughly 15000 lbs. The backhoe driver created an acoustic signal by repeatedly striking the ground with the backhoe bucket.

J-3274

Figure 98. The downhole gun close-up.

J-3166

Figure 99. Downhole gun in operation.

J-3167

Figure 100. Case 580 Super L backhoe.

PSI Proprietary Information

7.7.3 Results

In the following sections, we will evaluate the data from five different tests configurations and sources.

1. Configuration 1A (T-loam), down hole 30-06
2. Configuration 1B (T-shale), down hole 30-06
3. Configuration 2 (Longfield), down hole 30-06
4. Configuration 3 (Shortfield), down hole 30-06
5. Configuration 3 (Shortfield), Backhoe

All of the data was analyzed using the same basic process. First, the raw data is passed through a 500th order finite impulse response (FIR) 5 to 100 Hz band-pass filter. A relatively high order FIR filter was used in this situation because FIR filters are linear phase. This means that all signals regardless of spectral content are phase shifted equally as they are passed through the filter. Lower order infinite impulse response (IIR) filters, such as Butterworth filters, do not have linear phase, which result in a temporal distortion of the filtered data. The 5-100 Hz pass-band was selected in consultation with Prof. Don Steeples as a good balance between maximizing relevant seismic data, and minimizing background noise and air acoustics. The filtered data was then plotted.

Once the data is plotted, an analyst identifies both the time window in the data containing the threat signature and a portion of the data from which to calculate the background noise. Once the time windows are identified, the power within both the threat signature and background data samples are calculated to determine the signal to noise ratio. The time sequences containing threat signatures are then cross-correlated. Next the cross-correlation output is low pass filtered to smooth the correlation output. The time difference of arrival is determined from the filtered cross-correlation output. Additional analysis such as spectrographs is performed as necessary.

7.7.4 Configuration 1A – Sandy Loam Calibration

In configuration 1A three sensors were placed in the sandy loam for the purpose of characterizing the properties of the sandy loam. A total of 8 threat locations were excited with the down-hole 30-06 gun. Four shots were fired at each location. The distance from the sensors ranges from 10 ft to 900 ft. Each threat location is equidistant from sensors 2 and 3 such that the nominal time difference of arrival should be 0 s. The expected wave speed for this soil type is nominally 1000 ft/s. The data presented here utilizes a minimum of 3 of the four shots at each location[1].

All of the data presented here was band-pass filtered using a 500th order FIR filter with breakpoints of 5 and 100 Hz. All of the cross-correlation results have been low pass filtered through a 100th order FIR filter with a stop band starting at 20 Hz. The cross-correlation outputs

[1] At two of the locations a car was passing in close proximity to sensors 1 and 2 thus degrading the signal to noise ratio. To keep the results consistent these data points were not included.

have been generated using a Matlab function which automatically selects the maximum correlation value between -1 and 1 second.

Past data has demonstrated that we nominally need a signal to noise ratio of 20dB or greater to obtain an accurate time difference of arrival measurement using either the cross-correlation method or a manual selection of time of arrival. Figure 101 shows the average signal to noise ratio for each of the sensors at each of the threat locations (the x-axis notes the threat location number). As can be seen in Figure 101, all of the sensors have sufficient signal strength at threat locations 1 thru 6, while there is insufficient signal strength for analysis at threat locations 7 and 8.

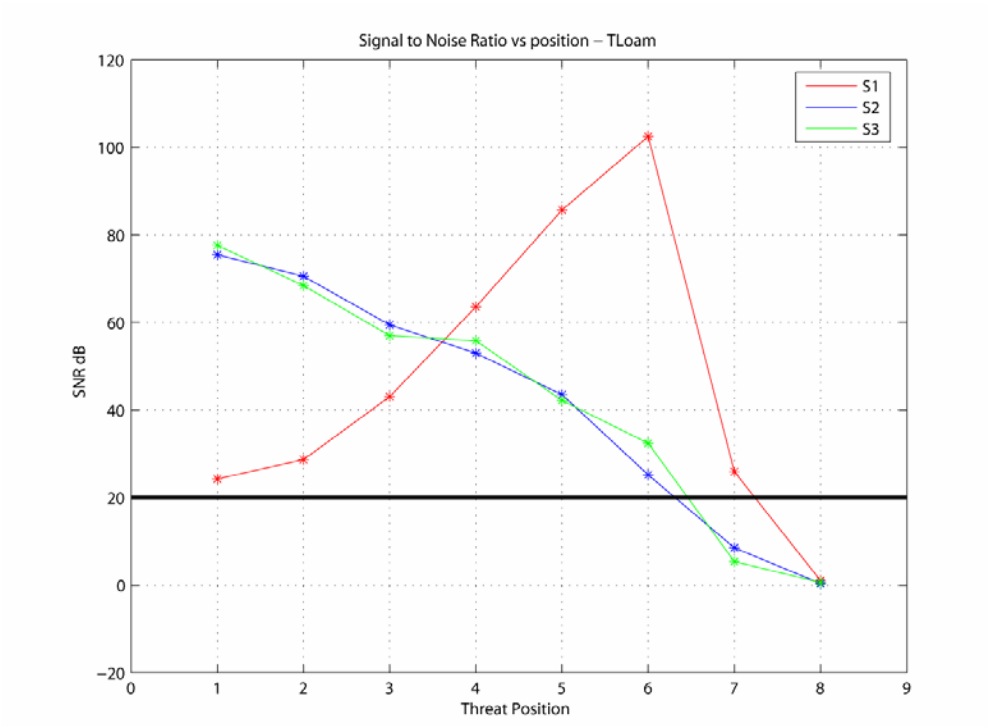

Figure 101. Average Signal to Noise ratio vs Threat Position in sandy loam. (Solid black line indicates the minimum SNR required for analysis).

Figure 102 shows the average signal to noise ratio versus threat distance for the sandy loam. This plot was generated using the data from all three sensors. As we can see, the approximate detection distance for the down-hole 30-06 rifle is 400 ft in the sandy loam.

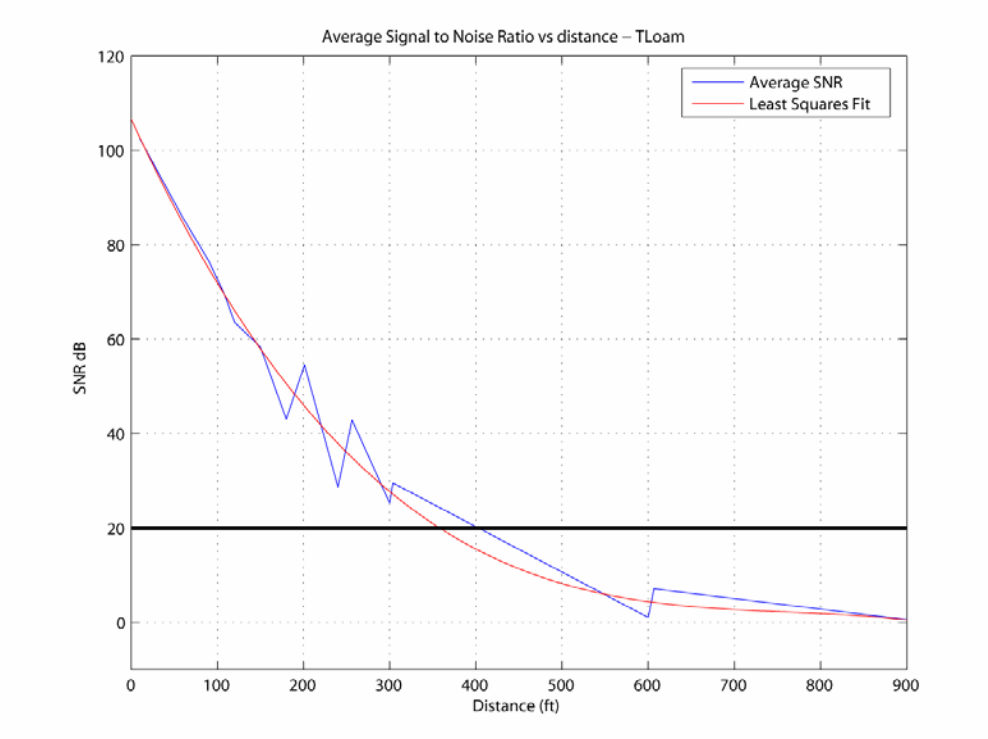

Figure 102. Average Signal to Noise ratio vs Threat Distance in sandy loam.

Figure 103 shows the average time difference of arrival between sensors 1 and 2 (X12), and sensors 1 and 3 (X13) versus path length difference for threat locations T1-T6. The time difference of arrival was determined using the cross correlation. As we can see in Figure 103, with the exception of the data gathered from threat location T2, the cross-correlation outputs form a line with a slope of 0.0024 sec/ft. This corresponds to a wave speed of 410 ft/sec which is lower than expected. However, the observed speed corresponds well to the soil speeds observed at the Andover, MA field site which is also composed of alluvial deposits.

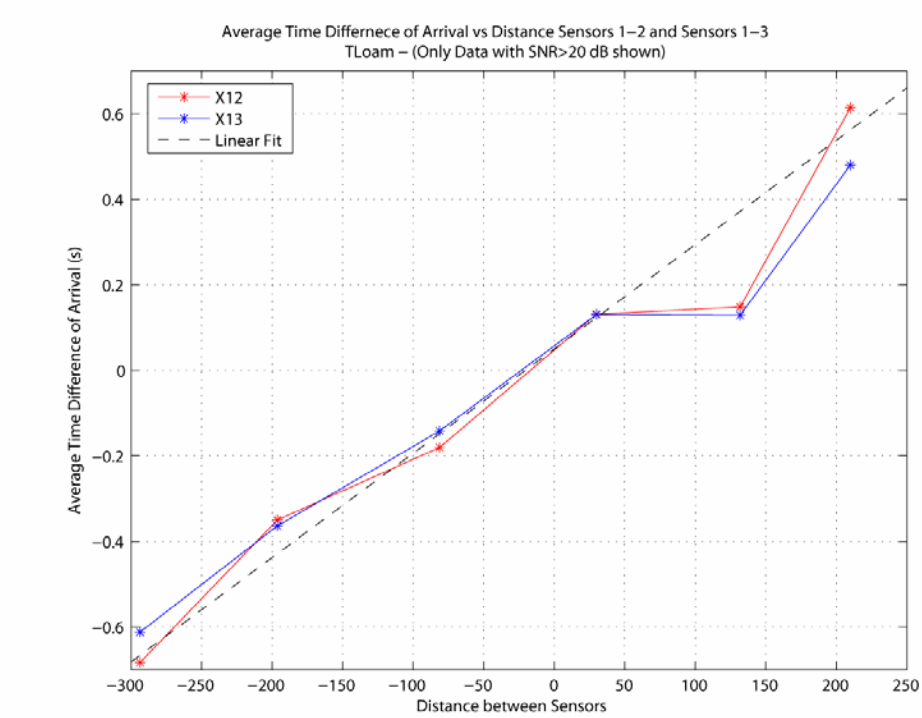

Figure 103. Average Time Difference of Arrival between Sensors 1 and 2, and Sensors 1 and 3 versus path length difference.

Figure 104 shows the average time difference of arrival between sensors 2 and 3 versus threat location (T1 through T6). In addition to displaying the average time difference of arrival, we have also displayed the time differences of arrival for each shot at each threat location. There are four shots shown at locations 2, 4, 5, and 6. There are three shots at locations 1 and 3. Thus at locations 2, 4, 5, and 6 a minimum of two shots are co-located on the plot. The expected time difference of arrival for all of the threat locations is 0 sec. As we can see in Figure 104, there is some deviation from the expected result. Specifically, as we progress from T1 to T6 there is linear increase in the time difference of arrival between sensor 2 and sensor 3. This likely indicates that the wave speed between the threats and sensor 2 is slightly slower than the wave speed between the threat and sensor 3. If we make the assumption that the wave speed for the entire field is 410 ft/s, the actual variations in the field will result in a positional error of ±6.5 ft. The maximum variance at any one the threat locations is 0.0025 s, which corresponds to a position error of ±1 ft.

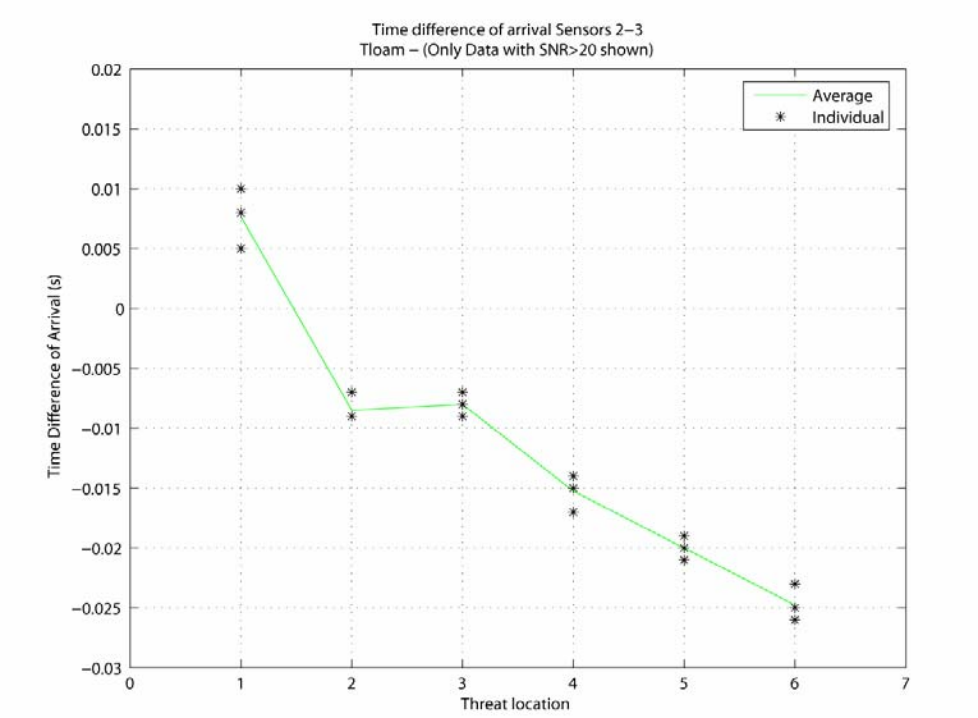

Figure 104. Time difference of arrival between sensors 2 and 3 versus threat location.

Similarly Figure 105 shows both the average time difference of arrival and the individual time difference versus path length difference for sensors 1 and 2, and sensors 3 and 4. Eliminating the outlying data point gathered at T6, we see that the maximum variance at each location is ±0.028 sec, which corresponds to a position error of ±11 ft. If we ignore all of the data collected at position T6, the maximum variance is ±0.018 sec, which corresponds to a position error of ±7 ft. The large variance seen in the T6 data is due to the saturation of sensor 1 (the threat is only 10 feet from sensor 1 at threat location 6). The saturation of sensor 1 results in a non-linear distortion of the measured waveform which then does not correlate well with the more distance signals. PSI also experienced this problem with data collected at the Andover test site. Similarly, there are some issues with the X13 correlation at T1.

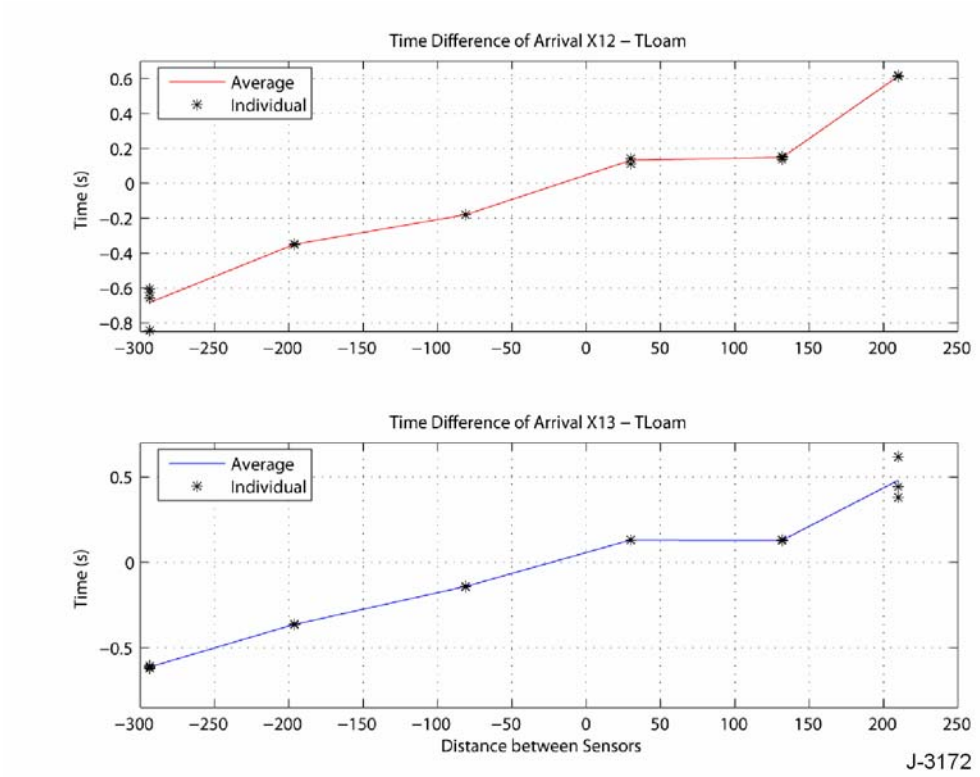

Figure 105. Time difference of arrival between sensors 1 and 2, and sensors 1 and 3 versus threat location.

Next we will discuss the acoustic spectral signatures observed. Figure 106 shows example data of the down-hole gun signature measured in the sandy loam at a distance of 108 feet (sensors 2 and 3) and 240 feet (sensor 1). Figure 107 shows the corresponding power spectral density (Figure 107A shows the PSD of the raw signal while Figure 107B shows the PSD of the filtered signal). Note that sensor 4 is not connected to the data acquisition system and then represents the electrical noise floor of the data acquisition system. Note also the different temporal profile at the longer distance. The PSD reflects this with sensors 2 and 3 having similar peaked spectral features and sensor 1 having a broader distribution.

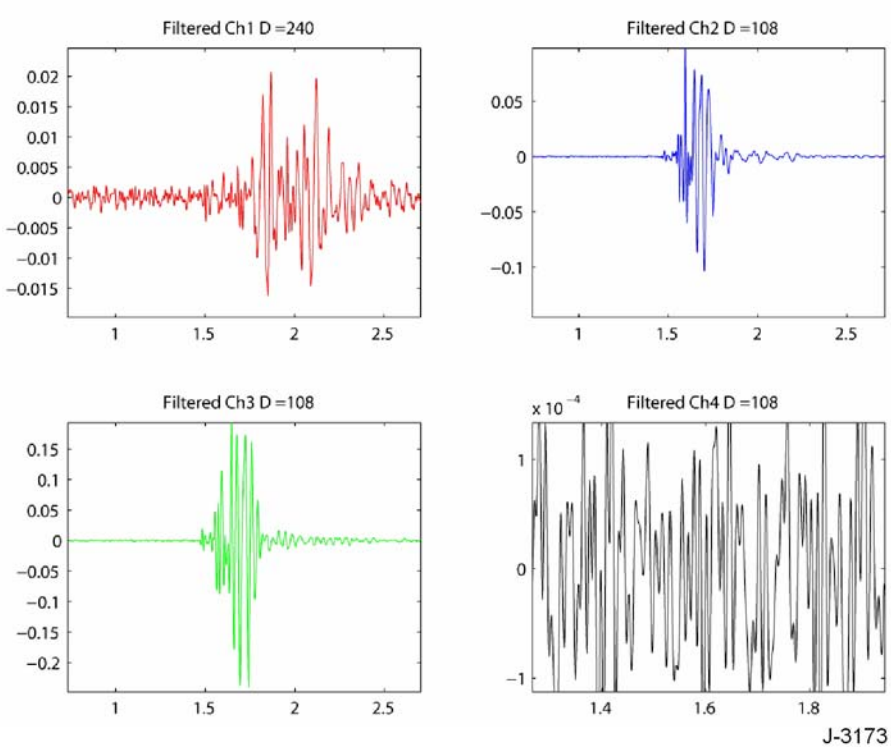

Figure 106. Down-hole gun signature in sandy loam.

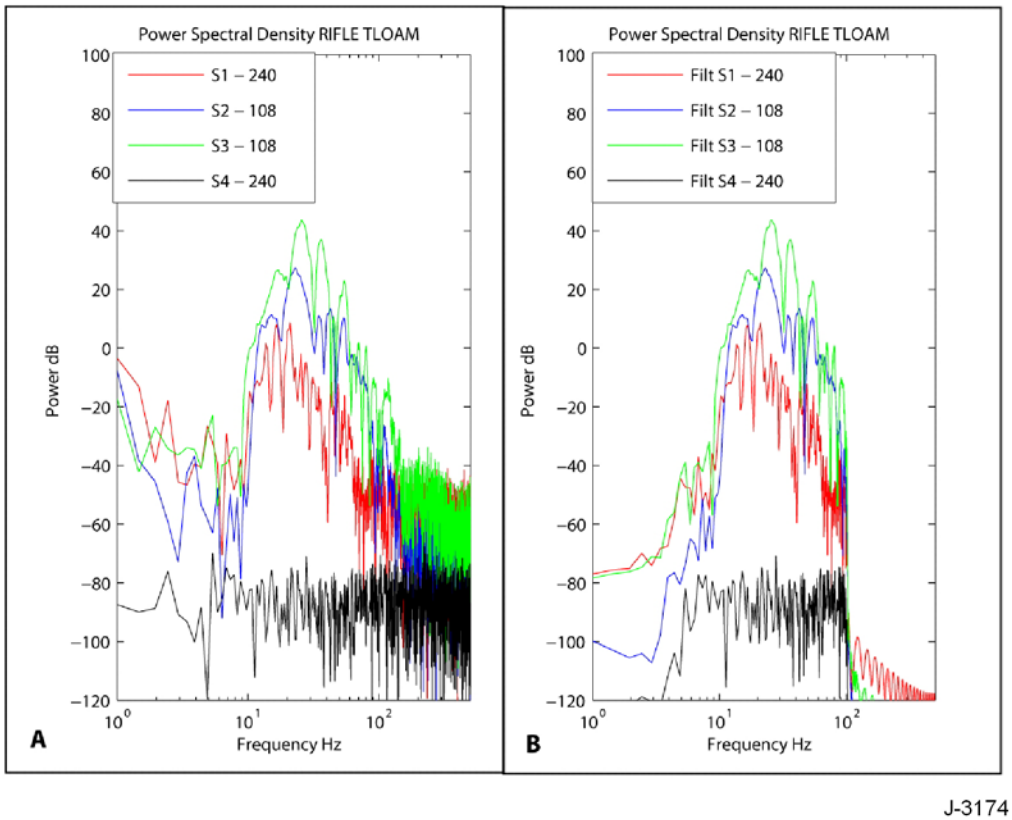

Figure 107. Down-hole gun power spectral density signature in sandy loam. (A – Raw data, B-Filtered Data)

Table 17 shows the individual and average cross-correlation outputs for all of the data points where all the signals have a signal to noise ratio greater than 20 dB for Configuration 1A.

Table 17. Cross-Correlation output for TLoam

	X12	X13	X23
T1	0.617	0.443	0.010
	0.612	0.380	0.008
	0.613	0.617	0.005
mean	**0.614**	**0.480**	**0.008**
T2	0.137	0.132	-0.007
	0.150	0.129	-0.009
	0.152	0.128	-0.009
	0.154	0.127	-0.009
mean	**0.148**	**0.129**	**-0.009**
T3	0.111	0.131	-0.007
	0.142	0.131	-0.008
	0.141	0.130	-0.009
mean	**0.131**	**0.131**	**-0.008**

	X12	X13	X23
T4	-0.181	-0.144	-0.017
	-0.180	-0.142	-0.015
	-0.180	-0.140	-0.015
	-0.180	-0.140	-0.014
mean	**-0.180**	**-0.142**	**-0.015**
T5	-0.348	-0.361	-0.019
	-0.352	-0.365	-0.020
	-0.350	-0.365	-0.020
	-0.349	-0.364	-0.021
mean	**-0.350**	**-0.364**	**-0.020**
T6	-0.843	-0.616	-0.026
	-0.626	-0.621	-0.025
	-0.658	-0.606	-0.025
	-0.606	-0.605	-0.023
mean	**-0.683**	**-0.612**	**-0.025**

7.7.5 Configuration 1B – Shale/Limestone Calibration

In configuration 1B three sensors were placed in the shale at the top of the hill for the purpose of characterizing the properties of the shale/limestone soil properties. A total of 6 threat locations were excited with the down-hole 30-06 rifle. Four shots were fired at each location. The distance from the sensors ranges from 10 ft to 310 ft. Each threat location is equidistant from sensors 2 and 3 such that the nominal time difference of arrival should be 0 s. The expected wave speed for this soil type is nominally 10,000 ft/s.

All of the data presented here was band-pass filtered using a 500th order FIR filter with breakpoints of 5 and 100 Hz. All of the cross-correlation results have been low pass filtered through a 100th order FIR filter with a stop band starting at 20 Hz. The cross-correlation outputs have been generated using a Matlab function which automatically selects the maximum correlation value between -1 and 1 second. As we will discuss and show later in this section, temporal and frequency distortions of the waveforms lead us to utilize and alternate method of deriving the time difference of arrival. In this method the analyst selected the point in the time sequence of each sensor in which the threat was clearly present. The time difference of arrival was then determined from the difference between the relative arrival time.

Figure 108 shows the average signal to noise ratio for each of the sensors at each of the threat locations (the x-axis notes the threat location number). As can be seen in Figure 108, in the shale the signal propagation is significantly attenuated. For this configuration in fact we only have sufficient signal strength to confidently compare all three sensors at threat locations 3 and 4. We also have sufficient signal strength to compare the signals from sensors 2 and 3 at locations 1 and 2. Figure 109 shows the average signal to noise ratio versus threat distance for the shale. This plot was generated using the data from all three sensors. As we can see, the approximate detection distance for the down-hole 30-06 rifle is 200 ft in the shale.

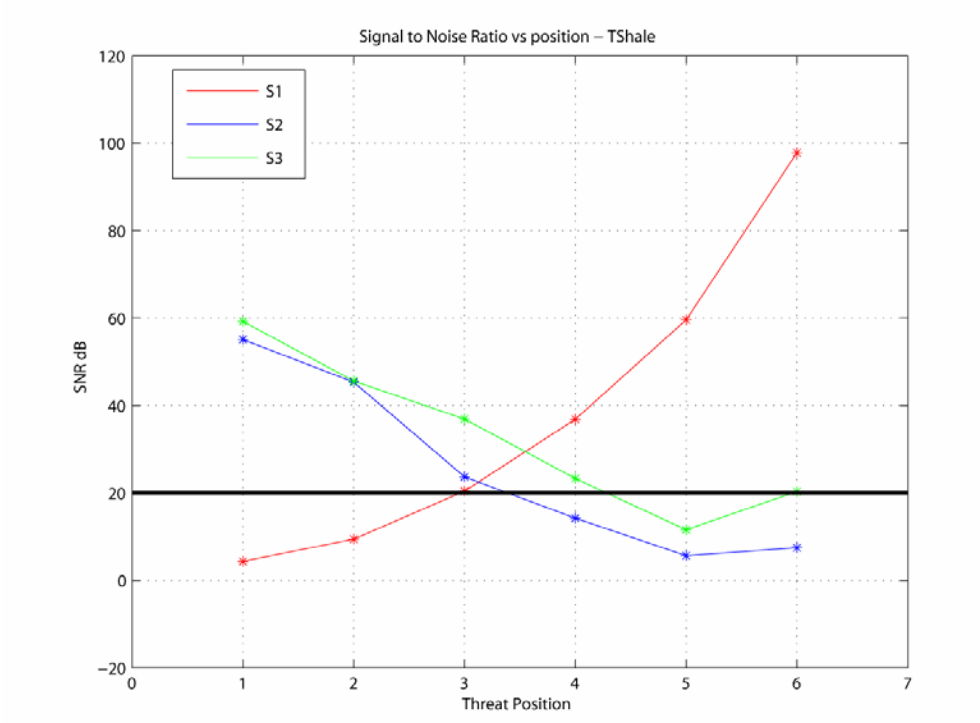

Figure 108. Average signal to noise ratio versus threat position for configuration 1B (TShale).

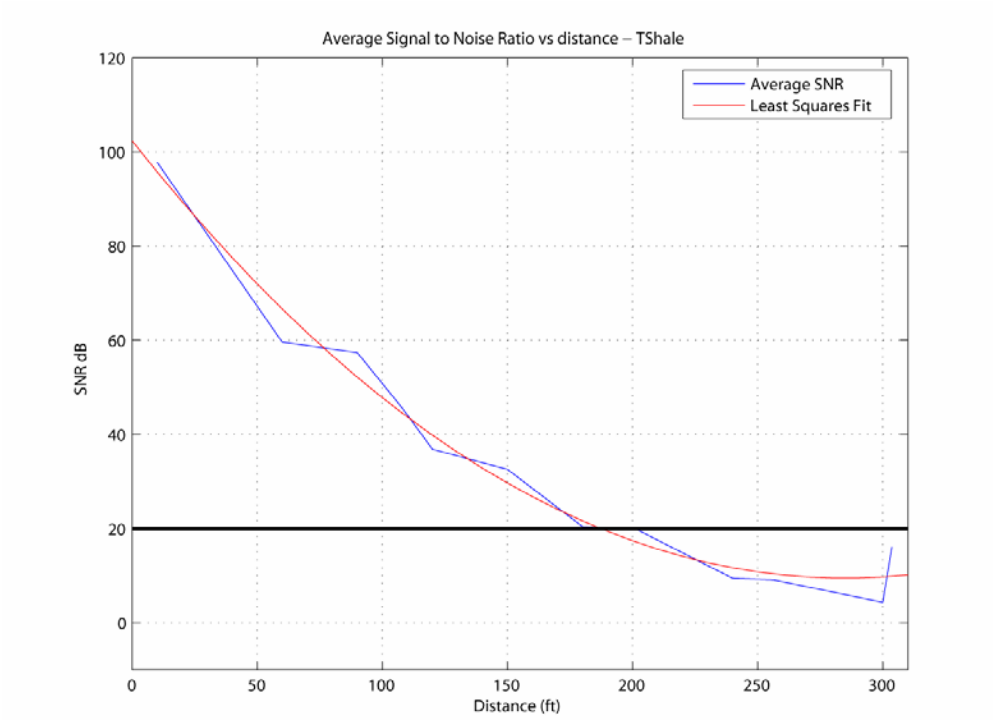

Figure 109. Average signal to noise ratio versus distance for configuration 1B (TShale).

Figure 110 shows the average time difference of arrival between sensors 1 and 2 (X12), and sensors 1 and 3 (X13) versus path length difference for threat locations T1-T6. The time difference of arrival was determined using the cross correlation. As we can see in Figure 110, while the general data trend is correct but the cross-correlation output for sensor locations T3 and T4, which is suppose to have a high level of confidence, trend the wrong way. A linear fit of this data results in a soil velocity of 2000 ft/sec. Figure 111 shows the both the average time difference of arrival and each of the individual cross-correlation results. As we can see, the cross-correlation results have a significant variance from shot to shot. For example the X12 cross-correlation at T3 (Δ-81 ft) has a variance of ±0.065 s which corresponds to a position variance of ±125 ft at a soil speed of 2000 ft/s.

Figure 112 shows the average time difference of arrival between sensors 2 and 3 versus threat location (T1 through T6). In addition to displaying the average time difference of arrival, we have also displayed the time differences of arrival for each shot at each threat location. As can be seen in Figure 112, while the shots at T1 through T4 are tightly grouped (this ignores the single outlier for T4) the locations are well offset from the expected zero mean. In fact the mean cross-correlation for the T1 location is -0.077 s which corresponds to an offset distance of 154 ft at a soil speed of 2000 ft/s (this is greater than the distance to sensors 2 and 3). This indicates that there is either a problem with the cross-correlation method or very non-uniform soil properties.

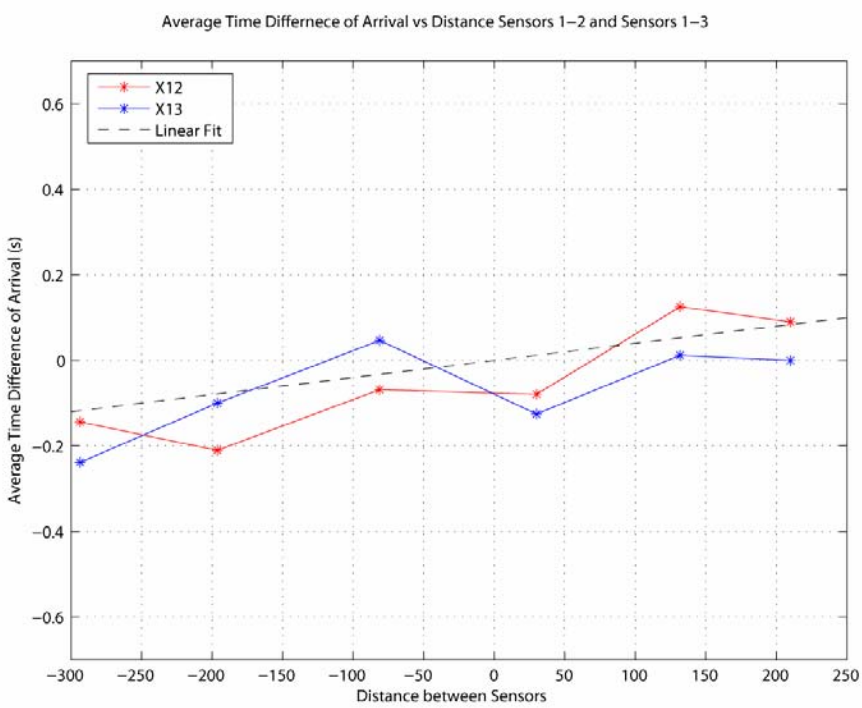

Figure 110. Average time difference of arrival for sensors 1 and 2, and sensors 1 and 3 versus path length difference. Time difference determined from cross-correlation.

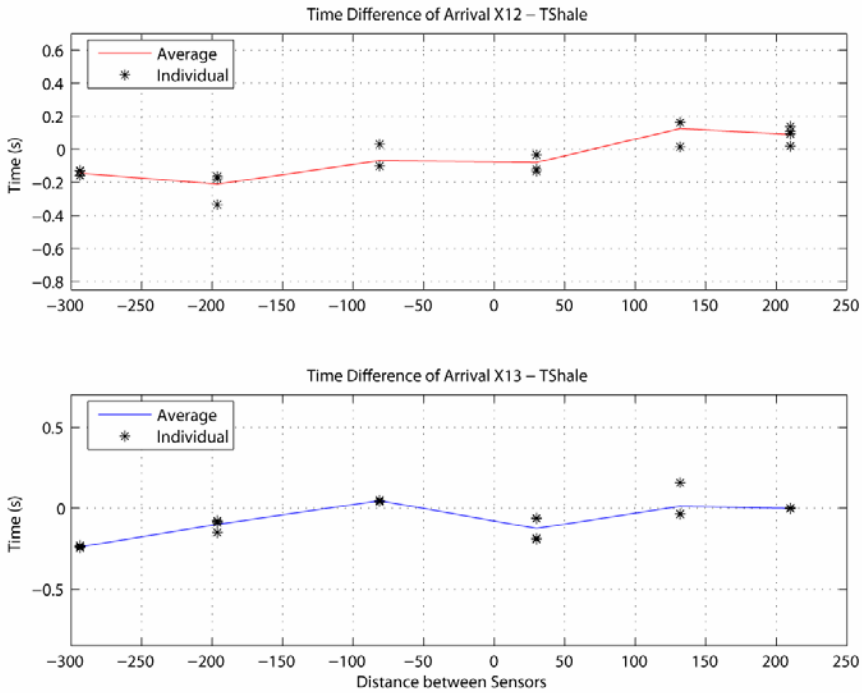

Figure 111. Time difference of arrival between sensors 1 and 2, and sensors 1 and 3 versus threat location.

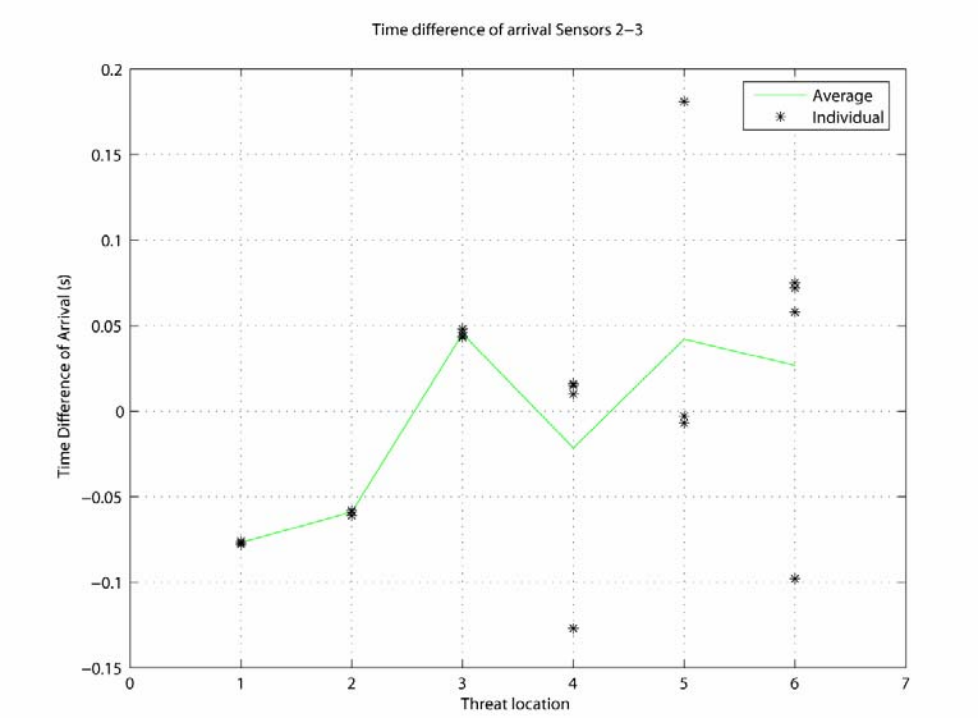

Figure 112. Time difference of arrival between sensors 2 and 3 for threat positions 1 through 6 in shale.

To try and resolve the issue with the cross-correlation output, PSI looked in detail at both the temporal and spectral signatures recorded at sensors 2 and 3 as well as the complete cross-correlation output. Figure 113 shows the temporal signatures for sensors 1, 2, and 3 for a test shot at location T1 in the shale (once again sensor 4 is displayed but not connected). As we can see in Figure 113, while sensors 2 and 3 are equal distances from the threat the recorded signatures are quite different. Specifically, the signature recorded by sensor 3 includes a low frequency component which persists approximately 0.3 seconds longer than the lower frequency component recorded at sensor 2. Figure 114 shows the power spectral density for this signature (the left hand plot shows the PSD for the unfiltered data while the right hand plot shows the PSD of the filtered data). As we can see, the spectral signatures for sensor 2 and 3 are quite similar so one would expect that they could be correlated (Note: the 5-100 Hz band-pass filter has eliminated a significant acoustic signature in the 200 Hz region).

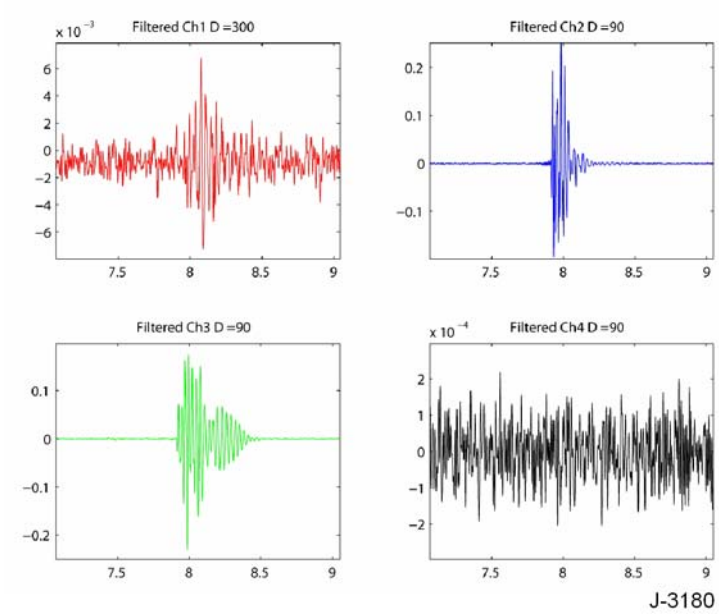

Figure 113. Time signature for a rifle shot at threat position T1 in the shale (Sensor 4 not active).

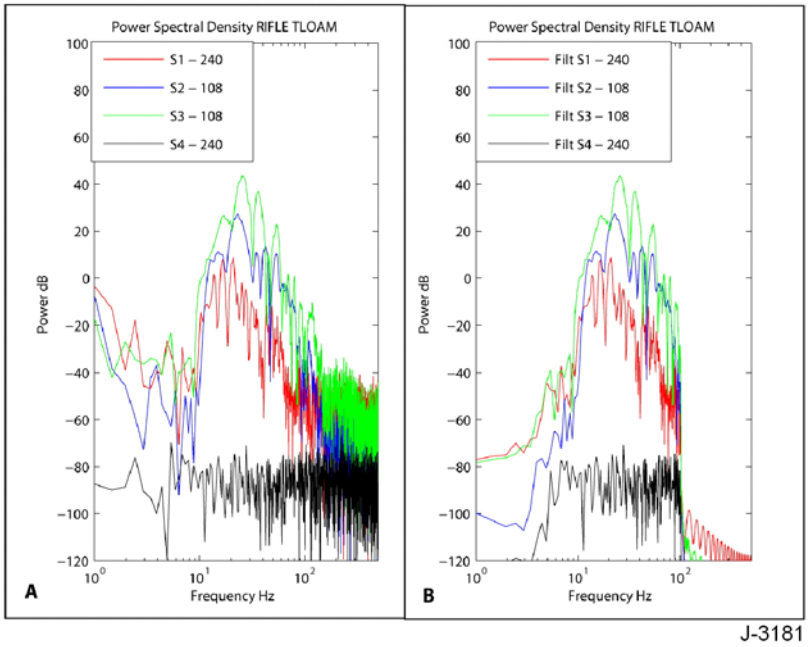

Figure 114. Power spectral density plot for a rifle shot at threat position T1 in the shale (time series shown in Figure 20).

Since the power spectral density plot shown in Figure 114 did not capture the temporal differences between the sensor 2 and sensor 3 signatures, we utilized an alternate method of viewing spectral data called a spectrograph. In a PSD plot, we achieve high resolution in the frequency axis by looking at a signal over a long time period. In a spectrograph, we trade off time and frequency resolution. By reducing the length of the time series which is transformed in to the frequency domain, we increase the time resolution of the frequency data but at the expense of frequency resolution. Figure 115 shows the spectrograph of the time series shown in Figure 113. For this spectrograph, we have divided the 2 second (2000 point) data series into thirty two 128 point packets. The packets have 50% overlap. This results in a series of frequency transforms with a spectral resolution of 8 Hz per data point and a temporal resolution of 64 ms.

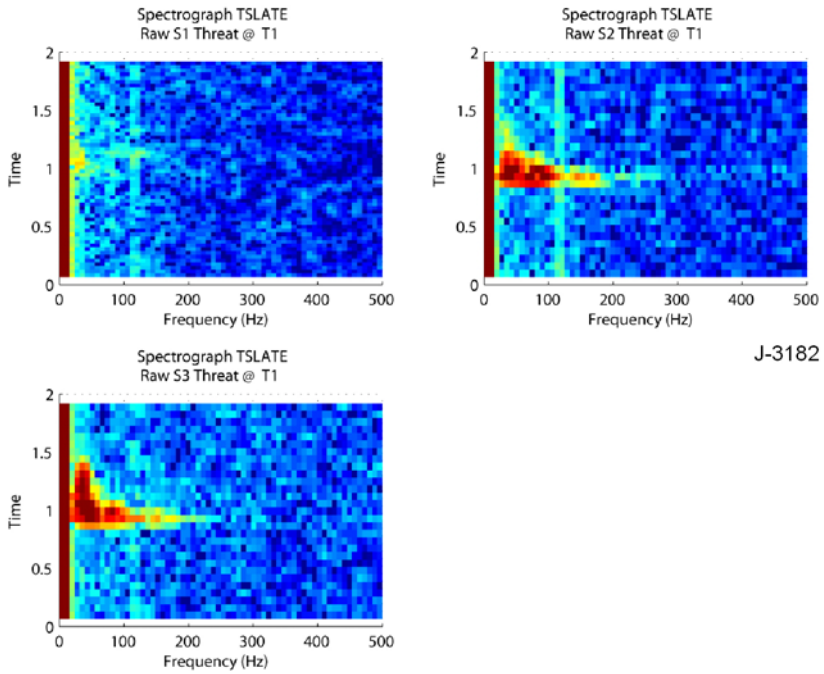

Figure 115. Spectrograph for a rifle shot at threat position T1 in the shale (time series shown in Figure 113).

As we can see in Figure 115, the signals from sensors 2 and 3 have a sharp onset at 0.83 seconds, and consist of a high frequency (80-88 Hz) and a low frequency component (32-48 Hz). At sensor 2, the high frequency component decays in 180 ms while the low frequency component decays in 384 ms. In comparison, the high frequency component at sensor 3 decays in 180 ms while the low frequency component persists for 512 ms (30% longer than the same component at sensor 2). Clearly these signals are different in both time and frequency. Since cross correlation is a mathematical tool developed to determine when two signals are most alike comparing signals which are significantly different often gives unanticipated results. Figure 116 shows the low pass filtered cross-correlation output for a shot at threat location T1 in the shale. As we can see there is a clearly defined peak at -77 ms and a much smaller peak at 51 ms. Neither of these peaks can be associated with the distinctive arrival wave front apparent in Figure 113.

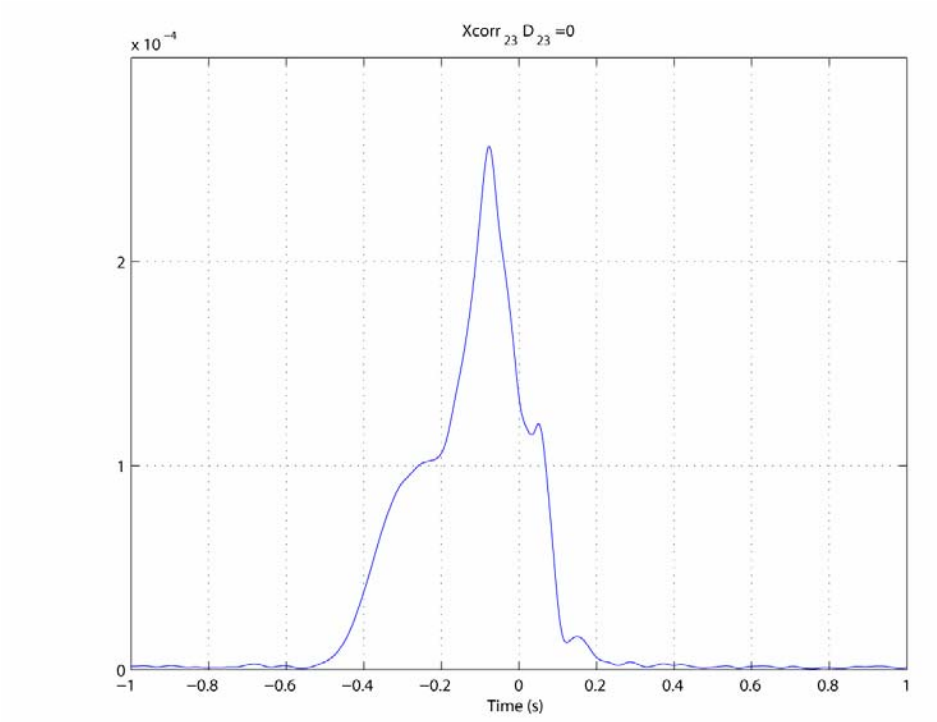

Figure 116. Low pass filtered cross-correlation output for a shot at threat location T1 in the shale.

To correct for this uncertainty PSI alternately chose to specify the time difference of arrival based upon the arrival time of the wave front. There are a number of ways to automatically select the wave front arrival. One is to specify a trigger threshold from which we automatically mark the arrival wave front. There are a number of problems with this method. The most prominent is that it is unable to scale the threshold for the wave magnitude. Thus for conditions where the sensor is quite close to the threat, the high speed p-wave would be sufficient to trigger the threshold limit (we are interested in the slower propagating s-wave). Alternately, we could use a shorter sequence/higher overlap spectrograph to measure changes in the signal power over a narrow time window. This approach is both computationally intensive and as noted earlier a compromise between temporal and spectral resolution. Rather than try and develop and automatic algorithm PSI elected as a temporary expedient to have the analyst manually identify the arrival time of the wave front. For this process to be accurate the signal amplitude needs to be sufficiently above the background noise so that the analyst has a clear arrival wave front. In practice, this requires a signal to noise ratio of approximately 20 dB which is equivalent to the limits observed for cross correlation.

Figure 117 shows the average time difference of arrival for sensor 1 and 2, and sensors 3 and 4 versus distance using the wave front arrival time technique. As can be seen in the figure, this more linear than the data shown in Figure 110 with a significantly shallower slope. Based upon the highest confidence data recorded at the T3, T4, and T5 locations, the measured wave speed is 4800 ft/s. Figure 118 shows the time difference of arrival for each of the individual shots. Looking at the highest confidence data (T3 and T4), we find that this method gives a variance of ±2 ms which corresponds to a position error of 9.6 ft at a wave speed of 4800 ft/s. The lower confidence data (T2 and T5) has a variance of ±20 ms which corresponds to a position error of 96ft at a wave speed of 4800 ft/s.

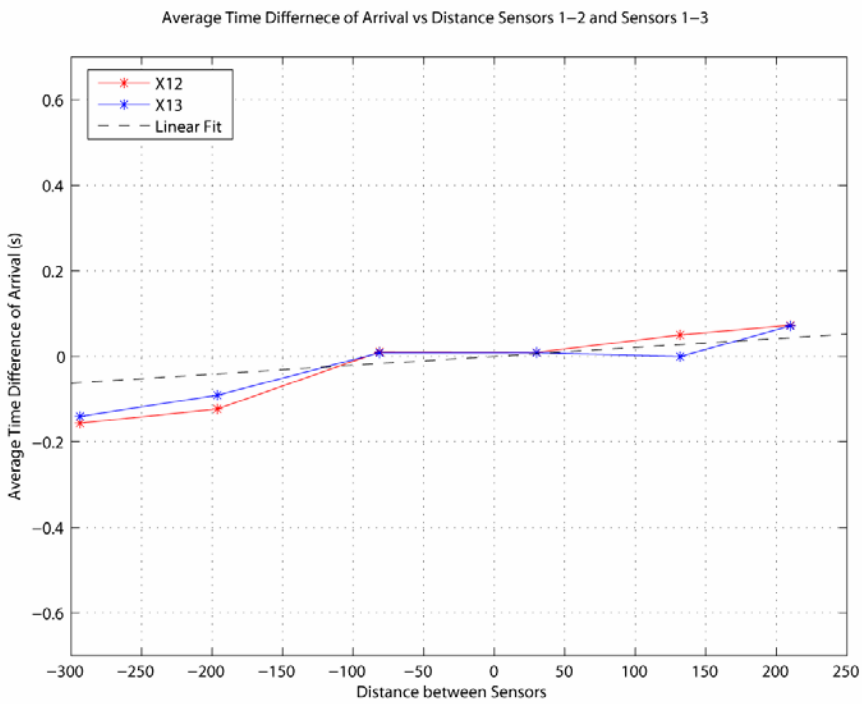

Figure 117. Average time difference of arrival for sensors 1 and 2, and sensors 1 and 3 versus distance. Time difference determined from wave front arrival.

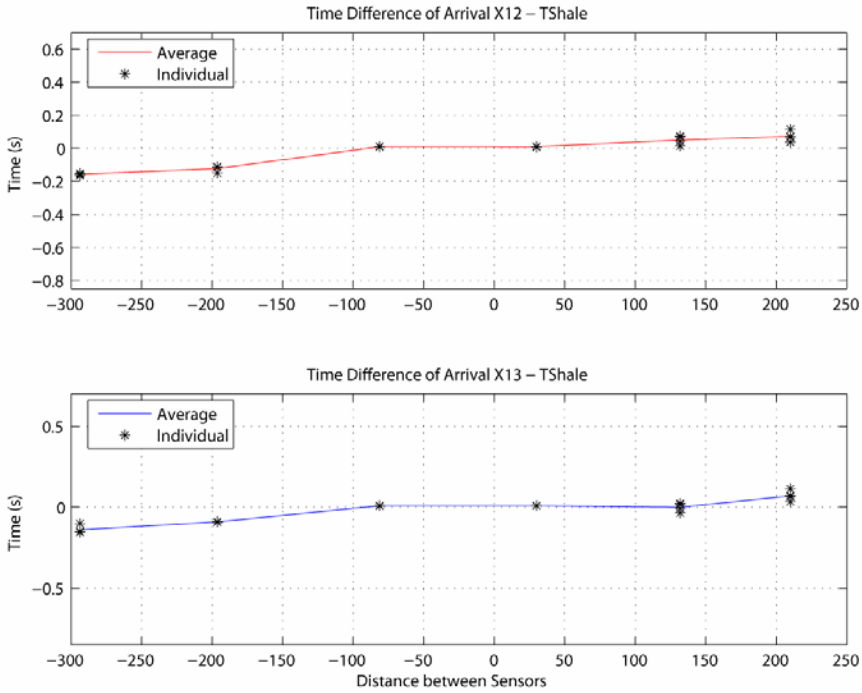

Figure 118. Average time difference of arrival for sensors 1 and 2, and sensors 1 and 3 versus distance. Time difference determined from wave front arrival.

Figure 119 shows the average time difference of arrival for sensors 2 and 3 versus distance using the wave front of arrival technique. As we can see, this technique has moved the average time difference of arrival much closer to the anticipated zero mean for locations T1, T3, and T4 (we should disregard the data for locations T5 and T6 since the signal strength at these locations is below our confidence limit of 20 dB). Unfortunately, the data for location T2 is still at -0.05 s, only nominally different than the answer arrived at by cross-correlation (Figure 112). This offset represents a 240 ft difference in the measure position versus the actual position for a wave speed of 4800 ft/s. PSI has not been able to develop a physical explanation for this apparent difference. The maximum variance for high confidence data with this method is ±1.5 ms which corresponds to a position error of ±7.2 ft at a wave speed of 4800 ft/s. Figures 120, 121, 122, and 123 show the time signature, PSD, cross-correlation, and spectrograph for a shot at threat location T2.

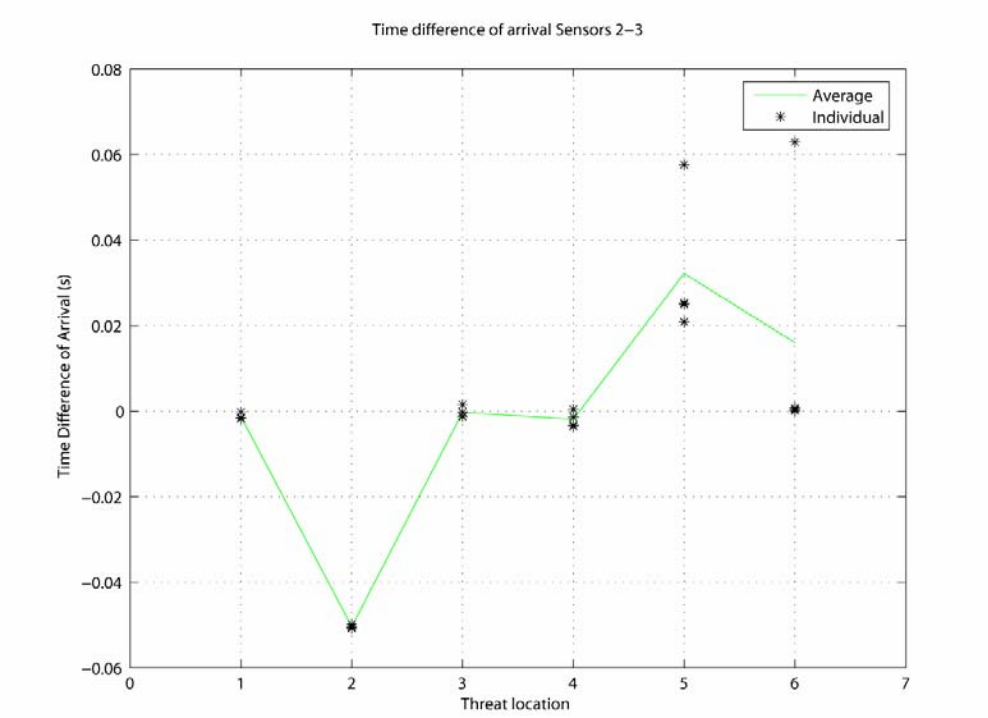

Figure 119. Average time difference of arrival for sensors 2 and 3 versus distance. Time difference determined from wave front arrival.

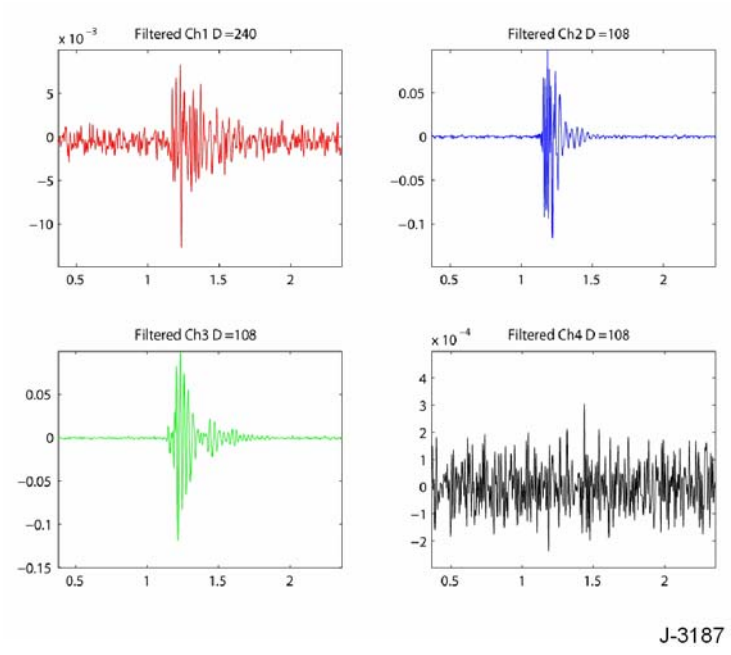

Figure 120. Time signature for a rifle shot at threat position T2 in the shale (Sensor 4 not active).

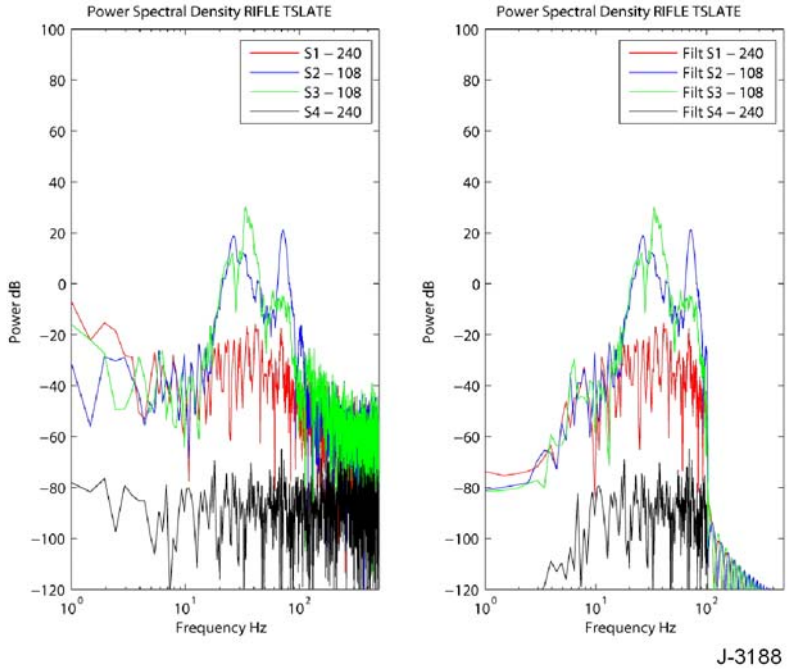

Figure 121. Power spectral density plot for a rifle shot at threat position T2 in the shale (time series shown in Figure 27).

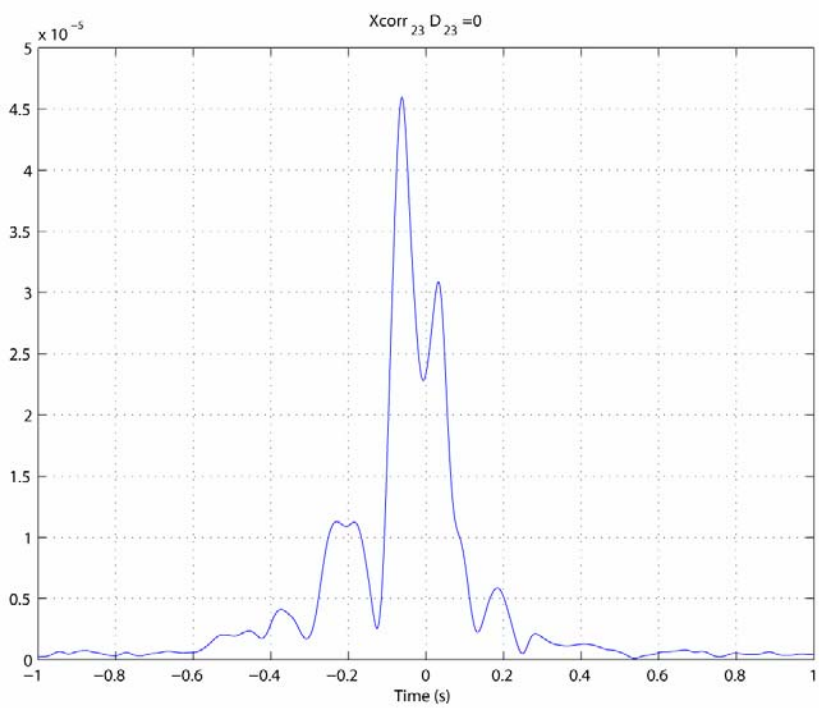

Figure 122. Low pass filtered cross-correlation output for a shot at threat location T1 in the shale.

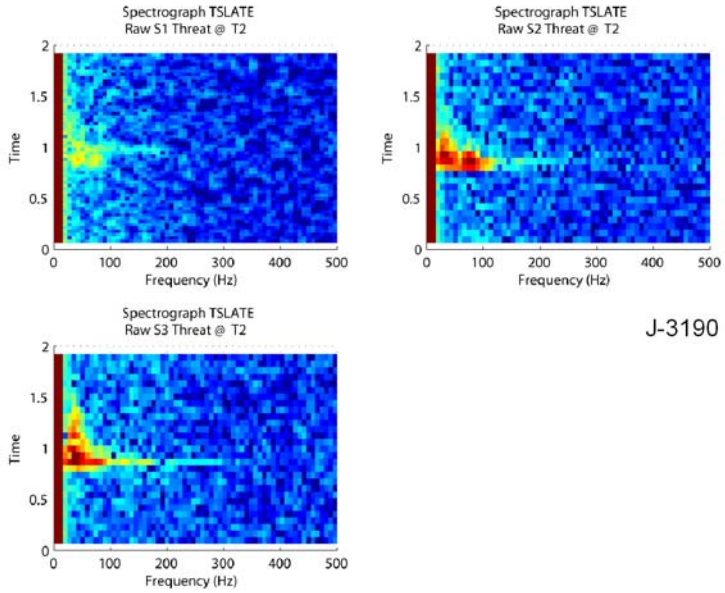

Figure 123. Spectrograph for a rifle shot at threat position T2 in the shale (time series shown in Figure 27).

Table 18 shows all of the cross-correlation and manual time difference of arrival results for configuration 1B.

Table 18. Cross-Correlation and Manual Time Difference of Arrival Values for Configuration 1B

	X12	X13	X23	M12	M13	M23
T1	0.109	0.002	-0.076	0.071	0.071	0.000
	0.018	-0.001	-0.078	0.037	0.035	-0.002
	0.138	0.000	-0.076	0.067	0.066	-0.002
	0.094	-0.003	-0.077	0.115	0.113	-0.002
Mean	**0.090**	**0.000**	**-0.077**	**0.073**	**0.071**	**-0.001**
T2	0.015	-0.037	-0.061	0.015	-0.036	-0.051
	0.163	-0.038	-0.059	0.069	0.019	-0.051
	0.161	0.158	-0.058	0.074	0.023	-0.050
	0.163	-0.035	-0.058	0.042	-0.008	-0.050
Mean	**0.126**	**0.012**	**-0.059**	**0.050**	**0.000**	**-0.050**
T3	-0.032	-0.063	0.043	0.010	0.009	-0.001
	-0.120	-0.062	0.048	0.009	0.010	0.002
	-0.132	-0.191	0.046	0.010	0.009	-0.001
	-0.033	-0.185	0.044	0.008	0.008	0.000
Mean	**-0.079**	**-0.125**	**0.045**	**0.009**	**0.009**	**0.000**
T4	-0.102	0.040	0.015	0.011	0.010	-0.001
	-0.101	0.047	0.016	0.010	0.010	0.000
	0.031	0.050	-0.127	0.010	0.007	-0.003
	-0.102	0.050	0.010	0.010	0.007	-0.004
Mean	**-0.069**	**0.047**	**-0.022**	**0.010**	**0.008**	**-0.002**
T5	-0.178	-0.081	-0.003	-0.114	-0.089	0.025
	-0.163	-0.078	-0.007	-0.115	-0.090	0.025
	-0.335	-0.150	0.181	-0.149	-0.091	0.058
	-0.165	-0.091	-0.003	-0.113	-0.092	0.021
Mean	**-0.210**	**-0.100**	**0.042**	**-0.123**	**-0.091**	**0.032**
T6	-0.157	-0.237	0.072	-0.164	-0.101	0.063
	-0.159	-0.230	0.058	-0.152	-0.151	0.001
	-0.128	-0.246	-0.098	-0.155	-0.154	0.000
	-0.132	-0.241	0.075	-0.154	-0.154	0.000
Mean	**-0.144**	**-0.239**	**0.027**	**-0.156**	**-0.140**	**0.016**

PSI Proprietary Information

7.7.6 Configuration 2 – LongField Down-Hole 30-06 Rifle

In configuration 2, two sensors (S1 and S2) were placed in the sandy loam near the north edge of the soy bean field and two sensors (S3 and S4) were place in the shale at the top of the limestone ridge. The east-west separation of the sensors was 360 feet and the north-south separation of the sensors was 420 feet (Both distances are quoted as the distance measured along the surface of the soil. As the crow fly distances are shorter). The east-west sensors lines are staggered by 180 ft. Three north-south threat lines were tested BE (aligned with sensor 2 and equidistant to sensors 3 and 4), C (aligned with the center of the test site), and BW (aligned with sensor 3 and equidistant to sensors 1 and 2). A minimum of two shots were fired at each location. As many as four shots were taken at the threat locations with in the soil discontinuity (BE300, C300, and BW 300). Figures 86 and 87 show the aerial photo and elevation contours for this test configuration.

This test configuration was laid out and tested prior to doing any analysis of the data gathered at the site. During a preliminary data analysis while we were onsite in Kansas, we realized that we were not getting the signal strength we desired across the transition for two reasons:

1. The poor signal transmission characteristics of the limestone/shale soil.
2. The large signal drop across the soil transition.

As a result, we elected to modify this configuration to the shortfield configuration (Configuration 2) with the goal of maximizing the data with a high confidence factor. A similar approach was taken with regards to data analysis, with the bulk of the analysis effort being spent on configurations 1A, 1B, and 3.

Figure 124 shows the signal to noise ratio versus distance along the BE threat line (i.e. the distance is measured from threat location BE0) for all four sensors. As we can see from Figure 124 there are only three locations on this threat line where we have cross-correlations with a high confidence factor. In this case the X12 correlations are valid at BE0 and BE60, while the X34 correlation is valid at BE420. Figure 125 shows the signal to noise ratio versus distance for sensors 1 and 2 (solid lines) as well as the expected to signal to noise ratio as derived from Configuration 1A (dashed line).

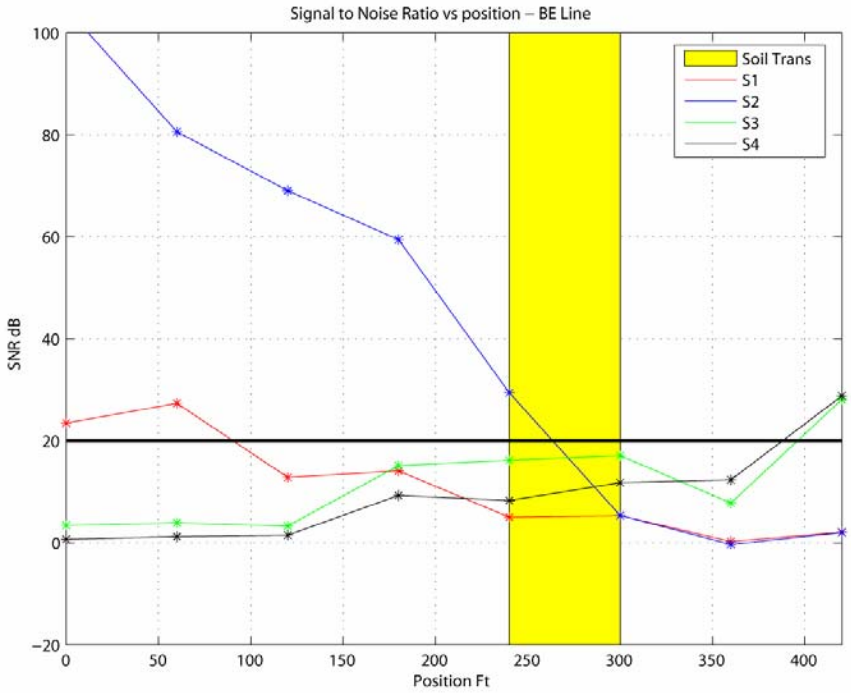

Figure 124. Signal to noise ratio vs distance along the BE threat line.

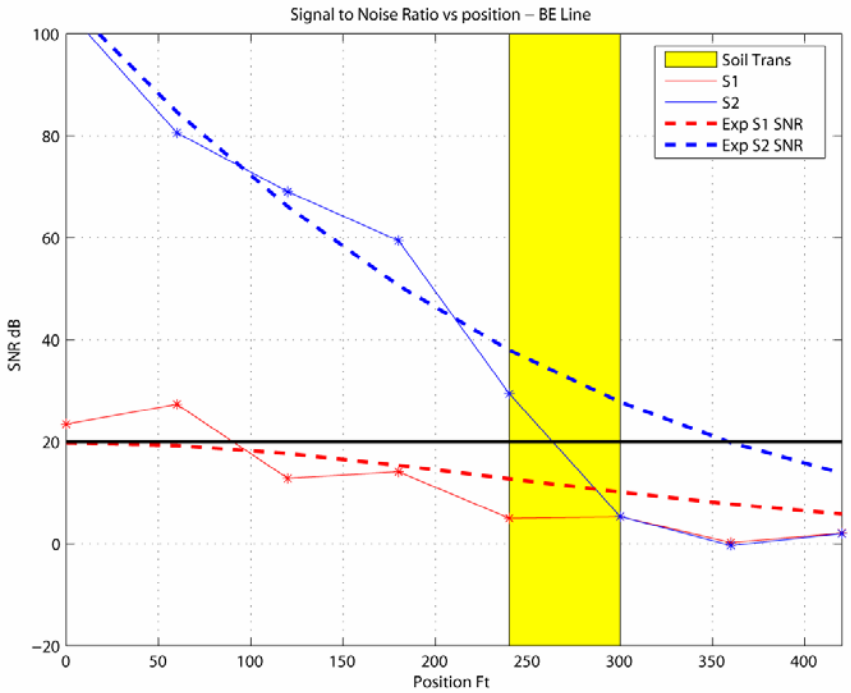

Figure 125. Signal to noise ratio for sensors 1 and 2 versus distance along BE threat line.

As we can see in Figure 125, the actual signal to noise ratio for sensor 2 is 20 dB lower than the expected value across the soil transition. The drop in the sensor 1 SNR ratio is much lower since the expected value is of the signal is already below our confidence level of 20 dB. Figure 126 shows the measured SNR for sensors 3 and 4 as well as the expected SNR value as derived from Configuration 1B (Note: since the sensors are equidistant from the BE line the expected SNR for sensors 3 and 4 are identical). Table 19 shows the cross-correlation and manual time difference of arrival values for the data above the confidence level.

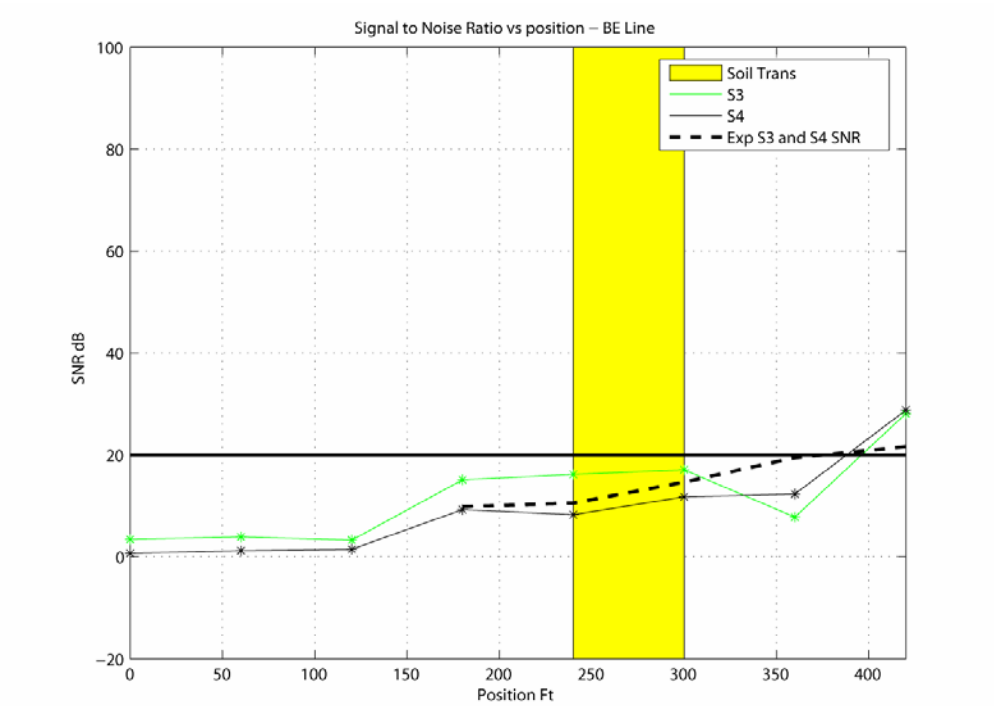

Figure 126. Signal to noise ratio for sensors 3 and 4 versus distance along the BE threat line.

Table 19. Cross-Correlation and Manual Time Difference of Arrival for Longfield BE Threat Line

	X12	M12
BE0	0.657	0.674
	0.660	0.679
mean	**0.659**	**0.677**

BE60	0.581	0.533
	0.534	0.534
mean	**0.558**	**0.533**

	X12	M12
BE0	-0.132	-0.002763
	-0.131	0.00023
mean	**-0.132**	**-0.001**

Figure 127 shows the signal to noise ratio versus distance for the longfield configuration along the C threat line. As we can see, we now have a larger range of high confidence data. Specifically, we can have high confidence in the sensor 1-2 correlation at positions C0 through C180 and marginal confidence in the C240 correlation. Similarly, we can have marginal confidence in the sensor 2-3 correlation at positions C180 through C300, and marginal confidence in the sensor 1-3 correlation at positions C180 and C240.

Figure 128 shows the signal to noise ratio versus distance for sensors 1 and 2 (solid lines) as well as the expected to signal to noise ratio along the C threat line. The magnitude drop in sensor 2 across the transition is 15 dB while the sensor 1 magnitude drop is 10 dB. Figure 129 shows the actual and expected SNR versus distance for sensors 3 and 4. The most notable result of this plot is the consistently lower SNR for sensor 3. Since the SNR for sensor 3 is consistently below the expected value it is difficult to estimate how much the signal is degraded as we cross the soil transition boundary.

Table 20 contains all high and marginal confidence cross-correlation and manual time difference of arrival results for the longfield C threat line.

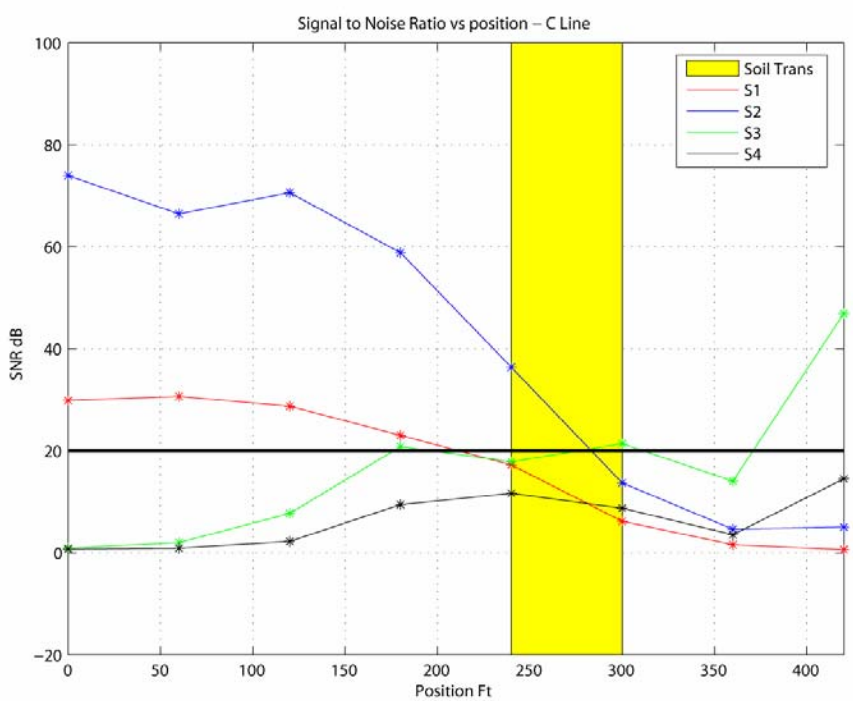

Figure 127. Signal to noise ratio vs distance along the C threat line.

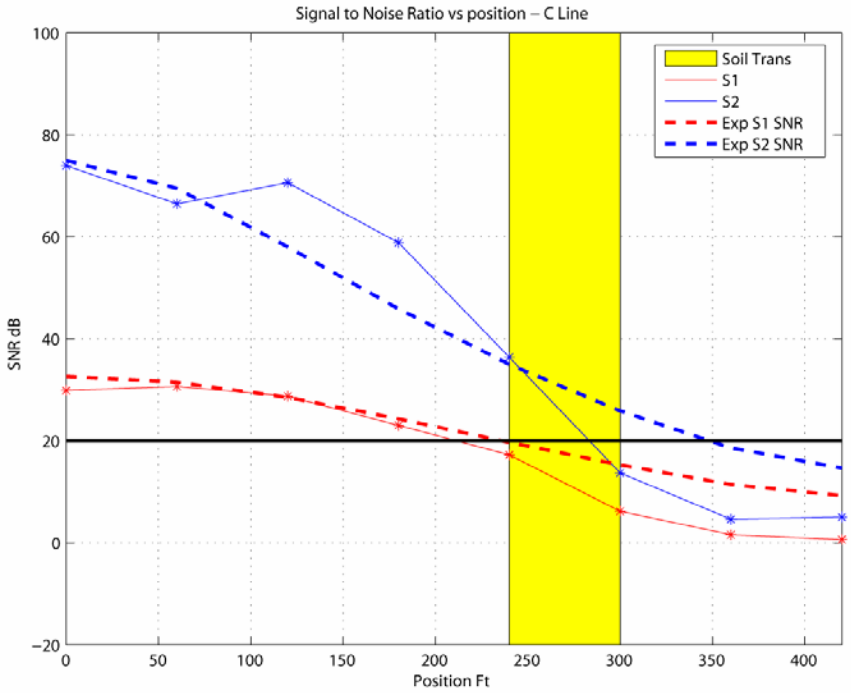

Figure 128. Signal to noise ratio for sensors 1 and 2 versus distance along C threat line.

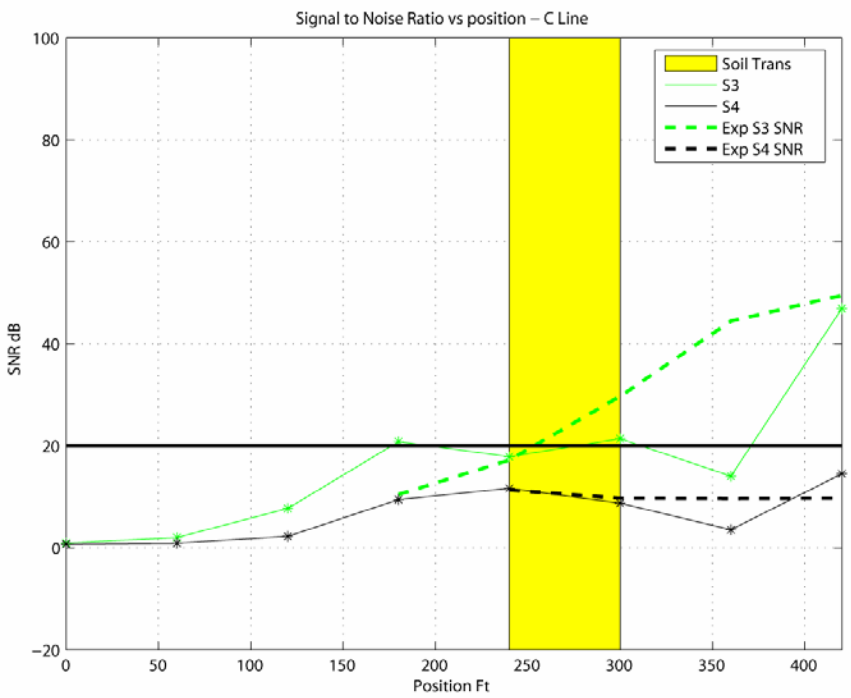

Figure 129. Signal to noise ratio for sensors 3 and 4 versus distance along the C threat line.

Table 20. Cross-Correlation and Manual Time of Arrival for Longfield C Threat Line

	X12	M12
C0	0.312	0.316
	0.317	0.293
mean	0.315	0.305

C60	0.508	0.531
	0.509	0.494
mean	0.509	0.512

C120	0.129	0.255
	0.300	0.255
mean	0.215	0.255

			X13	M13	X23	M23
C180	0.218	0.121	0.588	0.289	0.294	0.170
	0.300	0.225	0.491	0.245	0.233	0.223
mean	0.259	0.173	0.540	0.267	0.264	0.196
C240	-0.142	0.119	0.417	0.318	0.492	0.236
	-0.146	0.023	0.434	0.323	0.485	0.240
mean	-0.144	0.071	0.426	0.320	0.489	0.238

The SNR ratio along the BW threat line is shown in Figure 130. Since the BW threat line is equidistant from both sensors 1 and 2, the SNR ratios are roughly equal. As we can see from the figure, we should have a high degree of confidence in the sensor 1-2 correlations at threat locations BW 0 through BW 180, the sensor 2-3 correlation at location BW 240, and marginal confidence in the sensor 1-2 correlation at C300, the sensor 1-3 and sensor 2-3 correlation at location BW 180. The actual and expected SNR for sensors 1 and 2 is shown in Figure 131. Along the BW threat line, we are seeing a 10 dB drop across the soil transition. Figure 132 shows the measured and expected SNR ratios for sensors 3 and 4 along the BW threat line. In this case there is a 15 dB gap between the expected and measured values. It is unclear if this is due to the soil transition or other factors since the measure SNR at location BW360 is already 30 dB below the expected value. Table 21 contains the high and marginal confidence cross-correlations and manual time of arrival data for the longfield BW threat line.

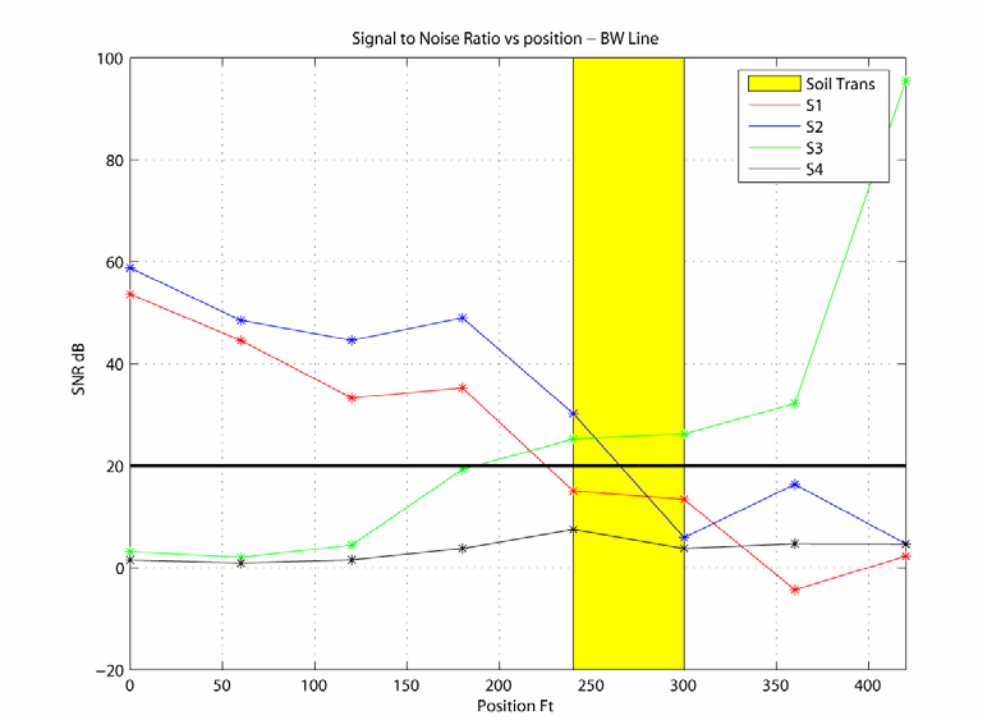

Figure 130. Signal to noise ratio vs distance along the BW threat line.

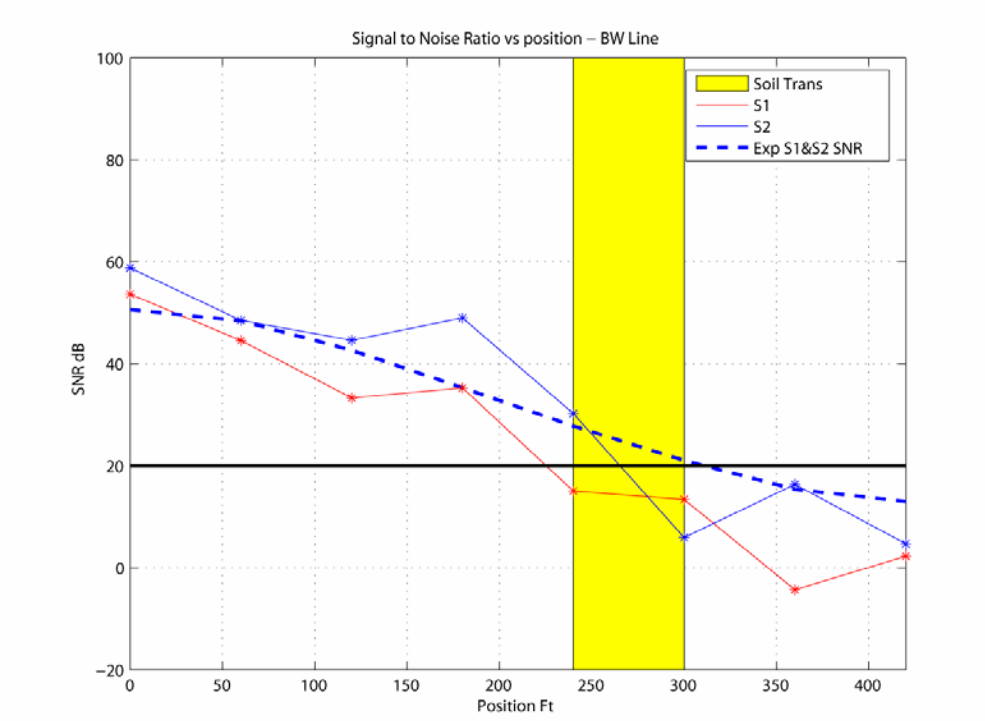

Figure 131. Signal to noise ratio for sensors 1 and 2 versus distance along BW threat line.

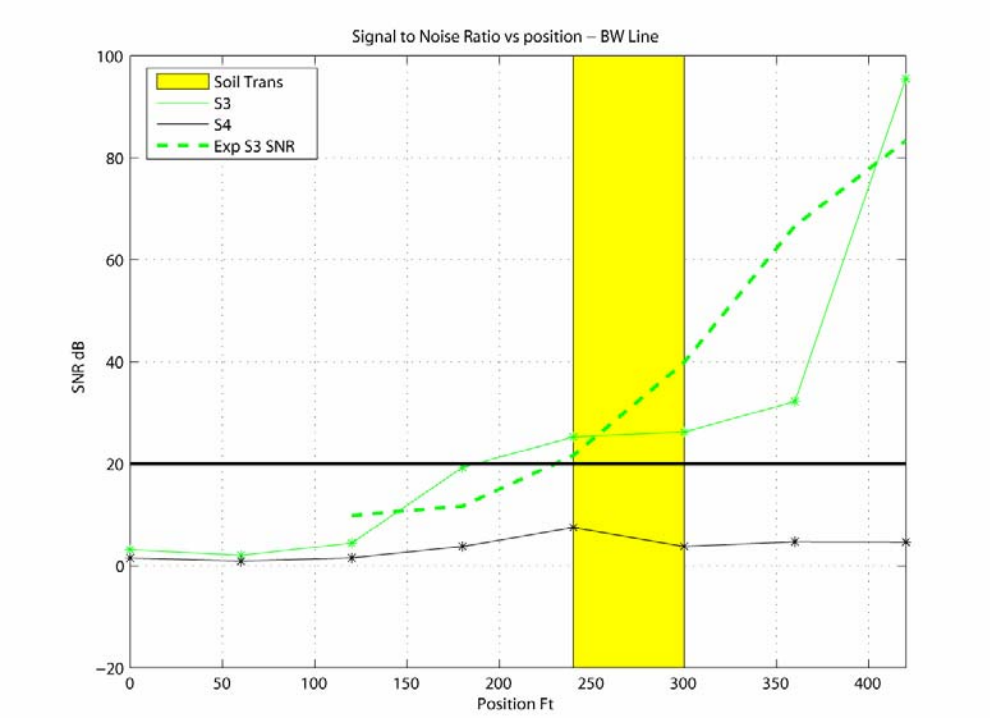

Figure 132. Signal to noise ratio for sensors 3 and 4 versus distance along the BW threat line.

Table 21. Cross-Correlation and Manual Time of Arrival for Longfield BW Threat Line

	X12	M12
C0	0.001	-0.059
	0.005	-0.060
mean	0.003	-0.059

C60	-0.029	-0.008
	-0.025	-0.018
mean	-0.027	-0.013

C120	0.060	-0.009
	0.055	-0.009
mean	0.058	-0.009

			X13	M13	X23	M23
C180	0.025	-0.157	0.169	0.098	0.602	0.374
	0.026	-0.151	0.171	0.198	0.602	0.370
mean	0.026	-0.154	0.170	0.148	0.602	0.372
C240	-0.023	-0.059	0.301	0.409	0.292	0.466
	0.044	-0.012	0.299	0.382	0.555	0.231
mean	0.011	-0.035	0.300	0.396	0.424	0.348

7.7.7 Configuration 3 – ShortField Down-Hole 30-06 Rifle

Configuration 3 is identical to that of Configuration 2 except that sensors one and two have been move closer to the soil transition. Specifically sensor 1 has been moved from the AW0 position to the AW120 position while sensor 2 has been moved from the BE0 position to the BE120 position. Sensors 3 and 4 remain in the shale at the top of the limestone ridge. The east-west sensors lines are staggered by 180 ft. Five north-south threat lines were tested: AE (90 feet east of the BE sensor line), BE (aligned with sensor 2 and equidistant to sensors 3 and 4), C (aligned with the center of the test site), BW (aligned with sensor 3 and equidistant to sensors 1 and 2), and AW (aligned with sensor 1). A minimum of two shots were fired at each location. As many as four shots were taken at the threat locations with in the soil discontinuity (BE300, C300, and BW 300). Figures 3 and 4 show the aerial photo and elevation contours for this test configuration.

Figure 133 shows the SNR ratio versus distance along the AE threat line. As we can see, the signal strengths are such that there is no position along the AE threat line with a high or marginal confidence correlation. The measured and expected values for the SNR ratio of sensors 1 and 2 are shown in Figure 134. Along the AE line, we see a 20 dB gap between the expected and measured SNR ratios for sensor 2. Figure 135 shows the expected and measured SNR ratios for sensors 3 and 4. As was the case for configuration 2, it is impossible to tell how much the signals measured by sensors 3 and 4 are degraded by the soil transition.

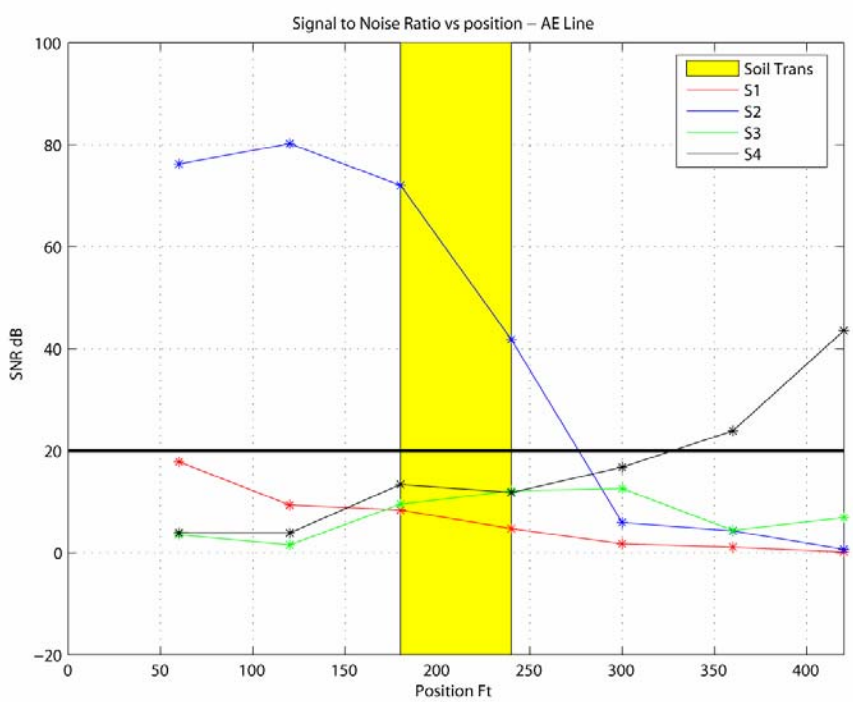

Figure 133. Signal to noise ratio vs distance along the AE threat line.

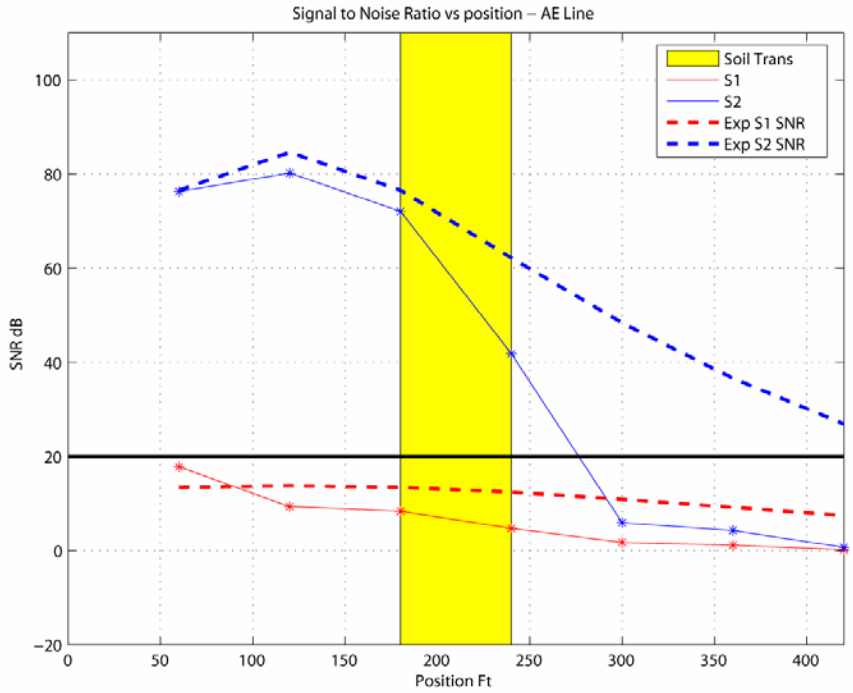

Figure 134. Signal to noise ratio for sensors 1 and 2 versus distance along AE threat line.

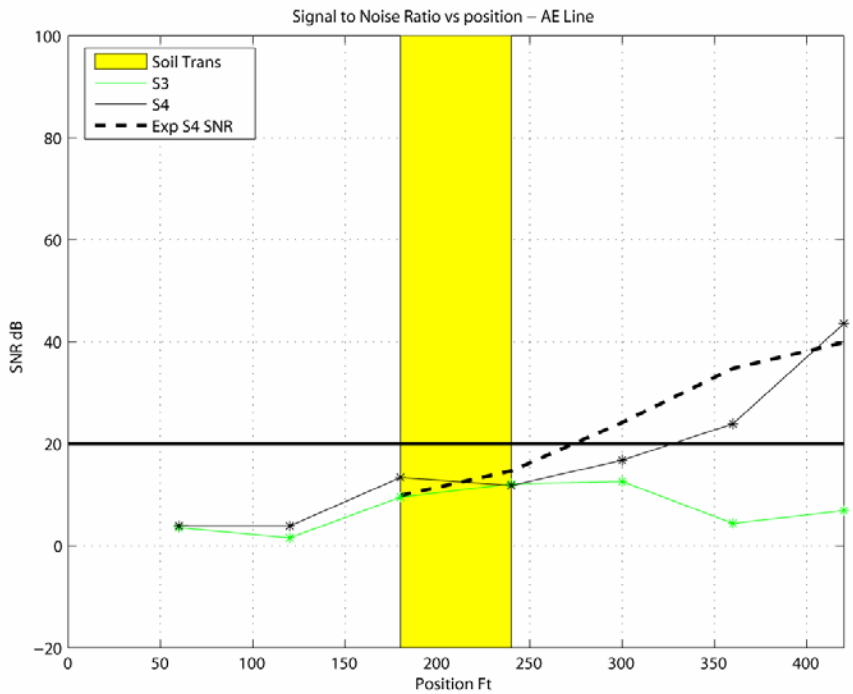

Figure 135. Signal to noise ratio for sensors 3 and 4 versus distance along the AE threat line.

Figure 136 shows the SNR ratio versus distance along the BE threat line. As was the case for the AE threat line, there is not threat position with sufficient signal strength to yield a high confidence correlation. Figure 137 shows the expected and measured SNR for sensors 1 and 2. There is a 30 dB drop across the transition for this threat line. Figure 138 shows the expected and measured SNR for sensors 3 and 4.

Figure 139 shows the SNR versus distance for the C threat line. For the C threat line we have sensor 1-2 correlations with a high degree of confidence at locations C0 through C240, sensor 1-3 correlation with marginal confidence at C180 and C240, and sensor 2-3 correlations with marginal confidence at locations C180 can C240. Figure 140 show the measure and predicted sensor 1 and 2 SNR versus distance for the C line. There is a 40 dB difference between the expected and measured SNR for sensor 2 and a 20 dB difference between the measured and expected SNR for sensor 1. Figure 141 shows the measured and expected SNR for sensors 3 and 4. Again there is a 20 db difference between the expected and measured values for sensor 3, but it is unclear if this difference is due solely to the soil discontinuity.

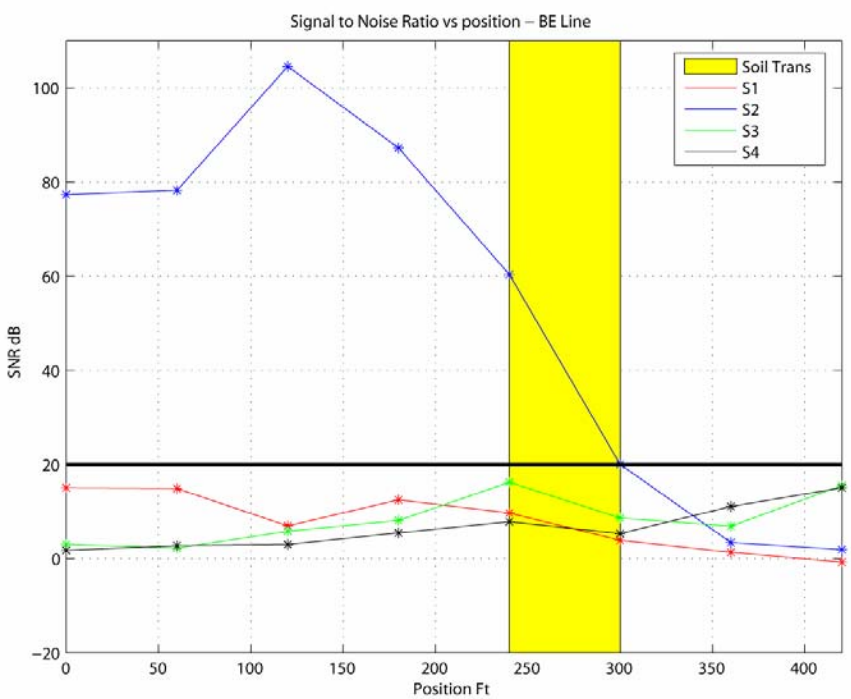

Figure 136. Signal to noise ratio vs distance along the BE threat line.

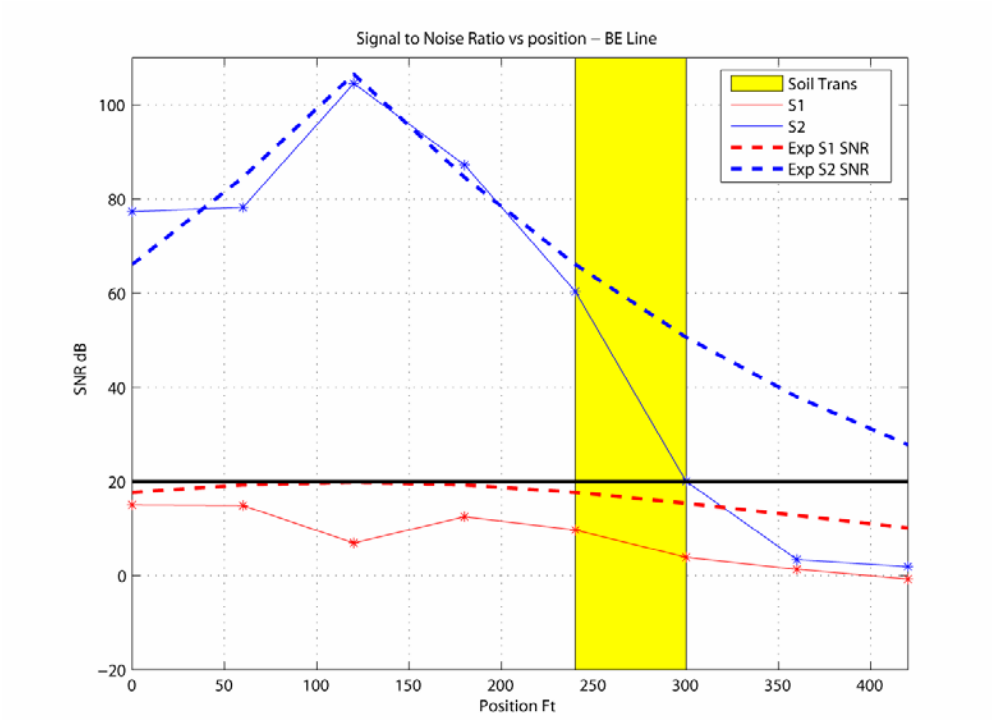

Figure 137. Signal to noise ratio for sensors 1 and 2 versus distance along BE threat line.

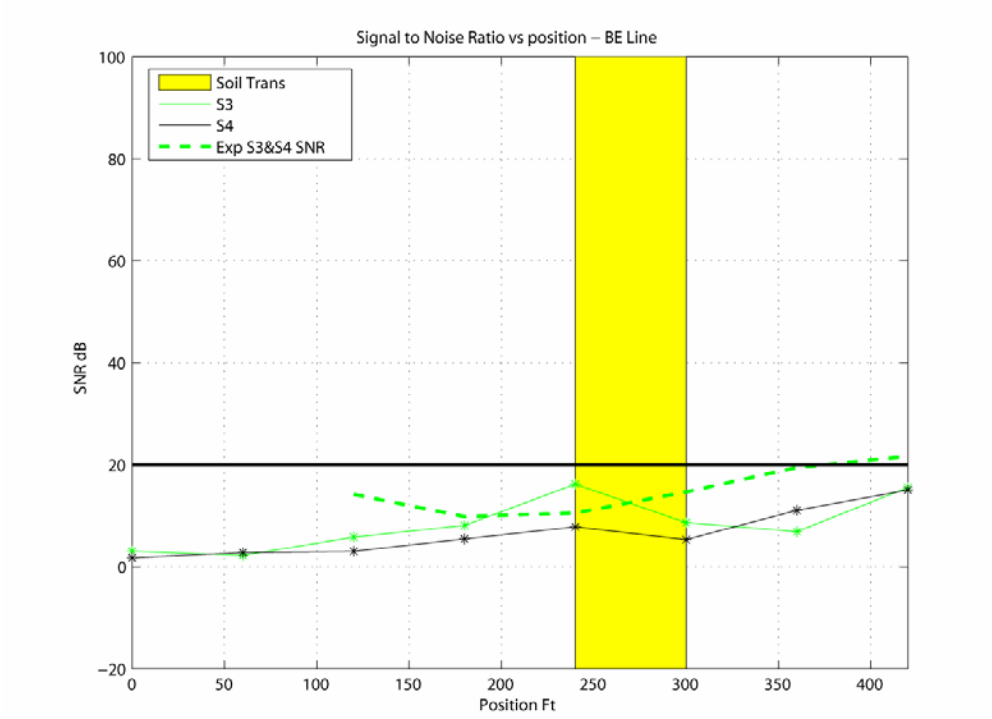

Figure 138. Signal to noise ratio for sensors 3 and 4 versus distance along the BE threat line.

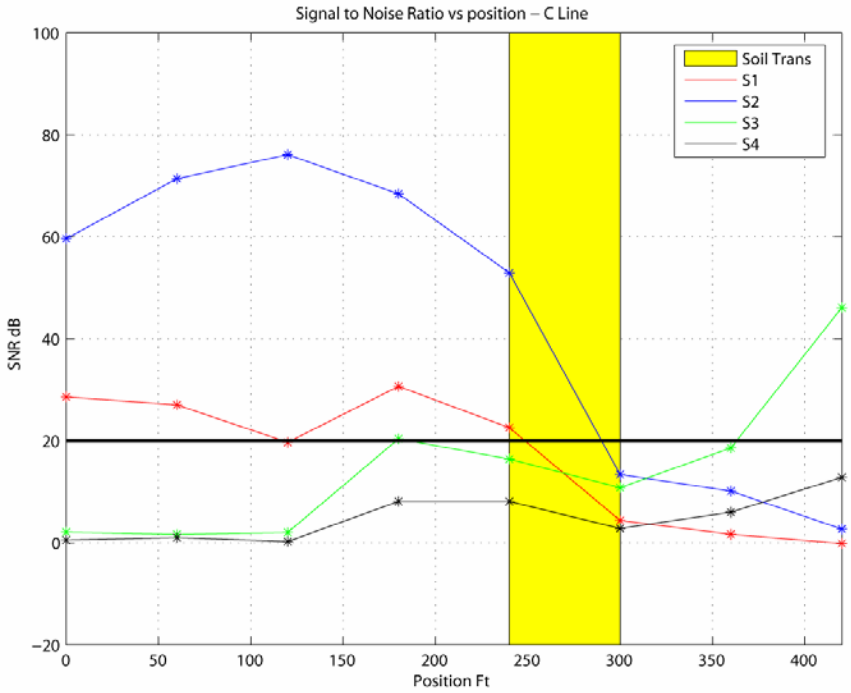

Figure 139. Signal to noise ratio vs distance along the C threat line.

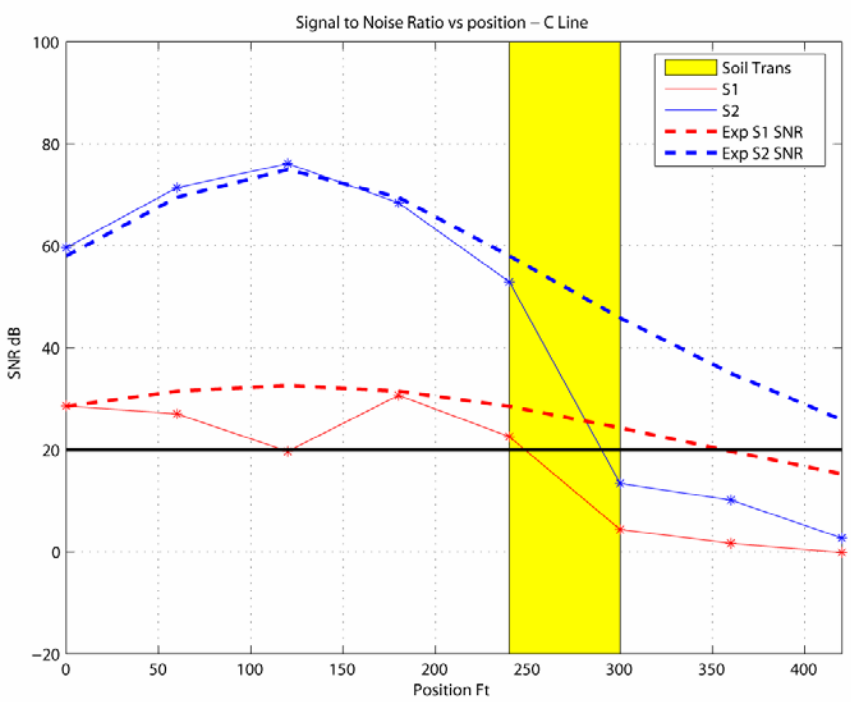

Figure 140. Signal to noise ratio for sensors 1 and 2 versus distance along C threat line.

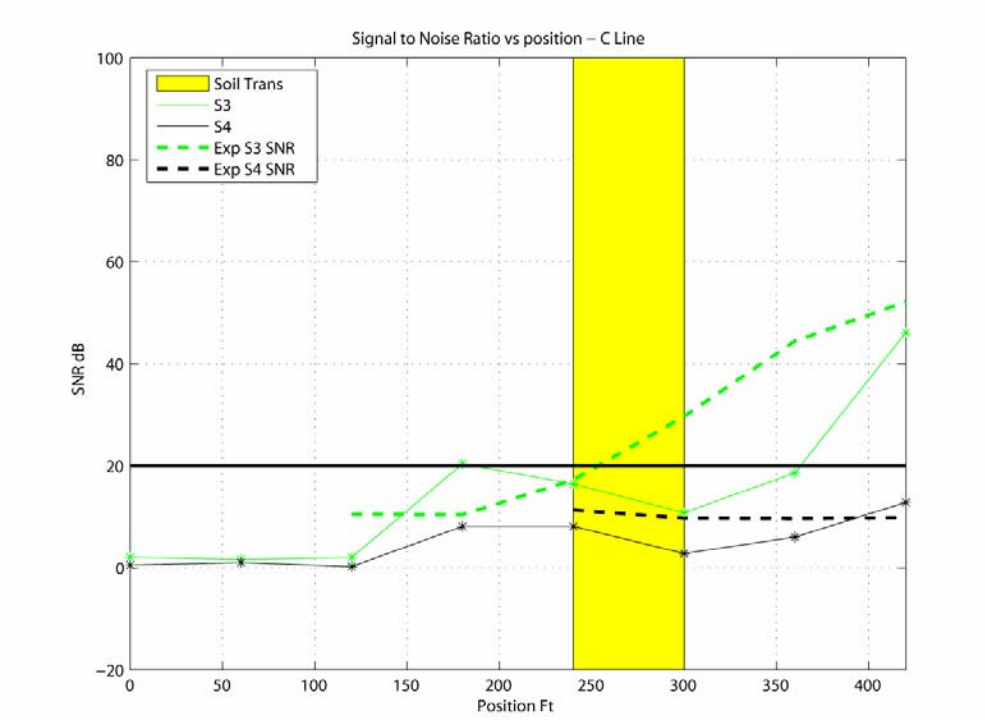

Figure 141. Signal to noise ratio for sensors 3 and 4 versus distance along the C threat line.

Figure 142 shows the average time difference of arrival for sensors 1 and 2 versus distance along the C threat line. In addition to the measured values, there is a line indicating the expected time difference. This expected time difference is determined using the method described in Appendix B. As we can see in the plots of the individual results, the correlation and manual results are tightly grouped at each location but do not match well with the expected values. The maximum variance in the high confidence correlation outputs (C0-C240) is ±10 ms which corresponds to a position error of ±4 ft at a soil speed of 400 ft/s (both sensors are located in the loam). Similarly, the maximum variance for the manually determined time difference is ±1.5 ms which corresponds to a position error of ±0.6 ft. There are a number of possible explanations for the discrepancy between the measured and predicted values. First, there is potentially a problem with how we are comparing signal. Since the spectral and temporal signature shifts as it travels through the soil, we are not really comparing apples to apples. Because the signals really are different, the comparisons that we are making to derive the time of arrival are not necessarily accurate. An alternate reason that our approach is not working well is that the soil conditions truly are not uniform and thus distort our results.

Table 22 contains the high and marginal confidence cross-correlation data for the C threat line.

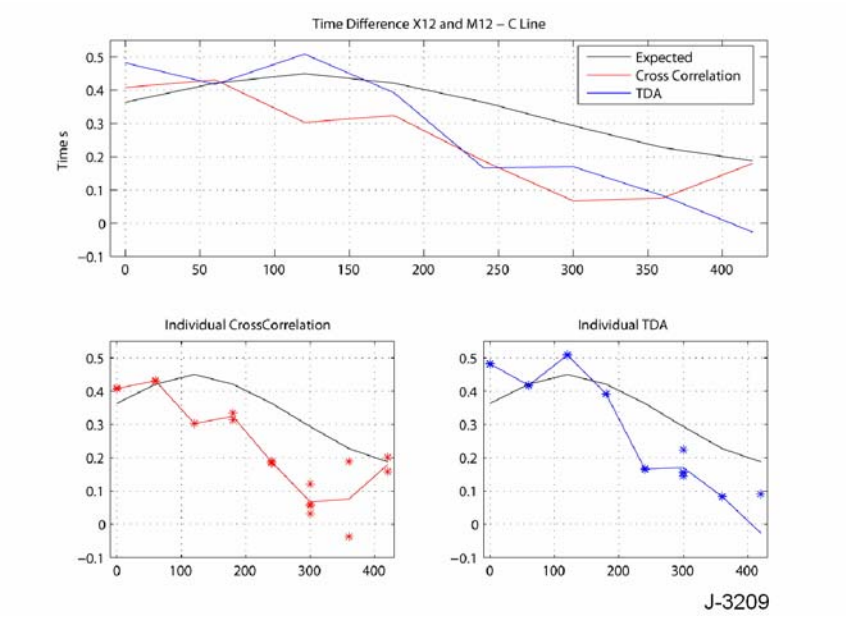

Figure 142. Average time difference of arrival for sensors 1 and 2 versus distance C threat line. Time difference determined from both wave front arrival and cross correlation.

Table 22. Cross-Correlation and Manual Time of Arrival for Shortfield C Threat Line

	X12	M12
C0	0.407	0.483
	0.409	0.481
mean	0.408	0.482

C60	0.432	0.418
	0.430	0.416
mean	0.431	0.417

C120	0.303	0.510
	0.303	0.507
mean	0.303	0.509

			X13	M13	X23	M23
C180	0.334	0.393	0.428	0.465	0.080	0.072
	0.314	0.391	0.434	0.464	0.082	0.072
mean	0.324	0.392	0.431	0.464	0.081	0.072
C240	0.188	0.165	0.398	0.460	0.269	0.296
	0.183	0.166	0.400	0.392	0.262	0.226
	0.188	0.167	0.405	0.339	0.270	0.172
	0.189	0.166	0.398	0.392	0.272	0.226
mean	0.187	0.166	0.400	0.396	0.268	0.230

Figure 143 shows SNR versus distance along the shortfield BW threat line. As was the case for the C threat line, we have sensor 1-2 correlations with a high degree of confidence at locations C0 through C240, sensor 1-3 correlation with marginal confidence at C180 and C240, and sensor 2-3 correlations with marginal confidence at locations C180 can C240. Figure 144 shows the expected and measured SNR for sensors 1 and 2 along the BW threat line. Since the two sensors are equidistant from the threat line the expected SNR's are equal. As we can see from the figure, the both signals are degraded 30 dB across the soil transition. Figure 145 shows the measured and expected SNR for sensors 3 and 4. As has been the situation for all of the sensor 3 and 4 data taken in the long and short-field configurations, it is unclear whether the large difference between the expected value and the measured SNR is a result of the soil transition or some other effect.

Figure 146 plots the average and expected time difference of arrival between sensor 1 and 2 along the BW threat line. In addition Figure 146 individually plots the cross-correlation and manual time difference of arrival results. The results shown in Figure 146 are mixed. On the positive side we see that the automatic cross-correlation results are tightly grouped (maximum variance ±1.5 ms / ±0.6 ft @ 400 ft/s) but there is a significant offset (-50 ms / -20 ft @ 400 ft/s) ignoring the data at C240) from the expected time difference (expected value at locations C0-C240 = 0 s). As we have noted earlier this likely indicates non-uniform soil conditions. This means that even in soils such as the loam in the soy bean field that we will need to calibrate the installation to accurately establish position. Table 23 contains the high and marginal confidence cross-correlation data for the BW threat line.

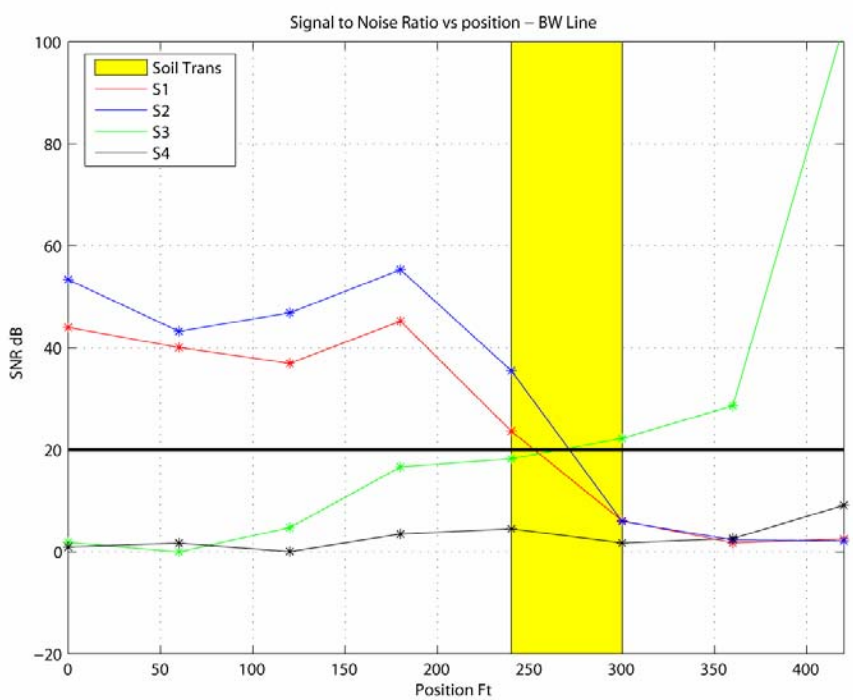

Figure 143. Signal to noise ratio vs distance along the BW threat line.

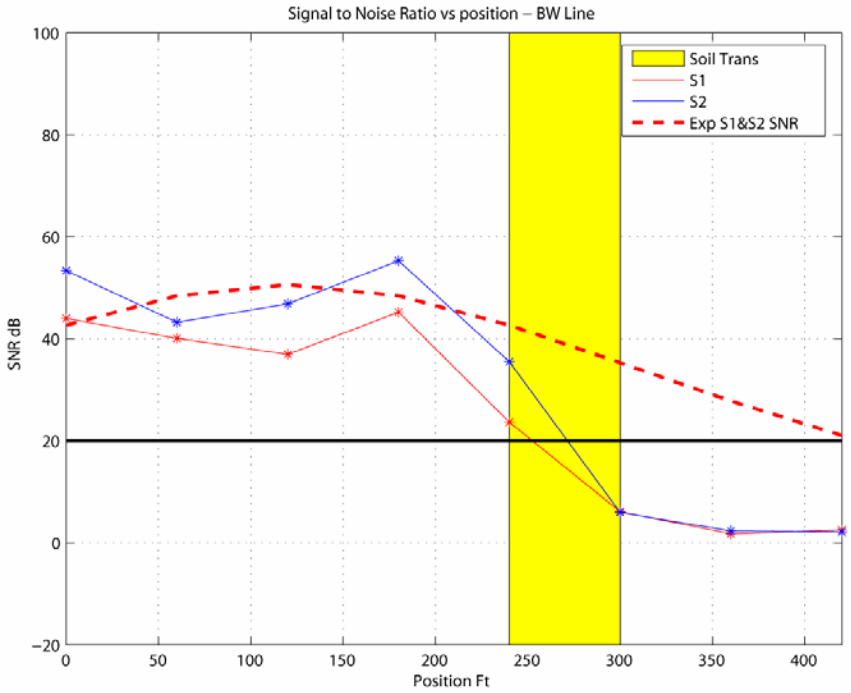

Figure 144. Signal to noise ratio for sensors 1 and 2 versus distance along BW threat line.

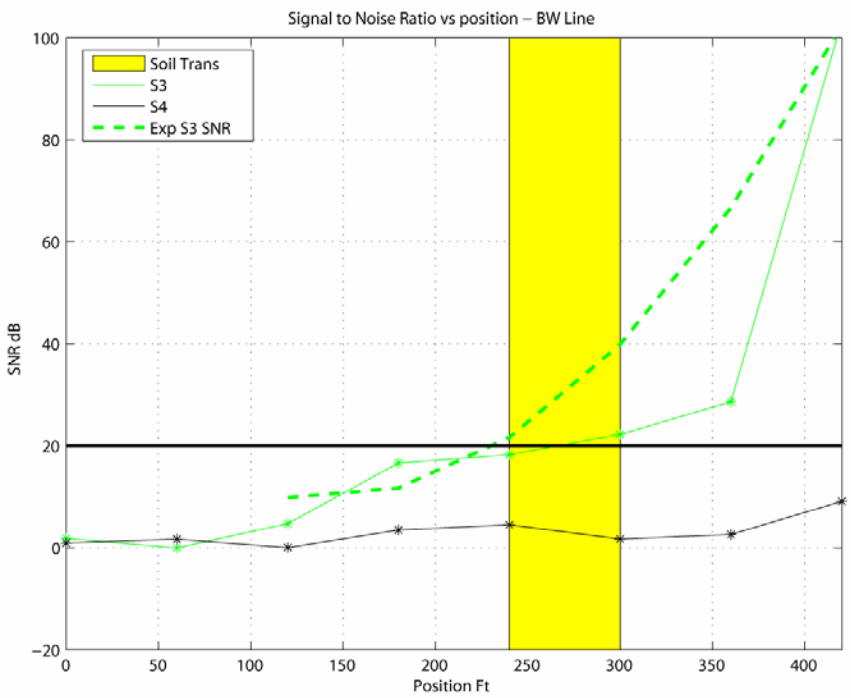

Figure 145. Signal to noise ratio for sensors 3 and 4 versus distance along the BW threat line.

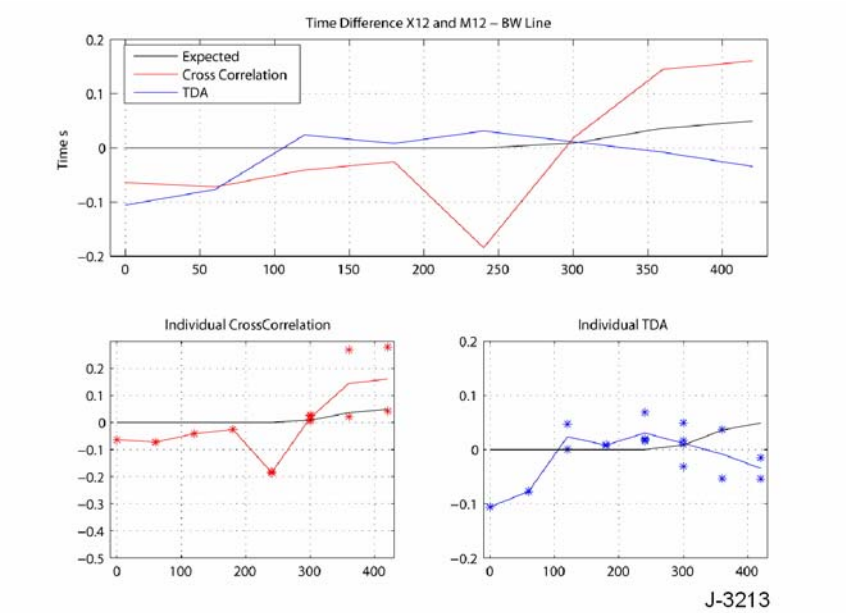

Figure 146. Average time difference of arrival for sensors 1 and 2 versus distance BW threat line. Time difference determined from both wave front arrival and cross correlation.

Table 23. Cross-Correlation and Manual Time of Arrival for Shortfield BW Threat Line

	X12	M12
C0	-0.064	-0.106
	-0.064	-0.106
mean	-0.064	-0.106

C60	-0.072	-0.077
	-0.073	-0.077
mean	-0.073	-0.077

C120	-0.041	0.047
	-0.041	0.000
mean	-0.041	0.024

			X13	M13	X23	M23
C180	-0.026	0.009	0.165	0.084	0.244	0.075
	-0.026	0.007	0.166	0.083	0.246	0.076
mean	-0.026	0.008	0.166	0.084	0.245	0.076
C240	-0.185	0.020	0.203	0.051	0.474	0.031
	-0.182	0.016	0.301	0.046	0.387	0.030
	-0.185	0.019	0.413	0.049	0.472	0.030
	-0.186	0.069	0.412	0.100	0.477	0.031
mean	-0.185	0.031	0.332	0.061	0.453	0.031

Figure 147 plots the measured SNR along the short field AW threat line which is aligned with sensor 1. As was the case for the AE and BE threat lines, there is marginal signal on three of the four sensors. As a result, we only have marginal sensor 1-2 correlation data at locations AW0 through AW240. Figure 148 plots the expected and measured SNR for sensors 1 and 2. There is a 20 dB drop in the sensor 1 signal magnitude across the soil transition. Figure 149 shows the average time difference of arrival versus expectation for both the cross-correlation and manual time difference of arrival measurements. Table 24 contains the cross-correlation numbers for the shortfield AW threat line. As we can see from the variance in the numbers, all of these correlations are marginal. Similarly, there is a wide discrepancy between the expected correlation values and the measured time of arrivals.

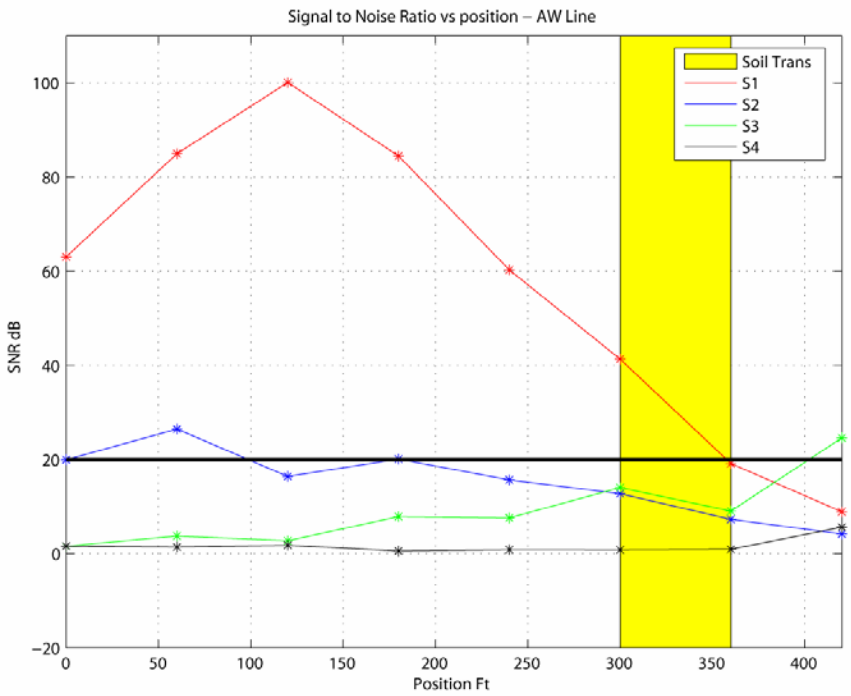

Figure 147. Signal to noise ratio vs distance along the AW threat line.

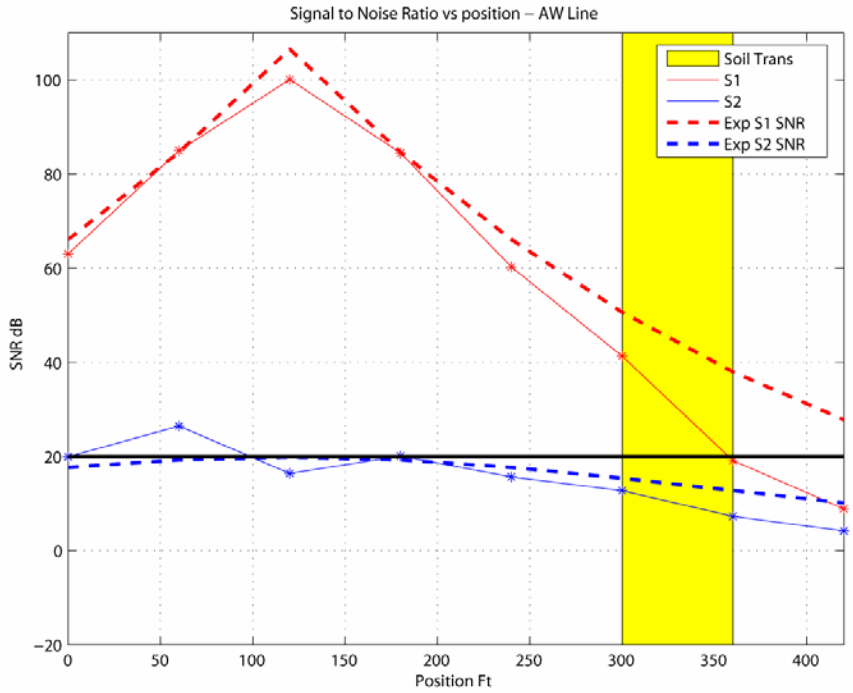

Figure 148. Signal to noise ratio for sensors 1 and 2 versus distance along AW threat line.

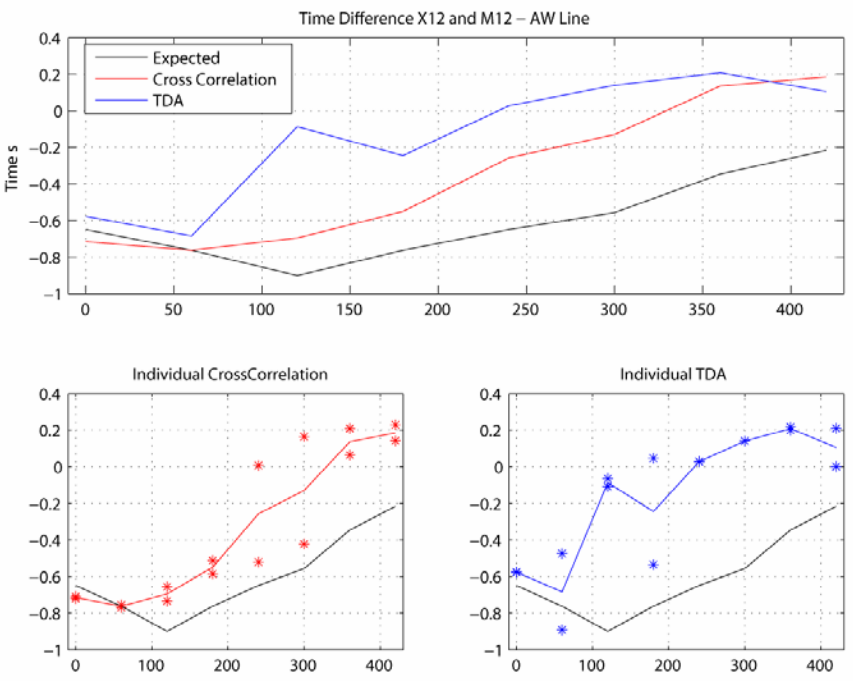

Figure 149. Average time difference of arrival for sensors 1 and 2 versus distance AW threat line. Time difference determined from both wave front arrival and cross correlation.

Table 24. Cross-Correlation and Manual Time of Arrival for Shortfield AW Threat Line

	X12	M12
C0	-0.720	-0.577
	-0.709	-0.575
mean	-0.715	-0.576
C60	-0.755	-0.892
	-0.769	-0.475
mean	-0.762	-0.684
C120	-0.734	-0.065
	-0.656	-0.109
mean	-0.695	-0.087

	X12	M12
C180	-0.586	-0.535
	-0.513	0.046
mean	-0.550	-0.244
C240	0.007	0.027
	-0.521	0.029
mean	-0.257	0.028

7.7.8 Configuration 4 – ShortField Backhoe

Configuration 4 is identical to Configuration 3, the only change is that instead of using the down-hole rifle as a source we are using a 15,000 lb backhoe as the threat source. Due to the geography of the test site, the backhoe could only be deployed to the edge of the soy bean field. This means that data could only be collect with the threat in the loamy soil (locations 0 through 180 for all 5 threat lines). Since we were not allowed by the land owner to dig in the field, the backhoe was used as an impact source. Specifically, the backhoe was driven to a location 8-10 feet from each of the threat locations (orientation of the tractor relative to the threat location varied) where the side support legs and front bucket were lowered to stabilize the tractor. The backhoe then extended the bucket arm and struck the bucket multiple times (5-7 times per data file) against the ground at the threat location. A minimum of three data files were recorded at each threat location.

Figure 150 shows the power spectral density for a typical backhoe impact. As was the case for the down-hole rifle, the majority of the signal energy is contained within the 5-100 Hz band, thus we utilized the same 500th order 5-100 Hz band-pass filter employed on all of the previous analysis. As we would expect, there is a strong acoustic signature from the backhoe in the 200-400 Hz band. As we can see in Figure 150, the 5-100 Hz filter does an excellent job attenuating this acoustic energy.

One of the issues with analyzing the backhoe data is defining exactly how the signal to noise ratio is determined. In all of the previous analysis, we have determined the signal to noise by calculating the power in a short time segment which includes the down-hole rifle shot, and comparing that power to the power of another time segment within the same data file which does not contain the rifle shot. In this way, we are able to determine the signal strength of the threat signature versus the current background/sensor conditions. In the case of the backhoe impacts, the analysis is complicated by the fact that the tractor is always running. Since the tractor is quite noisy, this results in a significant increase in the background "noise" (Note: Since the seismic signature from the tractor

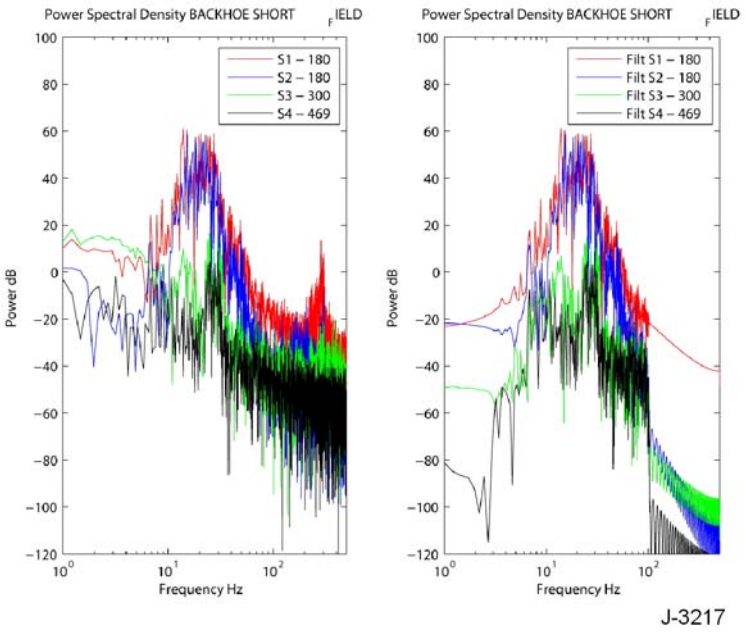

Figure 150. Power spectral density for the backhoe during bucket impact (Location AE180).

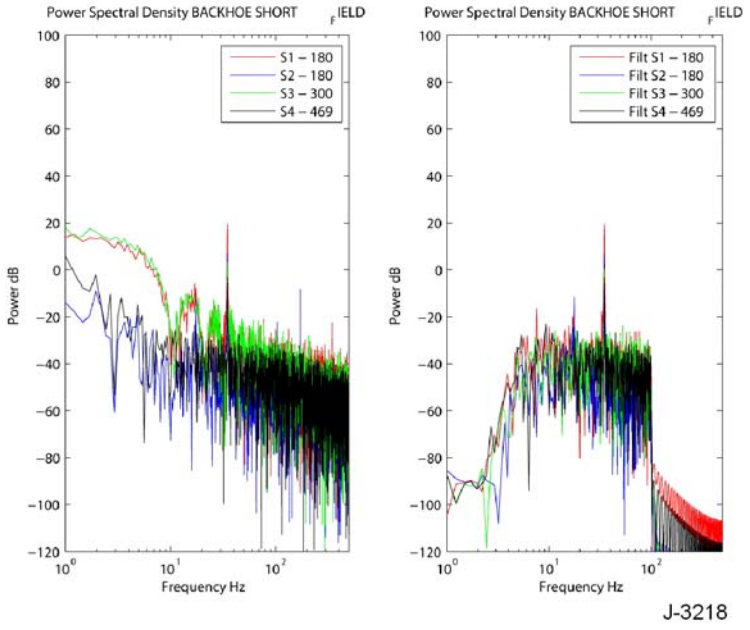

Figure 151. Power spectral density for the backhoe idling (Location BW120).

running is one of the tools we use to identify threat types, it can be argued that this background noise is in fact threat and not noise). Figure 151 shows the power spectral density of the backhoe idling. As we can see, there is a very sharp peak at 30 Hz (likely directly associated with the engine idle speed) and a 20 dB increase in the broad spectrum signature. To account for this uncertainty, we will present the signal to noise in three forms:

1. Bucket impact power versus backhoe idle background.
2. Bucket impact power versus quiet[2] background.
3. Backhoe idle power versus quite background.

Figure 152 shows all three forms of average SNR versus distance for the backhoe. In Figure 152(A), we see that for the two sensors located in the loam that the backhoe impacts are 40-60 dB above the backhoe background idle out to a range of 400 ft, while at sensors 3 and 4, located in the shale, the impact is 20 dB above the backhoe background out to a range of 600 ft. As can be seen, there is a large variance in the magnitudes of the signals with respect to range. This is largely due to the variance in the strength of the bucket impact with the ground. Figure 153 shows the SNR of the individual data points. As we can see, there is a large (as much as 60 dB) variance in the signal strength at any threat location. Thus it is not surprising that there is a large variance in the average data. This variance makes it impossible to estimate the maximum detection range of the backhoe impacts in each of the soil conditions.

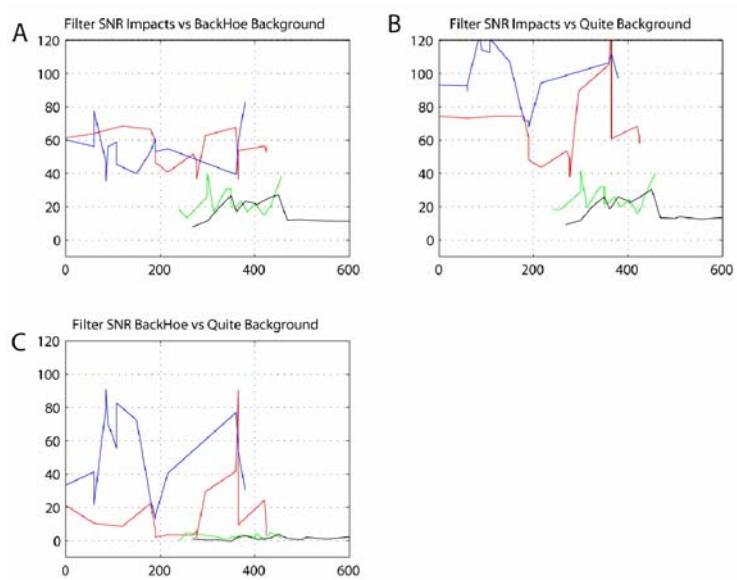

Figure 152. Backhoe signal to noise ratio versus distance. 59(A) Impact versus Backhoe Idle. 59(B) Impact versus quite background (no equipment). 59(C) Backhoe idle versus quite background.

[2] For this case, we have taken the background data from one of the Configuration 3 data files and used it as a sample background for all of the backhoe data.

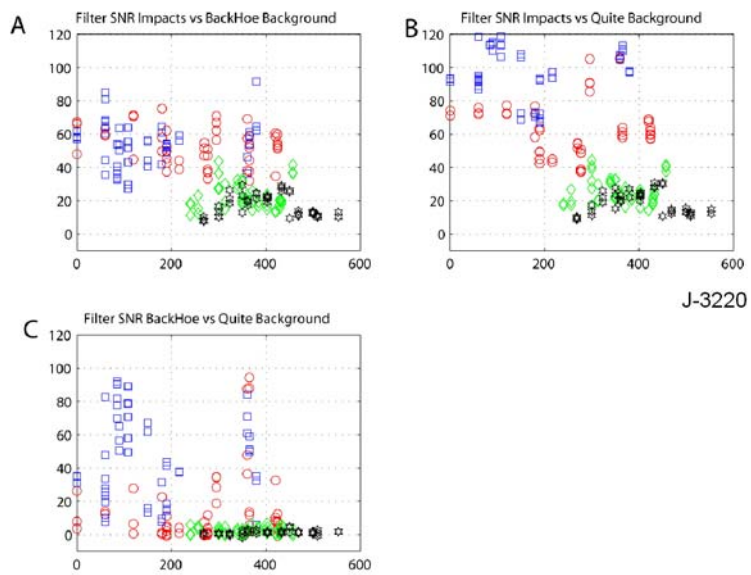

Figure 153. Backhoe signal to noise ratio versus distance. 60(A) Impact versus Backhoe Idle. 60(B) Impact versus quiet background (no equipment). 60(C) Backhoe idle versus quiet background.

Returning to Figure 152(B), we see that comparing the bucket impact power with respect to a quiet background results in a 20 dB increase of the SNR for sensors 1 and 2 while there is only a minimal increase in the SNR for sensors 3 and 4. This essentially means that the backhoe idle is not present in the sensor 3 and 4 data. When comparing the strength of signals in the loam and shale, we see that there is roughly a 60 dB strength advantage for the signal propagation in the loam. It is difficult to determine how much of this signal drop is due to the soil transition and how much is due to other factors. To try and estimate the power drop across the transition, we can compare the expected power drop versus distance in the various soil conditions. Using the data from the 240 ft range, we see that the signal strength in the loam is roughly 70db and the signal strength in the shale is 20 dB. Since sensors 3 and 4 are a minimum of 120 ft from the soil transition boundary, we can estimate from Figure 109 that there is a 60 dB attenuation of the signal while traveling through the shale. Similarly from Figure 102, we can estimate that the 80 feet the signal travels through the loam results in 20 dB of attenuation for a total signal attenuation of 80 dB. The same signal traveling 200 ft through loam only would be attenuated 60dB. If there were no attenuation due to the soil transition, we would expect a 20 dB difference between the signals measured in the loam versus the sensors in the shale. Thus we can estimate that the soil transition attenuates the signals 30-40 dB, which is comparable to the attenuation seen in Configurations 2 and 3.

Figure 154 shows a spectrogram for a series of backhoe impacts at location BW180. As we can see from the figure, the individual bucket strikes are clearly visible as large magnitude low frequency wave packets. What is interesting is that we can clearly pickup the variation in engine speed as the bucket is maneuvered by looking at the high frequency acoustic signature at 300 Hz. Figure 155 shows a spectrogram of the backhoe idling. As we can see from the figure, we can clearly pickup a strong seismic signature of the engine running at approximately 30 Hz. In fact, we can clearly see the changes in engine idle speed as the motor is further idled down.

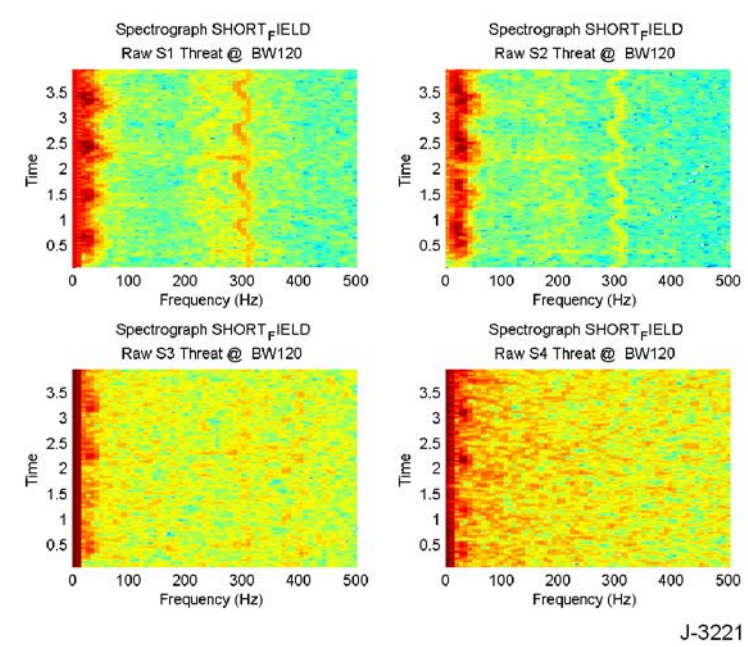

Figure 154. Spectrogram of the Backhoe impacts.

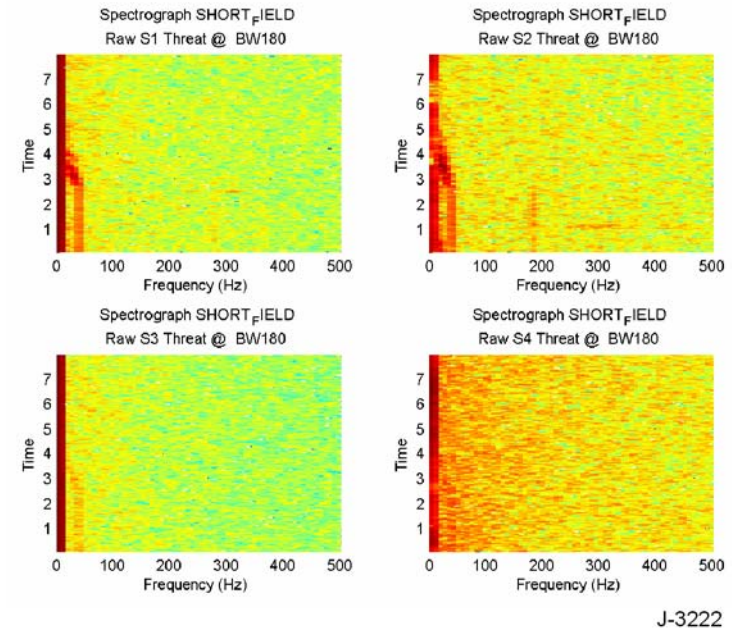

Figure 155. Spectrogram of the backhoe idling.

We have conducted some preliminary cross-correlation analysis of the backhoe data. Table 25 contains the preliminary sensor 1-2 correlation for the BW line and Table 26 contains the preliminary sensor 3-4 correlations for the BE line. In the case of the BW line, since sensors 1 and 2 are equidistant from the threat, we would expect that the time difference would be 0 s. Similarly, we would expect the sensor 3-4 correlation to be 0 s for the BE line. As we can see from the preliminary data, this is not true for all of the data. There are a number of explanations why this may be.

Table 25. Preliminary Cross-Correlation Backhoe BW Threat Line

Backhoe BW Line

D1	D2	D3	D4	S1-S2 time lag
				(sec)
216	216	420	553	-0.009
190	190	360	509	-0.027
180	180	300	469	0
190	190	240	433	0

Table 26. Preliminary Cross-Correlation Backhoe BE Threat Line

Backhoe BE line

D1	D2	D3	D4	S3-S4 time lag
				(sec)
379	120	457	457	-0.147
365	60	402	402	0.067
360	0	350	350	0.004
365	60	300	300	-0.191

First, the correlation method we are using for this analysis is the same used for evaluating the down-hole rifle shots. Specifically, we are taking time segments 2 seconds in length and correlating them. Since the backhoe data consist of multiple strikes, the number of strikes recorded at a given sensor may be different at each location due to transmission lags. Thus the correlations may be off due to the signals being different.

Alternately, we may be running into the situation that we experienced in configuration 1B, where the actual time and spectral signatures were different enough that it results in a poor correlation. Figure 156 shows the time signature of a series of impacts at location BE180. As we can see, while all of the signals meet our 20 dB criteria, the signature recorded for sensor 1 lacks the distinct peaking seen in the other 3 signals. While this may not preclude the use of correlation, it will reduce the fidelity of the correlation result.

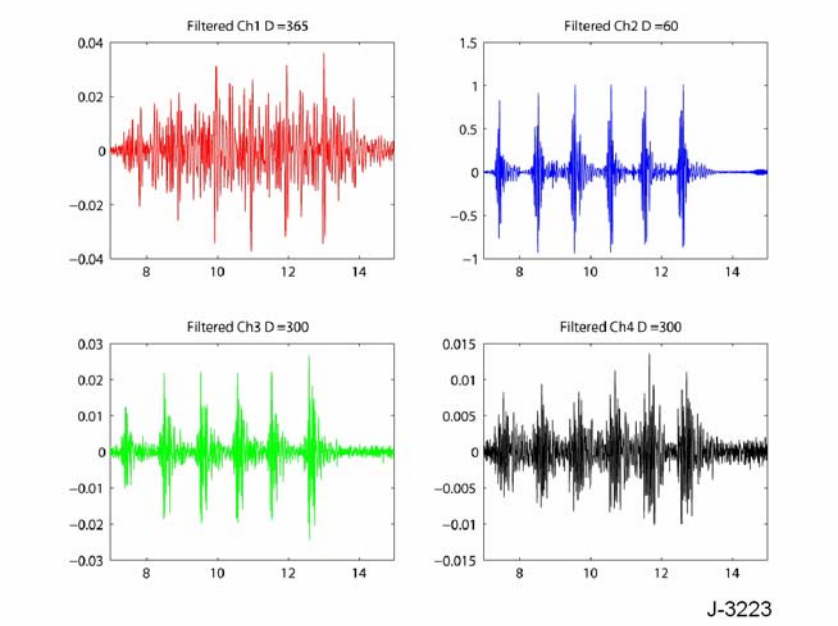

Figure 156. Time signature of the backhoe impacts at BE180.

Thirdly, the variance in the correlation results may be a direct result in our uncertainty in the origin location of the threat. As described earlier, the backhoe was driven near each of the threat locations at which point the bucket and side stabilizers where deployed to stabilize the vehicle. When the backhoe bucket is impacted with the ground, there are equal and opposite forces applied against the ground at the bucket and stabilizer contact points. Since the tractor is approximately 10 feet wide and 15 feet long, this results in a roughly 25 by 10 footprint for the source (the backhoe is 8-10 feet from the bucket impact point). Looking at the data for the BW line, we see that the position uncertainty is approximately 10 ft which could easily be accounted for by this uncertainty.

Lastly, as we have noted earlier, we could simply be documenting actual artifacts of the site geology.

7.8 Geophysical Modeling Effort

As part of the analysis effort, we have been working with Prof. George McMechan at the University of Texas/Dallas in an effort to model the geophysics at both our Andover test site and the complex soil conditions at the Kansas field site. Prof. McMechan has provided us with some preliminary results regarding the Andover site and continues to work at modeling the geophysics at

the Kansas field site (PSI has provided Prof. McMechan the details of the test site included in this report as well as sample data from test Configuration 3). Figure 157 show the results of the geophysical modeling of the Andover field site. Prof. McMechan summarizes the results as follows:

1. In the right hand (field data) plot, there are two traces superimposed at each distance, as there were two hammer strikes at each location
2. Both the synthetic and field data have (the same) distance-dependent scaling applied (for the plots only) to make the data more visible. Filters for both were about 10-100 Hz.
3. The S-waves and Rayleigh waves are highly dispersive, as a very low Q was needed to approximate the amplitude decay, so the nominal S velocity is lower than the observed.
4. One of the main concerns regarding details is that the field data is spatially aliased (about 6X for the surface waves).
5. Most of the main features are approximated in terms of time and relative amplitude. The source function is more complicated in the field data than in the synthetics.

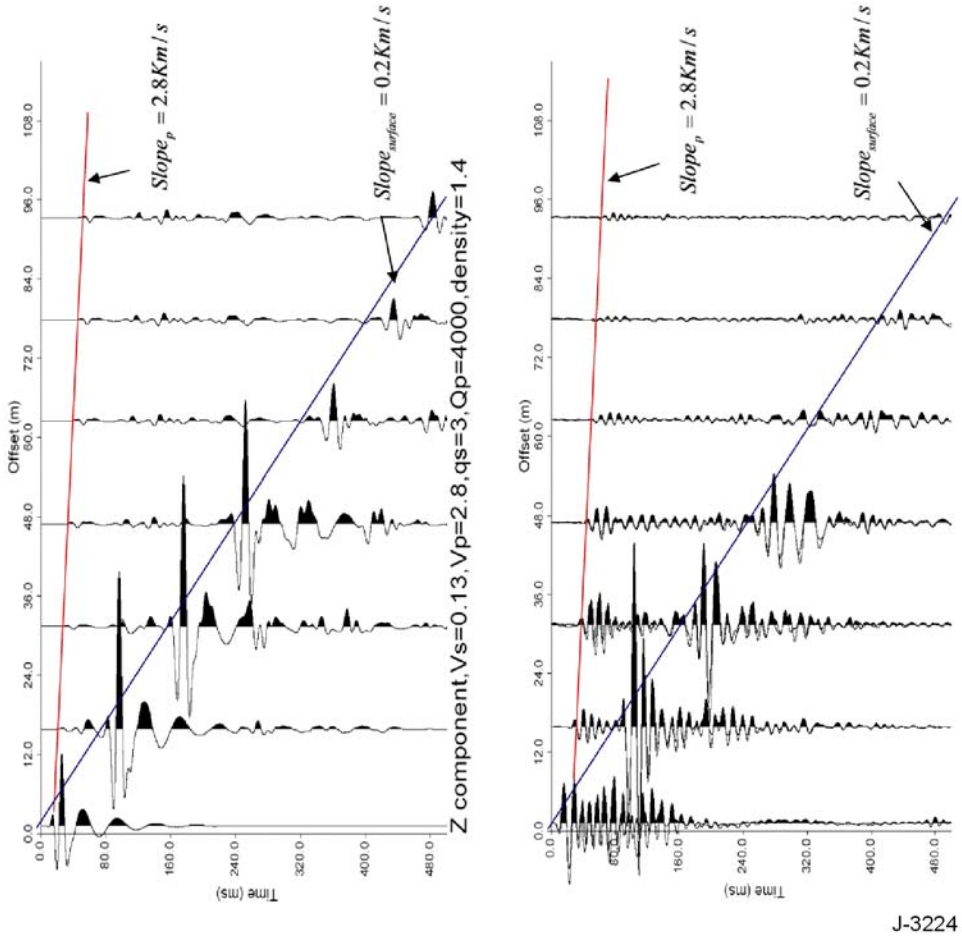

Figure 157. Geophysical modeling results for the Andover field site (Simulated results left, measured fieldtest data right).

7.9 Summary

We successfully collected a large amount of data at the Kansas field test site. We acknowledge the great assistance of Prof. Don Steeples in site selection, initial testing and many discussions. We collected data in a grid covering loam and shale/hillside using a down-hole gun as our primary stimulant threat acoustic source. This source was very reproducible and permitted repeated testing. The signature it generated was not as strong as many real threats and as a result it did not produce signals with large SNR at all the sensors, limiting the number of data sets where we were able to attempt triangulation.

We have presented the temporal signatures and acoustic frequency spectra acquired over the test site. Frequencies are not uniformly attenuated with distance as they propagate through the loam and shale, complicating time-of-arrival and PSD analyses. Loam attenuates the down-hole-gun signal less than shale. Acoustic signatures were observed in both directions across the soil discontinuity, but an attenuation of about 20-30 dB in signal strength was observed in the transition. The correlated arrival times at different sensors were tightly clustered for many shots

(to within a millisecond) indicating that precise measurement was possible (physics was not against us), however the propagation time was not as expected indicating that better understanding of the propagation is required. Both manual peak selection and automated cross-correlation approaches show promise. The derived arrival times are tightly clustered, with outliers often representing one acoustic cycle shift. Multiple strikes (in real world applications) would permit precise arrival time determination (just as the multiple shots in this field test did). However the accuracy remains to be determined. Neither algorithm is sufficiently robust presently to permit automatic triangulation. The system has demonstrated adequately low and invariant operating noise under a variety of environmental conditions (warm, cold, windy). The backhoe displayed a very strong acoustic signature that was observable across the soil discontinuity in all four sensors at distances up to the maximum 700 feet in this test site.

Once the algorithms are further improved, we believe that the installed sensor network could be "calibrated" with an acoustic source to permit the time-of-arrival and propagation to be characterized and train the Pigpen sensors for that location.

A summary of the sensor network performance at the end of this programbased on our analysis of the Kansas field test data is:

1. PIGPEN can detect the 30-06 down-hole rifle to a range of 400 ft in sand/loam.
2. PIGPEN can detect the 30-06 down-hole rifle to a range of 200 ft in limestone/shale.
3. Threat signatures are degraded 20-30 dB (depending on initial signal strength) as they transition from limestone to sand. We were able to observe attenuated threat signatures across this discontinuity in both directions.
4. In the best case, PIGPEN can localize threats repeatable to ±7 ft in sand
5. In the best case, PIGPEN can localize threats repeatable ±9.6 ft in slate
6. Worst cases exhibited much poorer performance.
7. We were able to observe the unique signature and repeated strikes from a Backhoe across the discontinuity at all sensors.

Due to the signal degradation across the soil discontinuity, PSI has not been able to establish the positional accuracy across the soil transition for the down-hole rifle acoustic source. In addition, positional accuracy may be degraded by steep slopes within soil types. Further algorithm development in conjunction with on-site calibration will be required to correct for non-uniform soil conditions.

A summary of responses to technical reviewers comments are included in Appendix C. The authors acknowledge the great assistance provided through many technical discussions and strong advocacy with Prof. Don Steeples of Kansas University, Ms. Daphne D. Zurko (of the Northern Gas Association and NYSERACH), and Mr. James Merritt of DOT. We appreciate the guidance and support of Prof. Steeples and Mr. George Janega during the Kansas field testing.

Appendix A
Test Plan for PIGPEN Testing in Complex Soil Conditions

Revision A

3 November 2006

Gary E. Galica

Physical Sciences Inc.
20 New England Business Center
Andover, MA 01810

tel. 978-689-0003
fax 978-689-3232
galica@psicorp.com

Revision History

Revision	date	explanation
Draft	3 Oct 06	Initial draft
A	3 Nov 06	Incorporating comments on Initial Release - sect 1.0 Northeast Gas Association changes to NYSEARCH / NGA - sect 2.0 discuss sensor separation - sect 2.0 add description of relationship between modeling and test results - sect 5.1 add description of rationale for Configuration 1 testing

1.0 Introduction

With funding from NYSEARCH / NGA and the Department of Transportation's Office of Pipeline Safety, Physical Sciences Inc. has been developing the Proactive Infrasonic Gas Pipeline Evaluation Network (PIGPEN). PIGPEN is a spare network of seismic sensors that protect gas pipeline infrastructure by detecting, identifying, and locating potential third-party threats.

While we have demonstrated threat location with an average accuracy of roughly 3 m at a range of 150 m in uniform soil conditions, NYSEARCH and their independent technical consultant (Dr. Don Steeples) have expressed concern about PIGPEN's ability to triangulate threats in complex soil conditions. In response, PSI proposed to plan and execute a field test designed specifically to characterize PIGPEN's performance under complex soil conditions.

NYSEARCH's geophysical consultant has raised several issues regarding triangulation accuracy under complex geological conditions. We acknowledge these issues and have had discussions with NYSEARCH and the consultant regarding techniques for improving accuracy in the field. The basic problem is illustrated in Figure A-1. Surface waves refract at interfaces of differing soil types leading to erroneous calculation of source location

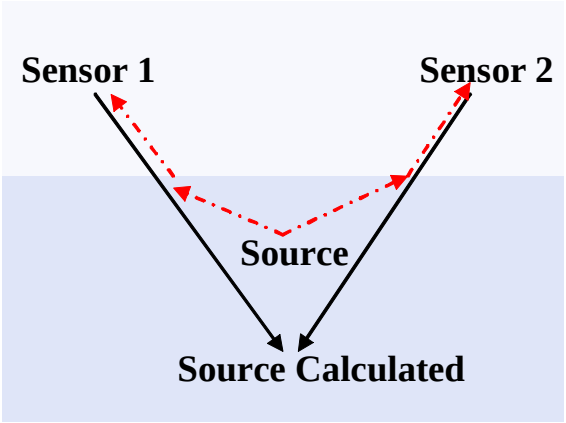

H-4248

Figure A-1 Surface waves refract at interfaces of differing soil types leading to erroneous calculation of source location.

In order to assess these effects on PIGPEN performance and to develop means of compensating for these effects, we proposed additional activities to address the remaining recommendations made by NYSEARCH's geophysical consultant:

- Conduct additional field testing to address PIGPEN performance in complex soil conditions

- Incorporate geophysical modeling components into the overall system model to address PIGPEN performance in complex soil conditions

2.0 Field Test Overview

We proposed a field test specifically designed to address the issues of performance in inhomogeneous soils, per the discussions with NYSEARCH and their geological consultant.

Figure A-2 shows the schematic field test configuration. We would deploy at least 4 EP-1 type PIGPEN sensors over a site that has non-uniform, but well characterized soil conditions. We would deploy threats at multiple locations and measure synchronized time-series data from each sensor. We will test at the maximum range allowed by the available sites. Ranges of 100-500 m are appropriate. Using those data, we will:

- Assess the performance of the existing PIGPEN triangulation algorithm.
- Develop compensation techniques (as discussed previously) to improve triangulation accuracy.
- Validate the error model

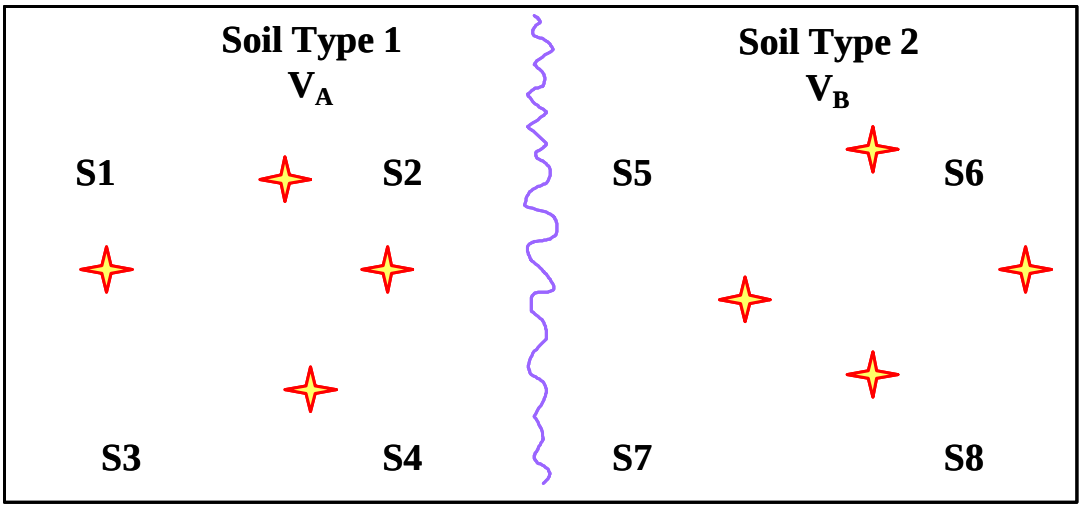

Figure A-2. Schematic configuration of the proposed complex soil condition field test.

We will also compare our field test results with the results of a geophysical model of the site. The geophysical model will be based on the soil characteristics and test geometry but will be developed independently of the test results.

3.0 Test Site

NYSEARCH's consultant has identified a site that is suitable for the complex soil testing. The site is located near Lawrence, KS at latitude 39 deg 2 min 8 sec North and longitude 95 deg 21 min 59 sec West. Figures A-3 and A-4 show the topographic map and aerial photographs of the site. The areas labeled A and B are identify different soil types. In addition, there is an elevation change (23% grade) between A and B.

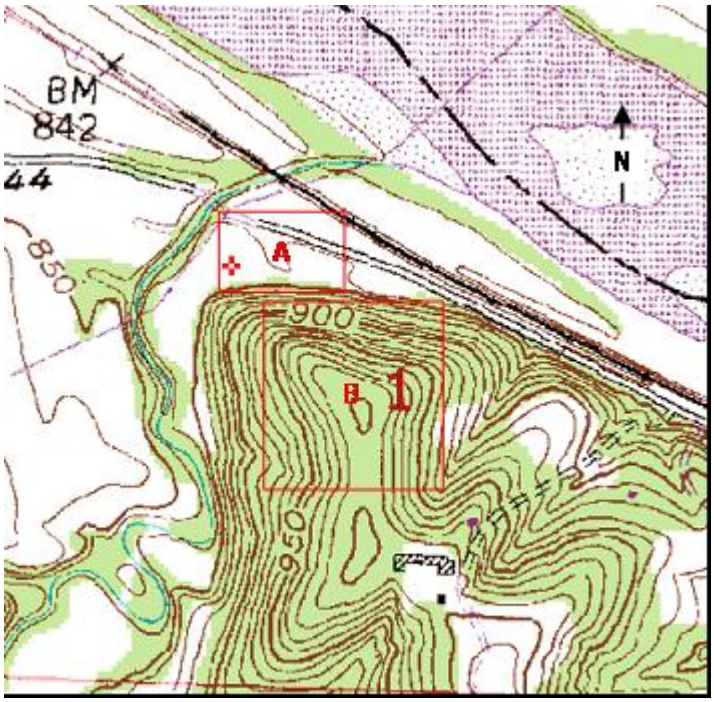

Figure A-3 Topographic map of the site.

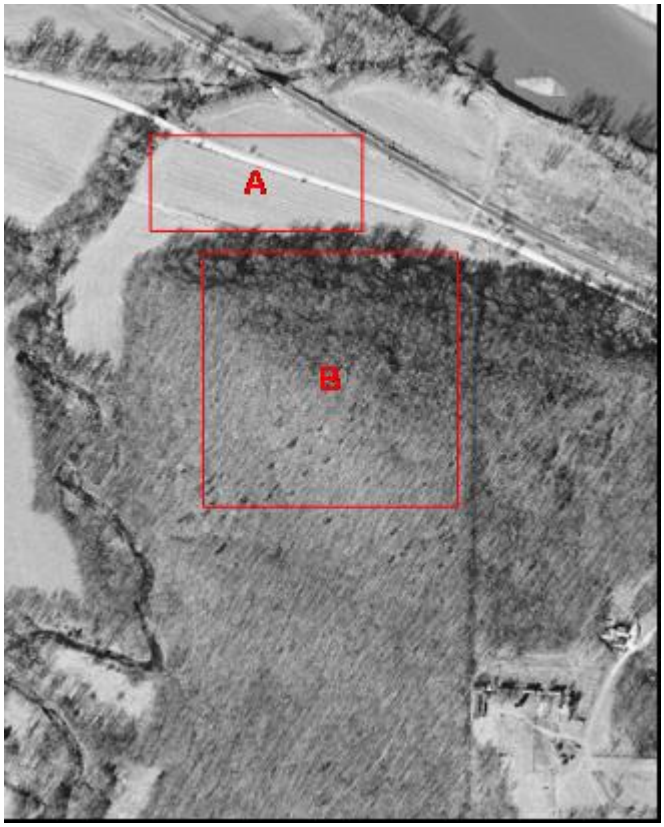

Figure A-4. Aerial photograph of the site.

The geology on the upland site (Area B) is alternating flat-lying limestones and shales of Pennsylvanian age with average P-wave velocity of about 10,000 feet per second, with Poisson's ratio of about 0.25. The geology on the river valley site (Area A) is about 50 feet of Pleistocene alluvial sands, gravels and clays with an average P-wave velocity of about 1600 feet per second and Poisson's ratio of 0.40 to 0.45. Water table is about 25 feet below ground surface. The seismic velocity in the dry alluvium is about 1000 feet per second. Bedrock at 50 foot depth is flat-lying limestones and shales of Pennsylvanian age.

4.0 Test Equipment

We will instrument the test site using four PIGPEN EP sensors connected to a data acquisition system by cables. We will use a combination of single impacts and a tamper as conditions allow. With the current cabling, the sensor separation can be as great at 250 m.

We will survey the sensor and impact locations on the site using a combination of GPS (+/-7 m accuracy), tape measures (+/-0.3 m accuracy), and rangefinders (+/- 1 m accuracy).

We will provide a separate analysis computer for data analysis and assessment. The analysis computer will include a post-processor for performing the triangulation algorithm

5.0 Test Configurations

We will instrument the site in three different configurations to accomplish our measurement objectives.

5.1 Configuration 1: Individual Area Characterization & Triangulation Performance

In Configuration 1, we will characterize the soil conditions in the two areas as well as determine the triangulation performance within the single soil types (Figure A-5). This configuration will show whether inhomogeneity and/or anisotropy are present within the single soil types. It is meant as a preliminary measurement to the complex soil testing (Configurations 2 and 3).

Within each area, a T-formation using 3 sensors will be used. Impacts using the sledgehammer or other impact source will be made every approximately 20 m down the long axis (see Figure A-6). Three sets of three strikes will be taken at each location. In this configuration, we expect the time of arrival of the signals at S1 and S2 to be simultaneous. Any time lags observed between S1 and S2 will indicate soil non-uniformities or errors in surveying.

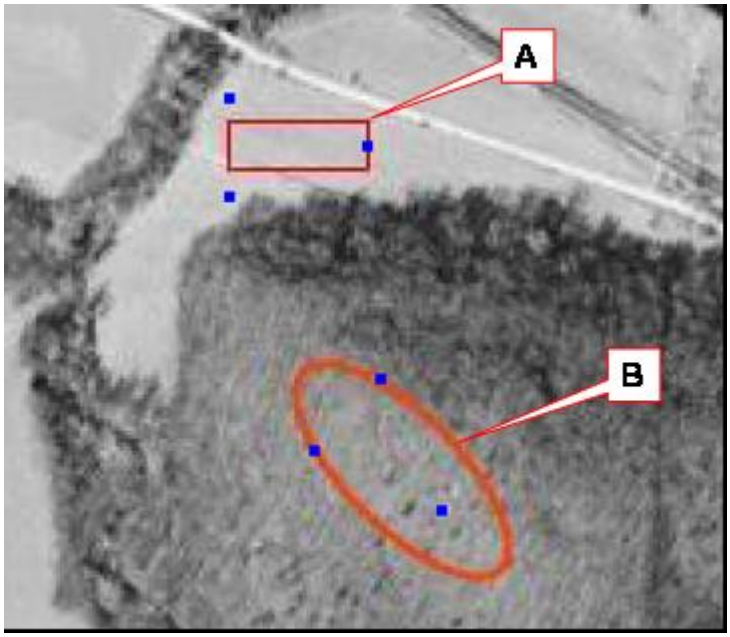

Figure A-4: Configuration 1: 3 sensor T formation in both soil types

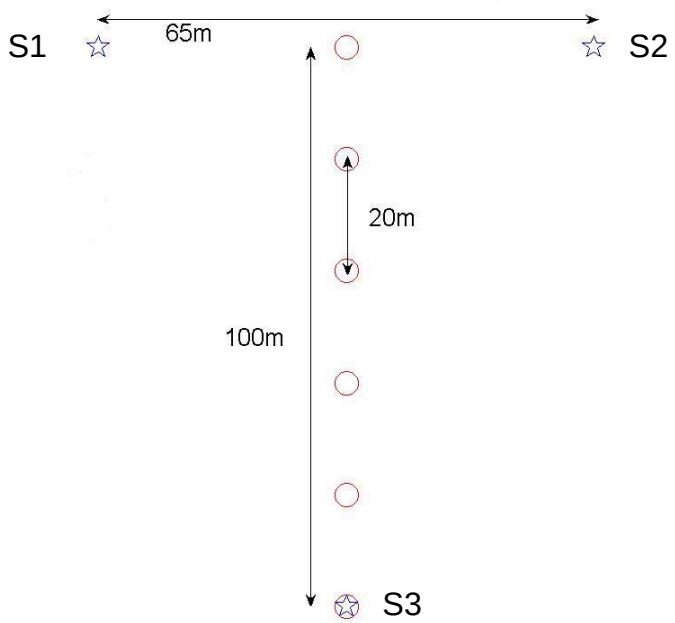

Figure A-5: Configuration 1: Three sensor T formation (blue stars) and impact locations (red circles)

5.2 Configuration 2: Short Field Complex Soils

A 4 sensor parallelogram deployment with two sensors in each type of soil will be used in the short and long field configurations. (Figure A-6) The desired length of one side between sensors is about 100m for the short field configuration. An impact source will be used along with a soil tamper (as conditions allow) for threat sources. Impact locations will include inside as well as outside the sensor parallelogram. Solution error plots were generated for the desired geometry under uniform soil condition assumptions (Figure A-7). This uniform soil solution gives a baseline to what solutions might be with a non-uniform soil. Locations where the solution is not strong will be explored, along with other locations outside the diamond formation.

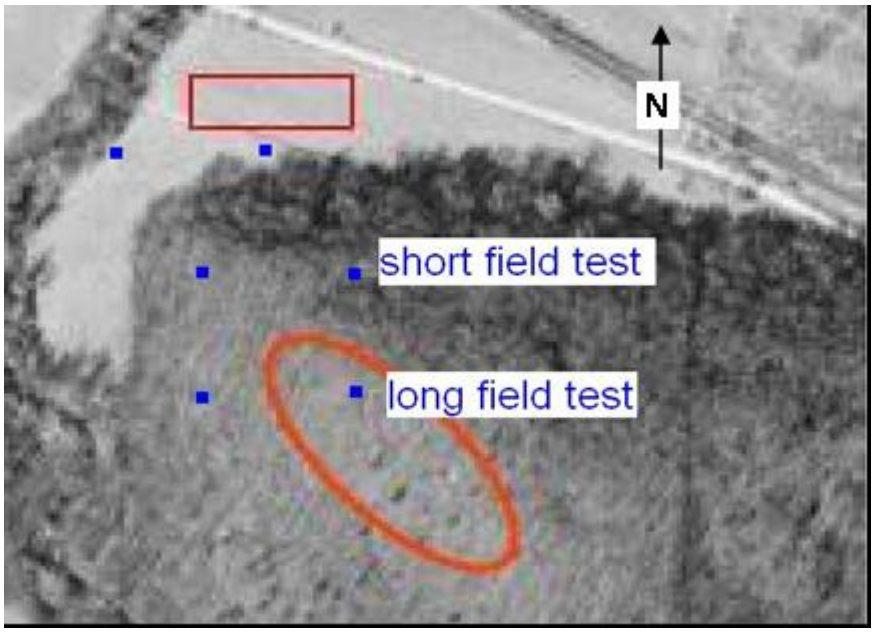

Figure A-6: Rough Sensor Locations for Long and Short Field Tests

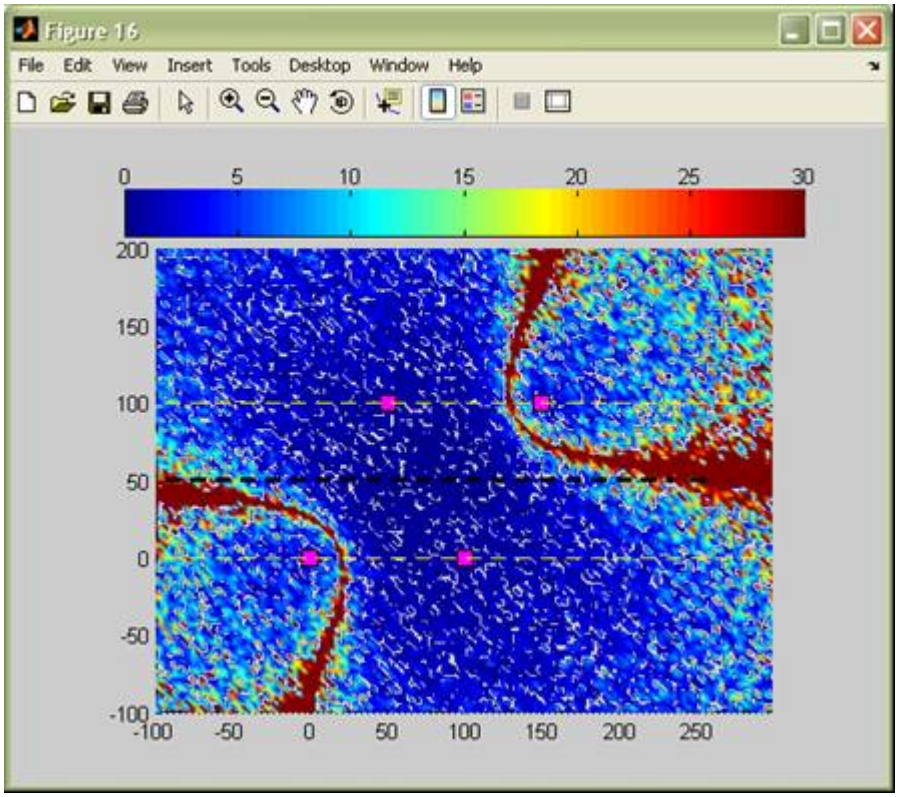

Figure A-7: Error Field for a 100 x 100 m Diamond for a uniform soil speed of 1600 ft/s with a zero mean 0.002 s Gaussian Time Error.

The source locations are defined in 5 separate north-south running lines (Figure A-8). Impact locations B serve both as locations of strong solutions and also allows for a similar T formation as done in the individual soil characterization. Impact locations A are those with weak algorithm solutions outside the parallelogram formation. Impact locations C are within the diamond formation and should have strong algorithm solutions. This will allow for soil characterization for that region of non-uniformity.

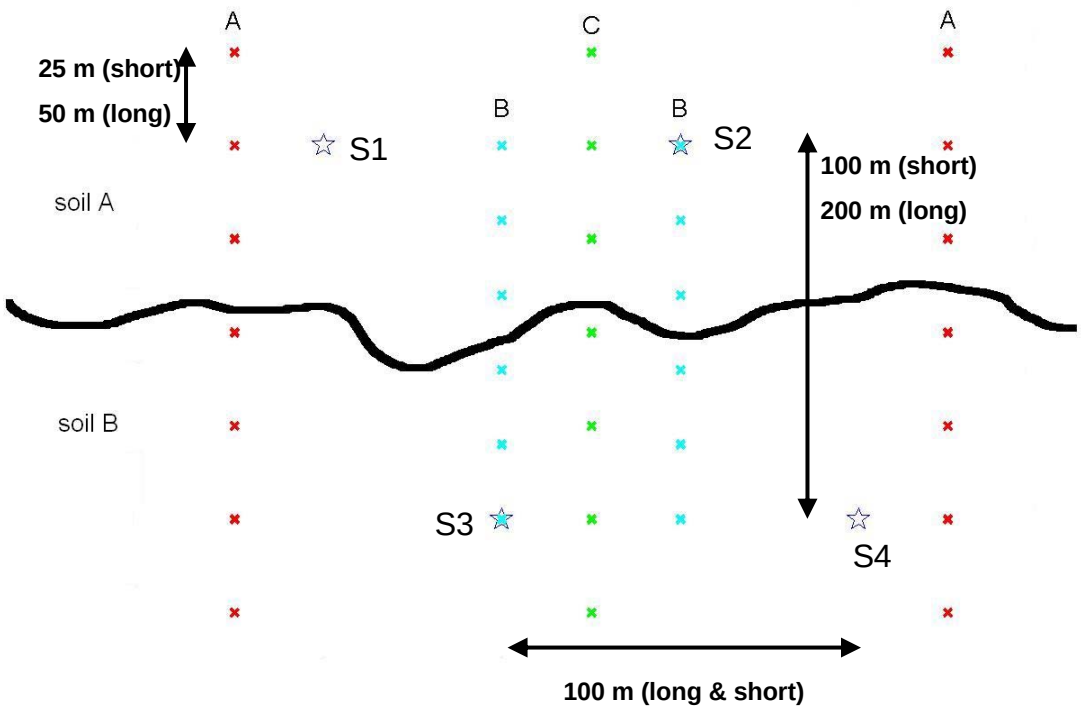

Figure A-8: Sensor (Blue Stars) and Impact Locations (A-C)

5.3 Configuration 3: Long Field Complex Soils

The long field configuration and test are analogous to the short field except with N-S sensor distances of about 200 to 250 meters. The E-W separation remains at 100 m. An analogous source location pattern with greater spacing than in the short field configuration.

6.0 Schedule

Table A-1 summarizes the test schedule.

Table A-1. Test Plan Summary

DAY 1	Arrival (PM)
DAY 2	Survey site Survey sensor and threat locations – Config-1 Deploy sensors - Config-1 Sensor and data acquisition system checkout Acquire data Config-1 Assess Config-1 data (PM)
DAY 3	Acquire additional data Config-1 (AM) Survey sensor and threat locations – Config-2 Deploy sensors - Config-2 Acquire data Config-2 Assess Config-2 data (PM)
DAY 4	Acquire additional data Config-2 (AM) Survey sensor and threat locations – Config-3 Deploy sensors - Config-3 Acquire data Config-3 Assess Config-3 data (PM)
DAY 5	Acquire additional data Config-3 (AM) Retrieve Equipment
DAY 6	Extra day

Appendix B – Time difference of arrival estimate across the soil discontinuity:

One of the major goals of the Kansas field test effort was to establish whether PSI could correctly establish position across a soil discontinuity. Since the soil velocities are an order of magnitude different across the boundary, it is necessary to compensate for the velocity differences. In this report, we have plotted the measured time difference of arrival relative to an estimated time difference of arrival. This estimated time difference was determined using the following simple analysis.

Figure B.1 shows a 2 dimensional projection of the test site. The red x's represent the threat locations while the sensor locations are noted by the red and green stars. The solid blue line in Figure B.1 shows a reasonable estimate of where the soil transition occurs. As we can see from the figure, the seismic signals from a threat must travel through different soil types to reach the various sensors. To correct for this, PSI proposed a simple linear model, where we plot the distance between the know threat location and all of the sensors. We then determine how much of that distance is contained in each soil type. Since the soil discontinuity shown in Figure B.1 is not uniform, we created a simplified model shown in Figure B.2.

In Figure B.2, we have simplified the 2D projection making a linear estimate of the soil discontinuity. Now we can easily break the path between a sensor and a know threat location into two segments l_1 (the portion of the path in the loam) and l_2 (the portion of the path in the shale). The estimated time difference of arrival can now be estimated using the following formula

$$\Delta t_{12} = t_1 - t_2$$

where

$t_1 = l_{11}/v_1 + l_{21}/v_2$

$t_2 = l_{12}/v_1 + l_{22}/v_2$

l_{11} = the distance between the threat and sensor 1 in the loam

l_{12} = the distance between the threat and sensor 2 in the loam

l_{21} = the distance between the threat and sensor 1 in the shale

l_{22} = the distance between the threat and sensor 2 in the shale

v_1 = the wave speed in loam

v_2 = the wave speed in shale.

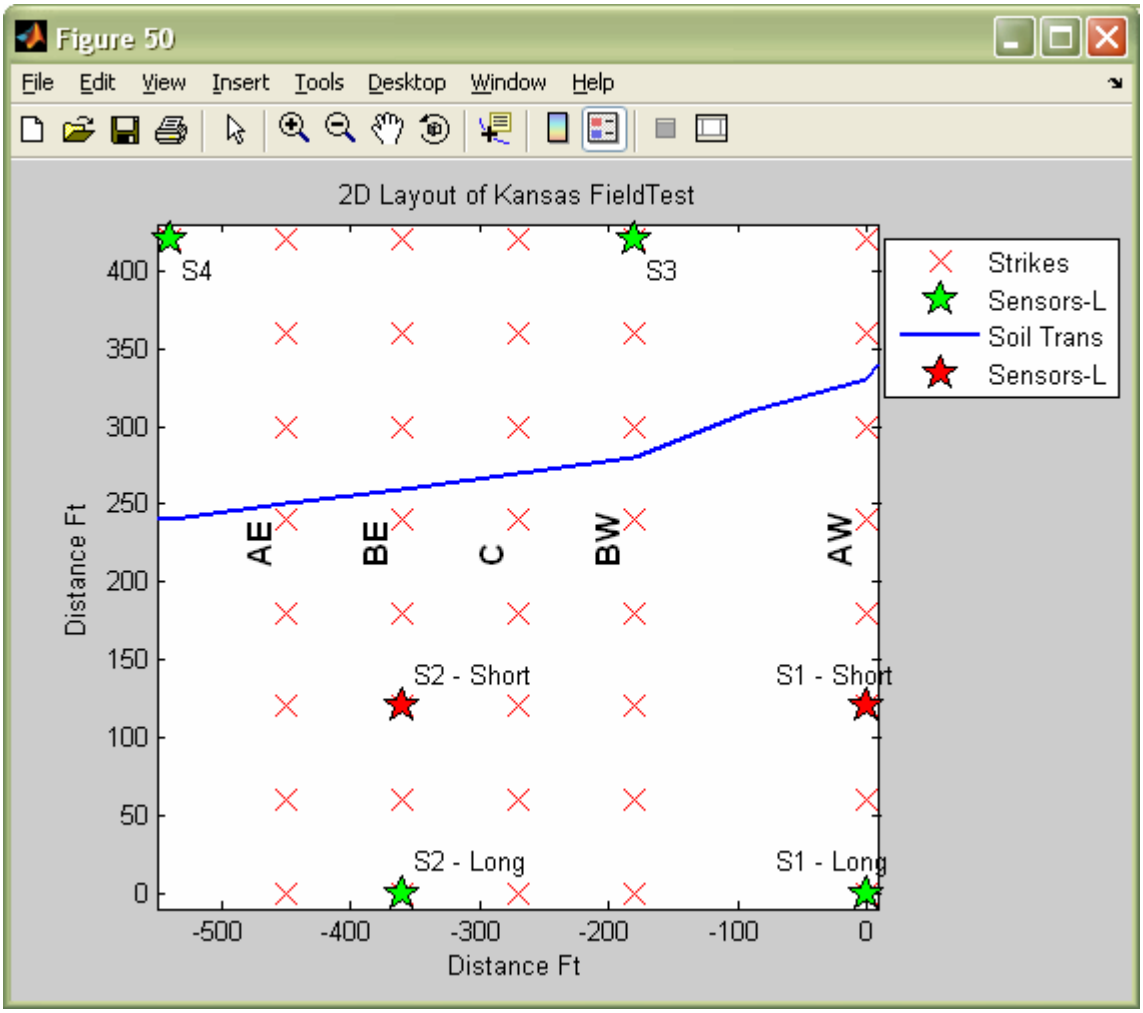

Figure B.1. 2D projection of the Kansas field site. The above the solid blue line the soil is shale while below the blue line the soil is loam.

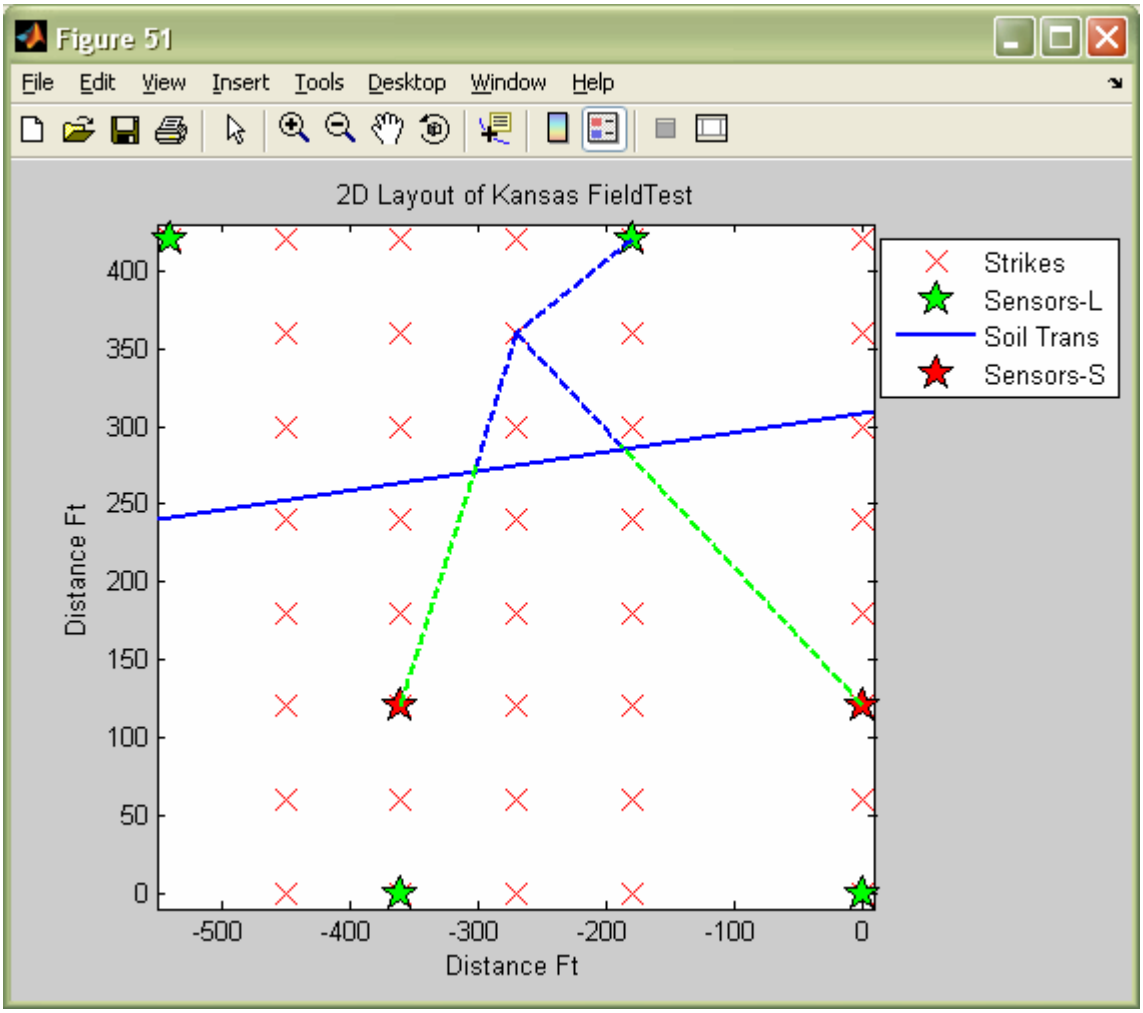

Figure B.2. Simplified 2D projection of the Kansas field site. The above the solid blue line the soil is shale while below the blue line the soil is loam.

Appendix C: Reviewers Comments and Response. We have mode changes in the report text to reflect these comments.

Chapter 7 covering the Kansas field testing was reviewed by Daphne D'Zurko, Executive Director NYSEARCH, and Prof. Don Steeples, Dept. Geophysics Univ. Kansas. Listed below are their comments and PSI's responses:

Comment 1 (D. D'Zurko)
Public Page - the conclusions on "threat detection range" are based on the highest confidence data and in one case the manual wave front time-of-arrival technique. In the details, the low confidence data shows positional errors of 96 ft or 10 times what is listed for the public section. I don't feel that this is a factual representation of where we are. Rather, while this "public" section may not go into the detail, it needs to be toned down AND somewhere we should have a summary establishing the explanation for the RANGE of results and what that range is.

D. Steeples:
I AGREE.

ON PAGE 1THEY STATE: "SIGNIFICANT ALGORITHM DEVELOPMENT WITH ON-SITE CALIBRATION WILL BE REQUIRED TO CORRECT FOR NON-UNIFORM SOIL CONDITIONS."

THIS IS A VERY IMPORTANT REALIZATION ON THEIR PART. TWO KEY ITEMS SHOULD BE RECOGNIZED HERE: "ON-SITE CALIBRATION" WILL NOT BE EASY AND IT WILL NOT BE CHEAP, AND "SIGNIFICANT ALGORITHM DEVELOPMENT" IMPLIES A HEAVIER PROCESSING LOAD THAN THEY HAD ANTICIPATED.

PSI Response:
The "threat detection range" is based upon the measured signal to noise ratio of the threat signal. PSI's algorithms require that the signal power of the threat be approximately an order of magnitude greater than the background noise (20 dB). The threat signal power drops below 20 dB at a range of 400 feet in the loam and 200 feet in the shale. This is a worst case range. In many instances PSI is able to extract valuable threat information with SNRs as low as 10 dB.

PSI has revised the summary and conclusion page to reflect the more mixed nature of the results.

PSI acknowledges that on-site calibration and additional algorithm development will be expensive. As a result, PSI has changed it's strategy for threat localization. All future development will focus on minimizing the complexity of the localization algorithm and the need for extensive on-site calibration.

Comment 2 (D. D'Zurko)
p. 8 - Results - third paragraph starting "Once the data is plotted, ..." This is where you talk about the process for figuring time of arrival, etc. I would like to see if Don Steeples agrees with this approach and will ask him.

D. Steeples:
WHAT THIS SAYS IS THAT, AT THIS TIME IN THEIR ALGORITHM DEVELOPMENT, A PERSON'S JUDGMENT IS REQUIRED TO SELECT A TIME WINDOW FOR ANALYSIS. I AGREE WITH THAT. I ALSO KNOW THAT EARTHQUAKE SEISMOLOGISTS HAVE WORKED FOR MANY YEARS TO DEVELOP FULLY RELIABLE AUTOMATIC PROCEDURES FOR SELECTING AND ANALYZING SUCH

WINDOWS IN SEISMIC DATA. I DO NOT THINK DEVELOPING AN AUTOMATIC PROCESS FOR THIS PROJECT WILL BE ACCOMPLISHED EASILY, CHEAPLY, OR QUICKLY.

PSI Response:

PSI has developed and demonstrated an automatic threat identification algorithm for the PIGPEN system. This algorithm was not used in this analysis for a number of reasons:

1. Since gunshots are not considered a significant threat to pipelines, gunshots have not been incorporated into the threat library.
2. At the time of this test, the threat identification algorithm and the localization algorithm have not been integrated together. Additional development is needed in this area.

Comment 3 (D. D'Zurko)

p.9 - 3rd paragraph - discussion of Fig 10 - I see this as one in a series of important pieces of information that I would like to get Steeples' comments. Also, I wonder if we have similar data for across soil boundaries. (Later in the report, we get into data across boundaries but I don't recall if it was it allowed calculation of varying wave speeds and if there were any assessment of the wave speed across the boundary.)

D. Steeples:

THE SEISMIC WAVES THAT ARE BEING RECORDED ARE DOMINANTLY SURFACE WAVES, AND THE WAVE SPEED OF 410 FT/SEC IS A REASONABLE VALUE. THE P-WAVES SPEED IS PROBABLY MORE IN THE RANGE OF 1200 TO 1500 FT/SEC, BUT THOSE WAVES ARE MUCH SMALLER IN AMPLITUDE THAN THE SURFACE WAVES.

Comment 4 (D. D'Zurko)

p. 11 - first paragraph - any data available to characterize change in wave speed?

D. Steeples:

VARIATIONS OF A FEW PERCENT ARE TO BE EXPECTED. ALSO, ANISTROPY (I.E., VELOCITY WITHIN A MATERIAL IS DIRECTIONALLY DEPENDENT) OF A FEW PERCENT WOULD NOT BE A SURPRISE. I DO NOT AGREE THAT ASSUMING 410 FT/SEC WAVE SPEED FOR THE ENTIRE FIELD WOULD BE EITHER VALID OR REASONABLE. THE MATERIALS UNDERLYING THE FIELD BEYOND DEPTHS OF A FEW FEET WERE LAID DOWN BY A RIVER, PROBABLY DURING FLOOD STAGE, SO HETEROGENEITY ON THE SCALE OF A FEW METERS IS ALMOST CERTAINLY PRESENT.

Comment 5 (D. D'Zurko)

p. 11 - bottom paragraph - discussion on outlier data because of saturated sensor- we need to acknowledge that this condition would also occur in real conditions. Any thoughts as to how to account for this in a live deployment?

PSI Response:

The sensor experiences two types of saturation: mechanical and electrical. In the case of electrical saturation, the voltage output of the PVDF sensor material (~±75 V max) exceeds the electrical limits of the pre-amplifier (±5 V max) and the analog to digital converter (±5 V max). To deal with this the EP units have a variable gain on the pre-amplifier which can be manually adjusted to prevent electrical saturation. In order to maintain consistency across data sets, this feature was not used during the Kansas field test. Future units should incorporate a circuit to automatically switch the pre-amplifier gains.

Mechanical saturation is more problematic. The sensor mass is intentionally restrained to prevent mechanical damage to the sensor. This restraint means that there is an upper limit to the voltage

output of the sensor. Since saturation distorts the signals being recorded, it may mask some important features of the signal. In the case of threat localization, this is not a big issue since any threat which is capable of mechanically saturating the sensor should be considered co-located with the sensor. On the other hand, it is unclear if data from a saturated sensor can be used to correctly identify the threat. PSI will explore this in greater detail in the next phase of the program.

Comment 6 (D. D'Zurko)
p.17 - second paragraph that starts Fig 19.... At end of paragraph, "This indicates that there is a problem with the cross-correlation method or very non-uniform soil properties." - What is Don Steeples reaction to this?

D. Steeples:
THERE APPEAR TO BE TWO REASONABLY LIKELY POSSIBILITIES HERE. ONE IS THAT SIGNIFICANT HETEROGENEITY IS PRESENT, WHICH CANNOT BE SUMMARILY DISCOUNTED. THE OTHER POSSIBILITY IS THAT THE CROSS CORRELATION WAS VICTIMIZED BY CYCLE-SKIP, IN WHICH CASE THE MAXIMUM CORRELATION COEFFICIENT OCCURRED IN THE WRONG PLACE. THIS CAN HAPPEN WITH DATA IN WHICH THE SIGNAL-TO-NOISE RATIO IS MARGINAL.

PSI Response:
The limitations of the cross-correlation approach are discussed in detail on pages 19-22. Specifically, using cross-correlation to determine the time difference of arrival assumes that the signals are both temporally and spectrally similar. As can be seen in Figure A- 20, there are clear differences in the temporal signatures recorded by the various sensors. This makes cross-correlation a poor method of determining time difference of arrival. PSI acknowledges that this a major weakness of it's localization approach. PSI is currently working to develop an alternate method of localization.

Comment 7 (D. D'Zurko)
p.22 - the approach for manually identifying the arrival time of the wave front - what does Don Steeples think about this approach?

D. Steeples:
HAVING AN ANALYST MANUALLY IDENTIFY THE WAVE FRONT WAS THE STANDARD IN EARTHQUAKE SEISMOLOGY FOR ALMOST A CENTURY, SO THIS IS NOT A PROBLEM

Comment 8 (D. D'Zurko)
p. 28 - middle - Reasons for not getting signal strength across the transition - are these reasons specific to this site or can you make a more general conclusion about soils and transitional areas in general?

PSI Response:
Item one is site specific. On the other hand, any soil discontinuity is going to attenuate signal transmission (item 2). The amount of attenuation is soil and site specific.

Additionally, in consultation with Don Steeples, item one should likely be restated as:

1. The poor signal **coupling** characteristics of the limestone/shale soil.

Comment 9 (D. D'Zurko)
p. 33 - bottom - comment on gaps between expected and measured dB values - in the particular case, there is a 15 dB gap. Is there any way to investigate the reasons for such a large gap with the data on hand? (Report says that it is unclear that this is related to soil transition.)

PSI Response:
As noted in Don Steeples response to comment 10, he believes that most of the signal attenuation is due to the complexities of the wave interaction at the soil transition. In addition, PSI has re-evaluated it's analysis of the signal propagation in shale. It now appears that the drop in signal power is primarily a function of the coupling between the rifle shot and the soil, and the sensor and the soil. The coupling of the rifle shot to the soil was particularly problematic along the soil transition due to the steepness of the slope and the mixed nature of the soil (the soil along the transition was a mixture of loam and small pieces of shale).

Comment 10 (D. D'Zurko)

p. 36 - 2nd paragraph - Figure A- 40 gaps, problems in attaining high confidence correlation - What can this data tell us? Does Don have a reaction?

D. Steeples:
AS FAR AS I CAN REMEMBER, THIS DATA SET IS THE FIRST ONE IN WHICH BEHAVIOR OF SEISMIC WAVES AT SIGNIFICANT GEOLOGIC BOUNDARIES HAS COME UP, EXCEPT FOR MY DISCUSSION A COUPLE OF YEARS AGO REGARDING REFRACTION AT SUCH BOUNDARIES.

WHEN A WAVE HITS A PLANAR BOUNDARY IN AN ORTHOGONAL DIRECTION, THE AMPLITUDE OF THE WAVE THAT CROSSES THE BOUNDARY IS GIVEN BY A RELATIVELY SIMPLE ACOUSTIC IMPEDANCE EQUATION:

TRANSMITTED AMPLITUDE = [(P1 * V1) - (P2 * V2)] / [(P1 * V1) + (P2 * V2)]

WHERE P1 AND P2 ARE MASS DENSITIES OF THE FIRST AND SECOND MEDIA AND V1 AND V2 ARE SEISMIC WAVE VELOCITIES IN THE FIRST AND SECOND MEDIA, RESPECTIVELY.

IN PRACTICE THE DENSITIES VARY BY ONLY ABOUT 20%, BUT THE WAVE VELOCITIES AT THE TEST SITE VARY BY AT LEAST A FACTOR OF 5 ACROSS THE GEOLOGIC BOUNDARY. CONSEQUENTLY, IF A SEISMIC WAVE HITS THE BOUNDARY ORTHOGONALLY, AT LEAST 3/4 OF THE SEISMIC AMPLITUDE IS LOST TO REFLECTION BACK FROM THE BOUNDARY.

IF THE WAVE HITS THE BOUNDARY AT AN ANGLE OTHER THAN 90 DEGREES, THE SITUATION BECOMES MUCH MORE COMPLICATED, AND A SET OF EQUATIONS DEVELOPED ABOUT 100 YEARS AGO BY ZOEPPRITZ MUST BE USED TO SOLVE FOR THE AMPLITUDES ON BOTH SIDES OF THE GEOLOGIC BOUNDARY. THE ZOEPPRITZ EQUATIONS CONTAIN SEVERAL TRIGONOMETRIC TERMS AND ARE NOT NECESSARILY INTUITIVE.

Comment 11 (D. D'Zurko)
p. 43 - bottom of 1st paragraph - "it is unclear whether the large difference between the expected value and the measured SNR is a result of soil transition or some other effect". Can we surmise other potential causes?

D. Steeples:
I THINK THE LARGE DIFFERENCE IS VERY LIKELY CAUSED BY THE SHARP BOUNDARY. ATTENUATION ACROSS THE BOUNDARY IS INDEPENDENT OF SOURCE TYPE AND STRENGTH.

Comment 12 (D. D'Zurko)
p. 51 - middle of text - "we can estimate that there is a 60 dB attenuation of signal while traveling through the shale" - What is Don's reaction to this?

IN GENERAL SHALE IS LESS ATTENUATIVE THAN SOIL.

PSI Response:
PSI has re-analyzed the signal to noise data from the shale. This re-analysis showed that the rate of attenuation in the shale and the loam is the same. What differs is the efficiency of the coupling of the source to the soil, and the sensor to the soil. Specifically with regards to the gun shot data, we are seeing a 30 dB attenuation of the **initial** signal strength in the shale versus the loam. Since we did not observe the backhoe impacting the shale, we are unable to specify exactly how much of the observed 60 dB attenuation is due to the soil discontinuity versus the sensor coupling with the shale. Using the gun shot data as a reference, it is likely that there is 30-40 dB of attenuation due to the soil discontinuity and 20 dB of attenuation due to the soil/sensor coupling.